Detection of Water Pollutants using Label-free Electrochemical Immunosensors and Electrolyte Gated Organic Field-Effect Transistors

Thi Thuy Khue Nguyen

USPC
Université Sorbonne
Paris Cité

université PARIS DIDEROT PARIS 7

THÈSE DE DOCTORAT

de l'Université Sorbonne Paris Cité

Préparée à l'Université Paris Diderot

Ecole doctorale: Chimie Physique et Chimie Analytique de Paris Centre

(ED 388)

Laboratoire Interfaces Traitements Organisation et DYnamique des Systèmes – ITODYS

Détection de polluants dans l'eau potable. Développement d'un immunocapteur sur la base d'un transistor organique à effet de champ à grille électrolytique

Par **Thi Thuy Khue NGUYEN**

Thèse de doctorat de **Chimie**

Dirigée par **Benoît PIRO**

Présentée et soutenue publiquement à Paris le 22 Octobre, 2018

Président du jury	François MAUREL	Professeur, Univ. Paris Diderot
Rapporteur	Florence LAGARDE	Directrice de Recherches CNRS, Univ. Lyon 1
Rapporteur	Hafsa KORRI-YOUSSOUFI	Chargée de Recherches CNRS, Univ. Paris Saclay
Examinateur	Corinne LAGROST	Directrice de Recherches CNRS, Univ. Rennes 1
Examinateur	Emmanuel BERGERET	Maître de conférences HDR, Univ. Aix-Marseille
Directeur de thèse	Benoît PIRO	Professeur, Univ. Paris Diderot

USPC
Université Sorbonne
Paris Cité

université PARIS DIDEROT PARIS 7

THÈSE DE DOCTORAT

de l'Université Sorbonne Paris Cité

Préparée à l'Université Paris Diderot

Ecole doctorale: Chimie Physique et Chimie Analytique de Paris Centre

(ED 388)

Laboratoire Interfaces Traitements Organisation et DYnamique des Systèmes – ITODYS

Detection of Water Pollutants using Label-free Electrochemical Immunosensors and Electrolyte Gated Organic Field-Effect Transistors

Par **Thi Thuy Khue NGUYEN**

Thèse de doctorat de **Chimie**

Dirigée par **Benoît PIRO**

Présentée et soutenue publiquement à Paris le 22 Octobre, 2018

Président du jury	François MAUREL	Professeur, Univ. Paris Diderot
Rapporteur	Florence LAGARDE	Directrice de Recherches CNRS, Univ. Lyon 1
Rapporteur	Hafsa KORRI-YOUSSOUFI	Chargée de Recherches CNRS, Univ. Paris Saclay
Examinateur	Corinne LAGROST	Directrice de Recherches CNRS, Univ. Rennes 1
Examinateur	Emmanuel BERGERET	Maître de conférences HDR, Univ. Aix-Marseille
Directeur de thèse	Benoît PIRO	Professeur, Univ. Paris Diderot

ACKNOWLEDGEMENTS

My PhD researches have been accomplished in the laboratory ITODYS (Interfaces, Traitements, Organisation et Dynamique des Systèmes) at University Paris Diderot, Sorbonne Paris Cité.

I would like to express my very great appreciation to my supervisor Prof. Benoît PIRO for giving me the opportunity to carry out my PhD and for his guidance, advices, supports, encouragements and inspiration during 3 years of PhD. He is one of the most patient and enthusiastic professor that I have ever known.

I am particularly grateful for the director of the laboratory, Prof. François MAUREL for his acception so that I could perform my PhD in ITODYS, and also for his help during my thesis process.

I would like to offer my special thanks to Prof. Minh Chau PHAM. She has given me precious advices and care in keeping my progress on schedule.

I wish to thank Dr. Guillaume ANQUETIN who, among other advices, guided my steps in organic compound syntheses, NMR and other characterization techniques.

My thanks are extended to the members of the Bioelectronics and Smart Surfaces group: Dr. Steeve REISBERG, Dr. Vincent NOEL, Dr. Giorgio MATTANA. and Dr. Samia ZRIG for the comfortable working environment.

I am heartily thankful to Dr. Jean-Marc NOEL, Mr. Alexandre CHEVILLOT, Dr. Philippe DECORSE (XPS), Mr. Pierre-François QUENIN, Ms. Brigitte EFTASSIOU, Ms. Brigitte DELAVAQUERIE and Mr. Jean-Claude PERTAYS for technical supports and helps.

I would like to thank Dr. Thanh HA-DUONG for the parties and kindness that helped me to participate in the ‘lab-life’.

My warm thanks go to Ha Anh NGUYEN, Thuan Nguyen PHAM TRUONG and Alexandra TIBALDI for their food and friendship.

I acknowledge the Vietnam International Education Development (VIED)-Ministry of Education and Training of Vietnam for offering me a PhD grant through the University of Science and Technology of Hanoi (USTH) program.

I take this opportunity to express my sincerest love and thanks to my family and my close friends, for the love and understanding.

ABSTRACT

Today, with the increase of the world population, the consumption of drugs and chemicals in agriculture has dramatically increased. It becomes a worrisome issue because a large amount of these molecules, excreted to the environment, are not well eliminated by water-treatment plants (when they exist) and are therefore released without control into the ecosystem. In large quantities, these chemicals are poisonous for living organisms, including humans.

Classical analytical methods for the detection of these chemicals already exist such as gas chromatography, high-performance liquid chromatography, possibly coupled with mass spectrometry, etc. However, despite their precision and reliability, these techniques are difficult to apply for on-site monitoring and costly, and they must be manipulated by skilled people. For this reason, my thesis proposes novel analytical approaches, which are easier to use and eventually cheap, to detect such pollutants in water (ground water or drinking water).

In the first part of my work, I developed an original immunosensor based on a competitive complexation and on an electrochemical (amperometric) transduction, for detection of diclofenac (DCF), which is a non-steroidal anti-inflammatory drug generally employed to protect patients from inflammation and relieve pain. The working electrode electrografted with two functional diazonium salts, one as molecular probe (a diclofenac derivative coupled with an arylamine) and the other as redox probe (a quinone) also coupled with an arylamine, was able to transduce the hapten-antibody association into a change in electroactivity. The transduction was designed to deliver a current increase upon detection of diclofenac ("signal-on" detection). The detection limit is ca. 20 fM in tap water, which is competitive compared to other label-free eletrochemical immunosensors.

In the following part of my thesis, I kept the same transduction approach (competitive immunoassay) but applied to an Electrolyte-Gated Organic Field-Effect Transistor (EGOFET) based on poly(N-alkyldiketopyrrolo-pyrrole dithienylthieno[3,2-b]thiophene) (DPP-DTT) as organic semiconductor, whose gate electrode was modified by electrografting a functional diazonium salt capable to bind an antibody specific to 2,4-dichlorophenoxyacetic acid (2,4-D), an herbicide well-known to be a soil and water pollutant. Molecular docking computations were performed to rationalize the design of the functional diazonium salt and improve the antibody capture on the gate surface.

In the last part of my work, I proposed an approach which takes profit not only of the capacitive coupling of the EGOFET but also of its sensitivity to electrostatic charges accumulated on the gate surface. To illustrate this in the field of sensors, I used a short peptide (Gly-Gly-His, GGH), known to selectively bind to copper ions Cu^{2+}. The peptide was grafted on the gate electrode of the transistor by direct electrooxidation of the primary amine of the first glycine moiety. I demonstrated that GGH-modified EGOFETs can transduce Cu^{2+} complexation through significant changes of their output and transfer characteristics, in particular their threshold voltage (V_{Th}).

KEYWORDS

2,4-dichlorophenoxyacetic acid detection, Cu^{2+} detection, diclofenac detection, displacement immunoassay, electrochemical immunosensor, peptide sensor, electrolyte-gated organic field-effect transistor, gate functionalization.

RESUME

Aujourd'hui, avec l'augmentation de la population mondiale, la consommation de médicaments et de produits phytosanitaires en agriculture a considérablement augmenté. Cela devient inquiétant car une grande partie de ces molécules, rejetée dans l'environnement, n'est pas bien éliminée par les stations d'épuration (lorsqu'elles existent). En trop grande quantité, ces produits deviennent des poisons pour tous les organismes vivants, y compris l'Homme.

Des méthodes analytiques classiques pour la mesure de ces produits chimiques existent déjà (méthodes séparatives classiques telles que la chromatographie en phase gazeuse, la chromatographie liquide à haute performance, éventuellement couplées à la spectrométrie de masse, etc.). Cependant, même si elles sont extrêmement précises et fiables, ces techniques sont difficiles à appliquer pour la surveillance sur site et sont généralement coûteuses. Pour cette raison, J'ai orienté ma thèse vers de nouvelles approches analytiques, plus simples d'utilisation pour des opérateurs non qualifiés et potentiellement moins chères, pour détecter de petites molécules en milieu aqueux telles que ces polluants.

Dans une première partie de mon travail, j'ai développé un immunocapteur basé sur une complexation compétitive originale et sur une transduction électrochimique (ampérométrique), pour la détection du diclofénac (DCF), un anti - inflammatoire non stéroïdien généralement utilisé pour soulager la douleur. L'électrode de travail a été fonctionnalisée par deux sels de diazonium, l'un utilisé comme sonde moléculaire (un dérivé du diclofénac couplé à une arylamine) et l'autre comme sonde redox (une quinone) également couplée à une arylamine, capable de transduire l'association haptène-anticorps par une variation de son électroactivité ; en particulier, la transduction a été conçue pour délivrer une augmentation de courant lors de la détection du diclofénac (soit une détection « signal-on »). J'ai montré une limite de détection d'environ 20 fM dans l'eau du robinet, ce qui rend ce type de capteur très compétitif.

Dans la suite de mon travail, j'ai conservé la même approche de transduction originale (immunoreconnaissance compétitive) mais appliquée à un transistor à effet de champ organique à grille électrolytique (EGOFET) dont le semiconducteur est le poly(N-alkyldiketopyrrolo-pyrrole dithiénylthiéno [3,2-b] thiophène) (DPP-DTT) et dont l'électrode de grille a été fonctionnalisée par électrogreffage d'un sel de diazonium fonctionnel capable de lier un anticorps spécifique de l'acide 2,4-dichlorophénoxyacétique (2,4-D), un herbicide

courant. Le design de la sonde moléculaire a été rationalisée par modélisation moléculaire afin d'optimiser la capture de l'anticorps en surface de grille.

Dans la dernière partie de mon travail, je propose une approche qui met à profit à la fois le couplage capacitif de l'EGOFET mais aussi sa sensibilité aux charges électrostatiques accumulées en surface de grille. J'ai immobilisé en surface de grille un peptide court (Gly-Gly-His, GGH) connu pour avoir une forte affinité envers les ions cuivre Cu^{2+}. Le peptide a été immobilisé par électro-oxydation directe de l'amine primaire du premier fragment glycine. J'ai démontré que les dispositifs EGOFET, modifiés par GGH, peuvent transduire la complexation de Cu^{2+} par des variations significatives de leurs caractéristiques de sortie et de transfert, en particulier par un décalage de la tension de seuil (V_{Th}).

MOT-CLÉS

Détection de l'acide 2,4-dichlorophenoyacétique, détection de l'ion Cu2+, détection du dichlofenac, immunoreconnaissance compétitive, immunocapteur électrochimique, capteur peptidique, transistor à effet de champ organique à grille électrolytique, fonctionnalisation de grilles.

ABBREVATIONS

2,4-D	2,4-dichlorophenoxyacetic acid
α6T	α-sexithiophene
Ab	Antibody
$Ab_{2,4\text{-}D}$	Anti-2,4-dichlorophenoxyacetic antibody
Ab_{DCF}	Anti-diclofenac antibody
ACTH	Adrenocorticotropin hormone
AFM	Atomic force microscopy
AFP	α-fetoprotein
Ag	Antigen
AHA	Aminohexanoic acid
AP	Alkaline phosphatase
APTES	3-aminopropyltriethoxysilane
ATZ	Atrazine
AuNPs	Gold nanoparticles
^{alk}BPA	Alkylbisphenol A
BA	4-formylphenyl boronic acid
BPA	Bisphenol A
BQ	Benzoquinone
BSA	Bovine serum albumin
CA	Cysteamine
CA-125	Cancer antigen 125
CEA	Carcinoembryonic antigen
Chi-TIC	Chitosan-titanium carbide
CRP	C-reactive protein
CV	Cyclic voltammetry
DBA	Diclofenac binding aptamer
DCF	Diclofenac
DCF-Probe	N-((1-(4-aminophenyl)-1H-1,2,3-triazol-4-yl)methyl)-2-(2-((2,6-dichlorophenyl)amino)phenyl)acetamide
DL	Diffuse layer (or double layer)

DNA	Deoxyribonucleic acids
DRS	Diffuse reflectance
DPP-DTT	Poly(N-alkyldiketopyrrolopyrrole dithienylthieno[3,2-b] thiophene
DPV	Differential pulse voltammetry
DTSP	Dithiobissuccinimidyl propionate
EDC	1-Ethyl-3-(3-dimethylaminopropyl)-carbodiimide
EDL	Electrical double layer
EGFR	Epidermal growth factor receptor
EGOFET	Electrolyte-Gated Organic Field-Effect Transistor
EIS	Electrochemical impedance spectroscopy
ELISA	Enzyme-linked immunosorbent assay
E-Probe	(2-((4-aminophenyl)sulfanyl)-8-hydroxy-1,4-naphthoquinone)
FAAS	Flame atomic absorption spectrometry
Fc	Ferrocene
FET	Field-Effect Transistor
FTO	Fluorine-doped Tin Oxide
GCE	Glassy carbon electrode
GC	Gas chromatography
GGH	Gly-Gly-His (glycine-glycine-histidine)
GOPS	3-glycidyloxypropyltrimethoxysilane
GOx	Glucose oxidase
GPP	Glycosylated Penta peptides
HbA1c	Glycosylated hemoglobin
HE4	Human epididymis-specific protein 4
HIV	Human immunodeficiency virus
HL	Helmholtz layer
HRP	Horseradish peroxidase
HOMO	Highest occupied molecular orbital
HPLC	High performance liquid chromatography
HQ	Hydroquinone
IgG	Immunoglobulins G
IL-10	Interleukin-10

ITO	Indium tin oxide
IUPAC	International Union of Pure and Applied Chemists
LG-FETs	Liquid-Gated Field-Effect Transistors
LoD	Limit of detection
LUMO	Lowest unoccupied molecular orbital
MB	Methylene blue
MS	Mass spectrometry
MWCNT	Multi-walled carbon nanotube
NHS	N-hydroxysuccinimide
NIOSH, USA	National Institute for Occupational Safety and Health
NSAID	Non-Steroidal Anti-Inflammatory Drug
NTs	Nanoparticles
ODN	Oligonucleotide
OECT	Organic electrochemical transistor
OFET	Organic field-effect transistor
OSC	Organic semiconductor
OTFT	Organic thin film transistor
P3HT	Poly(3-hexylthiophene)
PATP	p-aminothiophenol
PBA	Phenyl butyric acid
PBS	Phosphate buffer solution
pBTTT	Poly(2,5-bis(3-alkylthiophen-2-yl)thieno[3,2-b]-thiophene)
PEDOT	Poly(3,4-ethylenedioxythiophene)
PE-CVD	Plasma-enhanced chemical vapor deposition
PI	Photocurrent
PL	Phospholipid
pOBP	Odorant binding protein
PPC	Phenyl phosphoryl choline
RCA	Rolling circle amplification
SAM	Self-assembled monolayer
scFv	Single chain variable fragments
SPE	Screen-printed electrodes
SPR	Surface Plasmon Resonance

SWASV	Square wave anodic stripping voltammetry
QCM	Quartz crystal microbalance
TBBT	4,4′-thiobisbenzenethiol
TC	Tetracycline
TNF-α	Tumor necrosis factor α
WHO	World Health Organization
UV	Ultraviolet

CONTENTS

LIST OF FIGURES

LIST OF TABLES

LIST OF EQUATIONS

GENERAL INTRODUCTION

This thesis has been aacomplished in the group “Bioelectronics and Smart Surfaces” since November 2015. It focuses, in the first part, on the design and fabrication of an enzymeless electrochemical displacement heterogeneous immunosensor for diclofenac detection, and also in the second part, on gate functionalization of an Electrolyte-Gated Organic Field-Effect Transistor applied to biodetection of 2,4-dichlorophenoxyacetic acid (2,4-D) and Cu^{2+} in tap water.

For the development of the enzymeless electrochemical displacement heterogeneous immunosensor (Chapter II), the electrode interface was functionalized by an hapten which is an analogue of 2,4-D. The hapten is a molecule very close to 2,4-D but slightly different in its chemical structure so that the affinity of the antibody for this hapten is slightly lower than for the unmodified 2,4-D. The 2,4-D antibody is immobilized to the hapten; when antigens are present in the solution, a competition for binding the antibody between the antigen and the hapten takes place, so that the antibody is removed off the surface because it preferentialy binds to the free antigen. This reduces the steric hindrance on the electroactive surface and causes the current to increase.

For the development of the Electrolyte-Gated Organic Field-Effect Transistor (Chapters III and IV), we considered that this device is a capacitance-coupled one which can be modeled as two capacitors in series. The first corresponds to the gate/electrolyte interface while the second corresponds to the electrolyte/semiconductor interface. It is known that the drain current of such a transistor depends on the total capacitance. Therefore, if we are able to change this capacitance, we will be able to modulate the drain current. We decided to work on the gate/electrolyte capacitance because it is easier to chemically modify the gate than to the semiconductor (and also because it was much less investigated in the literature). To neglect the electrolyte/semiconductor interface capacitance, that of the other interface must be much smaller (this is because $1/C_{Total} = 1/C_{OSC} + 1/C_{Gate}$; if $C_{Gate} << C_{OSC}$, then $C_{Total} \approx C_{Gate}$). For this reason, we used microelectrodes as gate, of 100 to 250 µm in diameter.

Before these very last years, EGOFETs have been relatively poorly investigated. It is only since 2015 (at the beginning of this thesis work) that the gate/electrolyte interface started to be investigated. As stated above, changes in capacitance were shown to induce changes in

drain current; this has been studied in the most recent literature, in particular for application in biosensing where large probes or targets are able to modify the double layer capacitance of the gate. However, the effect of charges carried by these probes or targets have been poorly investigated, or only for application to DNA sensors. In my work on EGOFETs, I investigated both effects: bulky molecules on the interfacial capacitance (Chapter III) and electrostatic effect of ions complexed in peptides (Chapter IV).

My thesis therefore consists in three parts.

1. First part

Diclofenac is one of the most popular compounds used as Non-Steroidal Anti-Inflammatory Drug (NSAID). It is generally employed to protect patients from inflammation and relieve pain, e.g. for arthritis, acute injuries, menstrual pain or even nocturnal enuresis. Along with the increase of human population, the consumption of this drug has become a worrisome issue as diclofenac residues are excreted directly from the body to the environment via urine and faeces, in large quantities compared to the oral dosage. This molecule is not well eliminated by water-treatment plants, so it is released into the ecosystem and becomes a poisoning agent to living organisms. Recently, scientists have developed several methods for the assessment of diclofenac ecotoxicology. However, there are only few studies applying electrochemical sensors, as well as electronic devices, to detect diclofenac. Moreover, the sensitivity is low, with limits of detection of ca. a few tens of nM. It is, therefore, necessary to develop novel techniques to improve the limit of detection. In this first part of my thesis, I will report the development of an original approach for an electrochemical immunosensor to detect diclofenac.

For this, we designed two precursors of a diazonium salt: the first is N-((1-(4-aminophenyl)-1H-1,2,3-triazol-4-yl)methyl)-2-(2-((2,6-dichlorophenyl)amino)phenyl)acetamide used to immobilize a molecular probe on the surface of the working electrode (further referred to as DCF-Probe) onto which the diclofenac antibody (Ab_{DCF}) will bind; the second is (2-[(4-aminophenyl)sulfanyl]-8-hydroxy-1,4-naphthoquinone) (further referred to as E-Probe), a redox probe used to transduce the Ab_{DCF}/DCF-Probe binding into a change of redox current. The E-Probe contains quinone groups, which are known to be sensitive to ion strength, pH or to local ion transport. In my model, the binding of Ab_{DCF} to DCF-Probe prevents the access of cations to the redox probe (i.e. decreases the apparent diffusion coefficient), so a faradic

current decrease is observed (due to the slowing down of the overall charge transfer rate). Conversely, if DCF is added into the surrounding electrolyte, it competes with the immobilized DCF-Probe and induces dissociation of Ab_{DCF} from the electrode surface (i.e. displaces the Ab_{DCF}/DCF-Probe complexation equilibrium); this phenomenon leads to a decrease of the overall steric hindrance, which in turn leads to an observable current increase.

2. Second part

World population development requires a more intensive agriculture, in particular the use of herbicides and pesticides. Consequently, large amounts of pollutants have been released into the environment all over the world. 2,4-D is a widely-used herbicide employed to control broad leave in agriculture. Unfortunately, this compound presents a serious harm for the health of people working in-situ with high concentrations of 2,4-D for prolonged contact time, as reported by the National Institute for Occupational Safety and Health (NIOSH, USA) in 1996. It is, therefore, necessary to develop assays to detect 2,4-D. In this second part of my thesis, I would like to introduce a novel approach applying the gate functionalization of an Electrolyte-Gated Organic Field-Effect Transistor (EGOFET). In this device, metallic contacts were done using classical photolithography in cleanroom, while the organic semiconductor (poly(N-alkyldiketopyrrolopyrrole dithienylthieno[3,2-b]thiophene) (DPP-DTT) was deposited by spin coating. These EGOFETs use water as electrolyte; they were operated in ambient conditions, without taking particular care for humidity or oxygen levels.

A precursor of the 2,4-D diazonium salt was designed and used as immobilized molecular probe (further referred to as 2,4-D-Probe) onto which the 2,4-D antibody ($Ab_{2,4-D}$) can bind (both are immobilized on the gate). The binding of $Ab_{2,4-D}$ to 2,4-D-Probe was shown to modulate the capacitance of the gate, leading to change in drain current (while no gate current is measured, which demonstrates that the device operates in the field-effect mode). Conversely, 2,4-D target added into the surrounding electrolyte was shown to compete with 2,4-D-Probe and induce dissociation of $Ab_{2,4-D}$ (i.e. displaces the $Ab_{2,4-D}$ from the electrode surface). This phenomenon leads to an increase in gate capacitance, which in turn leads to an increase in drain current, shown to depend on the 2,4-D concentration.

3. Third part

Copper is a transition metal essential for all living organisms as a trace dietary mineral. However, at high concentrations, it becomes toxic. Negative influences of elevated copper

concentrations have been observed in human as the disorders in the gastrointestinal, hepatic, and renal systems. In 1993, the WHO (World Health Organization) reported that the level of copper in drinking water has to be at concentrations below 2 mg L^{-1}. However, this value has been still regarded as doubtful due to the limit of detection of the validated measurement protocols, which dictated the recommended value rather than true health reasons. Hence, I propose in the third part of my thesis to develop a sensitive method, in a point-of-use format, for the on-site determination of Cu^{2+} ions in aqueous media. Following the specific strategy mentioned in the previous part of my work, the gate of EGOFETs were functionalized by short peptides (Gly-Gly-His) known to efficiently complex Cu^{2+} in aqueous medium.

We propose here the direct electrografting of the Gly-Gly-His tripeptide (0.27 kDa) through the first primary amine-terminated Gly residue (due to steric effects, only primary amines are grafted, with the exclusion of secondary and tertiary amines).This peptide has been investigated these last years, mainly in electrochemical systems. Here, I show that the binding of Cu^{2+} to Gly-Gly-His slightly modulates the capacitance of the gate but also and maintly lead to a significant shift of the threshold voltage of the device, attributed to the electrostatic effect of the accumulation of copper cations at the gate/electrolyte interface. I demonstrates that such device can be used to detect Cu^{2+} even in tap water, that is to say in real conditions.

Chapter I BIBLIOGRAPHY

1 Biosensors: Generalities

In simple words, biosensors are analytical devices that convert a biological interaction into, at the very end, an electrical signal. Biosensors have been applied in many fields, e.g. food industry, medical field, defense, where they provide better sensitivity and ease of use as compared with traditional methods.

In food processing, biosensors are expected for simple, real-time, selective and inexpensive measures [(1)], i.e. for the detection of pathogens such as E. coli [(2)]. Enzymatic biosensors are also employed in the dairy industry, for example to quantify pesticides in milk [(3)]. In fermentation industries, process safety and product quality are crucial, thus effective monitoring of the fermentation process is imperative; biosensors have attracted a lot of attention in online monitoring in fermentation process due to their simplicity and quick response [(4)]. Biosensors are also being employed to detect heavy metals [(5-7)] or pesticides [(8-10)] in drinking water.

In the medical field, applications of biosensors are growing rapidly. For example, glucose biosensors are expected to be widely used in clinical applications for diagnosis of diabetes mellitus, which requires precise control over blood-glucose levels. Blood-glucose biosensors usage at home accounts for 85% of this expected gigantic world market [(11)]. Biosensors are also being used to diagnose infectious disease or cancer biomarkers human interleukin 10 (IL-10) [(12)].

1.1 Generalities on biosensors

Biosensors must absolutely be highly specific, which is usually obtained with bioprobes (enzymes, DNA, proteins, antibodies…) which present a high specificity for a given and unique molecule, i.e. their target. The term “biosensor” was introduced in 1977 by Cammann [(13)], and biosensors are now well-defined, e.g. by IUPAC (www.old.iupac.org/publications/books/author/mcnaught.html). Figure I.1 gives the very general scheme of a biosensor, for the three typical bioprobes: antibodies (in immunosensors), enzymes (in enzymatic biosensors) and DNA strands (in genosensors).

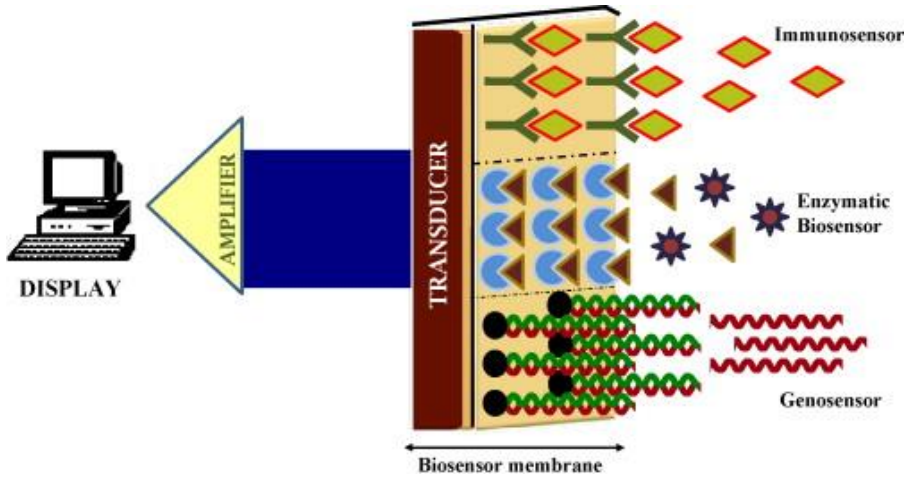

Figure I.1. Schematic representation of a biosensor [14]

Materials, transducing devices and immobilization methods involved in the fabrication of biosensors require multidisciplinarity in chemistry, biology and engineering. The first enzyme-based sensor was reported by Updike and Hicks in 1967 [15], in which they described an enzymatic glucose sensor. Enzymatic biosensors can be classified by their immobilization methods, i.e. adsorption of enzymes by van der Waals forces, ionic bonding or covalent bonding. The commonly used enzymes for this purpose are oxidoreductases, polyphenol oxidases, peroxidases [16], and aminooxidases [17]. Immunosensors were established on the fact that antibodies have high affinity towards their respective antigens, i.e. the antibodies specifically bind to pathogens or toxins, or interact with components of the host's immune system [18]. DNA biosensors were devised on the property that a single-stranded nucleic acid is able to recognize and bind to its complementary strand, even in a complex matrix containing a number of other molecules or non-complementary DNA strands. The interaction is due to the formation of stable hydrogen bonds between the two nucleic acid strands [19-24].

There are several approaches to transduce the various molecular recognitions involved in these biosensors into a measurable signal. These approaches will not be reviewed here but the reader can refer to the excellent review from Thompson and Krull [25], for example.

1.2 Immunoassays and immunosensors

Immunosensors are biosensors where antibody-antigen interactions (the antibody often being used as capture probe and the antigen being the target analyte) occurring on the sensor

surface are used to get a specific recognition. All concepts necessary to understand how immunosensors work are given below.

From the IUPAC gold book [1], an antigen is "*a substance that stimulates the immune system to produce a set of specific antibodies and that combines with the antibody through a specific binding site or epitope*". Also, from the same IUPAC document, an antibody is "*a protein (immunoglobulin) produced by the immune system of an organism in response to exposure to a foreign molecule (antigen) and characterized by its specific binding to a site of that molecule (antigenic determinant or epitope)*". The general structure of an antibody is given on Figure I.2 below.

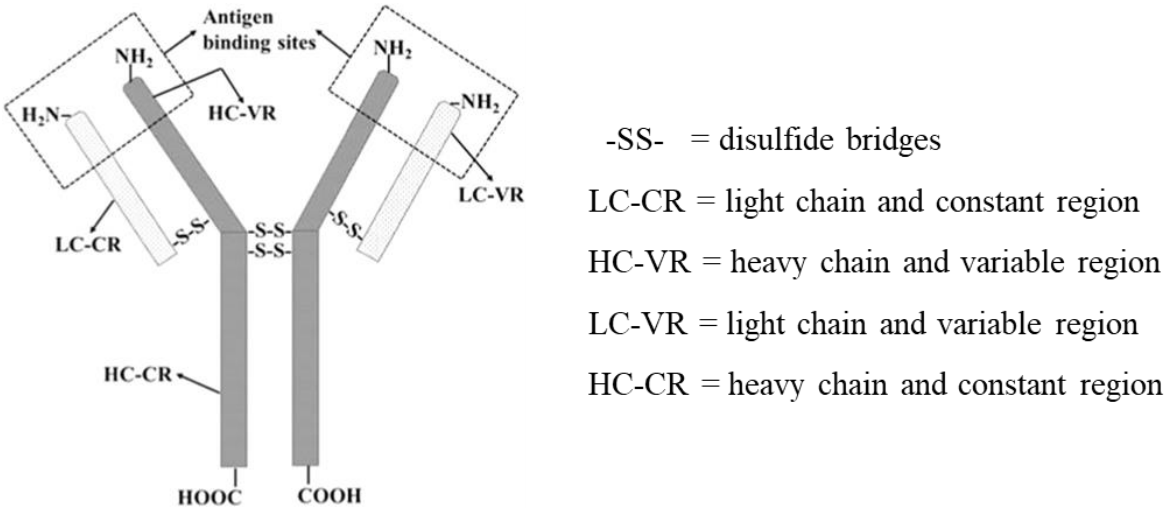

Figure I.2. Schematic representation of heavy and light chains combined to form the most common antibody (IgG) [26].

1.3 Antibody-antigen interactions

An antibody molecule includes two identical, of equal binding affinity, antigen-recognization sites consisting of the NH_2-terminated paratope. Their role is to bind antigens at this region and form a stable antibody-antigen complex. Antibody-antigen interactions are of different nature; one can consider that hydrogen bonds, hydrophobic interactions, van der Waals and colombic interactions are involved [27-29].

Antibody-antigen interactions are reversible; an equilibrium equation can be written [26].

[1] IUPAC gold book, version 2.3.3, 2014-02-24, p. 100

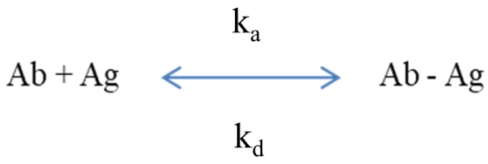

Equation I-1

Where k_a is the association rate constant and k_d is the dissociation rate constant. The equilibrium constant K_a can therefore be written:

$$K_a = \frac{k_a}{k_d} = \frac{[Ab-Ag]}{[Ab][Ag]}$$

Equation I-2

The dissociation constant (K_d = 1/ K_a) of a large number of antibody-antigen pairs have already been determined [30, 31] and are in all case very low, in the pM range (the dissociation constant of the avidin-biotin pair, one of the strongest known non-covalent bonds, is in the fM range).

2 Electrochemical immunosensors

2.1 General reviews describing electrochemical immunosensors

Electrochemical immunosensors are electrochemical biosensors where antibody-antigen interactions (the antibody being the capture probe and the antigen the target analyte) occurring on an electrode surface are transduced into an electrochemical signal. Compared to other transduction strategies, electrochemical transducing techniques are fast, sensitive, require simple equipment, use small quantity of material and can be portable. The field of electrochemical immunosensors is very rich and dynamic. To give a general but however concise overview of the current state-of-the-art, I focused this bibliographic section on reviews of the last 5 years only.

A relatively brief review was published by Ricci *et al.* in 2012 [(32)], presenting a guidance to all researchers who would like to enter the electrochemical immunosensor domain, particularly focusing on practical aspects. Another review, published by Yang *et al.* also in 2012 [(33)], focused on new trends in signal amplification in enzyme-based immunosensors (combination of enzymatic reactions, multienzyme labels, use of magnetic bead, etc.). Several reviews focus on precise applications. For example, Wan *et al.* [(28)] dealt in 2013 with generalities on point-of-care diagnostics for early detection of diseases. Bahadir *et al.* [(34)] did the same in 2015 for early clinical diagnostics of cancer and cardiac diseases. Chikkaveeraiah *et al.* [(35)] reviewed in 2012 the most recent advances at that time in electrochemical immunosensors for detection of cancer protein biomarkers, with strategies to increase densities of capture molecules and sensitivities. On their side, in 2013, Vidal *et al.* [(36)] reviewed electrochemical affinity biosensors for detection of mycotoxins in food. Also in 2013, Diaconu *et al.* [(37)] reviewed electrochemical immunosensors for precise applications in breast and ovarian cancer. At last, Campuzano *et al.* [(38)] reviewed very recently (2017) electrochemical bioaffinity sensors for salivary biomarkers.

Various transduction strategies have been employed up to now, on various antibody-antigens interactions. Here are some examples only. Hayat *et al.* employed anti-okadaic acid antibody to detect Okadaic acid [(39, 40)]. Antibodies were immobilized onto electrodes via protein A interactions [(40)] and amine groups [(39)]. Jarocka *et al.* mentioned interaction of anti-hemagglutinin H5 antibody (MAb 6-9-1) and his-tagged hemagglutinin antigen [(41, 42)]. Lim *et al.* [(43)] used porcine serum albumin antibody to detect biomarker for pork adulteration in raw

meat. Articles dealing with electrochemical imunosensors have continued to be published, even very recently in 2018, with the works of Sharma *et al.* [44] (prostate specific antigen detection), Khoshroo *et al.* [45] (carbohydrate antigen detection); Zeng *et al.* [46] (cytokeratin 19 fragment antigen); Amani *et al.* [47] (alpha-fetoprotein detection, a cancer biomarker); Rauf *et al.* [48] (Mucin 1 detection, also a cancer biomarker), etc.

Several assay formats were used for transduction, e.g. competitive, sandwich, displacement, using enzymatic or enzymeless amplification, or even without amplification.

2.2 Competitive assay

In a competitive immunoassay, unlabelled analyte in a sample competes with labelled analyte to bind an antibody. The amount of labelled, unbound analyte is then measured. In theory, the more analyte in the sample, the more labelled analyte gets displaced and then measured; hence, the amount of labelled unbound analyte is proportional to the amount of analyte in the sample.

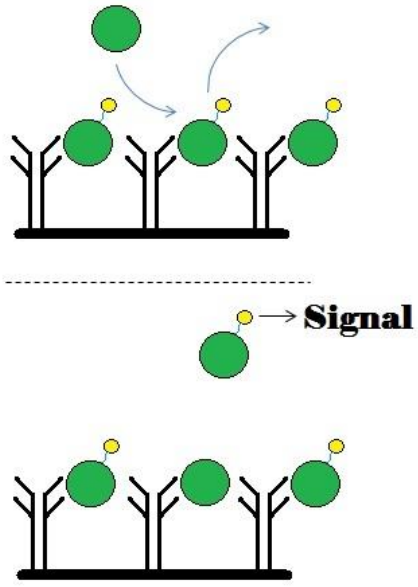

Figure I.3. A competitive homogeneous immunoassay, unlabeled analyte displaces bound labelled analyte, which is then detected or measured.

Competitive assays are performed using conjugated antigens. A good example of this approach is given on Figure I.3. Below are cited a few recent articles dealing with electrochemical competitive immunosensors.

M. Moreno Guzman *et al.* published an example of competitive electrochemical immunosensor in 2012, for adrenocorticotropin hormone (ACTH) detection. Competition was made between a mixture of the standard ACTH with its biotin-conjugated ACTH counterpart, for complexation on the specific antibody (anti-ACTH antibody) immobilized on the electrode surface [49]. Similarly, Liu *et al* [50], the same year, published a competitive inhibition assay for detection of haemoglobin variant (HbA1c, a diabete marker protein). They immobilized glycosylated pentapeptides (GPP) on the electrode, then incubated it with a mixture of HbA1c and anti-HbA1c antibody. Another example is competition between HRP-estradiol and estradiol to bind to biotinylated anti-estradiol immobilized on the electrode (Figure I.4) [51]. Conzuelo *et al.* also used this type of assay, for tetracycline detection [31].

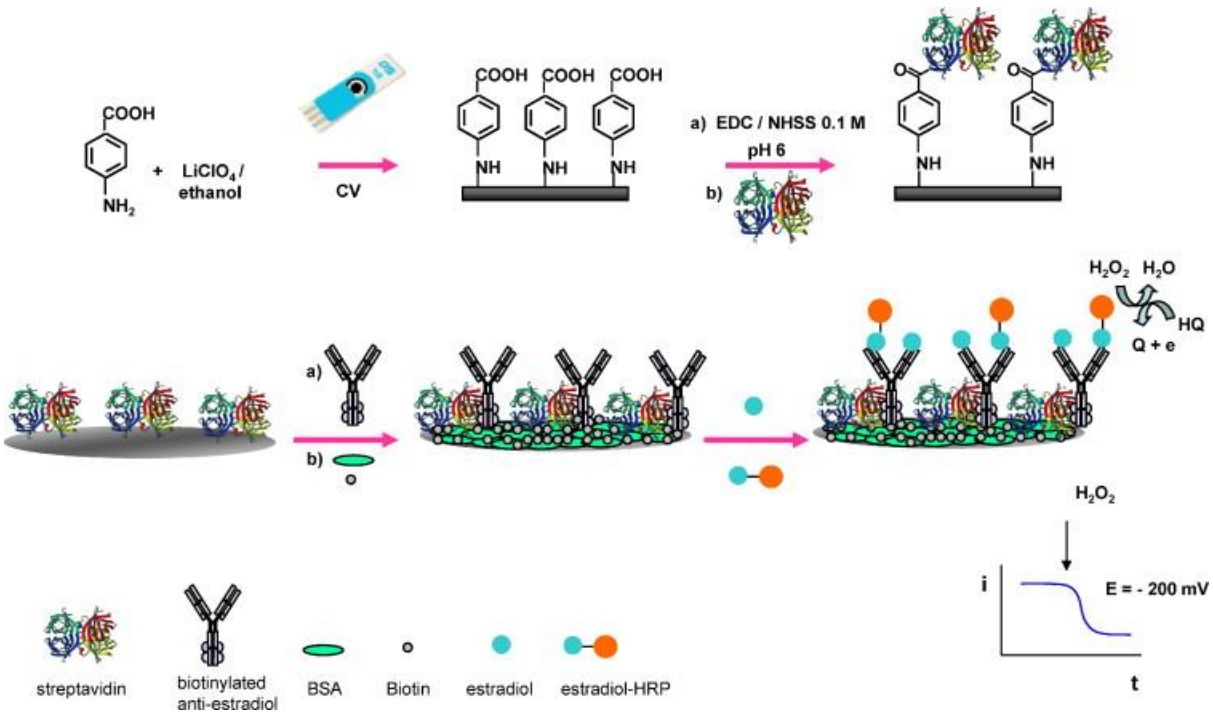

Figure I.4. Illustration of the different steps and protocols involved in an estradiol competitive immunosensor.

2.3 Sandwich assay

The basic principle relies on, first, the immobilization of a primary antibody on the electrode surface, then its binding with the antigen, and finally, complexation with a second antibody; this antibody is generally labelled with a redox enzyme which produces a detectable signal at the electrode.

For example, Singh *et al.* described in 2013 an immunosensor based on a sandwich architecture, to determine the cancer antigen 125 (CA-125, a protein) [(52)] (Figure I.5). They first immobilized the anti-CA-125 antibody on the electrode surface through biotin-avidin interactions, then incubated it in a medium containing the CA-125, for its first complexation. In the third step, they added the second antibody labelled with glucose oxidase (GOx). For transduction, the authors used $Ru(NH_3)_6^{3+}$ as mediator; recylcing of the mediator on the electrode was detected and quantified amperometrically.

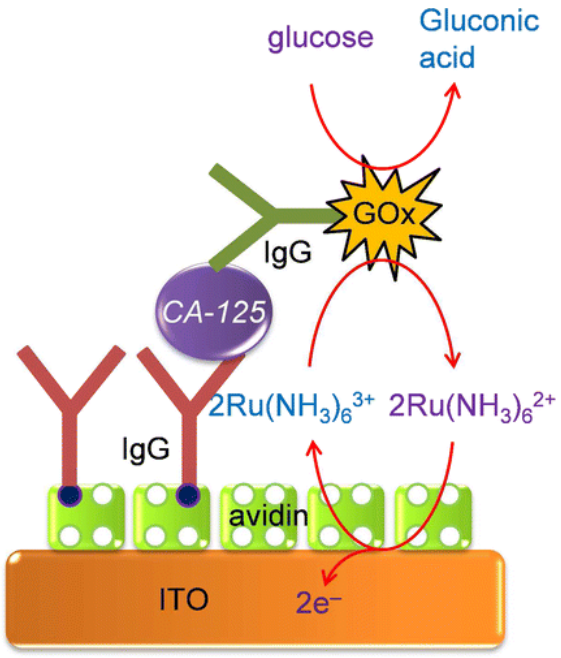

Figure I.5. Illustration of the sandwich asssay reported by Sing et al., 2013 [(52)].

More recently, in 2017, Serafin *et al.* published a similar approach to detect the receptor tyrosine kinase AXL [(53)]. In this work, the capture antibody was immobilized on an electropolymerized poly(pyrrolepropionic acid) film, and the second antibody was labelled not with GOx but with horseradish peroxidase (HRP), which is the most common enzyme

label. Hydroquinone (HQ) was used as mediator: HRP oxidizes HQ into benzoquinone (BQ), which is reduced amperometrically on the electrode and produces a detectable current.

2.4 Displacement assay

The displayment assay is a quite typical method applied to immunosensing. It is made of two main steps. A complex is made between the specific capture antibody attached to the surface and a labelled hapten (i.e. a molecule which is similar to the target analyte, having a quite good affinity for the antibody) (step 1, Figure I.6). Second step, in the presence of the true analyte, the first complex is dissociated in favour of the new complex between the antibody and the analyte. The labelled hapten leaves the electrode, so that its electrochemical signal decreases (step 2, Figure I.6). To insure the best efficiency, the antibody must have a higher affinity for the analyte than for the labelled hapten.

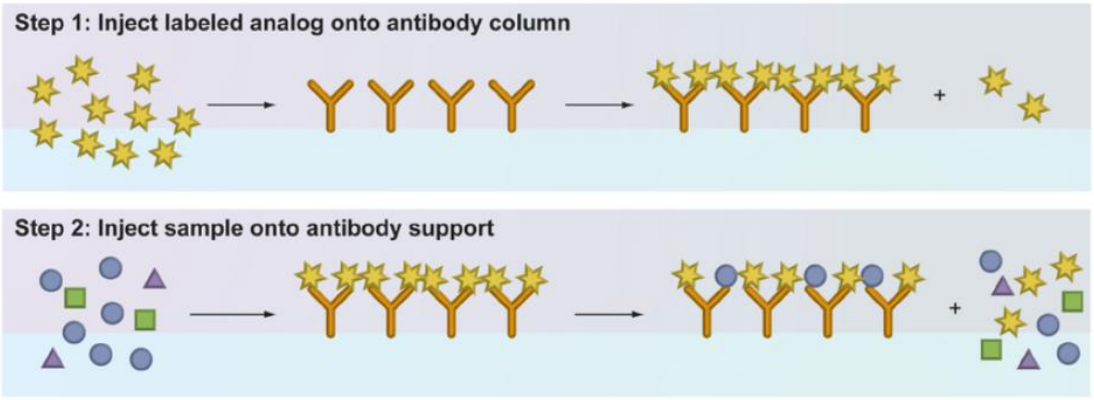

Figure I.6. General illustration of a displacement assay .

To illustrate this strategy, one can take the example of Tran *et al.* who published an electrochemical displacement immunoassay in 2013 [(54)]. For detection of atrazine (a common pesticide), he employed a displayment strategy with an immobilized hapten (hydroxyatrazine) on an electroactive conducting polymer (Figure I.7).

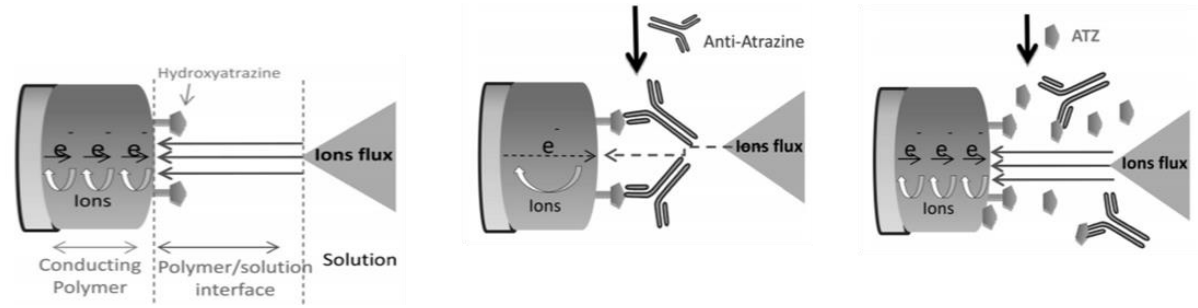

Figure I.7. Displacement assay coupled to an electrochemical transduction, by Tran et al. [54].

Khor *et al.* also proposed a displayment assay protocol for determination of antibiotics [55] (Figure I.8), which could be applied for detection of any type of small molecules.

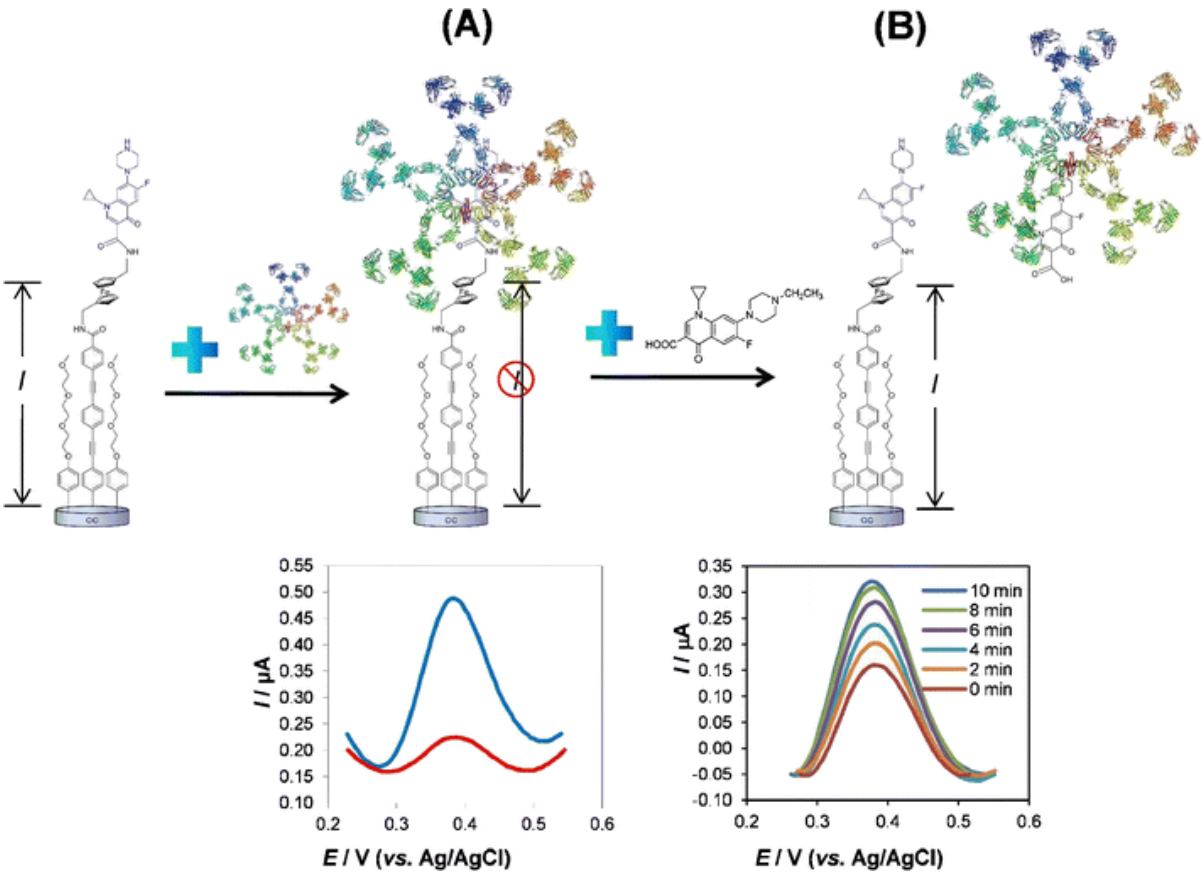

Figure I.8. Scheme of an electrochemical immunosensor: (A) shows the electrode surface after the antibody/epitope complexation with the corresponding attenuated electrochemical signal; (B) shows the detection of a small analyte via a displacement assay where the antibody is released, and the increase in eletroactivity as a function of time [55].

2.5 Enzyme labels and enzyme-based immunosensors

As explained before, labeling of analytes or secondary antibodies is often necessary for achieving an electrochemical transduction. Redox molecules can be used as labels; however, to achieve amplification, it is preferable to use redox enzymes which are capable to produce a large amount of electroactive molecules from only one antibody or one analyte molecule. For example, Guzman *et al.* reported that they could determine adrenocorticotropin hormone using alkaline phosphatase (AP)-labeled streptavidin and 1-naphtyl phosphate as the enzyme substrate. 1-Naphtol was generated by the enzyme reaction, and detected on the electrode surface (Figure I.9) [(49)].

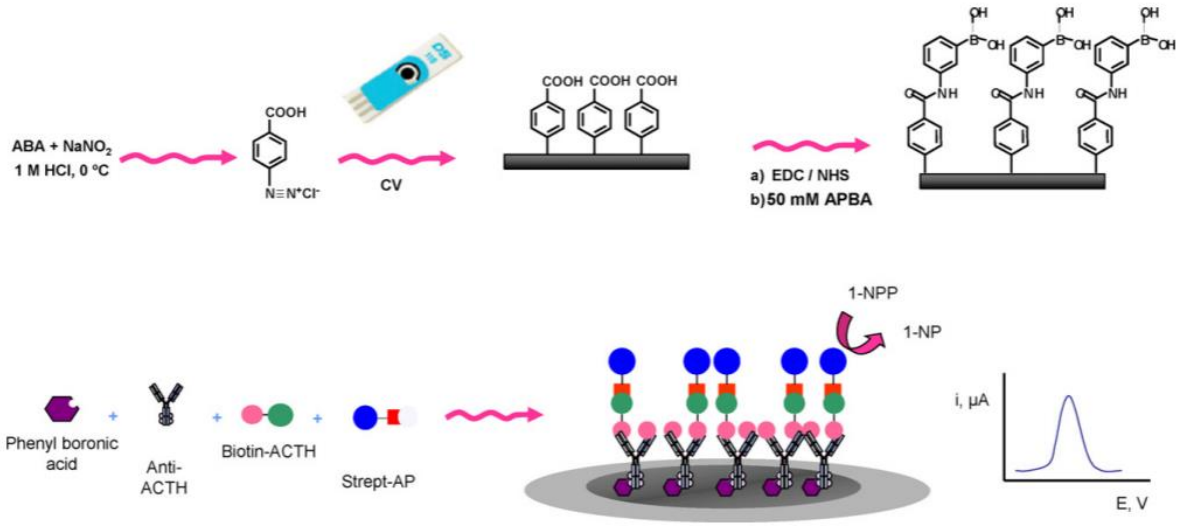

Figure I.9. Illustration of the different steps and protocols for adrenocorticotropin hormone (ACTH) detection via electrochemical immunosensor involved in the development of a disposable screen-printed electrodes modified with phenylboronic acid [(49)].

In addition to alkaline phosphatase, horseradish peroxidase (HRP) is also a popular enzyme for labelling, due to its robustness and high turnover. In this case, H_2O_2 is the enzyme substrate and most of the case, hydroquinone (HQ) is used as co-substrate: its catalytic oxidation produces benzoquinone (BQ) which can be detected amperometrically and be re-reduced into HQ. As examples, one can cite Ojeda *et al.* [(51)] for detection of estradiol, Conzuelo *et al.* for determination of antibiotic residues in milk [(56)] or Serafin *et al.* for

tyrosine kinase (by the presence of AXL versus anti-AXL) (Figure I.10) or natriuretic peptide detection [53, 57].

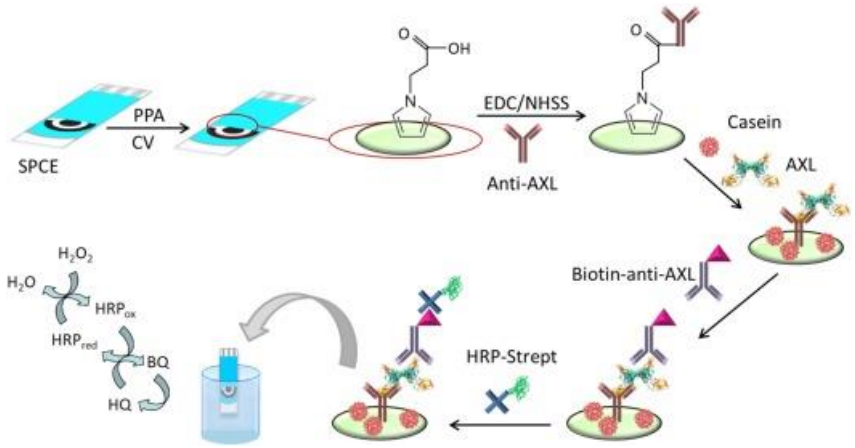

Figure I.10. Different steps construct the amperometric immunosensor for AXL detection involving pPPA-modified SPCEs and covalent immobilization of anti-AXL [53].

Glucose oxidase (GOx) is less used as label but, due to its wide availability and good robustness, several articles have reported its use. For example, GOx-conjugated antibody cancer 125 was used by Singh *et al.* [52]. Similarly, β-galactosidase was employed very recently (2018) by Sharma *et al.* [57].

Enzymes are generally used not for detection itself but for transduction and amplification, taking profit of the enzyme turn-over (for one event of biorecognition, one antibody or antigen captured, several molecules of enzyme product are produced at the vicinity of the electrode surface and electrochemically detected). HRP, horse radish peroxidase, is the most used enzyme label in immunosensors because it is commercially available and catalyzes the oxidation of numerous chromogenic substrates from H_2O_2 reduction. However, some other enzymes are also encountered such as alkaline phosphatase (AP) and glucose oxidase (GOx).

- Detection of antibodies

The term "immunosensor" could mean that the target could be either an antigen (Ag) or an antibody (Ab) as for example in the framework of serological diagnosis, i.e. the research and the determination of specific antibodies linked to a pathogenic infection. Even though the

most popular approach remains targeting antigens using antibodies, some works report targeting antibodies.

In 2013, Bhimji *et al.* [41] described an interesting route to detect human immunodeficiency virus (HIV) antibodies by immobilization of antigenic peptides derived from a complex transmembrane protein of HIV-1 gp41 or HIV-2 gp36, covalently attached to a SU-8 substrate (an epoxy photoresist) close to microelectrodes. The detection of HIV antibodies was achieved using an alkaline phosphatase (AP)-conjugated secondary antibody antibody (Figure I.11). The linear detection range was reported between 1 ng mL^{-1} and 1 µg mL^{-1}, with a limit of detection (LoD) of 1 ng mL^{-1} (6.7 pM).

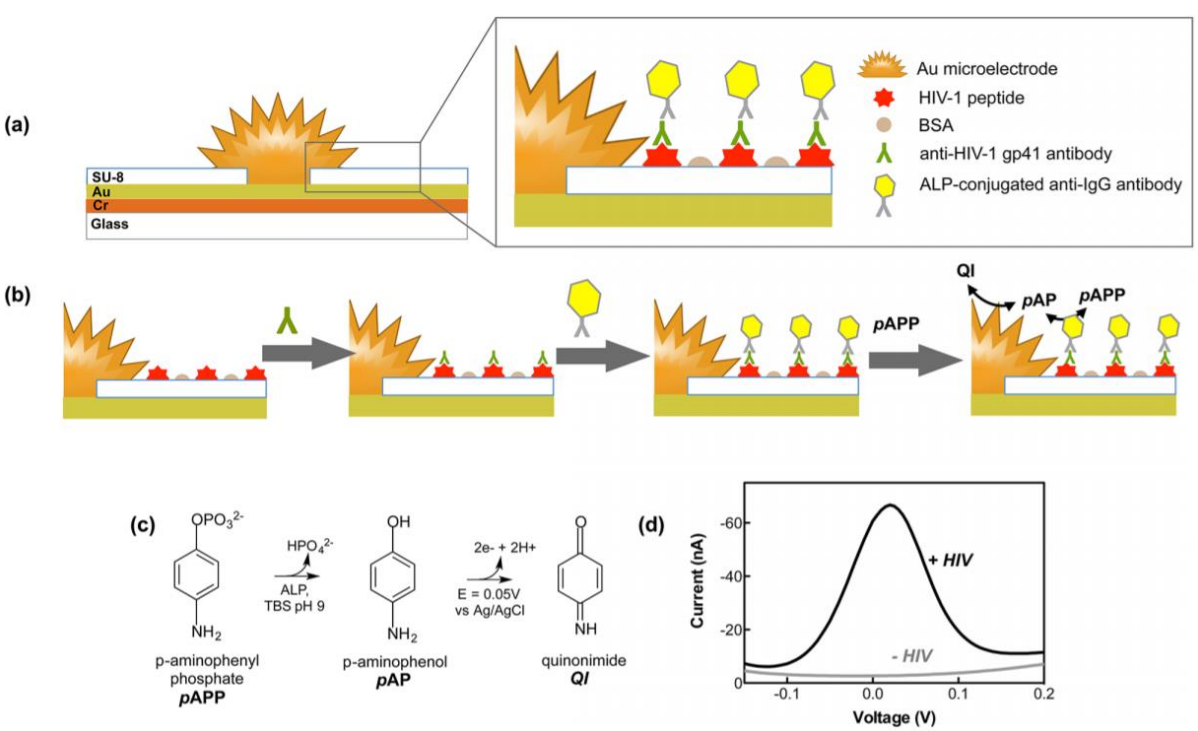

Figure I.11. Illustration of antibodies detection of HIV. (a) Au microelectrodes (b) Immunorecognition (c) Transduction (d) Resulting DPV [41]***.***

More recently in 2016, Montes *et al.* [58] used a composite graphite-epoxy substrate into which an HRP-labelled antibody was incorporated, for detection of IgG. Transduction was classical, with a competitive assay using H_2O_2 and hydroquinone (HQ) in solution. Amperometric measurements (reduction of benzoquinone BQ into HQ at the electrode) led to a LoD of 1.4 µg mL^{-1} and a relatively reduced linear range up to 2.8 µg mL^{-1}. There is no

other significantly cited work reporting enzyme-based immunosensor for detection of antibodies. In fact, detection of antigens is much more popular.

- Detection of antigens

For example, in 2012, Ojeda *et al.* [51] described an electrochemical immunosensor for estradiol sensing, based on carbon screen-printed electrodes (SPE) sequentially modified with p-aminobenzoic acid, streptavidin and biotinylated anti-estradiol. Transduction was performed by applying a competitive immunoassay between peroxidase-labeled estradiol (HRP-estradiol) and estradiol for the binding sites of the immobilized antibodies. The reaction between estradiol and biotinylated anti-estradiol was amperometrically detected by addition of H_2O_2 in the presence of HQ. The linear range was between 1 and 250 pg mL^{-1} and the LoD was 0.77 pg mL^{-1}.

Also in 2012, Qi *et al.* [59] reported an array of carbon SPE for simultaneous detection of several tumor biomarkers such as carcinoembryonic antigen (CEA) and α-fetoprotein (AFP). Electrodes were modified by grafting *p*-phenylenediamine via the diazonium route, followed by crosslinking the primary capture antibody using a Schiff base reaction. Transduction was made by using a sandwich assay with HRP-labelled secondary antibodies (Figure I.12 (C)). The detection range was from 0.10 to 50 ng mL^{-1} and the LoD of ca. 40 pg mL^{-1}. Still in 2012, Moreno-Guzmán *et al.* [49] described a competitive electrochemical immunosensor for adrenocorticotropin hormone (ACTH) using disposable phenylboronic-modified carbon SPE used to efficiently immobilize ACTH antibodies. Transduction was designed using a competitive equilibrium for the binding sites of the immobilized antibody, between the target ACTH and a biotinylated ACTH (Figure I.12 (A)). The electroanalytical response was generated by using an AP-labelled streptavidin and 1-naphtyl phosphate as enzyme substrate. Differential pulse voltammetry (DPV) was used to monitor the enzyme activity (instead of classical CV to suppress the capacitive component). A very low LoD of 18 fg mL^{-1} was obtained.

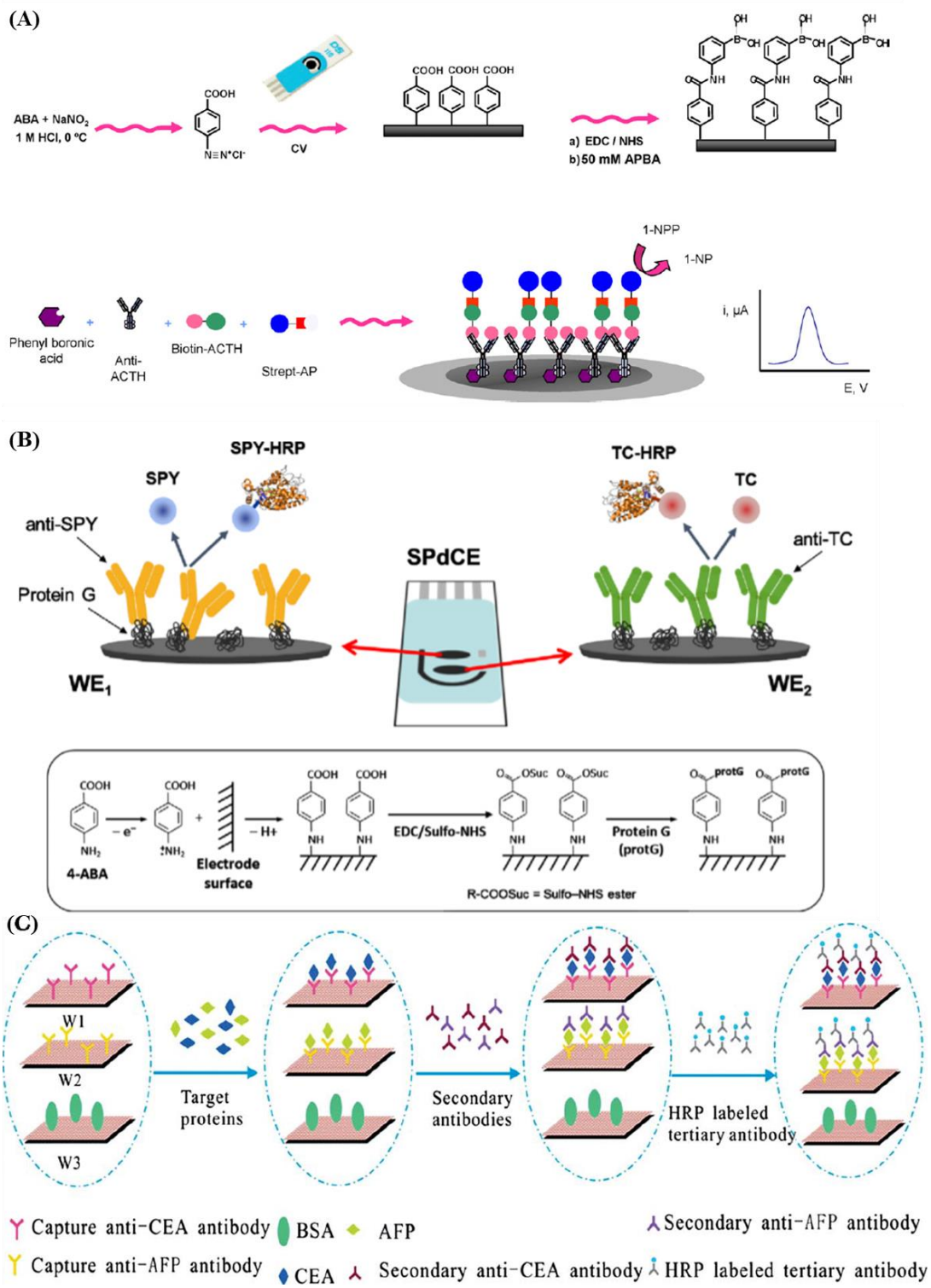

Figure I.12. Illustration of antigen detections: (A) Reactions involved in the ACTH immunosensor using SPEs modified with phenylboronic acid [(49)]. (B) Above, scheme of the immunosensor principle for SA and TC antibiotics. Below, surface chemistry involved for covalent binding of Protein G [(56)]. (C) Detection principle of the screen-printed bi-analyte array, including a BSA (reference) electrode [(59)].

A competitive immunosensing approach was also followed by Conzuelo *et al.* [56] in 2013, for determination of sulfonamide (SA) and tetracycline (TC), two antibiotics which could be present in milk. The originality was to use Protein G coupled to 4-aminobenzoic acid electrografted on the electrode, as anchoring point for oriented immobilization of anti-SA and anti-TC (Figure I.12 (B)). Using HRP-labelled TC, they obtained a LoD of ca. 1 nM (ca. 200-500 pg mL^{-1}) for both SA and TC. As for the previous ACTH competitive detection, no linear range was given, probably because it is relatively difficult to obtain such linear response with competitive transduction. For detection of cancer antigen 125 (CA-125), Singh *et al.* [52] described a $Ru(NH_3)_6^{3+}$-mediated glucose oxidase (GOx) labelling instead of routinely used enzymes such as HRP or AP. The LoD, for an incubation period of 5 min, was slightly lower 0.1 U mL^{-1} for CA-125, comparable to the other reported electrochemical immunosensors. However, the authors claimed a shorter incubation time compared to HRP or AP amplifications. More generally, for enzyme-based amplification routes, the turnover of the enzyme (more precisely the K_{cat}/K_M ratio, which should be as high as possible) is a crucial parameter for a good amplification. Jiang *et al.* [60] described an electrochemical immunosensor for detection of tumor necrosis factor α (TNF-α) with a strategy to avoid non-specific adsorption. For this purpose, they used an original layer of phenyl phosphoryl choline (PPC) and phenyl butyric acid (PBA). The capture antibody was grafted on the working ITO electrode along with this anti-adsorption layer and, in a sandwich configuration, the signaling (labelled) antibody was coupled to HRP. H_2O_2 was added in solution as well as ferrocene (Fc) to reuse HRP. The immunosensor was shown to detect TNF-α with a LoD of 10 pg mL^{-1} with a wide linear range between 0.01 ng mL^{-1} to 500 ng mL^{-1}. More recently, Serafín *et al.* [53] reported in 2017 a tyrosine kinase immunosensor involving a sandwich architecture with a capture antibody covalently immobilized on poly(pyrrolepropionic acid)-modified electrodes and a HRP-labeled secondary antibody. The LoD was 337 pg mL^{-1}.

Due to the relative instability, limited robustness and severe limitation of the operating conditions required for most enzymes, it is of interest to develop enzyme-free catalytically-amplified immunosensors, which could be considered as one of the most promising perspectives for electrochemical immunosensors. Another strategy to get rid of enzymes is to design non-amplified sensors. These two approaches are reviewed below.

2.6 Enzyme-free immunosensors

Ciani *et al.* [61] developed gold SPE electrodes modified with specific thiolated antibodies for direct detection of infection biomarkers, using electrochemical impedance spectroscopy (EIS), more particularly measuring the charge transfer resistance of $Fe(CN)_6^{3-/4-}$ on the gold electrode depending on the presence or not of the targeted proteinic antigen (Triggering Receptor-1 Expressed on Myeloid cells, Matrix MetalloPeptidase 9 and N-3-oxo-dodecanoyl-l-HomoSerineLactone). Limits of detection were between the pM and the nM range, depending on the target. Also with an enzyme-free transduction procedure, Tran *et al.* [54] described a label-free electrochemical competitive immunosensor based on an electroactive conducting polymer coupled with a slightly modified atrazine molecule, a common pesticide (Figure I.13 (A)). This quinone-based polymer presented a current decrease following anti-atrazine antibody complexation, and a current increase after atrazine addition in solution, with a very low detection limit of 1 pM, i.e. 0.2 pg mL^{-1} estimated by square wave voltammetry (SWV). One originality relies on the fact that the redox probe is not diffusing in solution but immobilized on the electrode surface, and another originality is the competitive equilibrium between an immobilized mimic of the target (so-called hapten) and the diffusing target to detect.

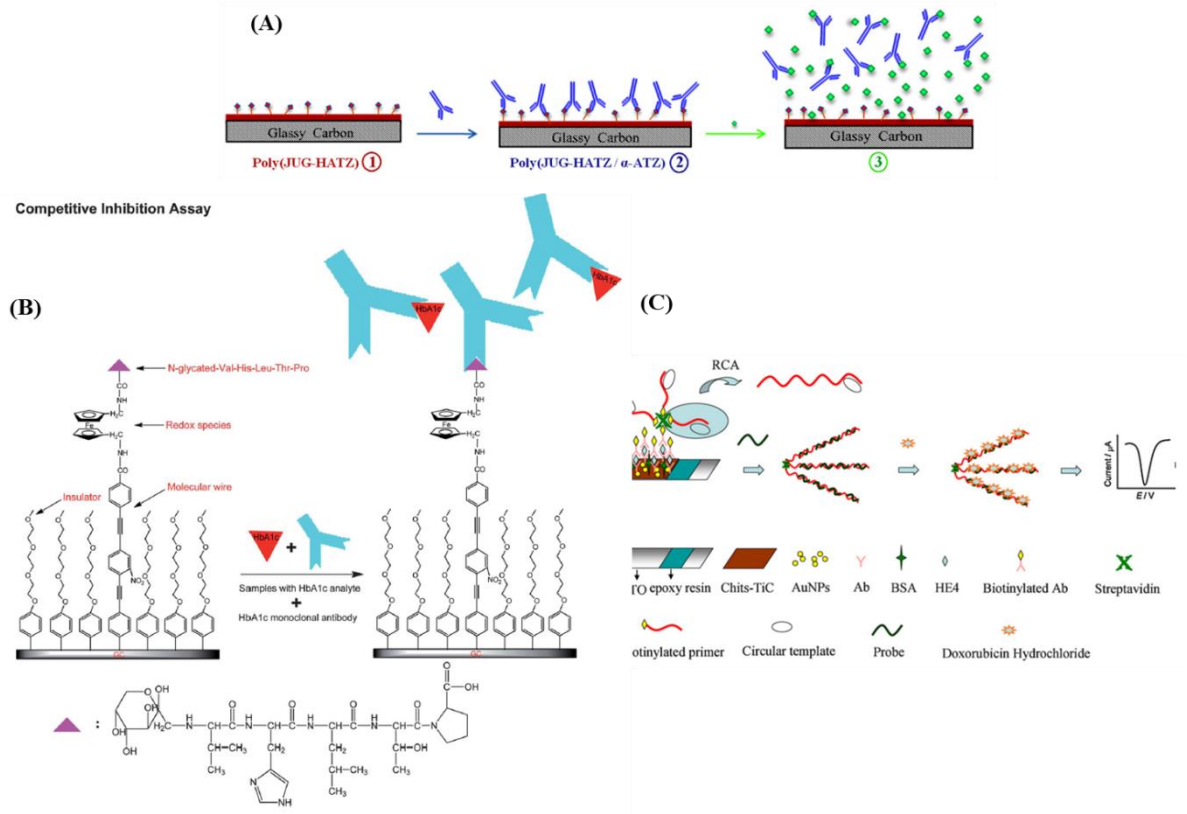

Figure I.13. Some examples of enzyme-free immunosensor applications: (A) Strategy for the electrochemical detection of atrazine based on the change in electroactivity of a polymer film poly(juglone-ATZ); (1) polymer/hapten-modified electrode; (2) after complexation with anti-ATZ; (3) after addition of ATZ in solution [(54)]. (B) Scheme of the competitive inhibition assay for detecting HbA1c (anti-HbA1c: blue Y; HbA1c: red triangle; GPP: pink triangle, surface bound)[(50)]. (C) RCA-based immunosensor for HE4 detection [(62)].

In the same year (2012), a similar idea was developed by Liu *et al.* [(50)] They reported an electrochemical immunosensor for detecting glycosylated hemoglobin (HbA1c) based on glassy carbon electrodes (GCEs) modified with a mixed layer of oligo(phenylethynylene) and oligo(ethyleneglycol), obtained by electrografting of the corresponding aryl diazonium salts. 1,1′-Di(aminomethyl)ferrocene and an epitope, the glycosylated pentapeptide (GPP) VHLTP, were covalently attached to oligo(phenylethynylene). GPP is a peptide mimetic to HbA1c, to which an anti-HbA1c antibody could bind. As for Tran *et al.*, HbA1c was detected by a competitive assay based on the competition for binding to anti-HbA1c between the analyte in solution, HbA1c, and the surface bound GPP peptide. Exposure of the GPP-modified interface to the mixture of anti-HbA1c IgG antibody and HbA1c resulted in the attenuation

of Fc electroactivity due to steric hindrance generated by the antibody bound to the surface (Figure I.13 (B)). The authors found that HbA1c could be detected from 4.5% to 15.1% of total hemoglobin in serum. The same authors, in the same year, adapted this method to AuNPs-modified surfaces (reference cited later in the section). Also, to avoid addition of a diffusing redox probe in solution, Wang *et al.* [(63)] reported later a similar approach, based on an electroactive polymer onto which an antibody was coupled, to detect bisphenol A (BPA) by competitive binding assay with a detection limit of 2 pg mL^{-1} using SWV. A current decrease was obtained upon anti-BPA binding and an opposite current increase upon BPA addition in solution. These authors also described a similar approach for detection of acetaminophen [(64)] with the detection limit of ca. 10 pM (1.5 pg mL^{-1}). An original approach using DNA was reported by Lu *et al.* [(62)]. They described detection of human epididymis-specific protein 4 (HE4) with a chitosan-titanium carbide-modified ITO electrode (Chi-TIC/ITO) onto which AuNPs were deposited. The capture antibody was adsorbed onto the Au and TiC NPs. For transduction and amplification, secondary antibodies were labelled with DNA strands, followed by rolling circle amplification (RCA). Using doxorubicin as DNA intercalator and DPV for detection, the redox current responded to HE4 linearly in the concentration range of 3–300 pM, with a LoD of 0.06 pM (3-300 ng L^{-1} and 0.06 pg mL^{-1}, respectively) (Figure I.13 (C)). This is a good example of enzyme-free amplification; amplification is provided by the numerous sites where doxorubicin can intercalate on each DNA strand. The high surface density of doxorubicin achieved by this strategy provided high currents leading to the high sentivitity of the method.

However, because this kind of amplification implies several successive steps, simple non-amplified procedures stayed popular, and particularly EIS combined with a diffusing redox probe. Hayat *et al.* [(40)] described the immobilization of anti-okadaic acid antibody on 4-carboxyphenyl film. The Ab-Ag binding was transduced simply using electrochemical impedance spectroscopy with $Fe(CN)_6^{3-/4-}$ as diffusing redox probe. The increase in electron transfer resistance was linearly proportional to the okadaic acid concentration in the range 0.195–12.5 µg L^{-1}, with a LoD of 0.3 ng mL^{-1}. In 2013, Vasudev *et al.* [(65)] described a similar procedure for epidermal growth factor receptor (EGFR) detection, by immobilizing anti-EGFR antibody on dithiobissuccinimidyl propionate (DTSP) SAM on Au electrodes. EIS measures with $Fe(CN)_6^{3-/4-}$ as redox probe exhibited a linear range from 1 pg mL^{-1} to 100 ng mL^{-1} and a LoD of 1 pg mL^{-1}. Vasudev *et al.* [(66)] also presented the same procedure

but replaced conventional Au electrode by microfabricated interdigitated ones. As a proof-of-concept, cortisol antibodies were immobilized using the same SAM as previously described. Cortisol (M_W of 362 g mol^{-1}) was detected using CV over a linear range of 10 pM to 100 nM (3.6 pg mL^{-1}-36 ng mL^{-1}).

This example is probably the occasion to recall here that the relative size of the target molecule compared to that of an antibody should determine the choice of the transduction architecture of an electrochemical immunosensor. Indeed, the most popular Ab reported in biosensors are immunoglobulins G (IgG), with a typical molecular weight of 150 kDa, i.e. a volume of between 300 and 700 nm^3 or a projected area, on the supporting surface, of ca. 60 nm^2. This should be compared to the molecular weight of the target antigen. If this one is for example a small protein of 30 kDa, it corresponds to a projected area of 22 nm^2, i.e. ca 30% of the antibody's. Nevertheless, for a molecule (such as pesticide, industrial or pharmaceutical pollutant) of 200 g mol^{-1}, this ratio falls to 1% of the antibody's projected surface, which is negligible and cannot play a significant role in changing the steric hindrance at the solution/electrode interface; for such situations, other transduction schemes should be considered, for example, by playing not only on steric hindrance but also on electrostatic repulsions, or reducing the size of the capture antibody by using only Ab fragments or an analog of protein (a peptidomimetic). For example, for detection of a bulky protein (porcine serum albumin), Lim *et al.* [(67)] reported a carbon nanofiber-modified SPE electrofunctionalized with a 4-carboxyphenyl diazonium salt onto which antibodies were covalently bound. Taking profit of the strong affinity of serum albumins towards anions, an anionic redox probe was used in solution. An increase in cathodic peak current was measured after immunocomplex formation between antibodies and proteins. The linear range was from 0.5 to 500 pg mL^{-1} and the LoD of 0.5 pg mL^{-1}. Also, using $Fe(CN)_6^{3-/4-}$ as an electroactive diffusing probe, Jarocka *et al.* [(68)] reported detection of hemagglutinin from avian influenza virus H5N1. Gold electrodes were modified with a SAM of 4,4′-thiobisbenzenethiol (TBBT), itself modified by gold nanoparticles (AuNPs) and single chain variable fragments of antibodies (scFv) against hemagglutinin H5 (Figure I.14 (A)). Interactions between the scFv of antibodies and hemagglutinin were sensed by EIS, giving a LoD of 0.6 pg mL^{-1} and a linear range from 4.0 to 20.0 pg mL^{-1}. This scFv makes 25 kDa and corresponds to the variable domains; it is the smallest fragment that holds a complete binding site of an antibody and therefore retains its specificity (Figure I.14 (B)).

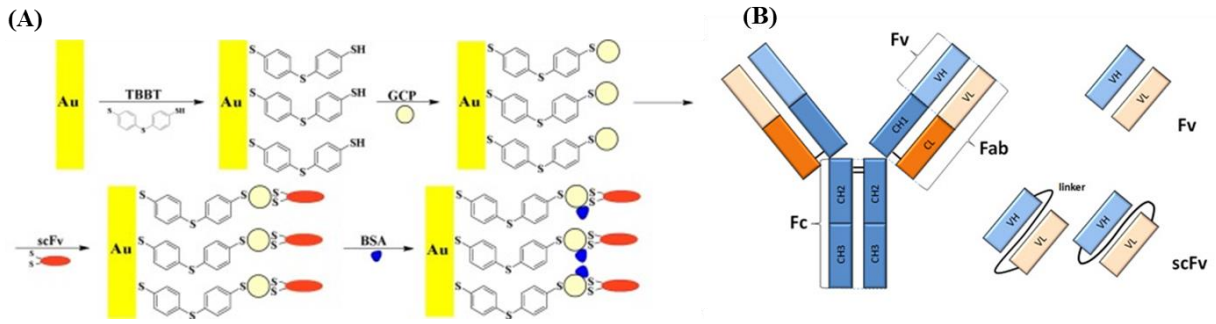

Figure I.14. Illustration of detection of hemagglutinin from avian influenza virus H5N1: (A) Hemagglutinin H5 immunosensor based on a SAM of 4,4'-thiobisbenzenethiol carrying single chain variable fragments (scFv) of antibodies as probes [(68)]. (B) Schematic representation of a scFv fragment. A scFv makes 25 kDa and corresponds to the VH+VL domains. From Antibody Design Laboratories. (http://www.abdesignlabs.com/technical-resources/scfv-cloning/); access January 29th 2017.

Table I-1. Figures of merit of enzyme-based and enzyme-free immunosensors using conventional electrode substrates.

Target	Probe	LoD	Method	Ref.
AbHIV	Peptides	1 ng mL^{-1}	AP/DPV	*(41)*
IgG	Ag	1.4 µg mL^{-1}	HRP/CV-Sandwich	*(58)*
Estradiol	Ab	0.77 pg mL^{-1}	HRP/CV-Competitive	*(51)*
CEA	Ab	40 pg mL^{-1}	HRP-Sandwich	*(59)*
ACTH	Ab	18 fg mL^{-1}	AP/DPV-Competitive	*(49)*
Sulfonamide	Ab	200-500 pg mL^{-1}	HRP-Competitive	*(56)*
CA-125	Ab	0.1 U mL^{-1}	GOx-Sandwich	*(52)*
TNF-α	Ab	10 pg mL^{-1}	HRP/CV-Sandwich	*(60)*
Tyrosine kinase	Ab	337 pg mL^{-1}	HRP-Sandwich	*(53)*
TREM-1	Ab	30 pg mL^{-1}	$Fe(CN)_6^{3-/4-}$ /EIS	*(61)*
Atrazine	Hapten	0.2 ng L^{-1}	ECP/SWV-Competitive	*(69)*
HbA1c	Peptide	-	Fc/CV-Competitive	*(50)*
Bisphenol A	Hapten	2 pg mL^{-1}	ECP/SWV-Competitive	*(70)*
Acetaminophen	Hapten	1.5 pg mL^{-1}	ECP/SWV-Competitive	*(71)*
HE4	Ag	0.06 ng L^{-1}	DNA/DNA-Sandwich	*(72)*
Okadaic acid	Ag	0.3 ng mL^{-1}	$Fe(CN)_6^{3-/4-}$ /EIS	*(39)*
EGFR	Ag	1 pg mL^{-1}	$Fe(CN)_6^{3-/4-}$ /EIS	*(65)*
Cortisol	Ag	3.6 ng L^{-1}	$Fe(CN)_6^{3-/4-}$ / CV	*(66)*
Porcine albumin	Ag	0.5 pg mL^{-1}	$Fe(CN)_6^{3-/4-}$ / CV	*(43)*
Hemagglutinin	scFv	0.6 pg mL^{-1}	$Fe(CN)_6^{3-/4-}$ /EIS	*(73)*

2.7 Application of immunosensors for pesticides detection

When pesticides are used, a part remains in soil and water, where they cause serious problems of contamination. There are several reviews dealing with application of biosensors to pesticide detection [74, 75]. A review of these existing electrochemical immunosensors for pesticide detection will be given as introduction of Chapter II. Some examples are given in Table I-2.

Table I-2. Characteristics of some electrochemical immunosensors

Target analyte	Immobilization technique	Electroactive materials	Linearity range (M)	Detection limit (M)	Ref.
		Amperometry			
Phenanthrene	Absorption of BSA-phenanthrene conjugate	-	2.8×10^{-9}-2.5×10^{-7}	4.5×10^{-9}	(76)
Paraoxon	Adsorption+nafion film	AuNPs	8.7×10^{-8}-6.9×10^{-6}	4.4×10^{-8}	(75)
Atrazine	Affinity	-	7×10^{-10}-1.35×10^{-8}	1.7×10^{-10}	(77)
Atrazine	Adsorption	PANI-PVS copolymers	5.5×10^{-10}-2.3×10^{-8}	4.6×10^{-10}	(78)
17-β estradiol	Absorption of BSA-estradiol conjugate	-	2.2×10^{-12}-3.6×10^{-5}	9.2×10^{-13}	(79)
Pichloram	Absorption of BSA-pichlogam conjugate	Gold nanoclusters	3.6×10^{-9}-3.6×10^{-5}	1.8×10^{-9}	(80)
Diuron	Absorption of hapten-BSA conjugate	Prussian blue, AuNPs	4.3×10^{-12}-4.3×10^{-5}	4.3×10^{-12}	(81)
Naphthalene	Absorption	AuNPs	3.9×10^{-9}-7.8×10^{-7}	6.2×10^{-10}	(82)
		Impedance spectroscopy			
Atrazine	Affinity	-	4.6×10^{-8}-1.4×10^{-6}	9.3×10^{-8}	(83)
Atrazine	Absorption of BSA-atrazine conjugate	-	ND	2.7×10^{-8}	(84)
Atrazine	Absorption of BSA-atrazine conjugate	-	ND	3.9×10^{-8}	(85)
Atrazine	Covalent immobilization of BSA-atrazine conjugate	-	ND	1.9×10^{-10}	(86)
Atrazine	Affinity	-	4.6×10^{-10}-4.6×10^{-6}	4.6×10^{-11}	(87)
2,4-D	Covalent binding	-	2×10^{-10}-2×10^{-6}	ND	(88)

3 Electrolyte-gated organic field-effect transistors (EGOFETs)

3.1 General concepts of field-effect transistors

A Field-Effect Transistor (FET) is made of three metallic conducting electrodes: source (S), drain (D) and Gate (G), a very thin insulating layer (dielectric) and a semiconductor, the latter being the active part of the device where the current flows. Numerous geometries were described, among which: the gate could be on top of the semiconductor (top-gate) or at the bottom of the semiconductor (bottom-gate). Similarly, the source and drain can contact the top (top-contact) or the bottom (bottom-contact) of the semiconductor. The working principle of a FET is the following: a voltage applied to the gate modifies the charge carrier density in the semiconductor in between source and drain, which therefore modulates the source-drain current. There are two kinds of charge carriers that make the current: electrons (e) and hole (h) for n- or p-type semiconductors, respectively. Dealing with organic FETs (OFETs), electron donating organic semiconductors involving a high level of the highest occupied molecular orbital (HOMO) are good candidates for p-type semiconductors, while electron-accepting ones with low HOMO levels are used as n-type semiconductors.

In OFETs, the gate is separated from the semiconductor by an insulator. Different dielectrics can be used, e.g. oxides, polymers, self-assembled monolayers. When the gate is, for instance, negatively polarized in a p-channel device, free holes in the semiconductor are drawn toward the semiconductor-insulator interface to compensate an equivalent negative charge at the gate-insulator interface (Figure I.15 (a)). When a negative voltage is applied between source and drain, holes are injected from the source and a current flows inside the channel. The first OFET was made by Tsumura *et al.*, in 1986, who reported a I_{on}/I_{off} ratio (i.e. the ratio between the maximum current flowing at saturation and the minimum current when the transistor is in its blocked state) of 100, and charge carrier mobility of 10^{-5} $cm^2 V^{-1}$ [(89)], using a polythiophene semiconductor. This was of course far from the best characteristics obtained with the silicium technology, but the two devices do not compete. Although inorganic FETs are fast, they are difficult to functionalize; on the contrary, OFETs are slow but extremely versatile from the chemical point of view, which is a great advantage when considering FETs for sensing purposes. Here, I will particularly focus on an inovative type of OFET, the EGOFET, of which I will show that it is more adapted for application in water environment.

3.2 EGOFETs

Electrolyte-gated OFETs are significantly different from classical OFETs; indeed, the organic semiconducting layer is in contact with an electrolyte instead of a classical dielectric. In EGOFETs, the conductivity of the semiconducting channel is modulated by a solid or a liquid electrolyte put in-between the semiconductor and the gate. EGOFETs display much higher gate capacitance (up to ~ 1000 higher) than other types of OFETs which use traditional inorganic or organic non-electrolytic dielectrics; as a consequence, biasing voltages used for EGOFETs are typically much smaller than those necessary for OFETs (< 1 V, versus > 10 V or higher). These two characteristics (water as electrolyte and low operation potential) make EGOFETs ideal candidates for the next generation of biosensors, particularly suitable for the detection and quantification of biological molecules in aqueous media. The extremely good sensing capabilities of EGOFETs rely on the possibility of properly functionalising the gate electrode by means of specific molecules or functional groups able to interact with the target molecules present inside the electrolyte. The most common architecture is the top-gate, bottom-contact configuration. The gate electrode is immersed into the electrolyte and source and drain electrodes, isolated from the electrolyte, provide electrical contact to the channel (Figure I.15 (b)). Actually, an EGOFET looks like an OECT (organic electrochemical transistor) [(90-93)]. However, in an OECT, the on/off switch is produced by electron transfer from the electrolyte and the semiconductor (doping/de-doping) [(94)] whereas only capacitive processes occur for EGOFETs but no charge transfer.

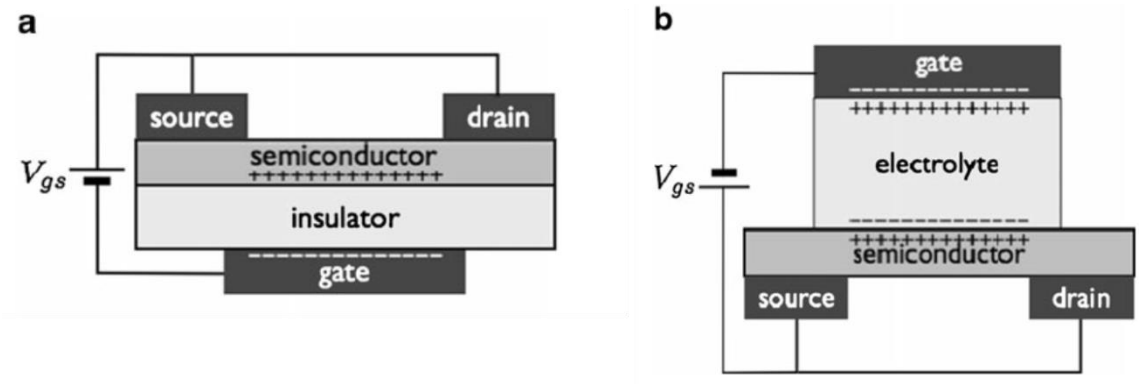

Figure I.15. General scheme of an OFET (a) and an EGOFET (b). [(94)]

In an EGOFET made with a p-type semiconductor, upon positive polarization of the gate, the anions of the electrolyte accumulate at the electrolyte/semiconductor interface while the cations accumulate at the electrolyte/OSC interface, resulting in the formation of an electrical double layer (EDL) at both interfaces. The EDL is composed of the Helmholtz layer (HL) and the diffuse layer (DL). The HL is a monolayer of ions whereas the DL is simply more concentrated in ions (either cations or anions) than in the bulk electrolyte. In other words, the excess of ions decreases with the distance from the interface. As shown on Figure I.16, when the gate is, for example, negatively polarized, the excess of electrons at the gate surface produces an accumulation of cations at the gate/electrolyte interface; conversely, accumulation of anions at the electrolyte/semiconductor interface produces accumulations of holes in the topmost layer of the semiconductor [(95)], which causes the OSC to become conducting. It has been shown that a significant double layer can form even for very low operating potentials, nevertheless sufficient to generate a locally high electrical field at the electrolyte/semiconductor interface, and therefore a high charge carrier density [(94)].

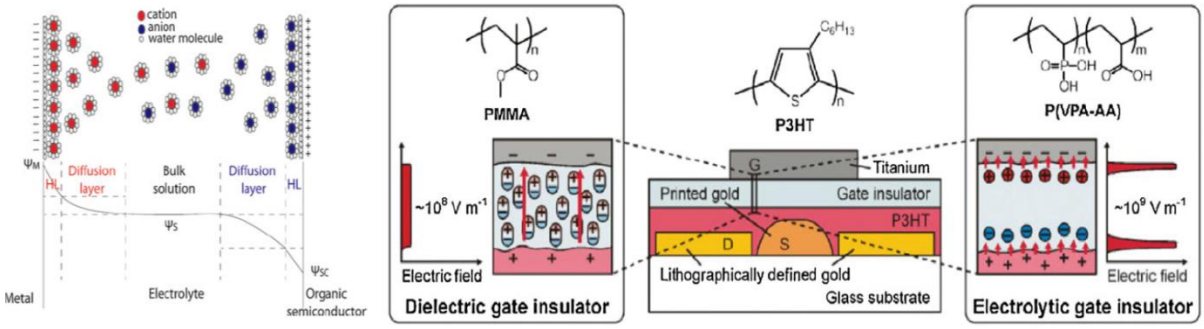

Figure I.16. Illustration of the compact and diffuse layers corresponding to an OFET and an EGOFET, respectively [(96)].

The electrolyte used can be polymers [(97-100)], ionic liquids [(101-103)] or ionic gels [(104-108)]. Aqueous liquid electrolytes were also reported. For example, Kergoat *et al.* [(109)] first reported a device gated with water (Figure I.17). By replacing the gate dielectric by a simple water droplet, they produced a transistor that entirely operates in the field-effect mode at voltages lower than 1 V. They have shown (unpublished results) that the electrical characteristics do not depend on the pH in a range between 4 and 8, which is well adapted to biomolecules.

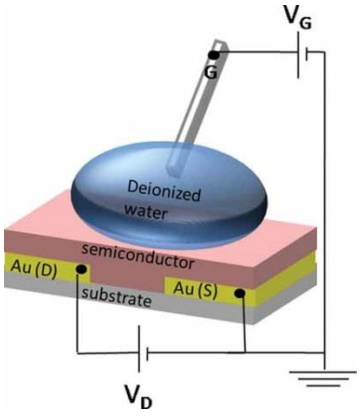

Figure I.17. Scheme of the first water-gated EGOFET. The semiconductor was rubrene and the gate a platinum wire [(109)].

This result creates opportunities for sensor applications. Indeed, water is the natural environment for biological receptors [(110)]. In this case, water must act both as the electrolyte and the media responsible for carrying the analytic sample, which is the current challenge to develop EGOFET-based biosensors. However, in such conditions, an electrochemical doping (i.e. insertion into the semiconductor of ions from the electrolyte) may occur, which decreases the capacitance and the field effect and therefore degrades the semiconductor electrical properties. This is the main reason why the performances of EGOFETs often decrease upon use [(111, 112)]; this constitutes an important issue which must be addressed; for example by developing highly hydrophobic polymeric OSC. However, some small analytes or even ions have no problems to pass a thin hydrophobic barrier. High crystallinity of the organic semiconductor can suppress diffusion of such species. Since most polymer films are semi-crystalline at best, this might be an aspect where crystalline films made from small molecules might be superior in terms of blocking and should be investigated. Another issue which must be addressed is their low subthreshold swing, typically of several hundreds of millivolts, which impede their sensitivity. A strategy may be to switch from classical OSC to graphene-based materials, e.g. graphene or reduced graphene oxide, which has already been reported [(113-126)] (the review from Yan *et al.*, 2013 [(127)] deals with graphene-based transistors for biological sensors). However, graphene has been shown to have low sensitivity due to lack of bandgap. For this reason, other electrolyte-gated inorganic FETs are also promising, for example based on MoS_2 semiconductor. In EGOFETs, the gate material influences also other figures of merit of the devices, particularly the threshold potential V_T [(128, 129)]. However,

most of the transistor characteristics come from the semiconducting material itself and from the quality of the contact between the source and drain electrodes and the OSC (which depends on the way the semiconductor is deposited).

3.3 Semiconducting materials

3.3.1 Deposition techniques

Several deposition techniques were described; among them: spin coating, vacuum thermal deposition, printing and spray deposition. Spin-coating and drop-casting remain the most popular in laboratory, whereas inkjet printing and spray deposition are preferentially used in industry; vacuum thermal evaporation is used in both environments.

- Vacuum thermal evaporation

For vacuum thermal evaporation, both the semiconducting material and the substrate are placed in high vacuum; The OSC is thermally sublimated then is condensed on the cold substrate to form a film, the thickness of which being controlled by the deposition time and the temperature [130, 131].

- Spin-coating

Spin-coating consists of spinning the substrate onto which a solution containing the semiconducting material is deposited. Spinning produces a centrifugal force which spread homogeneously the solution and forms a very thin film over the substrate; its thickness is a balance between the centrifugal force and the solution viscosity. During this operation, the solvent evaporates, leaving a thin film of semiconducting material. An additional annealing step is needed to crystalize the semiconductor molecules, which improves the electrical performances [132, 133]. Very roughly, the film thickness depends on the concentration of the solution (the more concentrated, the thicker), the rotation speed (the faster, the thinner) and the evaporation rate of the solvent (the faster, the thicker). Compared to vacuum thermal evaporation, the advantage of spin-coating is that it does not need heating, which avoids thermal degradation of semiconductors. The main limitation is that all semiconductors cannot dissolve in volatile solvents.

- Inkjet-printing and spray deposition

Inkjet-printing is a non-contact solution-processed technique which allows non-lithographic patterning, for a lateral resolution as small as 25 µm (at best), however depending on substrate preparation [134, 135]. Inkjet-printing is an additive technology and is therefore much less wasteful than other solution-based methods using subtractive patterning methods ; it generally ensures a better electrical contact with the underlying electrode/material than vacuum thermal evaporation [136] but it has the disadvantage of poor lateral resolution compared to lithography [111, 137-139].

Spray deposition is another non-contact solution-based method. In this case, instead of thermal or piezoelectric propulsion of the ink, the liquid is pumped and guided through a gas flow to the substrate. Like for inkjet-printing, the ink arrives at the substrate as micrometric droplets. For this reason, a challenge for both techniques is to achieve uniform films [131, 140].

3.3.2 Semiconducting materials

- Generalities

It is remarkable to note that no rationale has been published concerning chemical stability of OSCs applicable in EGOFETs. One may keep in mind that the HOMO and LUMO levels of the OSC should not allow electrolyte oxidation or reduction; another very important parameter is that the electrolyte should not penetrate into the OSC, which would become electroactive. Even though Buth *et al.* used α-sexithiophene (α6T) in 2011 and 2012 to make an EGOFET-based biosensor [141, 142], most of EGOFET biosensors were reported with poly(3-hexylthiophene) (P3HT) as the organic semiconductors [96, 112, 139, 143-152]. In the recent years, thienothiophene copolymers, especially the poly(2,5-bis(3-alkylthiophen-2-yl)thieno[3,2-b]-thiophene) (pBTTT) was also considered, due to a better stability in humid environment or even in water (Figure I.18) [153-156].

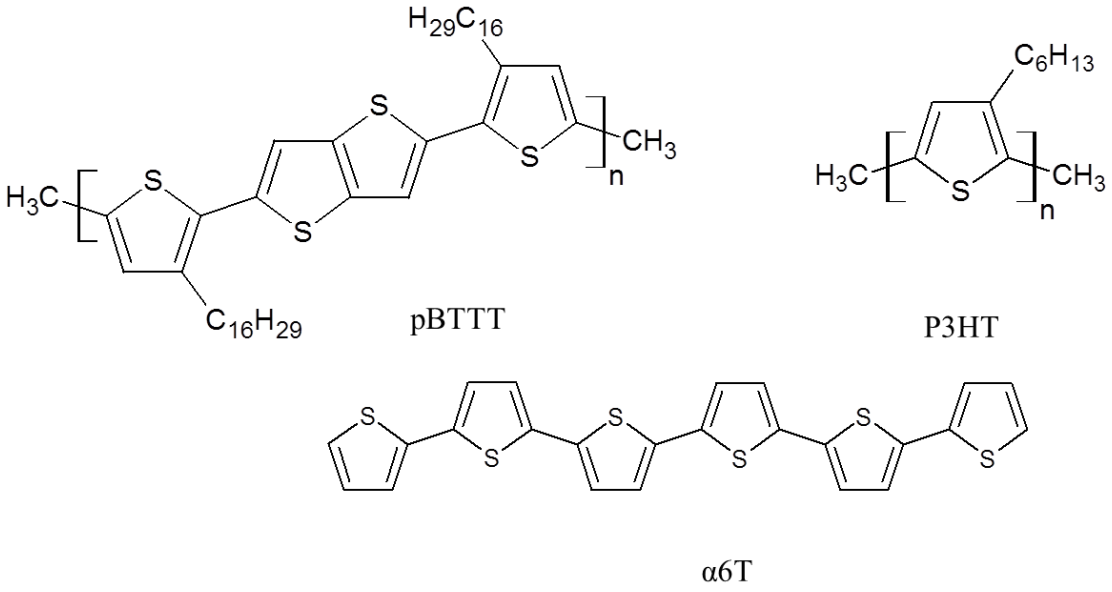

Figure I.18. Most highly commercial semiconducting oligomers and polymers in EGOFET biosensors.

- Poly(3-hexylthiophene) (P3HT)

P3HT is the most common OSC used during the last decade [(97)]. Kline *et al.* analyzed a series of regioregular polythiophenes in an OTFT device. They found that the crystallinity and molecular weight are two important parameters on the hole mobility, resulting from the well-defined molecular architecture of P3HT [(157)]. For example, 3-hexylthiophene units may polymerize through head-to-tail, head-to-head or tail-to-tail couplings; the percentage of head-to-tail coupling represents the degree of regioregularity of P3HT, which is critical to the electronic properties of the material. High-performance OFETs based on highly regioregular P3HT were successfully fabricated by solution process and showed hole mobilities higher than 0.1 $cm^2 V^{-1} s^{-1}$ and very high on/off ratios ($>10^5$) [(158)].

If P3HT is deposited by spin-coating, the best solvent is chloroform, due to its rapid evaporation which limits crystallization during the spin-coating process [(158, 159)]; this impose a thermal post-treatment process able to favor crystallization and π–π stacking of the P3HT backbone. It has been shown that this results in a lamellar structure formed by interchain stacking (Figure I.19). It has been also shown that the hole mobility varies by two orders of

magnitude depending on orientation (parallel or normal to the substrate) of the lamellae [132, 133, 160-165], the normal one giving the highest mobility.

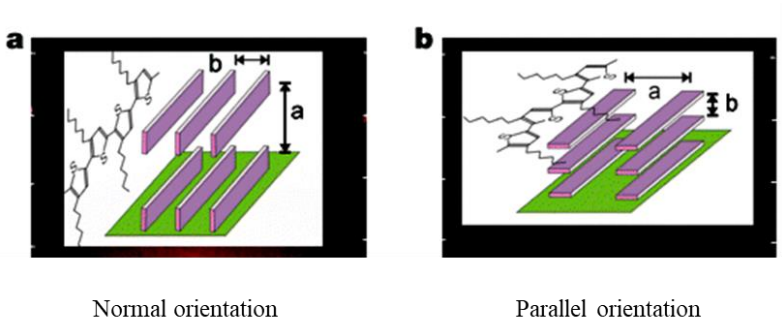

Figure I.19. Lamelar structure of P3HT, normal or parallel to the substrate, respectively [133].

According to the work of Alberga *et al.* [132], spin-coated then annealed P3HT displays three different zones: an interfacial zone close to the substrate (thickness of 10 Å), an intermediate zone 30 Å thick atop and an OSC/electrolyte interfacial zone over this distance; the first layers display the highest degree of order [132, 166-168].

Some strategies were proposed to improve the performances and/or biocompatibility of P3HT. For example, Liu *et al.* printed P3HT above another terrylene semiconductor to make a heterojunction of semiconductor [136]. Thiemann *et al.* spray-coated a layer of ion gel based of silane-ionic liquids on P3HT to obtain advantageous properties such as low modulus, solution processability and high specific capacitance [140]. Magliulo *et al.* modified the surface of P3HT by plasma-enhanced vapor chemical deposition (PE-CVD) of a mixture of ethylene, acrylic acid and argon in a 1:3:1 ratio, which increased the –COOH content at the surface, eventually used to covalently graft phospholipids on the OSC, themselves used to bind biological molecules [144, 151, 169]. Kergoat *et al.*, Sinno *et al.* and Toss *et al.* used chemical reactions to bind P3HT with another polymer to make new semiconductor polymer blends with improved stability, electronic performances and biocompatibility [138, 170, 171]. Suspène *et al.* used peptidic coupling to directly graft biotin on P3HT in order to make a proof-of-concept streptavidin or avidin sensor [172]. All these approaches impose to make compromises between the electrical and immobilization properties.

- Poly(2,5-bis(3-alkylthiophen-2-yl)thieno[3,2-b]-thiophene) (pBTTT)

Even though P3HT is certainly the mostly used semiconductor in OFETs, its well-known instability obviously limits its utilization for biosensors [173-175]. pBTTT has recently attracted attentions as another promising solution-processed semiconducting polymer. pBTTT shows better performances than P3HT (hole mobility up to 1.0 $cm^2 V^{-1}s^{-1}$ for pBTTT versus 0.1 $cm^2 V^{-1} s^{-1}$ for P3HT [176, 177]), less electrochemical doping and much better stability in aqueous environment [132, 178].

Liquid-crystalline pBTTT was firstly used as semiconductor layer in liquid-gated structure by Naim *et al.* [179]; Chao *et al.* showed that pBTTT has a similar lamellar structure to P3HT [180]; however, pBTTT has larger crystalline domains extended over several hundreds of nm [155, 176, 178] (Fig. I.20). This probably explains why pBTTT has better performances [181, 182].

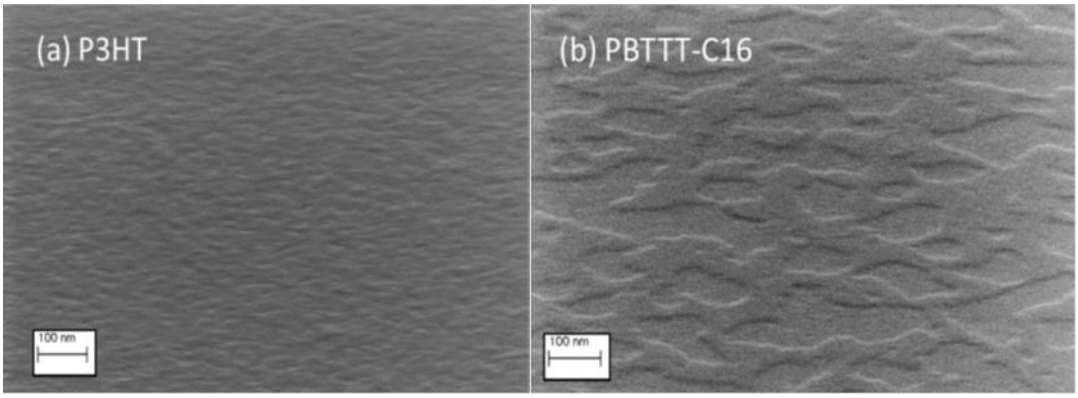

Figure I.20. Lamelar structure of P3HT(a), pBTTT-C16 (b), normal or parallel to the substrate [133].

The best solvent for spin-coating pBTTT is chlorobenzene. It was shown that, because the boiling point of chlorobenzene is high, few residual solvent molecules may remain after annealing, and these solvent molecules may behave as plasticizer, increase free space between chains thus facilitate orientation and crystallization [132, 177, 181].

- Dithienothiophene and diketopyrrolopyrrole based polymers (DPP-DTT)

Figure I.21. Chemical structure and product image of DPP-DTT polymers

The chemical formula of DPP-DTT is $(C_{60}H_{88}N_2O_2S_4)_n$, with a molecular weight around 500 kD (Figure I.21). It is a p-type OSC, with a HOMO of -5.2 eV and a LUMO of -3.5 eV *(183)*. DPP-DTT is stable at ambient conditions (humidity and temperature) *(184)*. It is suitable for flexible substrates with different radius of curvature, which has been shown by Kwon *et al*. in 2017 *(184)* (Figure I.22). In addition, they also mentioned that the on/off ratio of DPP-DTT-based devices can reach 10^4, with an average hole mobility of 5.5×10^{-2} cm^2 V^{-1} s^{-1} (we will see below that the hole mobility can be higher) while the gate-leakage current was low (10^{-9}A).

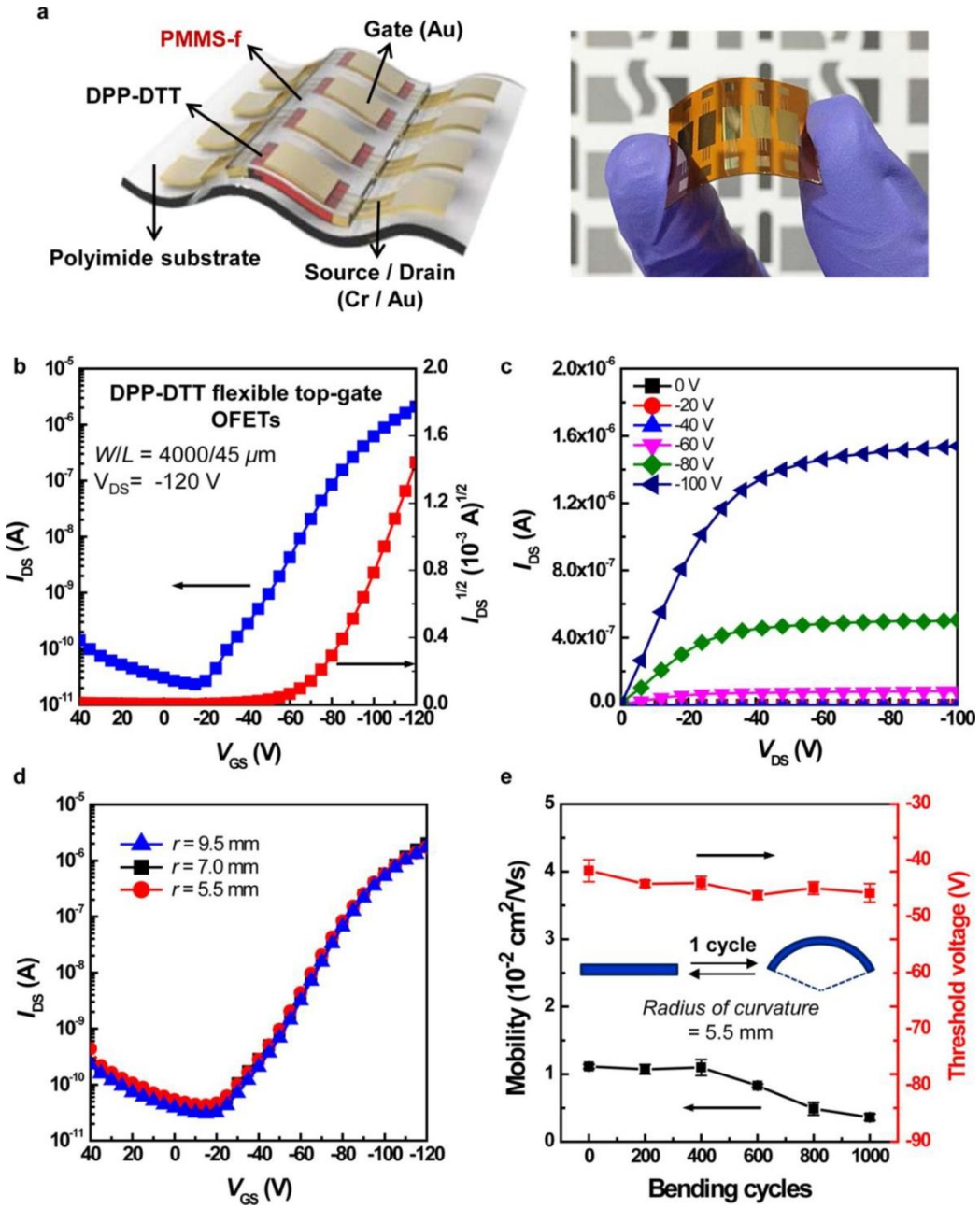

Figure I.22. Flexible DPP-DTT top-gate OFETs fabricated on flexible polyimide substrate. (a) Scheme and picture of the device. (b) Transfer and (c) output characteristics of flexible DPP-DTT top-gate OFETs with the solvent-free PMMS-f dielectric. (d) Transfer characteristics of the DPP-DTT top-gate OFETs as a function of the radius of curvature. (e) Mobility and threshold-voltage variations with increasing number of bending cycles (at radius of curvature of 5.5 mm) [(184)].

Remarkably, DPP-DTT polymers consist of both the electron acceptor (DPP) and the electron donor (DTT), so to increase donor-acceptor interactions at short distances within the polymer

chains. It is used to explain that DPP-DTT has a highly crystalline structure which results in higher mobilities than other polymers [185, 186]. In the other hand, DPP-DTTs is poorly soluble compared to other polymers, so the solution process must be operated at elevated temperature with solvents such as chloroform, chlorobenzene or dichlorobenzene. Although such polymers are quite thermally stable [187], DPP-DTTs tends to be oxidized and loose adherence to the solid support [185]. The mobility of DPP-DTT depends on the temperature of annealing; in the range 100°C-140°C, the mobility is of 0.5-0.85 $cm^2\ V^{-1}\ s^{-1}$; at 200°C, the mobility is of 0.88-0.84 $cm^2\ V^{-1}\ s^{-1}$ [185, 186]. The Figure I.23 shows a on/off ratio of 10^6 and a mobility of 0.94 $cm^2\ V^{-1}\ s^{-1}$. Whatever the conditions, the mobility of DPP-DTT is definitely higher than that of P3HT (max of 0.2 $cm^2\ V^{-1}\ s^{-1}$ for P3HT, max. of 1.5 $cm^2\ V^{-1}\ s^{-1}$ for DPP-DTT) [188].

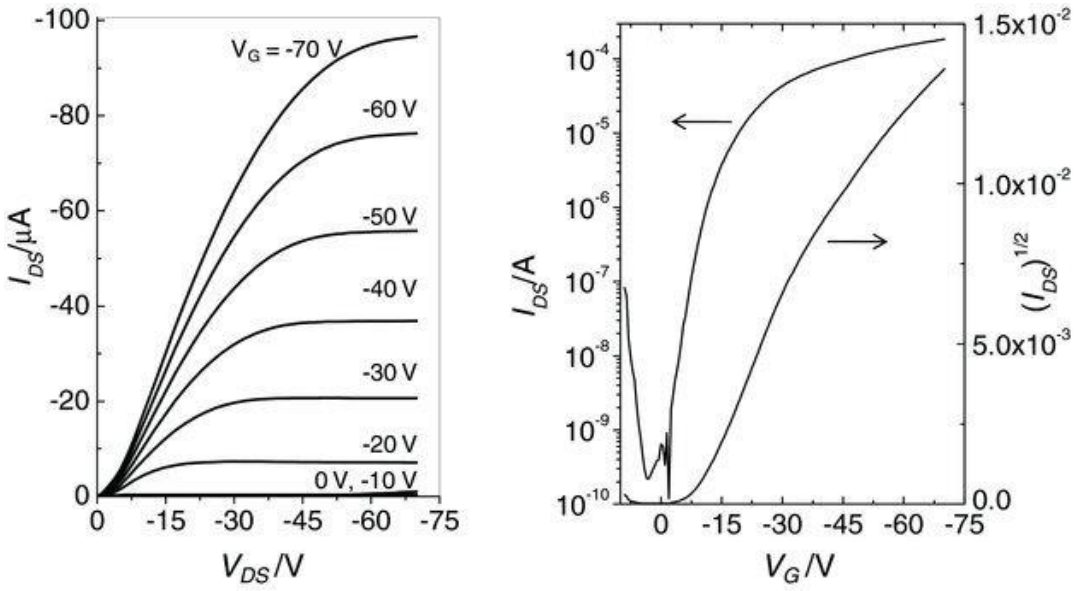

Figure I.23. Characteristics of an OTFT device with a DPP-DTT thin film annealed at 200 °C for 15 min: Output (left: V_G = 0 V to −70 V) and transfer (right: V_{DS} = −70 V) curves. Device dimensions: channel length (L) = 100 µm; channel width (W) = 1 mm. Hole mobility of 0.94 $cm^2\ V^{-1}\ s^{-1}$ in the saturation regime, calculated by using a slope obtained from linear fitting of the $(I_{DS})^{1/2}$ versus V_G curve in the V_G range from −14 V to −31 V [188].

3.4 Biosensors based on EGOFETS

Hereafter are reviewed the various EGOFET-based biosensors reported in the literature since 2012.

3.4.1 α-sexithiophene (α6T)-based EGOFET sensor for detection of enzyme activity

Buth *et al.* described in 2012 [141] an EGOFET which they named solution-gated organic field-effect transistors. The semiconductor (α-sexithiophene) surface was modified by -OH or -NH_2 groups, leading to a pH sensor operating in a pH range relative to the pK_a of the added surface functions. The hydroxyl groups were added by oxidation under UV, and the amine groups were added by grafting 3-aminopropyltriethoxysilane (APTES). The on/off ratio at V_{DS} = –50 mV was between 10^2 and 10^3, with a field-effect mobility of 4 × 10^{-2} cm^2 V^{-1} s^{-1}. The authors found a sensitivity of 14 mV pH^{-1}. As a proof-of-concept, they immobilized the penicillinase enzyme on the semiconductor and sensed penicillin (Figure I.24) by the way of an acid-base titration. They found a detection limit of ca. 5 µM. At low penicillin concentration, the sensitivity of the device was ca. 80 µV $µM^{-1}$.

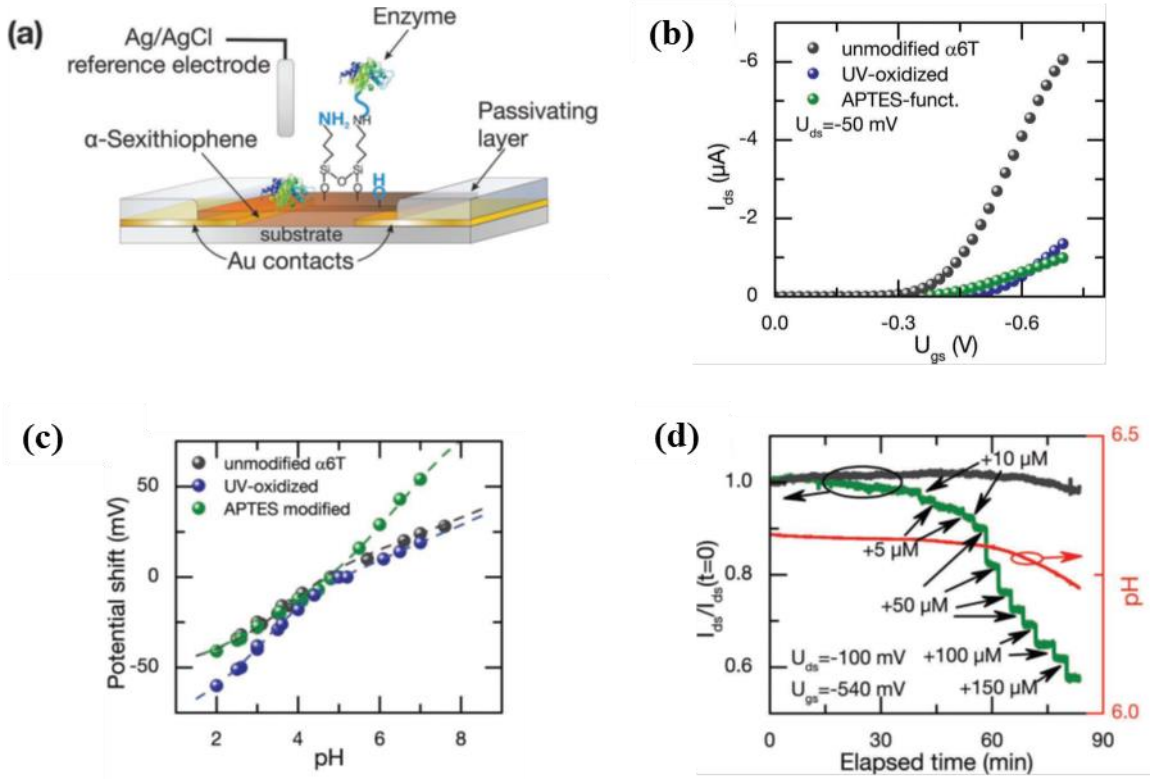

Figure I.24. The EGOFET described by Buth et al. (2012): (a) Schematic drawing of the transistor architecture and the different functionalizations investigated. (b) Transfer curves of untreated, oxidized and APTES-functionalized transistors, measured at pH 5. (c) Threshold voltage shift of untreated, APTES-functionalized and UV-oxidized α6T as a function of pH. (d) I_D versus time, during a penicillin titration in PBS buffer. The green line corresponds to the response of a device functionalized with APTES and penicillinase, while the grey line depicts the I_D response of an untreated α6T [141].

3.4.2 P3HT-based EGOFET sensor for DNA detection

A DNA EGOFET sensor was first reported by Kergoat *et al.*in 2012 [(150)], in which the dielectric is constituted by a simple droplet of aqueous phosphate buffer saline (PBS, pH 7.2) solution and the gate is not made of a reference electrode but a simple gold wire (Figure I.25 (A)). This device allows to operate at very low voltages (below 1 V). This renders the use of buffer solutions possible within their electrochemical stability window. A P3HT bearing carboxylic acid moieties was used to perform covalent oligonucleotide (ODN) grafting, providing that they are modified at one end with a –COOH group. Changes in the output characteristics of the device were observed upon DNA immobilization and after DNA hybridization (Table I-3), of 40 to 60 mV of gate voltage shift for 100 nM target DNA. This shift towards negative values was attributed to the negative charge of the DNA backbone. The *off* current was also modified and decreased after DNA immobilization. This behavior was attributed to the steric hindrance of DNA chains that eventually prevents ion penetration into the bulk of the semiconductor (Figure I.25 (B)). Other experiments, obtained with various ionic strengthes, pointed out the importance of the Debye length that can screen negative DNA charges.

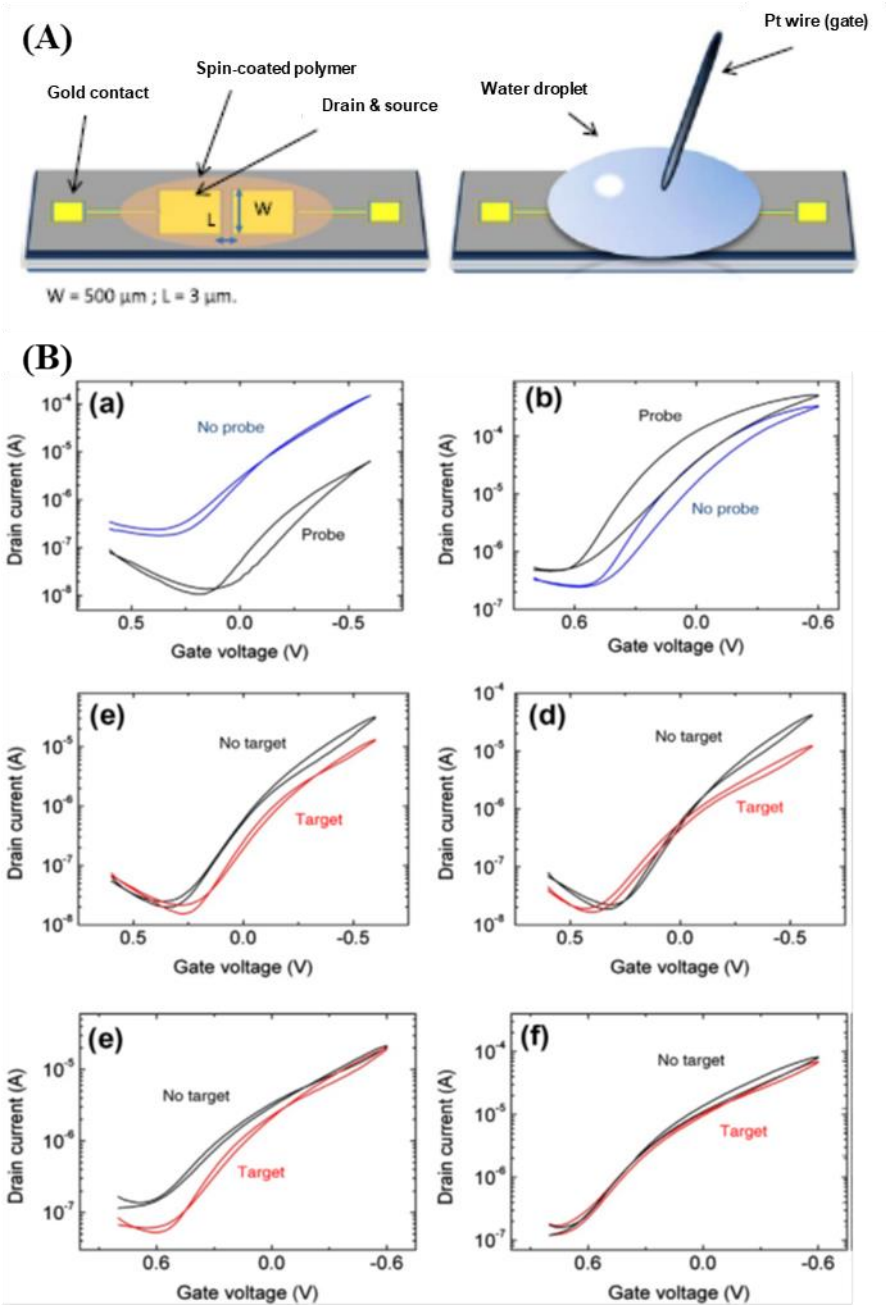

Figure I.25. The EGOFET device for DNA detection:(A) Schematic view of device; (B) Transfer characteristics after (a) immobilization of ODN probes and (b) a blank sample after soaking in a bath similar to (a) but without ODN; Transfer curves for hybridization with (c) a complementary target and (d) a random target; Transfer curves for (e) a complementary target and (f) a random target in water instead of PBS [(150)]***.***

Table I-3. Influence of probe grafting and target hybridization on the threshold voltage and I_{on}/I_{off} ratio, with PBS or water as electrolyte

ODN probe	ΔV_{Cmin}/ V	$I_{off\ (bare\ film)}$/ $I_{off\ (probe\ –\ modified\ film)}$
Yes	-0.31 ± 0.05	11.1 ± 3.7
No	+0.16 ± 0.05	0.5 ± 0.12
DNA hybrid in PBS (Figure I.25 c and d)		
ODN target	ΔV_{Cmin}/ V	$I_{off\ (bare\ film)}$/ $I_{off\ (probe\ –\ modified\ film)}$
HIV	-0.06 ± 0.02	1.7 ± 0.45
RAND	+0.03 ± 0.03	1.3 ± 0.28
DNA hybrid in H_2O (Figure I.25 e and f)		
ODN probe	ΔV_{Cmin}/ V	$I_{off\ (bare\ film)}$/ $I_{off\ (probe\ –\ modified\ film)}$
HIV	-0.03 ± 0.02	3.4 ± 1.5
RAND	+0.04 ± 0.07	1.04 ± 0.04

Schmoltner *et al.* reported an EGOFET based on P3HT for which they investigated the effect of the gate material and of the ionic strength of the electrolyte on the device performances [(189)]. Magliulo *et al.* published in 2013 a work where they demonstrated PE-CVD of an hydrophilic thin layer (plasma deposited ethylene/acrylic acid-pdEthAA) bringing COOH groups on P3HT (Figure I.26) [(151)]. The thickness of the coating was particularly monitored because it should be minimized to avoid adverse effect on the EGOFET performances. A comparison between pristine P3HT and pdEthAA/P3HT bilayer is given on Figure I.27. It was also shown that the gate current (I_G, red curves and right Y-scale) stayed low, which demonstrated the field-effect mode of operation and excluded the electrochemical mode of operation; this showed that the hydrophobic layer fully played its role by impeding ion penetration in the OSC. In addition, the authors reported that chemical or biological species could be covalently immobilized on such functional hydrophobic/hydrophilic bilayer, even though it was not described in their article.

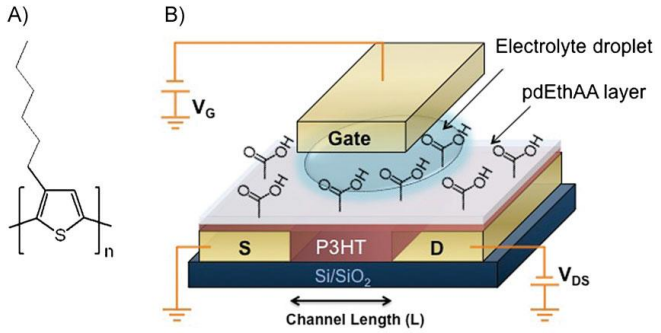

Figure I.26. P3HT organic semiconductor: (A) Chemical structure. (B) Schematic view of an electrolyte gated organic field-effect transistor with the pdEthAA coating deposited by PE-CVD on the P3HT layer [(151)].

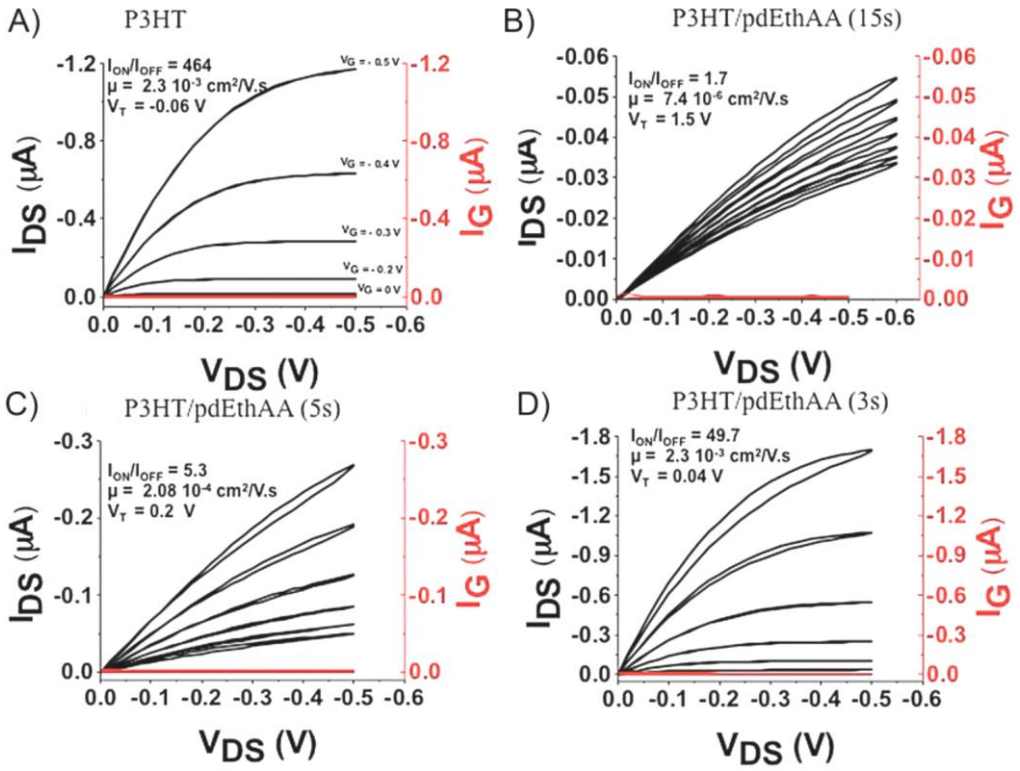

Figure I.27. I_{DS}–V_{DS} curves of EGOFET devices fabricated with (a) pristine P3HT and (b), (c) and (d) with the pdEthAA/ P3HT bilayer deposited by PE-CVD for 15, 5 and 3 s, respectively. L = 2 μm and W = 10 000 μm [(151)].

3.4.3 P3HT-based EGOFET for protein (streptavidin) detection

Suspene *et al.* reported in 2013 on the sensing of streptavidin with an EGOFET using a copolymer of P3HT, P3HT-COOH and biotinylated P3HT (Figure I.28A) as the active sensing and semiconducting material [(172)]. The biotin-streptavidin couple was chosen as a proof-of-concept, for its extremely low dissociation constant. Non-specific interactions were reduced due to the presence of the COOH function; it was further reduced when the polymer surface was pretreated with 1-octanol, which interacted non-covalently with P3HT by its C_8 alkyl chain. In this case, human serum albumin had no effect on the transistor characteristics whereas streptavidin led to a decrease of the drain current (Figure I.28B).

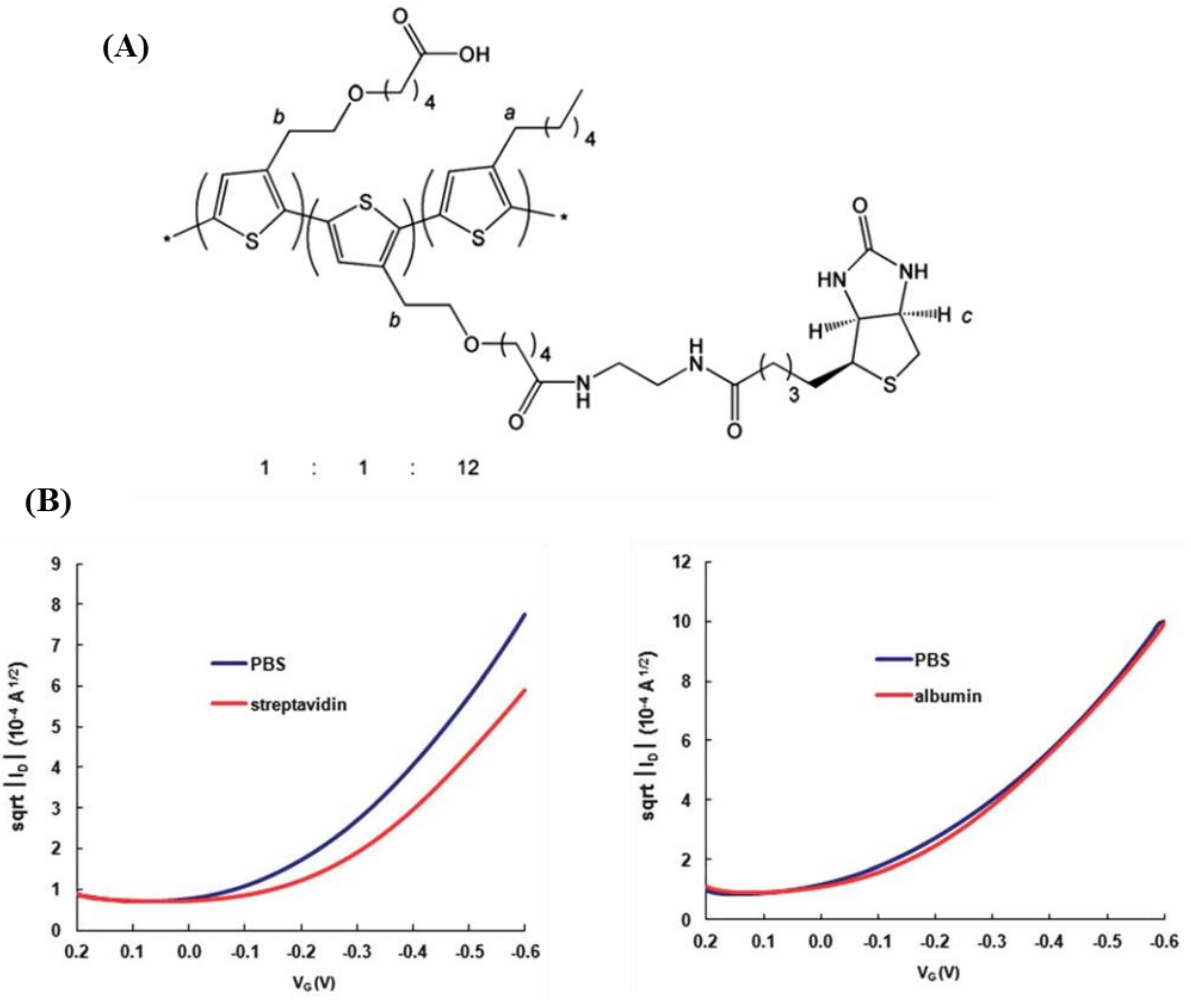

Figure I.28. P3HT:P3HT-COOH:P3HT-biotin terpolymer: (A) Structure. (B) Transfer curves at saturation for this semiconductor based transistors treated with 1-octanol before and after incubation with proteins [(172)].

In order to investigate the transduction mechanisms of such EGOFETs, Palazzo *et al.* [30] investigated in 2015 the sensitivity of their EGOFET as a function of the Debye's length, the receptor charge, and the distance at which the binding event takes place. For this, they used biotin/avidin and antigen/antibody (C-reactive protein CRP versus anti-CRP) interactions. The sensor was shown to successfully detect binding events occurring at distances that are 30 times the Debye's length value from the transistor electronic channel, and even to deliver higher responses in the presence of high salt concentrations (Figure I.29A). The sensitivity was not calculated, but the limit of detection was ca. 10 μg mL^{-1} of CRP. Transduction of the molecular recognition was explained by capacitance changes at the electrolyte/OSC interface rather than by electrostatic effects of the charges carried by the target molecules (Figure I.29B).

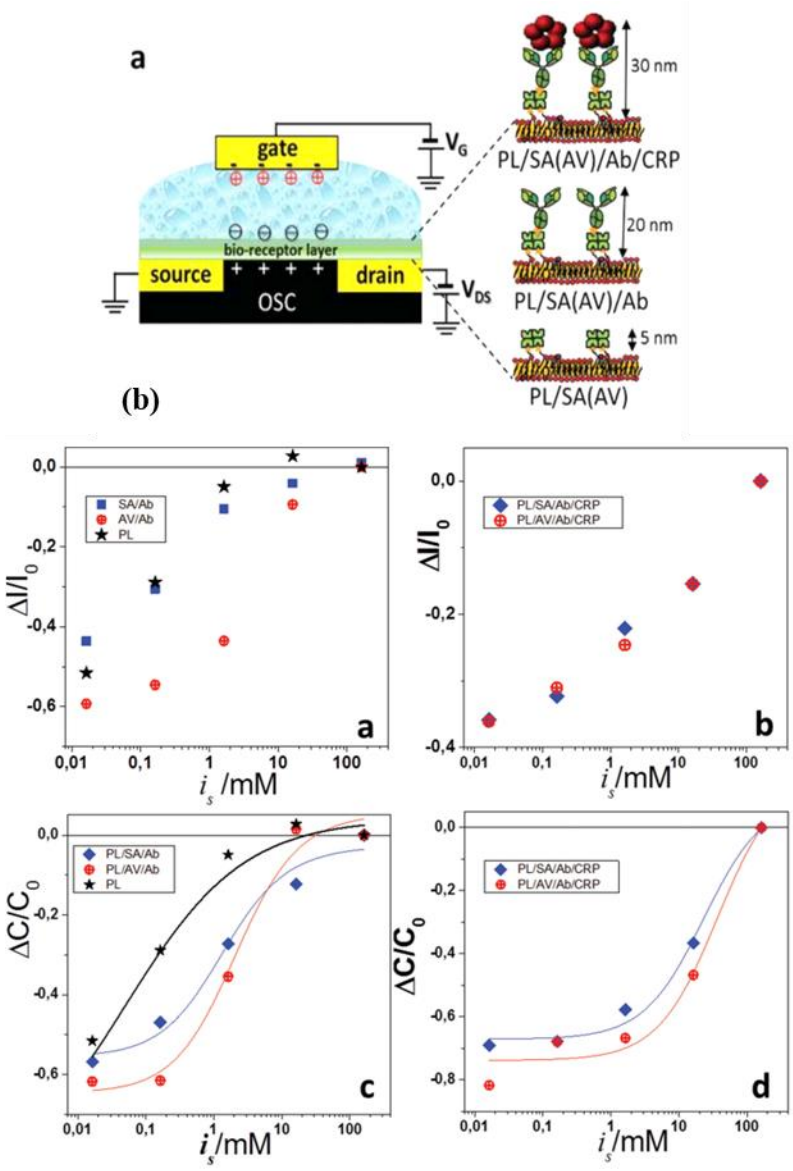

Figure I.29. Illustration of CRP detection: (A) Schematic view with different thicknesses of the bioreceptor layer. (B) Effect of the ionic strength on the fractional changes of the (a,b) current and (c,d) capacitance for a phospholipid/streptavidin/antibody (PL/SA/Ab) (a,c) and PL/SA/Ab/CRP (b,d) multilayers.

3.4.4 Non-covalent functionalization of the semiconductor

Still with the objective to functionalize the semiconductor and impede its doping by ions present in the electrolyte, Cotrone *et al.* described a non-covalent approach using a phospholipid bilayer [(172)]. They compared the electric performances of the EGOFET including a phospholipid film to those with the organic semiconductor directly in contact

with the gating solution. Impedance spectroscopy was employed to show that this phospholipid bilayer minimizes the penetration of ions into the OSC thus improves the field-effect mode of operation and discriminates the electrochemical one. No bioprobes were immobilized on or into this bilayer but this work is a significant step toward EGOFETs biocompatibilization.

One year later, Magliulo *et al.* used biotin-labelled phospholipids, in order to form a streptavidin binding layer. They achieved detection with a LoD of 10 nM even in a high ionic strength solution. They attributed the sensing mechanism to the capacitive effect across the phospholipid bilayer, involving the charges carried by streptavidin. Because the biotinylated phospholipid can easily be functionalized with virtually any receptors, this work paved the way for immunosensors, capture antibodies being usually modified by streptavidin for heterogeneous ELISA immunoassay (Figure I.30).

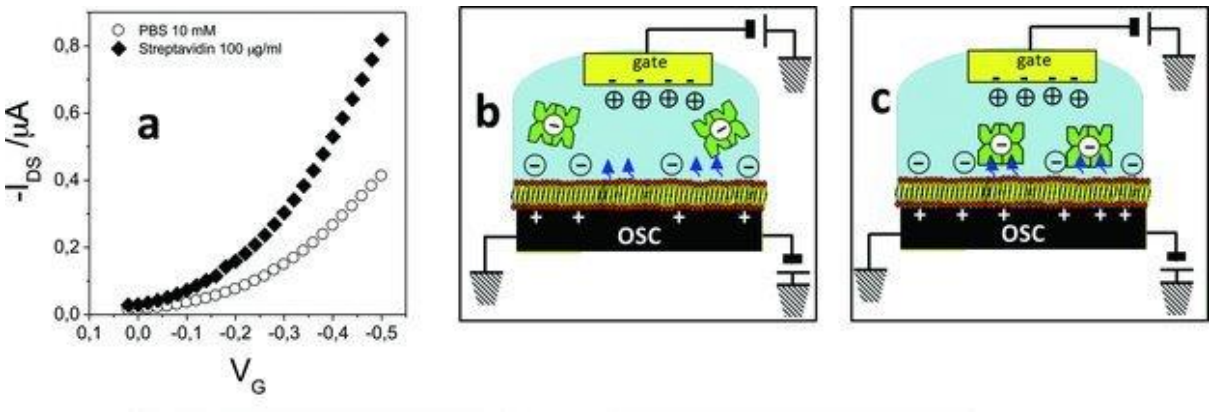

Figure I.30. Illustration of streptavidin detection via biotin-streptavidin binding: (a) Transfer characteristics of the biotin-functionalized phospholipid bilayer-EGOFET in PBS, pH 7.4 (open symbols) and streptavidin (plain symbols) solutions. (b) and (c) Diagram for the rationale leading to the I_{DS} current increase.

3.4.5 pBTTT-based EGOFET for protein (streptavidin) detection

Mulla *et al.* [155] reported a pBTTT-based EGOFET sensor for streptavidin detection. pBTTT was spin-coated on the device, then a layer of poly(acrylic acid) was spin-coated on the pBTTT layer to have carboxyl functionalities acting as anchoring sites for phospholipid bilayers. The proof-of-concept of the sensor was demonstrated with the streptavidin/biotin couple (Figure I.31).

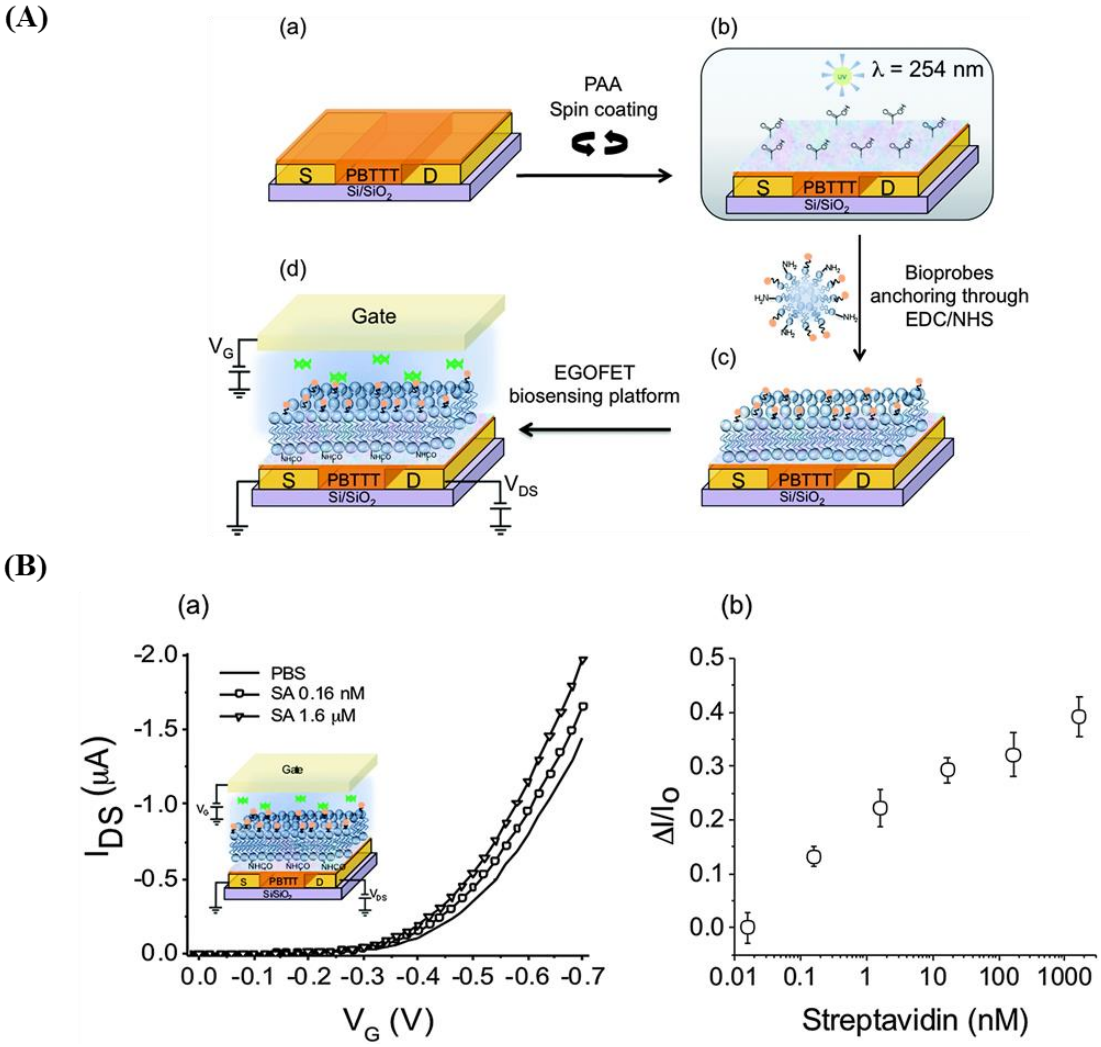

Figure I.31. pBTTT-based EGOFET for protein (streptavidin) detection: (A) Schematic illustration of the fabrication process of an EGOFET biosensor. (a) after deposition of pBTTT on the substrate; (b) poly(acrylic acid) coating spin-coated and cross-linked ; (c) biotinylated phospholipids anchored on the PAA coating; (d) EGOFET configuration comprising a gold gate electrode and a droplet of PBS as dielectric. (B) (a) I_{DS}–V_G transfer curves in PBS, pH 7.4 (line), and streptavidin solutions at concentrations of 0.16 nM (circles) and 1.6 µM (triangles) in PBS; (b) relative response of the EGOFET as a function of the streptavidin concentration [(155)].

3.4.6 Gate functionalization

Casalini *et al.* [(112)] have reported in 2013 a P3HT-based EGOFET biosensor for dopamine detection where a gold gate was used as the sensing area instead of the semiconductor. They modified the gate/electrolyte interface with a self-assembled monolayer of cysteamine and 4-

formylphenyl boronic acid. This modified gate enabled the selective covalent binding of dopamine which in turn modulates both the work function of the gate electrode and the capacitance of the electrode/electrolyte double layer. The strong dependence of the EGOFET transfer curve upon dopamine coupling at the gate electrode is a proof of its sensitivity to small changes in gate capacitance. For dopamine detection, the threshold voltage shift was of ca. 50 mV for 0.1 nM dopamine. The selectivity of boronic acid for dopamine was supported by the fact that boronic acid is known to act as a Lewis acid for association with vicinal glycols such as sugars or catechol, via formation of a boronate ester. This reaction works also well on dopamine and is therefore specific, providing that no other vicinal diols are present in the analyzed sample (this reaction has been often reported in the literature dedicated to dopamine sensing since 2013).

Casalini *et al.* [190] published more recently another work using a Au gate as sensing area, instead of the semiconductor, using thiol-modified protein G or a 6-aminohexanethiol (HSC_6NH_2) self-assembled monolayer followed by covalent coupling (protein G was used here for its property to bind IgG antibodies). They found that the most sensitive EGOFET was obtained with the first (affinity) immobilization strategy. They explained this result by the best orientation of the antibodies on the gate surface, which they probed by force spectroscopy (Figure. I.32). The lowest concentration of antigen (interleukin 4, IL4) detected was ca. 5 nM. These results and particularly the coupling between sensing experiments and surface characterizations were very powerful to rationalize the response of an EGOFET using antibodies grafted on the gate.

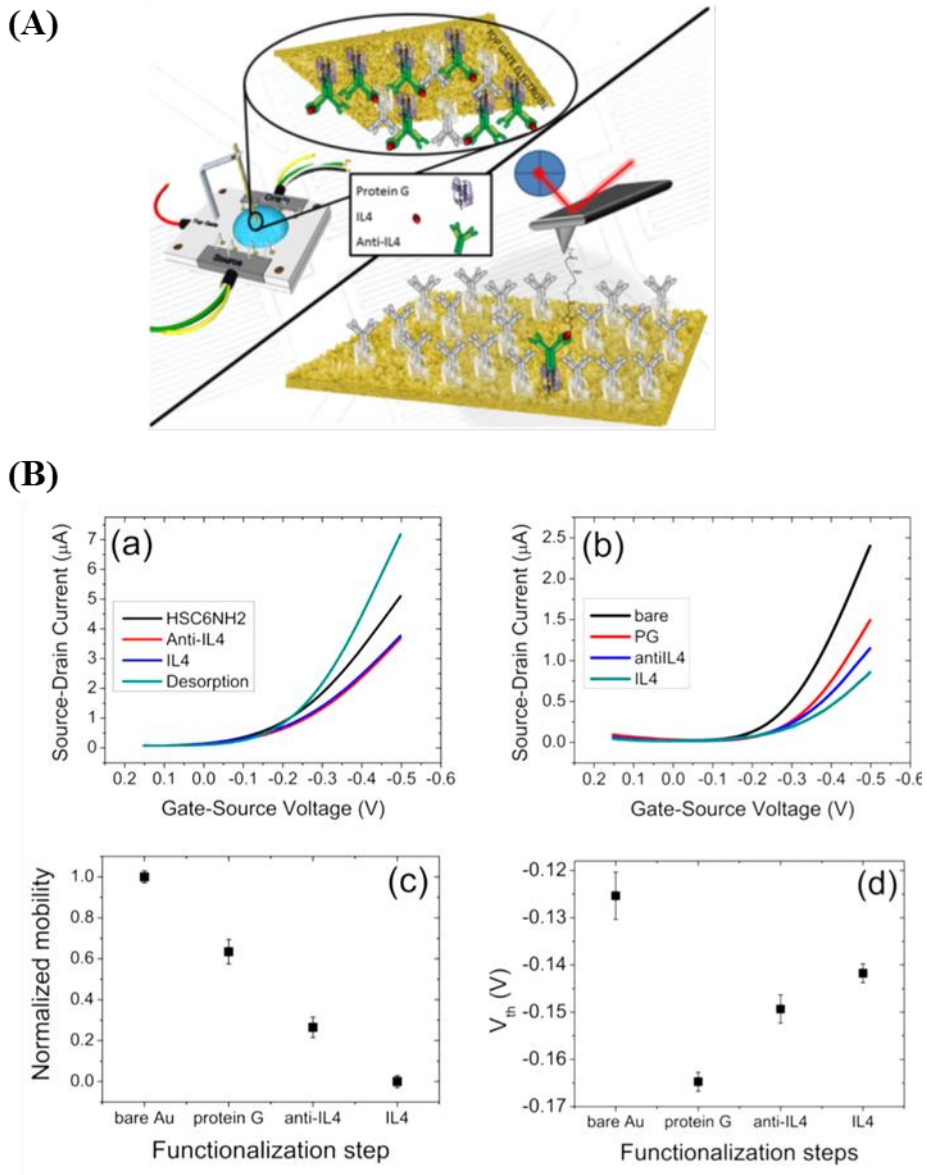

Figure I.32. The gate-modified EGOFET for interleukin detection: (A) Schematic illustration of the modified gate and of the AFM measurements. (B) I-V transfer characteristics for (a) HSC_6NH_2- and (b) Protein G-based protocols. Normalized charge carriers mobility ratio (c) and threshold voltage (d) trends corresponding to the stepwise functionalization [(190)].

Mulla *et al.* [(156)] also described an EGOFET where the gate was the sensing element. They immobilized proteins on the Au gate through a self-assembled monolayer and shown that the transduction capability of the device was governed by the capacitance of the gate/electrolyte interface. The authors applied this architecture to the detection of odorant molecules (Figure.

I.33), by following drain current as a function of the target molecule concentration (carvone). The sensor presented a limit of detection estimated around 10 pM and was enantioselective.

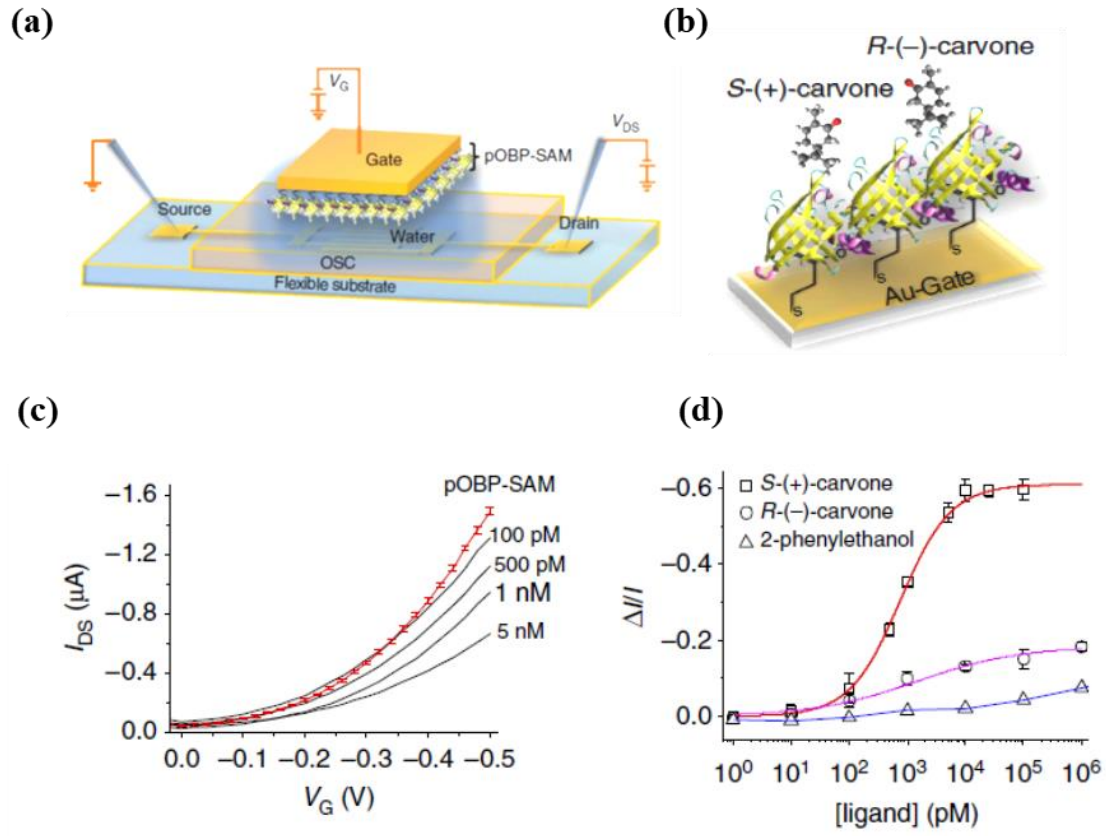

Figure I.33. EGOFET where the gate is modified by a SAM of odorant binding protein (pOBP-SAM). (a) Schematic structure. The OSC is pBTTT-C14. (b) pOBP protein structure and interaction with the odorant molecule. (c) I_{DS}-V_G transfer characteristics reported as a function of concentrations of the odorant molecule (carvone). (d) Calibration curves for the (R)-(-)- and (S)-(+)-carvone and for a non-specific molecule [156].

4 Conclusions

As shown by this extensive bibliography, electrochemical immunosensors have been thoroughtly investigated since these last fifteen years, even though those based on displacement assay were scarce. To move forward, I will propose in my thesis work to transfer some electroanalytical approaches to electrolyte-gated organic field-effect transistors (EGOFETs), which have, it has been clearly shown, a huge range of application field. Because of their advantages (simple architecture, easiness of fabrication, simplicity to use, intrinsic amplification, ability to work in water), they are excellent candidates to be employed as transducers of molecular recognition events such as immunological ones. Beyond the capacitive effect that has been demonstrated in the literature (and that I will again evidence in Chapter III), I will also show that the electrostatic effect, i.e. the effect of charges carried on by target molecules, may also have a significant effect on the transistors characteristics. The possibility of a displacement immunoassay is shown in Chapter II, its application on an EGOFET is demonstrated in Chapter III, and the possibility to use charges carried by targets is shown in Chapter IV.

5 References

1. Scognamiglio, V., Arduini, F., Palleschi, G., and Rea, G. (2014) Biosensing technology for sustainable food safety, *TrAC Trends in Analytical Chemistry 62*, 1-10.

2. Torun, O., Hakki Boyaci, I., Temur, E., and Tamer, U. (2012) Comparison of sensing strategies in SPR biosensor for rapid and sensitive enumeration of bacteria, *Biosensors & bioelectronics 37*, 53-60.

3. Mishra, R. K., Dominguez, R. B., Bhand, S., Munoz, R., and Marty, J. L. (2012) A novel automated flow-based biosensor for the determination of organophosphate pesticides in milk, *Biosensors & bioelectronics 32*, 56-61.

4. Yan, C., Dong, F., Chun-yuan, B., Si-rong, Z., and Jian-guo, S. (2014) Recent Progress of Commercially Available Biosensors in China and Their Applications in Fermentation Processes, *Journal of Northeast Agricultural University (English Edition) 21*, 73-85.

5. Amaro, F., Turkewitz, A. P., Martin-Gonzalez, A., and Gutierrez, J. C. (2011) Whole-cell biosensors for detection of heavy metal ions in environmental samples based on metallothionein promoters from Tetrahymena thermophila, *Microbial biotechnology 4*, 513-522.

6. March, G., Nguyen, T. D., and Piro, B. (2015) Modified electrodes used for electrochemical detection of metal ions in environmental analysis, *Biosensors 5*, 241-275.

7. Tekaya, N., Saiapina, O., Ben Ouada, H., Lagarde, F., Ben Ouada, H., and Jaffrezic-Renault, N. (2013) Ultra-sensitive conductometric detection of heavy metals based on inhibition of alkaline phosphatase activity from Arthrospira platensis, *Bioelectrochemistry 90*, 24-29.

8. Arduini, F., Ricci, F., Tuta, C. S., Moscone, D., Amine, A., and Palleschi, G. (2006) Detection of carbamic and organophosphorous pesticides in water samples using a cholinesterase biosensor based on Prussian Blue-modified screen-printed electrode, *Analytica chimica acta 580*, 155-162.

9. Ivanov, A., Evtugyn, G., Budnikov, H., Ricci, F., Moscone, D., and Palleschi, G. (2003) Cholinesterase sensors based on screen-printed electrodes for detection of organophosphorus and carbamic pesticides, *Analytical and bioanalytical chemistry 377*, 624-631.

10. Tekaya, N., Saiapina, O., Ben Ouada, H., Lagarde, F., Ben Ouada, H., and Jaffrezic-Renault, N. (2013) Ultra-sensitive conductometric detection of pesticides based on inhibition of esterase activity in Arthrospira platensis, *Environmental pollution 178*, 182-188.

11. Yoo, E.-H., and Lee, S.-Y. (2010) Glucose Biosensors: An Overview of Use in Clinical Practice, *Sensors 10*, 4558.

12. Lee, M., Zine, N., Baraket, A., Zabala, M., Campabadal, F., Caruso, R., Trivella, M. G., Jaffrezic-Renault, N., and Errachid, A. (2012) A novel biosensor based on hafnium oxide: Application for early stage detection of human interleukin-10, *Sensors and Actuators B: Chemical 175*, 201-207.

13. Cammann, K. (1977) Bio-sensors based on ion-selective electrodes. *Fresenius Z. anal. Chem*, 287, 1-9

14. Dhand, C., Das, M., Datta, M., and Malhotra, B. D. (2011) Recent advances in polyaniline based biosensors, *Biosensors & bioelectronics 26*, 2811-2821.

15. Hicks, S. J. U. G. P. (1967) The enzyme electrode, *Nature 214*, 986-988.

16. El Ichi, S., Marzouki, M. N., and Korri-Youssoufi, H. (2009) Direct monitoring of pollutants based on an electrochemical biosensor with novel peroxidase (POX1B), *Biosensors & bioelectronics 24*, 3084-3090.

17. Wang, C., Xi, J. Y., and Hu, H. Y. (2008) Chemical identification and acute biotoxicity assessment of gaseous chlorobenzene photodegradation products, *Chemosphere 73*, 1167-1171.

18. Ybarra, C. M. a. G. (2012) Fundamentals and Applications of Immunosensors, *Advances in Immunoassay Technology*.

19. J, W. (2000) From DNA biosensors to gene chips, *Nucleic acids research 28*, 3011-3016.

20. Bizid, S., Blili, S., Mlika, R., Haj Said, A., and Korri-Youssoufi, H. (2017) Direct Electrochemical DNA Sensor based on a new redox oligomer modified with ferrocene and carboxylic acid: Application to the detection of Mycobacterium tuberculosis mutant strain, *Analytica chimica acta 994*, 10-18.

21. Tlili, C., Korri-Youssoufi, H., Ponsonnet, L., Martelet, C., and Jaffrezic-Renault, N. J. (2005) Electrochemical impedance probing of DNA hybridisation on oligonucleotide-functionalised polypyrrole, *Talanta 68*, 131-137.

22. Miodek, A., Mejri-Omrani, N., Khoder, R., and Korri-Youssoufi, H. (2016) Electrochemical functionalization of polypyrrole through amine oxidation of poly(amidoamine) dendrimers: Application to DNA biosensor, *Talanta 154*, 446-454.

23. Miodek, A., Mejri, N., Gomgnimbou, M., Sola, C., and Korri-Youssoufi, H. (2015) E-DNA sensor of Mycobacterium tuberculosis based on electrochemical assembly of nanomaterials (MWCNTs/PPy/PAMAM), *Analytical chemistry 87*, 9257-9264.

24. Bizid, S., Blili, S., Mlika, R., Haj Said, A., and Korri-Youssoufi, H. (2018) Direct E-DNA sensor of Mycobacterium tuberculosis mutant strain based on new nanocomposite transducer (Fc-ac-OMPA/MWCNTs), *Talanta 184*, 475-483.

25. Krull, M. T. a. U. J. (1991) Biosensors and the transduction of molecular recognition, *Anal. Chem. 63*, 393A–405A.

26. Felix, F. S., and Angnes, L. (2018) Electrochemical immunosensors - A powerful tool for analytical applications, *Biosensors & bioelectronics 102*, 470-478.

27. Omidfar, K., Khorsand, F., and Darziani Azizi, M. (2013) New analytical applications of gold nanoparticles as label in antibody based sensors, *Biosensors & bioelectronics 43*, 336-347.

28. Wan, Y., Su, Y., Zhu, X., Liu, G., and Fan, C. (2013) Development of electrochemical immunosensors towards point of care diagnostics, *Biosensors & bioelectronics 47*, 1-11.

29. Zhang, X., Sun, J., Liu, J., Xu, H., Dong, B., Sun, X., Zhang, T., Xu, S., Xu, L., Bai, X., Zhang, S., Mintova, S., Lu, G., and Song, H. (2018) Label-free electrochemical immunosensor based on conductive Ag contained EMT-style nano-zeolites and the application for α-fetoprotein detection, *Sensors and Actuators B: Chemical 255*, 2919-2926.

30. B.B.Kim, E. B. D., U.Sheller, M.M.Dikov, E.M.Gavrilova, A.M.Egorov. (1990) Evaluation of dissociation constants of antigen-antibody complexes by ELISA., *Journal of Immunological Methods. 131*, 213-222.

31. Landry, J. P., Ke, Y., Yu, G. L., and Zhu, X. D. (2015) Measuring affinity constants of 1450 monoclonal antibodies to peptide targets with a microarray-based label-free assay platform, *Journal of immunological methods 417*, 86-96.

32. Ricci, F., Adornetto, G., and Palleschi, G. (2012) A review of experimental aspects of electrochemical immunosensors, *Electrochimica Acta 84*, 74-83.

33. Yang, H. (2012) Enzyme-based ultrasensitive electrochemical biosensors, *Current opinion in chemical biology 16*, 422-428.

34. Burcu Bahadir, E., and Kemal Sezginturk, M. (2015) Applications of electrochemical immunosensors for early clinical diagnostics, *Talanta 132*, 162-174.

35. Bhaskara V. Chikkaveeraiah, A. A. B., Nicole Y. Morgan, Henry S. Eden, and Xiaoyuan Chen. (2012) Electrochemical Immunosensors for Detection ofCancerProtein Biomarkers, *ACS Nano 6*, 6546–6561.

36. Vidal, J. C., Bonel, L., Ezquerra, A., Hernandez, S., Bertolin, J. R., Cubel, C., and Castillo, J. R. (2013) Electrochemical affinity biosensors for detection of mycotoxins: A review, *Biosensors & bioelectronics 49*, 146-158.

37. Diaconu, I., Cristea, C., Harceaga, V., Marrazza, G., Berindan-Neagoe, I., and Sandulescu, R. (2013) Electrochemical immunosensors in breast and ovarian cancer, *Clinica chimica acta; international journal of clinical chemistry 425*, 128-138.

38. Campuzano, S., Yánez-Sedeño, P., and Pingarrón, J. M. (2017) Electrochemical bioaffinity sensors for salivary biomarkers detection, *TrAC Trends in Analytical Chemistry 86*, 14-24.

39. Hayat, A., Barthelmebs, L., and Marty, J.-L. (2012) Electrochemical impedimetric immunosensor for the detection of okadaic acid in mussel sample, *Sensors and Actuators B: Chemical 171-172*, 810-815.

40. Hayat, A., Barthelmebs, L., Sassolas, A., and Marty, J. L. (2012) Development of a novel label-free amperometric immunosensor for the detection of okadaic acid, *Analytica chimica acta 724*, 92-97.

41. Bhimji, A., Zaragoza, A. A., Live, L. S., and Kelley, S. O. (2013) Electrochemical enzyme-linked immunosorbent assay featuring proximal reagent generation: detection of human immunodeficiency virus antibodies in clinical samples, *Analytical chemistry 85*, 6813-6819.

42. Jarocka, U., Sawicka, R., Stachyra, A., Gora-Sochacka, A., Sirko, A., Zagorski-Ostoja, W., Saczynska, V., Porebska, A., Dehaen, W., Radecki, J., and Radecka, H. (2015) A biosensor based on electroactive dipyrromethene-Cu(II) layer deposited onto gold electrodes for the detection of antibodies against avian influenza virus type H5N1 in hen sera, *Analytical and bioanalytical chemistry 407*, 7807-7814.

43. Lim, S. A., and Ahmed, M. U. (2016) A label free electrochemical immunosensor for sensitive detection of porcine serum albumin as a marker for pork adulteration in raw meat, *Food chemistry 206*, 197-203.

44. Sharma, D., Lee, J., and Shin, H. (2018) An electrochemical immunosensor based on a 3D carbon system consisting of a suspended mesh and substrate-bound interdigitated array nanoelectrodes for sensitive cardiac biomarker detection, *Biosensors & bioelectronics 107*, 10-16.

45. Khoshroo, A., Mazloum-Ardakani, M., and Forat-Yazdi, M. (2018) Enhanced performance of label-free electrochemical immunosensor for carbohydrate antigen 15-3 based on catalytic activity of cobalt sulfide/graphene nanocomposite, *Sensors and Actuators B: Chemical 255*, 580-587.

46. Zeng, Y., Bao, J., Zhao, Y., Huo, D., Chen, M., Yang, M., Fa, H., and Hou, C. (2018) A sensitive label-free electrochemical immunosensor for detection of cytokeratin 19 fragment antigen 21-1 based on 3D graphene with gold nanopaticle modified electrode, *Talanta 178*, 122-128.

47. Amani, J., Khoshroo, A., and Rahimi-Nasrabadi, M. (2017) Electrochemical immunosensor for the breast cancer marker CA 15–3 based on the catalytic activity of a CuS/reduced graphene oxide nanocomposite towards the electrooxidation of catechol, *Microchimica Acta 185*.

48. Rauf, S., Mishra, G. K., Azhar, J., Mishra, R. K., Goud, K. Y., Nawaz, M. A. H., Marty, J. L., and Hayat, A. (2018) Carboxylic group riched graphene oxide based disposable electrochemical immunosensor for cancer biomarker detection, *Analytical biochemistry 545*, 13-19.

49. Moreno-Guzman, M., Ojeda, I., Villalonga, R., Gonzalez-Cortes, A., Yanez-Sedeno, P., and Pingarron, J. M. (2012) Ultrasensitive detection of adrenocorticotropin hormone (ACTH) using disposable phenylboronic-modified electrochemical immunosensors, *Biosensors & bioelectronics 35*, 82-86.

50. Liu, G., Khor, S. M., Iyengar, S. G., and Gooding, J. J. (2012) Development of an electrochemical immunosensor for the detection of HbA1c in serum, *The Analyst 137*, 829-832.

51. Ojeda, I., Lopez-Montero, J., Moreno-Guzman, M., Janegitz, B. C., Gonzalez-Cortes, A., Yanez-Sedeno, P., and Pingarron, J. M. (2012) Electrochemical immunosensor for rapid and sensitive determination of estradiol, *Analytica chimica acta 743*, 117-124.

52. Singh, A., Park, S., and Yang, H. (2013) Glucose-oxidase label-based redox cycling for an incubation period-free electrochemical immunosensor, *Analytical chemistry 85*, 4863-4868.

53. Serafín, V., Torrente-Rodríguez, R. M., Batlle, M., García de Frutos, P., Campuzano, S., Yáñez-Sedeño, P., and Pingarrón, J. M. (2017) Electrochemical immunosensor for receptor tyrosine kinase AXL using poly(pyrrolepropionic acid)-modified disposable electrodes, *Sensors and Actuators B: Chemical 240*, 1251-1256.

54. Tran, H. V., Reisberg, S., Piro, B., Nguyen, T. D., and Pham, M. C. (2013) Label-Free Electrochemical Immunoaffinity Sensor Based on Impedimetric Method for Pesticide Detection, *Electroanalysis 25*, 664-670.

55. Khor, S. M., Thordarson, P., and Gooding, J. J. (2013) The impact of antibody/epitope affinity strength on the sensitivity of electrochemical immunosensors for detecting small molecules, *Analytical and bioanalytical chemistry 405*, 3889-3898.

56. Conzuelo, F., Campuzano, S., Gamella, M., Pinacho, D. G., Reviejo, A. J., Marco, M. P., and Pingarron, J. M. (2013) Integrated disposable electrochemical immunosensors for the simultaneous determination of sulfonamide and tetracycline antibiotics residues in milk, *Biosensors & bioelectronics 50*, 100-105.

57. Serafin, V., Torrente-Rodriguez, R. M., Gonzalez-Cortes, A., Garcia de Frutos, P., Sabate, M., Campuzano, S., Yanez-Sedeno, P., and Pingarron, J. M. (2018) An electrochemical immunosensor for brain natriuretic peptide prepared with screen-printed carbon electrodes nanostructured with gold nanoparticles grafted through aryl diazonium salt chemistry, *Talanta 179*, 131-138.

58. Montes, R., Cespedes, F., and Baeza, M. (2016) Highly sensitive electrochemical immunosensor for IgG detection based on optimized rigid biocomposites, *Biosensors & bioelectronics 78*, 505-512.

59. Qi, H., Ling, C., Ma, Q., Gao, Q., and Zhang, C. (2012) Sensitive electrochemical immunosensor array for the simultaneous detection of multiple tumor markers, *The Analyst 137*, 393-399.

60. Jiang, C., Alam, M. T., Silva, S. M., Taufik, S., Fan, S., and Gooding, J. J. (2016) Unique Sensing Interface That Allows the Development of an Electrochemical Immunosensor for the Detection of Tumor Necrosis Factor α in Whole Blood, *ACS Sensors 1*, 1432-1438.

61. Ciani, I., Schulze, H., Corrigan, D. K., Henihan, G., Giraud, G., Terry, J. G., Walton, A. J., Pethig, R., Ghazal, P., Crain, J., Campbell, C. J., Bachmann, T. T., and Mount, A. R. (2012) Development of immunosensors for direct detection of three wound infection

biomarkers at point of care using electrochemical impedance spectroscopy, *Biosensors & bioelectronics 31*, 413-418.

62. Lu, R., Sun, X., Xiao, R., Zhou, L., Gao, X., and Guo, L. (2012) Human epididymis protein 4 (HE4) plays a key role in ovarian cancer cell adhesion and motility, *Biochemical and biophysical research communications 419*, 274-280.

63. Wang, R., Liu, W. D., Wang, A. J., Xue, Y., Wu, L., and Feng, J. J. (2018) A new label-free electrochemical immunosensor based on dendritic core-shell AuPd@Au nanocrystals for highly sensitive detection of prostate specific antigen, *Biosensors & bioelectronics 99*, 458-463.

64. Wang, R., Wang, A. J., Liu, W. D., Yuan, P. X., Xue, Y., Luo, X., and Feng, J. J. (2018) A novel label-free electrochemical immunosensor for ultra-sensitively detecting prostate specific antigen based on the enhanced catalytic currents of oxygen reduction catalyzed by core-shell Au@Pt nanocrystals, *Biosensors & bioelectronics 102*, 276-281.

65. Vasudev, A., Kaushik, A., and Bhansali, S. (2013) Electrochemical immunosensor for label free epidermal growth factor receptor (EGFR) detection, *Biosensors & bioelectronics 39*, 300-305.

66. Vasudev, A., Kaushik, A., Tomizawa, Y., Norena, N., and Bhansali, S. (2013) An LTCC-based microfluidic system for label-free, electrochemical detection of cortisol, *Sensors and Actuators B: Chemical 182*, 139-146.

67. Lim, S. A., and Ahmed, M. U. (2015) A carbon nanofiber-based label free immunosensor for high sensitive detection of recombinant bovine somatotropin, *Biosensors & bioelectronics 70*, 48-53.

68. Jarocka, U., Sawicka, R., Gora-Sochacka, A., Sirko, A., Zagorski-Ostoja, W., Radecki, J., and Radecka, H. (2014) An immunosensor based on antibody binding fragments attached to gold nanoparticles for the detection of peptides derived from avian influenza hemagglutinin H5, *Sensors 14*, 15714-15728.

69. Tran, H. V., Yougnia, R., Reisberg, S., Piro, B., Serradji, N., Nguyen, T. D., Tran, L. D., Dong, C. Z., and Pham, M. C. (2012) A label-free electrochemical immunosensor for direct, signal-on and sensitive pesticide detection, *Biosensors & bioelectronics 31*, 62-68.

70. Wang, X., Reisberg, S., Serradji, N., Anquetin, G., Pham, M. C., Wu, W., Dong, C. Z., and Piro, B. (2014) E-assay concept: detection of bisphenol A with a label-free electrochemical competitive immunoassay, *Biosensors & bioelectronics 53*, 214-219.

71. Shi, S., Reisberg, S., Anquetin, G., Noel, V., Pham, M. C., and Piro, B. (2015) General approach for electrochemical detection of persistent pharmaceutical micropollutants: Application to acetaminophen, *Biosensors & bioelectronics 72*, 205-210.

72. Lu, L., Liu, B., Zhao, Z., Ma, C., Luo, P., Liu, C., and Xie, G. (2012) Ultrasensitive electrochemical immunosensor for HE4 based on rolling circle amplification, *Biosensors & bioelectronics 33*, 216-221.

73. Jarocka, U., Sawicka, R., Góra-Sochacka, A., Sirko, A., Dehaen, W., Radecki, J., and Radecka, H. (2016) An electrochemical immunosensor based on a 4,4′-thiobisbenzenethiol self-assembled monolayer for the detection of hemagglutinin from avian influenza virus H5N1, *Sensors and Actuators B: Chemical 228*, 25-30.

74. Jiang, X., Li, D., Xu, X., Ying, Y., Li, Y., Ye, Z., and Wang, J. (2008) Immunosensors for detection of pesticide residues, *Biosensors & bioelectronics 23*, 1577-1587.

75. Sassolas, A., Prieto-Simón, B., and Marty, J.-L. (2012) Biosensors for Pesticide Detection: New Trends, *American Journal of Analytical Chemistry 03*, 210-232.

76. K.A. Fa¨hnrich, M. P., G.G. Guilbault. (2003) Disposable amperometric immunosensor for the detection of polycyclic aromatic hydrocarbons (PAHs) using screen-printed electrodes, *Biosensors and Bioelectronics 18*, 73-82.

77. Zacco, E., Galve, R., Marco, M. P., Alegret, S., and Pividori, M. I. (2007) Electrochemical biosensing of pesticide residues based on affinity biocomposite platforms, *Biosensors & bioelectronics 22*, 1707-1715.

78. Grennan, K., Strachan, G., Porter, A. J., Killard, A. J., and Smyth, M. R. (2003) Atrazine analysis using an amperometric immunosensor based on single-chain antibody fragments and regeneration-free multi-calibrant measurement, *Analytica chimica acta 500*, 287-298.

79. Butler, D., and Guilbault, G. G. (2006) Disposable amperometric immunosensor for the detection of 17-β estradiol using screen-printed electrodes, *Sensors and Actuators B: Chemical 113*, 692-699.

80. Chen, L., Zeng, G., Zhang, Y., Tang, L., Huang, D., Liu, C., Pang, Y., and Luo, J. (2010) Trace detection of picloram using an electrochemical immunosensor based on three-dimensional gold nanoclusters, *Analytical biochemistry 407*, 172-179.

81. Sharma, P., Sablok, K., Bhalla, V., and Suri, C. R. (2011) A novel disposable electrochemical immunosensor for phenyl urea herbicide diuron, *Biosensors & bioelectronics 26*, 4209-4212.

82. Zhang, Y., and Zhuang, H.-S. (2010) Amperometric Immunosensor Based on Layer-by-layer Assembly of Thiourea and Nano-gold Particles on Gold Electrode for Determination of Naphthalene, *Chinese Journal of Analytical Chemistry 38*, 153-157.

83. Helali, S., Martelet, C., Abdelghani, A., Maaref, M. A., and Jaffrezic-Renault, N. (2006) A disposable immunomagnetic electrochemical sensor based on functionalised magnetic beads on gold surface for the detection of atrazine, *Electrochimica Acta 51*, 5182-5186.

84. Rodríguez, Á., Valera, E., Ramón-Azcón, J., Sanchez, F. J., Marco, M. P., and Castañer, L. M. (2008) Single frequency impedimetric immunosensor for atrazine detection, *Sensors and Actuators B: Chemical 129*, 921-928.

85. Valera, E., Ramón-Azcón, J., Rodríguez, Á., Castañer, L. M., Sánchez, F. J., and Marco, M. P. (2007) Impedimetric immunosensor for atrazine detection using interdigitated μ-electrodes (IDμE's), *Sensors and Actuators B: Chemical 125*, 526-537.

86. Ramon-Azcon, J., Valera, E., Rodriguez, A., Barranco, A., Alfaro, B., Sanchez-Baeza, F., and Marco, M. P. (2008) An impedimetric immunosensor based on interdigitated microelectrodes (IDmicroE) for the determination of atrazine residues in food samples, *Biosensors & bioelectronics 23*, 1367-1373.

87. Ionescu, R. E., Gondran, C., Bouffier, L., Jaffrezic-Renault, N., Martelet, C., and Cosnier, S. (2010) Label-free impedimetric immunosensor for sensitive detection of atrazine, *Electrochimica Acta 55*, 6228-6232.

88. Navratilova, I., and Skladal, P. (2004) The immunosensors for measurement of 2,4-dichlorophenoxyacetic acid based on electrochemical impedance spectroscopy, *Bioelectrochemistry 62*, 11-18.

89. Tsumura, A., Koezuka, H., and Ando, T. (1986) Macromolecular electronic device: Field- effect transistor with a polythiophene thin film, *Applied Physics Letters 49*, 1210-1212.

90. Kergoat, L., Herlogsson, L., Braga, D., Piro, B., Pham, M. C., Crispin, X., Berggren, M., and Horowitz, G. (2010) A water-gate organic field-effect transistor, *Advanced materials 22*, 2565-2569.

91. Buth, F., Donner, A., Sachsenhauser, M., Stutzmann, M., and Garrido, J. A. (2012) Biofunctional electrolyte-gated organic field-effect transistors, *Advanced materials 24*, 4511-4517.

92. Dhoot, A. S., Yuen, J. D., Heeney, M., McCulloch, I., Moses, D., and Heeger, A. J. (2006) Beyond the metal-insulator transition in polymer electrolyte gated polymer field-effect transistors, *Proceedings of the National Academy of Sciences of the United States of America 103*, 11834-11837.

93. Kim, S. H., Hong, K., Xie, W., Lee, K. H., Zhang, S., Lodge, T. P., and Frisbie, C. D. (2013) Electrolyte-gated transistors for organic and printed electronics, *Advanced materials 25*, 1822-1846.

94. Kergoat, L., Piro, B., Berggren, M., Horowitz, G., and Pham, M. C. (2012) Advances in organic transistor-based biosensors: from organic electrochemical transistors to electrolyte-gated organic field-effect transistors, *Analytical and bioanalytical chemistry 402*, 1813-1826.

95. Stern, E., Klemic, J. F., Routenberg, D. A., Wyrembak, P. N., Turner-Evans, D. B., Hamilton, A. D., LaVan, D. A., Fahmy, T. M., and Reed, M. A. (2007) Label-free immunodetection with CMOS-compatible semiconducting nanowires, *Nature 445*, 519-522.

96. Kergoat, L., Piro, B., Berggren, M., Horowitz, G., and Pham, M.-C. (2012) Advances in organic transistor-based biosensors: from organic electrochemical transistors to electrolyte-gated organic field-effect transistors, *Analytical and bioanalytical chemistry 402*, 1813-1826.

97. Liao, C., and Yan, F. (2013) Organic Semiconductors in Organic Thin-Film Transistor-Based Chemical and Biological Sensors, *Polymer Reviews 53*, 352-406.

98. Said, E., Crispin, X., Herlogsson, L., Elhag, S., Robinson, N. D., and Berggren, M. (2006) Polymer field-effect transistor gated via a poly (styrenesulfonic acid) thin film, *Applied physics letters 89*, 143507.

99. Herlogsson, L., Crispin, X., Robinson, N. D., Sandberg, M., Hagel, O. J., Gustafsson, G., and Berggren, M. (2007) Low- Voltage Polymer Field- Effect Transistors Gated via a Proton Conductor, *Advanced Materials 19*, 97-101.

100. Said, E., Larsson, O., Berggren, M., and Crispin, X. (2008) Effects of the Ionic Currents in Electrolyte- gated Organic Field- Effect Transistors, *Advanced Functional Materials 18*, 3529-3536.

101. Ono, S., Miwa, K., Seki, S., and Takeya, J. (2009) A comparative study of organic single-crystal transistors gated with various ionic-liquid electrolytes, *Applied Physics Letters 94*, 063301.

102. Xia, Y., Cho, J. H., Lee, J., Ruden, P. P., and Frisbie, C. D. (2009) Comparison of the Mobility–Carrier Density Relation in Polymer and Single- Crystal Organic Transistors Employing Vacuum and Liquid Gate Dielectrics, *Advanced Materials 21*, 2174-2179.

103. Hamedi, M., Herlogsson, L., Crispin, X., Marcilla, R., Berggren, M., and Inganäs, O. (2009) Fiber- Embedded Electrolyte- Gated Field- Effect Transistors for e- Textiles, *Advanced Materials 21*, 573-577.

104. Lee, J., Panzer, M. J., He, Y., Lodge, T. P., and Frisbie, C. D. (2007) Ion gel gated polymer thin-film transistors, *Journal of the American Chemical Society 129*, 4532-4533.

105. Cho, J. H., Lee, J., Xia, Y., Kim, B., He, Y., Renn, M. J., Lodge, T. P., and Frisbie, C. D. (2008) Printable ion-gel gate dielectrics for low-voltage polymer thin-film transistors on plastic, *Nature Materials 7*, 900-906.

106. Lee, J., Kaake, L. G., Cho, J. H., Zhu, X.-Y., Lodge, T. P., and Frisbie, C. D. (2009) Ion gel-gated polymer thin-film transistors: operating mechanism and characterization of gate dielectric capacitance, switching speed, and stability, *The Journal of Physical Chemistry C 113*, 8972-8981.

107. Cho, J. H., Lee, J., He, Y., Kim, B., Lodge, T. P., and Frisbie, C. D. (2008) High-Capacitance Ion Gel Gate Dielectrics with Faster Polarization Response Times for Organic Thin Film Transistors, *Advanced materials 20*, 686-690.

108. Facchetti, A. (2008) Dielectric materials: Gels excel, *Nature materials 7*, 839-840.

109. Kergoat, L., Herlogsson, L., Braga, D., Piro, B., Pham, M. C., Crispin, X., Berggren, M., and Horowitz, G. (2010) A Water- Gate Organic Field- Effect Transistor, *Advanced Materials 22*, 2565-2569.

110. Palazzo, G., De Tullio, D., Magliulo, M., Mallardi, A., Intranuovo, F., Mulla, M. Y., Favia, P., Vikholm- Lundin, I., and Torsi, L. (2014) Detection Beyond Debye's Length with an Electrolyte- Gated Organic Field- Effect Transistor, *Advanced Materials*.

111. Belkhir, A. (2009) Contribution à la modélisation des transistors organiques, Reims.

112. Casalini, S., Leonardi, F., Cramer, T., and Biscarini, F. (2013) Organic field-effect transistor for label-free dopamine sensing, *Organic Electronics 14*, 156-163.

113. Cai, B., Wang, S., Huang, L., Ning, Y., Zhang, Z., and Zhang, G.-J. (2014) Ultrasensitive Label-Free Detection of PNA–DNA Hybridization by Reduced Graphene Oxide Field-Effect Transistor Biosensor, *ACS nano 8*, 2632-2638.

114. Vasu, K., Chakraborty, B., Sampath, S., and Sood, A. (2010) Probing top-gated field effect transistor of reduced graphene oxide monolayer made by dielectrophoresis, *Solid State Communications 150*, 1295-1298.

115. Liao, R., Tang, Z., Lei, Y., and Guo, B. (2011) Polyphenol-Reduced Graphene Oxide: Mechanism and Derivatization, *The Journal of Physical Chemistry C 115*, 20740-20746.

116. Liu, F., Kim, Y. H., Cheon, D. S., and Seo, T. S. (2013) Micropatterned reduced graphene oxide based field-effect transistor for real-time virus detection, *Sensors and Actuators B: Chemical 186*, 252-257.

117. Zhao, Y., Wei, Q., Xu, C., Li, H., Wu, D., Cai, Y., Mao, K., Cui, Z., and Du, B. (2011) Label-free electrochemical immunosensor for sensitive detection of kanamycin, *Sensors and Actuators B: Chemical 155*, 618-625.

118. Chen, T.-Y., Loan, P. T. K., Hsu, C.-L., Lee, Y.-H., Wang, J. T.-W., Wei, K.-H., Lin, C.-T., and Li, L.-J. (2013) Label-free detection of DNA hybridization using transistors based on CVD grown graphene, *Biosensors and Bioelectronics 41*, 103-109.

119. Park, J. W., Lee, C., and Jang, J. (2015) High-performance field-effect transistor-type glucose biosensor based on nanohybrids of carboxylated polypyrrole nanotube wrapped graphene sheet transducer, *Sensors and Actuators B: Chemical 208*, 532-537.

120. Williams, G., and Kamat, P. V. (2009) Graphene− Semiconductor Nanocomposites: Excited-State Interactions between ZnO Nanoparticles and Graphene Oxide†, *Langmuir 25*, 13869-13873.

121. Feng, L., Chen, Y., Ren, J., and Qu, X. (2011) A graphene functionalized electrochemical aptasensor for selective label-free detection of cancer cells, *Biomaterials 32*, 2930-2937.

122. Ohno, Y., Maehashi, K., Yamashiro, Y., and Matsumoto, K. (2009) Electrolyte-gated graphene field-effect transistors for detecting pH and protein adsorption, *Nano letters 9*, 3318-3322.

123. Tran, H., Piro, B., Reisberg, S., Nguyen, L. H., Nguyen, T. D., Duc, H., and Pham, M. (2014) An electrochemical ELISA-like immunosensor for miRNAs detection based on screen-printed gold electrodes modified with reduced graphene oxide and carbon nanotubes, *Biosensors and Bioelectronics 62*, 25-30.

124. Dong, X., Shi, Y., Huang, W., Chen, P., and Li, L. J. (2010) Electrical Detection of DNA Hybridization with Single- Base Specificity Using Transistors Based on CVD- Grown Graphene Sheets, *Advanced Materials 22*, 1649-1653.

125. Ge, S., Lan, F., Yu, F., and Yu, J. (2015) Applications of graphene and related nanomaterials in analytical chemistry, *New Journal of Chemistry*.

126. Tran, H., Piro, B., Reisberg, S., Duc, H., and Pham, M. (2013) Antibodies directed to RNA/DNA hybrids: An electrochemical immunosensor for microRNAs detection using graphene-composite electrodes, *Analytical chemistry 85*, 8469-8474.

127. Yan, F., Zhang, M., and Li, J. (2014) Solution- Gated Graphene Transistors for Chemical and Biological Sensors, *Advanced healthcare materials 3*, 313-331.

128. Kergoat, L., Herlogsson, L., Piro, B., Pham, M. C., Horowitz, G., Crispin, X., and Berggren, M. (2012) Tuning the threshold voltage in electrolyte-gated organic field-effect transistors, *Proceedings of the National Academy of Sciences 109*, 8394-8399.

129. Fabiano, S., Braun, S., Fahlman, M., Crispin, X., and Berggren, M. (2014) Effect of Gate Electrode Work- Function on Source Charge Injection in Electrolyte- Gated Organic Field- Effect Transistors, *Advanced Functional Materials 24*, 695-700.

130. Demelas, M., Lai, S., Spanu, A., Martinoia, S., Cosseddu, P., Barbaro, M., and Bonfiglio, A. (2013) Charge sensing by organic charge-modulated field effect transistors: application to the detection of bio-related effects, *Journal of Materials Chemistry B 1*, 3811.

131. Myers, J. D., and Xue, J. (2012) Organic semiconductors and their applications in photovoltaic devices, *Polymer Reviews 52*, 1-37.

132. Alberga, D., Mangiatordi, G. F., Torsi, L., and Lattanzi, G. (2014) Effects of Annealing and Residual Solvents on Amorphous P3HT and PBTTT Films, *The Journal of Physical Chemistry C 118*, 8641-8655.

133. Sirringhaus, H., Brown, P., Friend, R., Nielsen, M. M., Bechgaard, K., Langeveld-Voss, B., Spiering, A., Janssen, R. A., Meijer, E., and Herwig, P. (1999) Two-dimensional charge transport in self-organized, high-mobility conjugated polymers, *Nature 401*, 685-688.

134. Derby, B. (2010) Inkjet printing of functional and structural materials: fluid property requirements, feature stability, and resolution, *Annual Review of Materials Research 40*, 395-414.

135. de Gans, B. J., Duineveld, P. C., and Schubert, U. S. (2004) Inkjet printing of polymers: state of the art and future developments, *Advanced materials 16*, 203-213.

136. Liu, C., Xu, Y., Liu, Z., Tsao, H. N., Müllen, K., Minari, T., Noh, Y.-Y., and Sirringhaus, H. (2014) Improving solution-processed n-type organic field-effect transistors by transfer-printed metal/semiconductor and semiconductor/semiconductor heterojunctions, *Organic Electronics 15*, 1884-1889.

137. Noh, Y.-Y., Zhao, N., Caironi, M., and Sirringhaus, H. (2007) Downscaling of self-aligned, all-printed polymer thin-film transistors, *Nature nanotechnology 2*, 784-789.

138. Sinno, H., Nguyen, H. T., Hägerström, A., Fahlman, M., Lindell, L., Coulembier, O., Dubois, P., Crispin, X., Engquist, I., and Berggren, M. (2013) Amphiphilic semiconducting copolymer as compatibility layer for printing polyelectrolyte-gated OFETs, *Organic Electronics 14*, 790-796.

139. Wang, X., Nilsson, D., and Norberg, P. (2013) Printable microfluidic systems using pressure sensitive adhesive material for biosensing devices, *Biochimica et Biophysica Acta (BBA)-General Subjects 1830*, 4398-4401.

140. Thiemann, S., Sachnov, S., Gruber, M., Gannott, F., Spallek, S., Schweiger, M., Krückel, J., Kaschta, J., Spiecker, E., and Wasserscheid, P. (2014) Spray-coatable ionogels based on silane-ionic liquids for low voltage, flexible, electrolyte-gated organic transistors, *Journal of Materials Chemistry C 2*, 2423-2430.

141. Buth, F., Donner, A., Sachsenhauser, M., Stutzmann, M., and Garrido, J. A. (2012) Biofunctional Electrolyte- Gated Organic Field- Effect Transistors, *Advanced Materials 24*, 4511-4517.

142. Buth, F., Kumar, D., Stutzmann, M., and Garrido, J. (2011) Electrolyte-gated organic field-effect transistors for sensing applications, *Applied Physics Letters 98*, 153302.

143. Scarpa, G., Idzko, A., Götz, S., Neumaier, T., and Thalhammer, S. (2009) Biocompatibility studies of solution-processable organic thin-film transistors for sensing applications, In *Nano/Molecular Medicine and Engineering (NANOMED), 2009 IEEE International Conference on*, pp 265-268, IEEE.

144. Magliulo, M., Mallardi, A., Mulla, M. Y., Cotrone, S., Pistillo, B. R., Favia, P., Vikholm- Lundin, I., Palazzo, G., and Torsi, L. (2013) Electrolyte- Gated Organic Field-Effect Transistor Sensors Based on Supported Biotinylated Phospholipid Bilayer, *Advanced Materials 25*, 2090-2094.

145. Sokolov, A. N., Roberts, M. E., and Bao, Z. (2009) Fabrication of low-cost electronic biosensors, *Materials today 12*, 12-20.

146. Angione, M. D., Cotrone, S., Magliulo, M., Mallardi, A., Altamura, D., Giannini, C., Cioffi, N., Sabbatini, L., Fratini, E., and Baglioni, P. (2012) Interfacial electronic effects in functional biolayers integrated into organic field-effect transistors, *Proceedings of the National Academy of Sciences 109*, 6429-6434.

147. Yan, F., Mok, S. M., Yu, J., Chan, H. L., and Yang, M. (2009) Label-free DNA sensor based on organic thin film transistors, *Biosensors and Bioelectronics 24*, 1241-1245.

148. Maddalena, F., Kuiper, M. J., Poolman, B., Brouwer, F., Hummelen, J. C., de Leeuw, D. M., De Boer, B., and Blom, P. W. (2010) Organic field-effect transistor-based biosensors functionalized with protein receptors, *Journal of Applied Physics 108*, 124501.

149. Roberts, M. E., Mannsfeld, S. C., Queraltó, N., Reese, C., Locklin, J., Knoll, W., and Bao, Z. (2008) Water-stable organic transistors and their application in chemical and biological sensors, *Proceedings of the National Academy of Sciences 105*, 12134-12139.

150. Kergoat, L., Piro, B., Berggren, M., Pham, M.-C., Yassar, A., and Horowitz, G. (2012) DNA detection with a water-gated organic field-effect transistor, *Organic Electronics 13*, 1-6.

151. Magliulo, M., Pistillo, B. R., Mulla, M. Y., Cotrone, S., Ditaranto, N., Cioffi, N., Favia, P., and Torsi, L. (2013) PE- CVD of Hydrophilic- COOH Functionalized Coatings on Electrolyte Gated Field- Effect Transistor Electronic Layers, *Plasma Processes and Polymers 10*, 102-109.

152. Cotrone, S., Ambrico, M., Toss, H., Angione, M. D., Magliulo, M., Mallardi, A., Berggren, M., Palazzo, G., Horowitz, G., and Ligonzo, T. (2012) Phospholipid film in electrolyte-gated organic field-effect transistors, *Organic electronics 13*, 638-644.

153. Minamiki, T., Minami, T., Kurita, R., Niwa, O., Wakida, S.-i., Fukuda, K., Kumaki, D., and Tokito, S. (2014) Accurate and reproducible detection of proteins in water using an extended-gate type organic transistor biosensor, *Applied Physics Letters 104*, 243703.

154. Dumitru, L. M., Manoli, K., Magliulo, M., Palazzo, G., and Torsi, L. (2014) Low-voltage solid electrolyte-gated OFETs for gas sensing applications, *Microelectronics Journal 45*, 1679-1683.

155. Mulla, M., Seshadri, P., Torsi, L., Manoli, K., Mallardi, A., Ditaranto, N., Santacroce, M., Di Franco, C., Scamarcio, G., and Magliulo, M. (2015) UV crosslinked poly (acrylic acid): a simple method to bio-functionalize electrolyte-gated OFET biosensors, *Journal of Materials Chemistry B*.

156. Mulla, M. Y., Tuccori, E., Magliulo, M., Lattanzi, G., Palazzo, G., Persaud, K., and Torsi, L. (2015) Capacitance-modulated transistor detects odorant binding protein chiral interactions, *Nature communications 6*.

157. Kline, R. J., McGehee, M. D., Kadnikova, E. N., Liu, J., and Frechet, J. M. (2003) Controlling the field- effect mobility of regioregular polythiophene by changing the molecular weight, *Advanced Materials 15*, 1519-1522.

158. Chang, J.-F., Sun, B., Breiby, D. W., Nielsen, M. M., Sölling, T. I., Giles, M., McCulloch, I., and Sirringhaus, H. (2004) Enhanced mobility of poly (3-hexylthiophene) transistors by spin-coating from high-boiling-point solvents, *Chemistry of materials 16*, 4772-4776.

159. Heffner, G. W., and Pearson, D. S. (1991) Molecular characterization of poly (3-hexylthiophene), *Macromolecules 24*, 6295-6299.

160. Bao, Z., Dodabalapur, A., and Lovinger, A. J. (1996) Soluble and processable regioregular poly (3- hexylthiophene) for thin film field- effect transistor applications with high mobility, *Applied Physics Letters 69*, 4108-4110.

161. Sirringhaus, H., Tessler, N., and Friend, R. H. (1998) Integrated optoelectronic devices based on conjugated polymers, *Science 280*, 1741-1744.

162. Hugger, S., Thomann, R., Heinzel, T., and Thurn-Albrecht, T. (2004) Semicrystalline morphology in thin films of poly (3-hexylthiophene), *Colloid and Polymer Science 282*, 932-938.

163. Cho, S., Lee, K., Yuen, J., Wang, G., Moses, D., Heeger, A. J., Surin, M., and Lazzaroni, R. (2006) Thermal annealing-induced enhancement of the field-effect mobility of regioregular poly (3-hexylthiophene) films, *Journal of Applied Physics 100*, 114503-114503-114506.

164. Gurau, M. C., Delongchamp, D. M., Vogel, B. M., Lin, E. K., Fischer, D. A., Sambasivan, S., and Richter, L. J. (2007) Measuring molecular order in poly (3-alkylthiophene) thin films with polarizing spectroscopies, *Langmuir 23*, 834-842.

165. Alexiadis, O., and Mavrantzas, V. G. (2013) All-Atom Molecular Dynamics Simulation of Temperature Effects on the Structural, Thermodynamic, and Packing Properties of the Pure Amorphous and Pure Crystalline Phases of Regioregular P3HT, *Macromolecules 46*, 2450-2467.

166. Mårdalen, J., Samuelsen, E. J., Gautun, O. R., and Carlsen, P. H. (1991) Chain configuration of poly (3-hexylthiophene) as revealed by detailed X-ray diffraction studies, *Solid state communications 77*, 337-339.

167. Prosa, T., Winokur, M., Moulton, J., Smith, P., and Heeger, A. (1992) X-ray structural studies of poly (3-alkylthiophenes): an example of an inverse comb, *Macromolecules 25*, 4364-4372.

168. Marchant, S., and Foot, P. (1997) Annealing behaviour of conductive poly (3-hexylthiophene) films, *Polymer 38*, 1749-1751.

169. Favia, P., Sardella, E., Gristina, R., and d'Agostino, R. (2003) Novel plasma processes for biomaterials: micro-scale patterning of biomedical polymers, *Surface and Coatings Technology 169-170*, 707-711.

170. Kergoat, L., Battaglini, N., Miozzo, L., Piro, B., Pham, M.-C., Yassar, A., and Horowitz, G. (2011) Use of poly (3-hexylthiophene)/poly (methyl methacrylate)(P3HT/PMMA) blends to improve the performance of water-gated organic field-effect transistors, *Organic Electronics 12*, 1253-1257.

171. Toss, H., Suspène, C., Piro, B., Yassar, A., Crispin, X., Kergoat, L., Pham, M.-C., and Berggren, M. (2014) On the mode of operation in electrolyte-gated thin film transistors based on different substituted polythiophenes, *Organic Electronics 15*, 2420-2427.

172. Suspène, C., Piro, B., Reisberg, S., Pham, M.-C., Toss, H., Berggren, M., Yassar, A., and Horowitz, G. (2013) Copolythiophene-based water-gated organic field-effect transistors for biosensing, *Journal of Materials Chemistry B 1*, 2090.

173. Chabinyc, M. L., Endicott, F., Vogt, B. D., DeLongchamp, D. M., Lin, E. K., Wu, Y., Liu, P., and Ong, B. S. (2006) Effects of humidity on unencapsulated poly (thiophene) thin-film transistors, *Applied physics letters 88*, 113514.

174. Hoshino, S., Yoshida, M., Uemura, S., Kodzasa, T., Takada, N., Kamata, T., and Yase, K. (2004) Influence of moisture on device characteristics of polythiophene-based field-effect transistors, *Journal of Applied Physics 95*, 5088-5093.

175. Caronna, T., Forte, M., Catellani, M., and Meille, S. V. (1997) Photodegradation and photostabilization studies of poly (3-butylthiophene) in the solid state, *Chemistry of materials 9*, 991-995.

176. Manoli, K., Dumitru, L. M., Mulla, M. Y., Magliulo, M., Franco, C. D., Santacroce, M. V., Scamarcio, G., and Torsi, L. (2014) A Comparative Study of the Gas Sensing Behavior in P3HT-and PBTTT-Based OTFTs: The Influence of Film Morphology and Contact Electrode Position, *Sensors 14*, 16869-16880.

177. Do, K., Huang, D. M., Faller, R., and Moulé, A. J. (2010) A comparative MD study of the local structure of polymer semiconductors P3HT and PBTTT, *Phys. Chem. Chem. Phys. 12*, 14735-14739.

178. Porrazzo, R., Bellani, S., Luzio, A., Lanzarini, E., Caironi, M., and Antognazza, M. R. (2014) Improving mobility and electrochemical stability of a water-gated polymer field-effect transistor, *Organic Electronics 15*, 2126-2134.

179. Al Naim, A. F., and Grell, M. (2012) Organic solvents as gate media for thin-film transistors, *Journal of Applied Physics 112*, 114502.

180. Cho, E., Risko, C., Kim, D., Gysel, R., Cates Miller, N., Breiby, D. W., McGehee, M. D., Toney, M. F., Kline, R. J., and Bredas, J.-L. (2012) Three-dimensional packing structure and electronic properties of biaxially oriented poly (2, 5-bis (3-alkylthiophene-2-yl) thieno [3, 2-b] thiophene) films, *Journal of the American Chemical Society 134*, 6177-6190.

181. McCulloch, I., Heeney, M., Bailey, C., Genevicius, K., MacDonald, I., Shkunov, M., Sparrowe, D., Tierney, S., Wagner, R., and Zhang, W. (2006) Liquid-crystalline semiconducting polymers with high charge-carrier mobility, *Nature materials 5*, 328-333.

182. Tsao, H. N., and Müllen, K. (2010) Improving polymer transistor performance via morphology control, *Chemical Society Reviews 39*, 2372-2386.

183. Li, J., Zhao, Y., Tan, H. S., Guo, Y., Di, C. A., Yu, G., Liu, Y., Lin, M., Lim, S. H., Zhou, Y., Su, H., and Ong, B. S. (2012) A stable solution-processed polymer semiconductor with record high-mobility for printed transistors, *Scientific reports 2*, 754.

184. Kwon, J. S., Park, H. W., Kim, D. H., and Kwark, Y. J. (2017) Solvent-Free Processable and Photo-Patternable Hybrid Gate Dielectric for Flexible Top-Gate Organic Field-Effect Transistors, *ACS applied materials & interfaces 9*, 5366-5374.

185. Li, Y., Singh, S. P., and Sonar, P. (2010) A high mobility P-type DPP-thieno[3,2-b]thiophene copolymer for organic thin-film transistors, *Advanced materials 22*, 4862-4866.

186. Seah, K. Y., Li, J., Ong, K.-H., Tan, H.-S., Lim, S.-L., Wong, H.-K., and Chen, Z.-K. (2013) An alternating copolymer based on dithienothiophene and diketopyrrolopyrrole units for thin-film transistors and organic solar cells, *Polym. Chem. 4*, 260-263.

187. Zhang, G., Fu, Y., Xie, Z., and Zhang, Q. (2011) Synthesis of low bandgap polymer based on 3,6-dithien-2-yl-2,5-dialkylpyrrolo[3,4-c]pyrrole-1,4-dione for photovoltaic applications, *Solar Energy Materials and Solar Cells 95*, 1168-1173.

188. Zhang, G., McBride, M., Persson, N., Lee, S., Dunn, T. J., Toney, M. F., Yuan, Z., Kwon, Y.-H., Chu, P.-H., Risteen, B., and Reichmanis, E. (2017) Versatile Interpenetrating

Polymer Network Approach to Robust Stretchable Electronic Devices, *Chemistry of Materials 29*, 7645-7652.

189. Schmoltner, K., Kofler, J., Klug, A., and List-Kratochvil, E. (2013) Electrolyte-gated organic field-effect transistors for sensing in aqueous media, In *SPIE Organic Photonics+ Electronics*, pp 88311N-88311N-88312, International Society for Optics and Photonics.

190. Casalini, S., Dumitru, A. C., Leonardi, F., Bortolotti, C. A., Herruzo, E. T., Campana, A., de Oliveira, R. F., Cramer, T., Garcia, R., and Biscarini, F. (2015) Multiscale Sensing of Antibody–Antigen Interactions by Organic Transistors and Single-Molecule Force Spectroscopy, *ACS nano 9*, 5051-5062.

Chapter II ENZYME-LESS ELECTROCHEMICAL DISPLACEMENT HETEROGENEOUS IMMUNOSENSOR FOR DICLOFENAC DETECTION

1 Introduction

1.1 Diclofenac

Diclofenac is a non-steroidal anti-inflammatory drug (NSAID). Table II-1 summarizes its main physical, chemical and pharmacological properties.

Table II-1. Physical, chemical and pharmacological properties of diclofenac

Diclofenac (DCF)	
Structure, formula, CAS No. and molecular weight	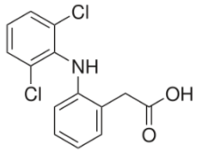 $C_{14}H_{11}Cl_2NO_2$ CAS 15307-86-5 296.16 g mol^{-1}
Usage	Analgesic, anti-inflammatory
Water solubility	23.73 mg L^{-1} (25°C)
pKa	4.15
Elimination half-life	2h
Dosage	75-150 mg daily

It is generally employed to protect from inflammation and relieves pain, e.g. for arthritis, acute injuries, menstrual pain or even nocturnal enuresis. Because of those proved pharmaceutical benefits, diclofenac has been employed in a large number of widely available commercial drugs. Table II-2 shows the outrageous consumption of people in several developed countries. It is clear that human usage of diclofenac has already been excessive due to painkiller abusing, which is popular in the modern world. In fact, although the human usage has played an important part in the total consumption of diclofenac in the world, it is

still better controlled, in comparison to veterinary usage, which is much more massive, thus more worrying.

Table II-2. Annual consumed volumes of diclofenac in some Western countries.

Country	Annual consumption (tons)	Population (10^6)	Dose per capital (mg)
Australia [1]	4	19	211
Austria [2]	6 in 1997	8	750
France [3]	16	59	271
England [4]	26 in 2000	49	531

Moreover, residues are excreted into the ecosystem via urine and faeces, in large quantities compared to the oral dosage. For example, Figure II.1 shows that approximately 35% of the diclofenac dosage is excreted through faecal metabolites; the remaining part is excreted via urine.

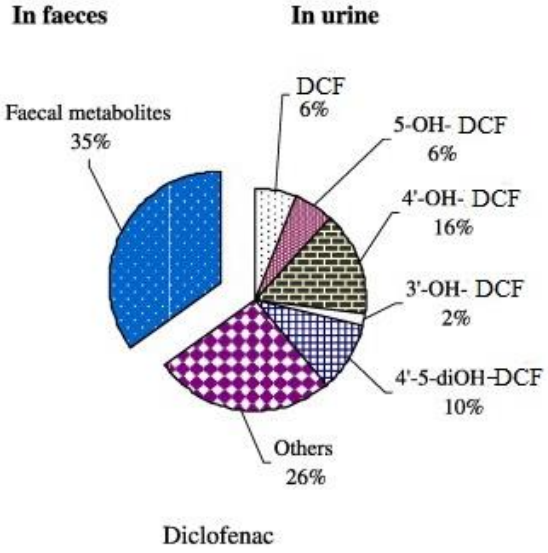

Figure II.1. Identified metabolites of diclofenac and its percentages of oral dosage [5-7]

In addition, this molecule is not well eliminated by water-treatment plants. There have been many studies to assess diclofenac aquatic ecotoxicology (Table II-3). Besides, the negative influences of diclofenac on the terrestorial ecosystem was obvious as the decline of vulture population was proven to be related to the excessive usage for cattles in India [8] and Pakistan [9]. Hence, it was reasonable for diclofenac to be banned for veterinary uses in Europe in 2008

(but some derivatives are still used, however, mainly for factory farming where livestocks are exposed to stress and blows).

Table II-3. Aquatic toxicity data of diclofenac in the literature [5]

Acute toxicity EC_{50} (concentrations that cause 50% of effect)	Chronic toxicity NOEC (no observed effect concetration)	PNEC (predicted no effect concentration)
11.5-22.7 mg L^{-1}	1-10 mg L^{-1}	116 µg L^{-1}
1-10 mg L^{-1}		139 µg L^{-1}
3.3-142.2 mg L^{-1}		
90 ± 20 µg L^{-1} on zebra fish embryos		
68 mg L^{-1}	45 mg L^{-1}	
	1 mg L^{-1} on Daphnia magna	
	1 µg L^{-1} on histopathological lesions	

1.2 Biosensors for detection of diclofenac

There have been numerous methods reported for detecting diclofenac. For example, capillary column gas chromatography with electron-capture detection was employed to determine diclofenac sodium and its hydroxy metabolites, with a detection range of 30-800 ng for 50 µL samples [7]. Detection of diclofenac and its metabolites in human urine was also studied by Sawchuk *et al.* in 1994 using HPLC on a reversed-phase column [10]; the limit of detection was 0.4 µg mL^{-1}. However, in the following, I will focus on sensors rather than on classical analytical methods.

Deng *et al.*, in 2003, compared the efficiency of utilization of an enzyme-linked immunosorbent assay (ELISA) and classical GC-MS to detect diclofenac [11]. ELISA showed a limit of detection of 6 ng L^{-1}, only 25% higher than GC-MS. An example of dose-response using this method is given on Figure II.2.

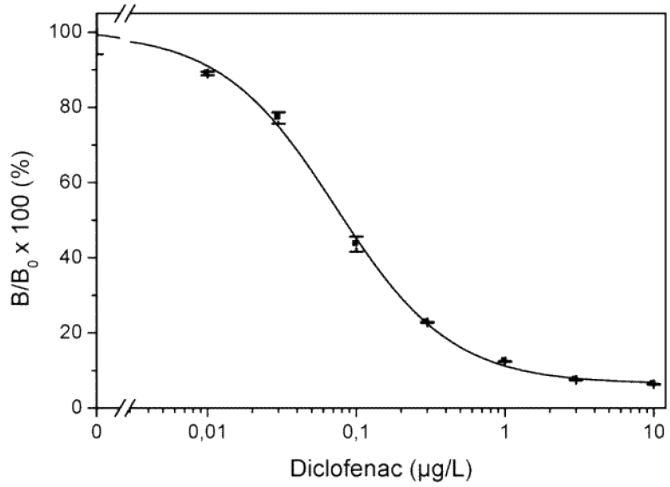

Figure II.2. Dose-response curve for diclofenac spiked into ultrapure water samples. Error bars represent the standard deviation and the ratio B/B_0 (sample absorbance at a given DCF concentration over the maximum absorbance) [(11)]***.***

Huebner *et al.*, in 2015, also applied ELISA for rapid analyzation of diclofenac in freshwater and wastewater [(12)]. Microtiter plates were coated with diclofenac-ovalbumin conjugate, and then detection was performed through a competitive format assay between diclofenac added and anti-diclofenac antibody, both added in solution. The last step consisted in the addition of the secondary HRP-labelled antibody. The range of detection was 11-180 ng L^{-1}, with a limit of detection of 7.8 ng L^{-1}. In 2014, Pschenitza *et al.* also reported the determination of diclofenac and related substances using ELISA using HRP-labeled goat anti-rabbit antibody and H_2O_2 as the enzyme substrate, at extremely low concentrations down to 0.01 ng mL^{-1} [(13)].

In 2011, Kheyrabadi *et al*. described a label-free aptasensor to electrochemically detect sodium diclofenac [(14)] using a sandwich format assay. Glassy carbon electrodes (GCE) were modified by electrooxidation of 6-aminohexanoic acid (AHA), onto which the diclofenac binding aptamer (DBA) was grafted. The complexation happening in the presence of DBA is illustrated on Figure II.3 (A). These authors used electrochemical impedance spectroscopy (EIS) for the measurements, and obtained the limit of detection of 2.7×10^{-7} M, with a linear response between 5 and 1000 µM (Figure II.3 (B))

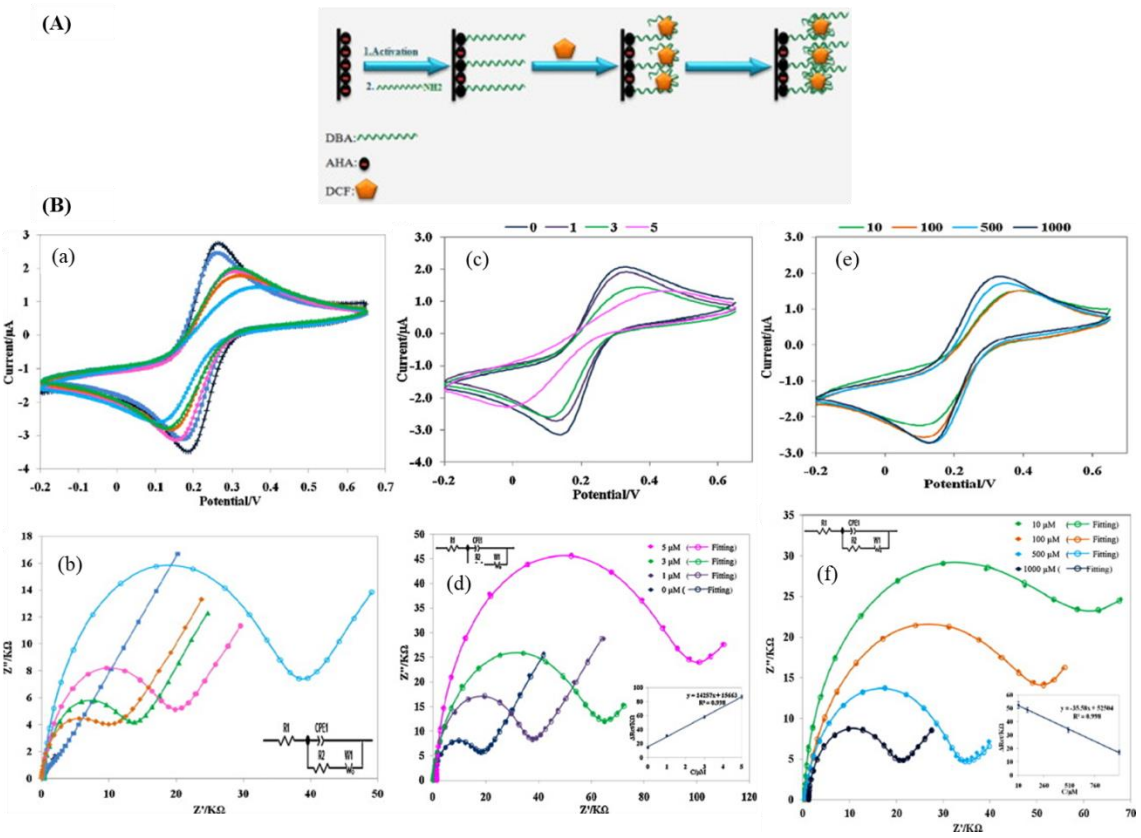

Figure II.3. The aptamer-base diclofenac sensor (Kheyrabadi et al., 2011). (A) Principle of the assay (B) Characterization of the sensing interface by CVs (a), (c), (e) corresponding to (b) EIS: Bare GCE (+), GCE/AHA (■) GCE/AHA/DBA (▲), GCE/AHA/DBA/1 μM DCF (●), GCE/AHA/DBA/5 μM DCF (○) and GCE/AHA/DBA/500 μM DCF (♦), (d) EIS: after treatment of the GCE/AHA/DBA complex with different concentrations of DCF, (f) the EIS: after treatment of the GCE/AHA/DBA complex with different concentrations of DCF. EIS obtained in the presence of 5.0 × 10^{-4} M $Fe(CN)_6^{3-/4-}$ as redox probe [(14)].

Okoth *et al.*, in 2017, also used a label-free aptasensor [(15)]. Instead of applying pure electrochemistry, they focused on photocurrent from a FTO electrode modified by graphene doped with CdS and Au nanoparticles (Figure. II.4 (A)) [(14)]. Interaction between diclofenac and the grafted aptamer led to a photocurrent (PI) change, as illustrated on Figure. II.4 (B). The limit of detection was 0.78 nM, with a linear range from 1 to 150 nM.

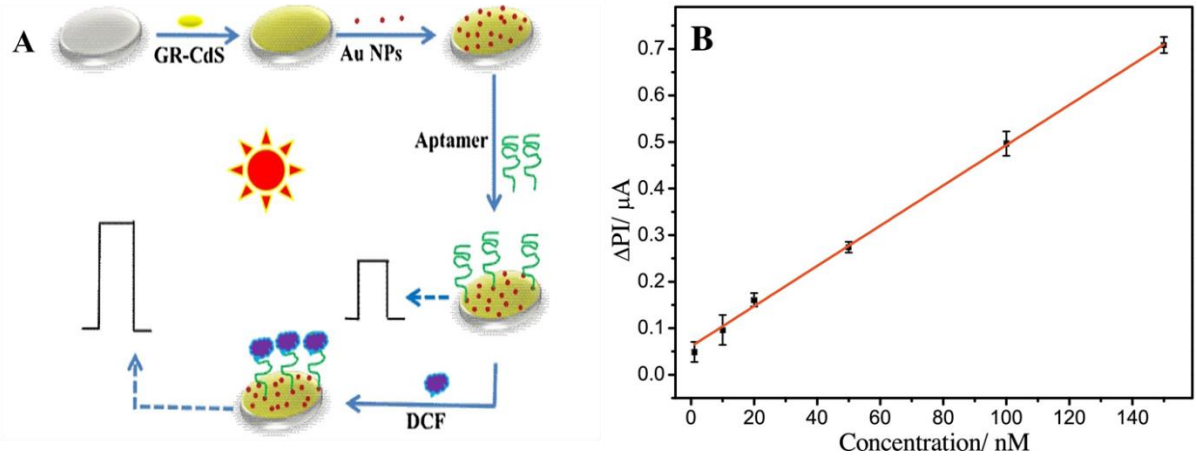

Figure II.4. Label-free aptasensor for DCF detection: (A) Fabrication process of the DCF aptasensor from Okoth et al.; (B) Corresponding calibration curve. ΔPI: change in photocurrent intensity as a function of DCF concentration [(15)]***.***

As an example of very practical application, Rau *et al.* described in 2014 a label-free biosensor to determine diclofenac in milk [(16)] using reflectometric interference spectroscopy. After silanisation of the sensor surface with 3-glyciyoxypropyltrimethoxysilane (GOPS) and immobilization of di-amino-poly(ethylene glycol) and aceclofenac (the glycolic acid ester of diclofenac) onto the surface, anti-diclofenac antibody was immobilized by affinity. The competitive assay occurred upon the addition, in solution, of both diclofenac target and anti-diclofenac antibody. They obtained a limit of detection of 0.11 µg L^{-1} and an operating range of 0.4 to 6 µg L^{-1} (Figure II.5).

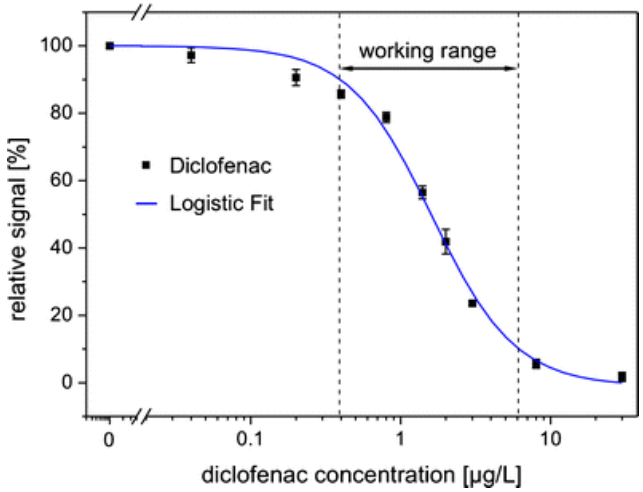

Figure II.5. Calibration curve obtained for DCF in pasteurised milk. The working range, between 0.44 and 6.2 µg L^{-1} is indicated by dotted lines [16].

In another work, Oliveira *et al.* [17] electropolymerized polypyrrole films on graphite pencil electrode, which played the role of anion-exchanger. Diclofenac was detected via potentiometric changes when it penetrates within the polymer film. The working range was from 3×10^{-4} to 1×10^{-2} M, with a LoD of 2×10^{-4} M (Figure. II.6). These figures of merit were far from expectations, however.

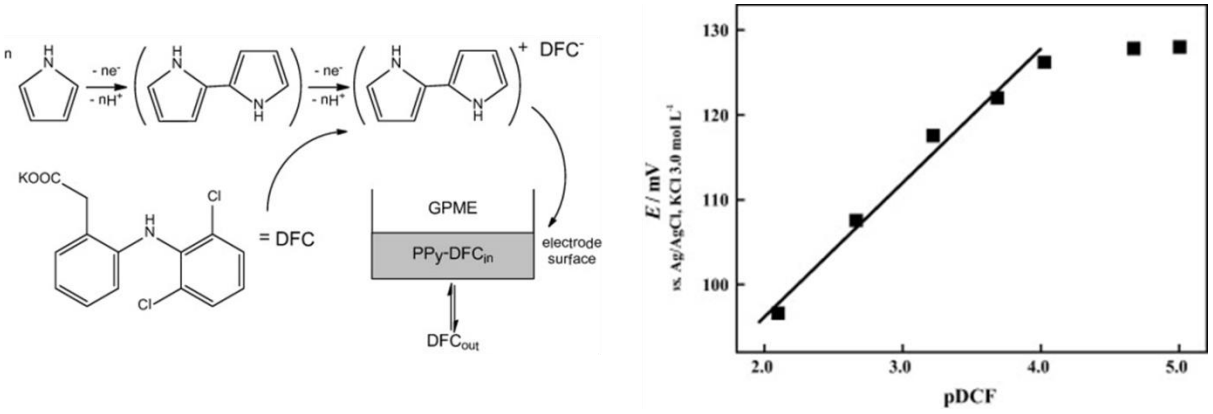

Figure II.6. Electropolymerized polypyrrole films-based sensor for DCF detection: (Left) schematic representation of the preparation of the polypyrrole membrane doped with diclofenac anions; (Right) potentiometric response obtained in $(NH_4)_2SO_4$ using MGPE/PPy–DCF for reference solutions content of 9.9×10^{-6}, 2.1×10^{-5}, 9.4×10^{-5}, 2.1×10^{-4}, 6.0×10^{-4}, 2.2×10^{-3} and 8.0×10^{-3} mol L^{-1} of DCF [17].

Besides, several works reported the use of nanomaterials (mostly AuNPs and carbon nanotubes). For example, Sarhangzadeh *et al.*, in 2013, determined simultaneously diclofenac and indomethacin via an electrochemical sensor in which multiwalled carbon nanotubes and ionic liquids were immobilized on a carbon electrode [(18)]. Diclofenac was measured through the oxidation reaction as given in Figure II.7. The linear range of the calibration curve was found between 0.05 and 50 µmol L^{-1}.

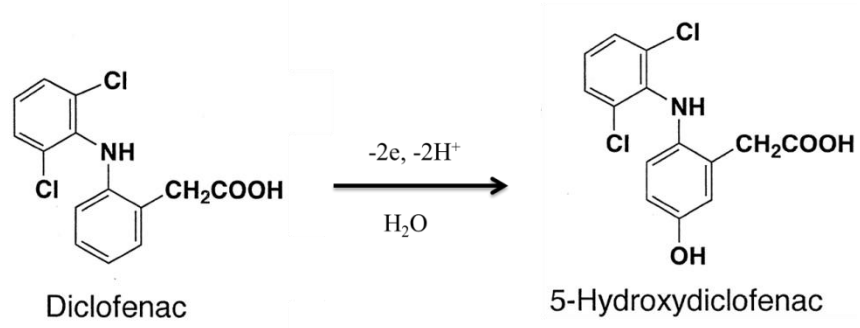

Figure II.7. Oxidation mechanism of DCF

Haddada *et al.* used gold nanoparticles assembly on silicon and gold surfaces to sense anti-diclofenac antibodies using a quartz crystal microbalance (QCM) [(19)]. For that, they treated the substrates with APTES (3-aminopropyltriethoxysilane), GOPS (3-glycidyloxypropyltrimethoxysilane), cysteamine or 11-mercaptoundecanoic (Figure II.8) and immobilized diclofenac by EDC/NHS coupling via the carboxylic function of diclofenac. As the anti-diclofenac antibody was added in solution, it bound to the modified surface, which led to the shifts of resonance frequency due to the changes of the mass of the absorbed layer and dissipation.

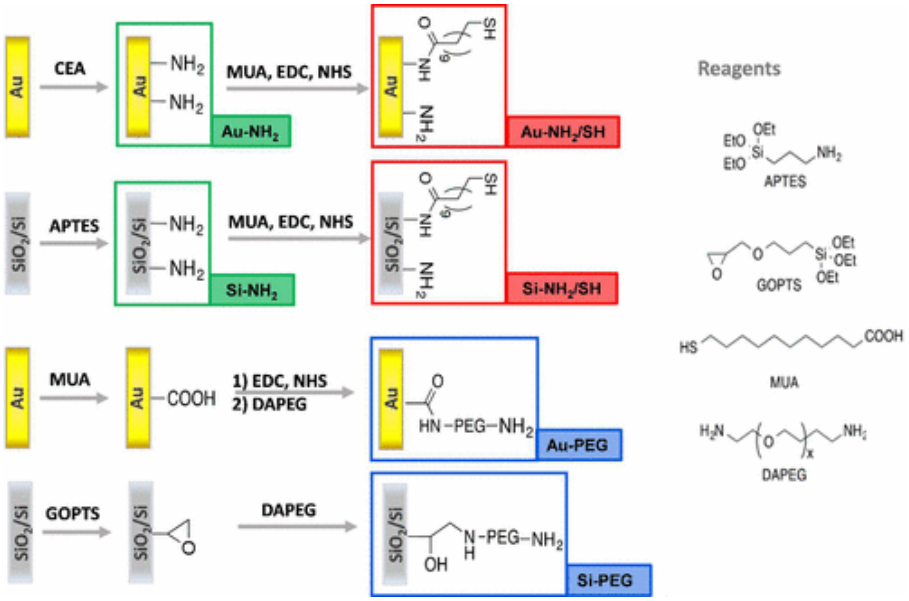

Figure II.8. Surface functionalization strategies for immobilization of AuNPs on gold and silicon substrates [(19)]**.**

The last example is that of Hu and coworkers, reported in 2017 [(20)]. They described the combination of graphene oxide coupled with graphite-like carbon nitride (C_3N_4) used as antibody label, and AuNP-modified multiwalled carbon naonotubes immobilized on an electrode, for making an electrochemiluminescent sensor. The sensor is based on a displayment assay format between diclofenac immobilized on the electrode surface and diclofenac diffusing in solution, with anti-diclofenac antibody coupled to the graphene sheets. The operating range was 0.005-1000 ng mL^{-1} with a detection limit of 1.7 pg mL^{-1} (Figure II.9).

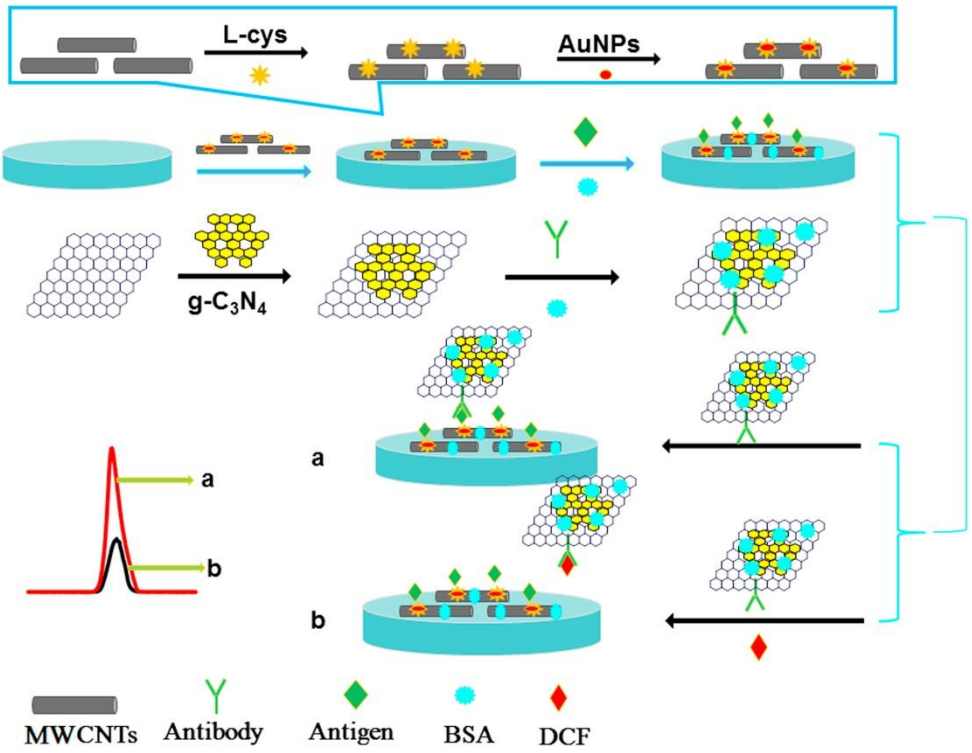

Figure II.9. ECL detection mechanism for DCF based on GCE/MWCNTs-AuNPs/coating antigen/BSA/GO-g-C_3N_4 labeled DCF antibody [(20)].

In conclusion, diclofenac was determined not only via current methods such as GC-MS [(11)], HPLC [(10)] and ELISA [(12, 13)] but also with new technologies, including biosensors featuring nanomaterials such as graphene [(18-20)]. Several methods present low sensitivity and among the most sensitive ones, some are extremely complicated. It is therefore crucial to continue to develop other methods.

Next Section is reproduced the article I published in Biosensors and Bioelectronics in 2017, dealing with an enzyme-less electrochemical displacement heterogeneous immunosensor for diclofenac detection.

2 References

1. Khan, S. J., and Ongerth, J. E. (2004) Modelling of pharmaceutical residues in Australian sewage by quantities of use and fugacity calculations, *Chemosphere 54*, 355-367.

2. Strenn, B., Clara, M., Gans, O., and Kreuzinger, N. (2004) Carbamazepine, diclofenac, ibuprofen and bezafibrate - investigations on the behaviour of selected pharmaceuticals during wastewater treatment, *Water Science and Technology 50*, 269-276.

3. Ferrari, B. t., Paxéus, N., Giudice, R. L., Pollio, A., and Garric, J. (2003) Ecotoxicological impact of pharmaceuticals found in treated wastewaters: study of carbamazepine, clofibric acid, and diclofenac, *Ecotoxicology and Environmental Safety 55*, 359-370.

4. O.A.H. Jones, N. V., J.N. Lester. (2002) Aquatic environmental assessment of the top 25 English prescription pharmaceuticals, *Water Research 36*, 5013–5022.

5. Zhang, Y., Geissen, S. U., and Gal, C. (2008) Carbamazepine and diclofenac: removal in wastewater treatment plants and occurrence in water bodies, *Chemosphere 73*, 1151-1161.

6. I. Bernus, W. D. H., R.G. Dickinson, M.J. Eadie. (1995) Metabolism of carbamazepine and co-administered anticonvulsants during pregnancy, *Elsevier Science B.V. 21*, 65-75.

7. Degen, W. S. a. P. H. (1981) Simultaneous determination of diclofenac sodium and its hydroxy metabolites by capillar colume gas chromatograpy with electron-capture detection, *JOWMI of Chromatography 2*, 263-271.

8. Shultz, S., Baral, H. S., Charman, S., Cunningham, A. A., Das, D., Ghalsasi, G. R., Goudar, M. S., Green, R. E., Jones, A., Nighot, P., Pain, D. J., and Prakash, V. (2004) Diclofenac poisoning is widespread in declining vulture populations across the Indian subcontinent, *Proceedings. Biological sciences 271 Suppl 6*, S458-460.

9. J. Lindsay Oaks, M. G., Munir Z. Virani2, Richard T. Watson, Carol U. Meteyer3, Bruce A. Rideout, H. L. Shivaprasad, Shakeel Ahmed, Muhammad Jamshed Iqbal Chaudhry, Muhammad Arshad6, Shahid Mahmood6, Ahmad Ali & Aleem Ahmed Khan. (2004) Diclofenac residues as the cause of vulture population decline in Pakistan *Nature 427*.

10. Sawchuk, J. J. (1995) Analysis of diclofenac and four of its metabolites in human urine by HPLC, *Pharmaceutical research 12*.

11. Anping Deng, M. H., Qing-Zhi Zhu, Siegfried Frey, Manfred Sengl, Wolfgang Buchberger, Reinhard Niessner, and Dietmar Knopp. (2003) Residue Analysis of the

Pharmaceutical Diclofenac in Different Water Types Using ELISA and GC-MS, *Environmental science & Technology 37*, 3422-3429.

12. Huebner, M., Weber, E., Niessner, R., Boujday, S., and Knopp, D. (2015) Rapid analysis of diclofenac in freshwater and wastewater by a monoclonal antibody-based highly sensitive ELISA, *Analytical and bioanalytical chemistry 407*, 8873-8882.

13. Pschenitza, M., Gavrilova, E. S., Tarasov Scapital A, C., Knopp, D., Niessner, R., and Epstein, O. I. (2014) Application of a heterogeneous immunoassay for the quality control testing of release-active forms of diclofenac, *International immunopharmacology 21*, 225-230.

14. Kashefi-Kheyrabadi, L., and Mehrgardi, M. A. (2012) Design and construction of a label free aptasensor for electrochemical detection of sodium diclofenac, *Biosensors & bioelectronics 33*, 184-189.

15. Okoth, O. K., Yan, K., Feng, J., and Zhang, J. (2018) Label-free photoelectrochemical aptasensing of diclofenac based on gold nanoparticles and graphene-doped CdS, *Sensors and Actuators B: Chemical 256*, 334-341.

16. Rau, S., Hilbig, U., and Gauglitz, G. (2014) Label-free optical biosensor for detection and quantification of the non-steroidal anti-inflammatory drug diclofenac in milk without any sample pretreatment, *Analytical and bioanalytical chemistry 406*, 3377-3386.

17. Oliveira, M. C., Bindewald, E. H., Marcolino, L. H., and Bergamini, M. F. (2014) Potentiometric determination of Diclofenac using an ion-selective electrode prepared from polypyrrole films, *Journal of Electroanalytical Chemistry 732*, 11-16.

18. Sarhangzadeh, K., Khatami, A. A., Jabbari, M., and Bahari, S. (2013) Simultaneous determination of diclofenac and indomethacin using a sensitive electrochemical sensor based on multiwalled carbon nanotube and ionic liquid nanocomposite, *Journal of Applied Electrochemistry 43*, 1217-1224.

19. Ben Haddada, M. H., Maria Casale, Sandra Knopp, Dietmar Niessner, Reinhard Salmain, Michèle Boujday, Souhir. (2016) Gold Nanoparticles Assembly on Silicon and Gold Surfaces: Mechanism, Stability, and Efficiency in Diclofenac Biosensing, *The Journal of Physical Chemistry C 120*, 29302-29311.

20. Hu, L., Zheng, J., Zhao, K., Deng, A., and Li, J. (2018) An ultrasensitive electrochemiluminescent immunosensor based on graphene oxide coupled graphite-like carbon nitride and multiwalled carbon nanotubes-gold for the detection of diclofenac, *Biosensors & bioelectronics 101*, 260-267.

3 Article (Biosens. Bioelectron. 2017, 97, 246-252)

Enzyme-less Electrochemical Displacement Heterogeneous Immunosensor for Diclofenac Detection

T.T. K. Nguyen [a,b], T.T. Vu [b], G. Anquetin [a], H.V. Tran [c], S. Reisberg [a], V. Noël [a], G. Mattana [a], Q.V. Nguyen [b], Tran Dai Lam [d,e], M.C. Pham [a], B. Piro [a*]

[a] *Univ. Paris Diderot, Sorbonne Paris Cité, ITODYS, UMR 7086 CNRS, 15 rue J-A de Baïf, 75205 Paris Cedex 13, France*

[b] *USTH – Université des Sciences et Technologies de Hanoï, Nghĩa Đô, Cầu Giấy, Hanoi, Viet Nam.*

[c] *Department of Inorganic Chemistry, School of Chemical Engineering, Hanoi University of Science and Technology (HUST), 1st Dai Co Viet Road, Hanoi, Viet Nam*

[d] *Graduate University of Science and Technology, Vietnam Academy of Science and Technology, 18, Hoang Quoc Viet, Ha Noi, Viet Nam.*

[e] *Center for High Technology Development, Vietnam Academy of Science and Technology, 18 Hoang Quoc Viet, Ha Noi, Viet Nam*

Abstract

We describe an electrochemical immunosensor based on functionalization of a working electrode by electrografting two functional diazonium salts. The first one is a molecular probe, diclofenac, coupled with an arylamine onto which a specific antibody is immobilized by affinity interactions; the second is a redox probe (a quinone) also coupled with an arylamine, able to transduce the hapten-antibody association into a change in electroactivity. The steric hindrance induced by the antibody leads to a current decrease upon binding of the antibody on the grafted molecular probe; conversely, when diclofenac is present in solution, a displacement equilibrium occurs between the target diffusing into the solution and the grafted probe. This leads to dissociation of the antibody from the electrode surface, event which is

transduced into a current increase ("signal-on" detection). The detection limit is ca. 20 fM, corresponding to 6 pg L^{-1} diclofenac, which is competitive compared to other label-free immunosensors. We demonstrate that the sensor is selective and is able to quantify diclofenac in tap water.

Keywords: Diclofenac; Diazonium salts; Electrochemical Immunosensor; Hapten probe; Displacement immunoassay.

** Corresponding authors. B Piro: Tel. +33-1-57277224. Email: piro@univ-paris-diderot.fr*

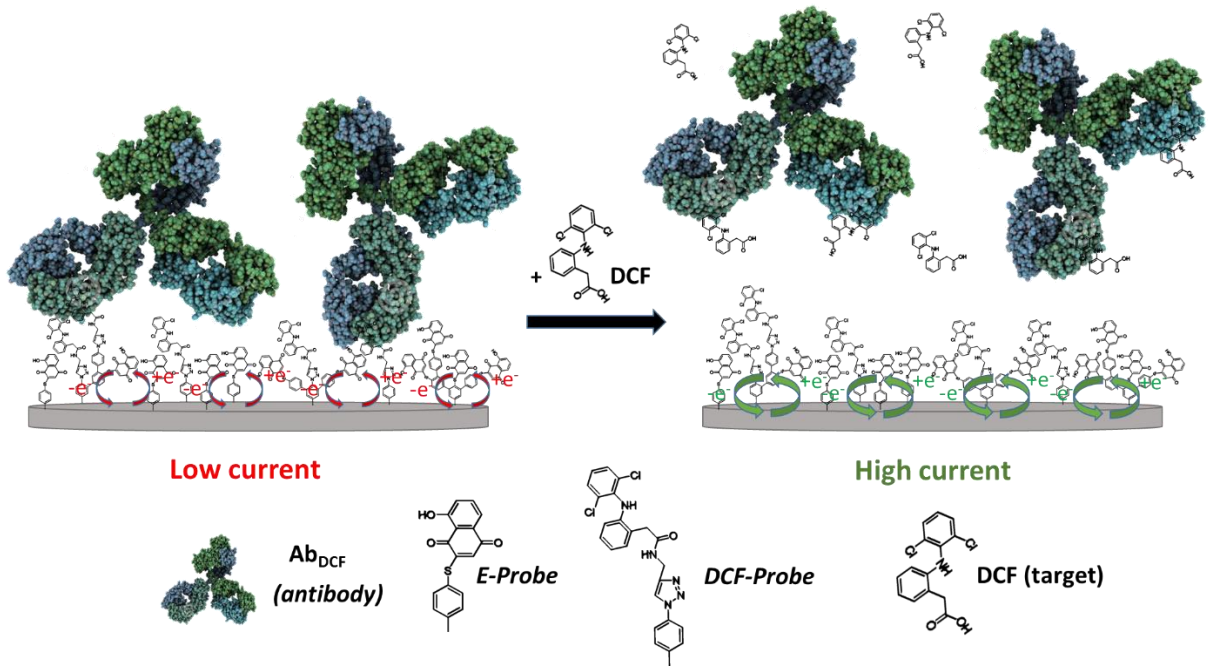

Graphical Abstract

1. Introduction

An increasing number of molecules routinely used in everyday life, in the industry or for livestock farming, and more particularly drugs, accumulate continuously in aqueous ecosystems. Some of these molecules are now considered as pollutants, having a negative impact on human health. Among them, diclofenac (DCF) is a commonly used non-steroidal

anti-inflammatory drug of IUPAC name 2-[2-(2,6-dichloroanilino)phenyl]acetic acid (commercial names are Pennsaid® or Voltaren®). It is one of the most frequently found drugs in fresh waters (Aldekoa et al., 2013).

There have been few researches on diclofenac detection. Most of them use traditional methods (mass spectrometry MS, high performance liquid chromatography HPLC (Sacher et al., 2001; Petrovic et al., 2005), or capillary electrophoresis (Cunha et al., 2013; Gimenes et al., 2013). Some procedures coupling MS, HPLC or GC (gas chromatography) with electrochemistry have been also described (Damiri et al., 2016; Zecca et al., 1991; Jin and Zhang, 2000; Chmielewska et al., 2006) with various sensitivities ranging from the μM down to the nM range. These methods are efficient in terms of detection limits and selectivity, but they cannot be easily transferred to continuous or in-the-field monitoring applications, for example. For these reasons, biosensors and more precisely electrochemical biosensors represent good replacement or complementary analytical tools.

Few publications describe diclofenac electrochemical sensors, for example based on potentiometry (Oliveira et al., 2014) or on catalytic DCF electrooxidation on nanostructured surfaces, including graphene or carbon nanotubes (Thiagarajan et al., 2012; Sarhangzadeh et al., 2013; Karuppiah et al., 2015). However, limits of detection (LoD) reached with these techniques are not lower than a few tens of nM. Capture of DCF at the electrode/transducing surface using biomolecules specific for DCF could be an interesting method for improving the limit of detection. Such an approach has already been published using nucleic acid aptamers, which present several advantages over antibodies and have already demonstrated high affinities for small organic molecules. However, in the particular case of DCF aptamers, these aptasensors showed detection limits significantly higher than immunosensors, in the μM range (Kashefi-Kheyrabadi et al., 2012), thus demonstrating the fact that antibodies

performing better than the existing aptamers were available. It should be noticed that using nanostructured electrodes, Derikvand et al., 2016 demonstrated an improved LoD (in the nM range), equivalent to LoDs obtained for DCF immunosensors (Huebner et al., 2015). It should also be noticed that sub-nM DCF concentrations were reached by Hlaváček et al., 2016, using antibodies according to a classical ELISA (Enzyme-Linked ImmunoSorbent Assay). The figure of merits of these works are summarized in Table 1.

Even if such assay format has proven its efficiency and versatility, some drawbacks relative to the multiplexing, miniaturization and automation still remain and require the development of alternative analytical approaches.

Table 1. *Characteristics of the above-cited DCF electrochemical and ELISA sensors.*

Principle	Detection range	LoD	Ref.
DCF embedded in polypyrrole; Potentiometry	310 µM – 11 mM	190 µM	Oliveira et al., 2014
TiO_2 -PEDOT; Electrooxidation	Not given	0.03 µM	Thiagarajan et al., 2012
Graphene oxide/GCE; Linear sweep voltammetry	Not given	0.09 µM	Karuppiah et al., 2015
MWCNT/Ionic liquid; Cyclic voltammetry	0.05 – 50 µM	18 nM	Sarhangzadeh et al., 2013
Aptamer; Electrochemical impedance	< 5.0 µM	0.27 µM	Kashefi-Kheyrabadi et al., 2012
PtNPs/CNTs/Aptamer; Electrochemical impedance	10 - 200 nM	2.7 nM	Derikvand et al., 2016
ELISA (monoclonal antibodies)	37 – 600 pM	26 pM	Huebner et al., 2015
Photon-upconverting NPs / antibodies	Not given	0.17 nM	Hlaváček et al., 2016

*PEDOT: poly(3,4-ethylenedioxythiophene); MWCNT: multiwalled carbon nanotubes; PtNPs: platinum nanoparticles; CNTs: Carbon nanotubes.

In this work, we developed the first example of electrochemical displacement immunosensor for diclofenac detection based on the functionalization of an electrode by electroreduction of diazonium salts. Two precursors of the diazonium salts were designed:

The first is N-((1-(4-aminophenyl)-1*H*-1,2,3-triazol-4-yl)methyl)-2-(2-((2,6-dichlorophenyl)amino)phenyl)acetamide used as immobilized molecular probe (further referred to as *DCF-Probe*) onto which the diclofenac antibody (Ab_{DCF}) can bind; the second is (2-[(4-aminophenyl)sulfanyl]-8-hydroxy-1,4-naphthoquinone) (further referred to as *E-Probe*), a redox probe, in order to transduce the Ab_{DCF}/*DCF-Probe* binding into a change of redox current. The *E-Probe* contains quinone groups, the electroactivity of which being known to be sensitive to ion strength, pH or to local ion transport depending on the layer thickness.

On one hand, when quinone derivatives are immobilized onto the electrode through a method leading to thick films, their charge injection kinetics depends on counter-ions diffusion rate (Piro et al., 2007). Ab_{DCF} binding to *DCF-Probe* may reduce access of cations to the redox probe, leading to a current decrease (decrease of the apparent charge transfer rate). Conversely, if DCF is added into the surrounding electrolyte, it competes with *DCF-Probe* and induces dissociation of Ab_{DCF} (i.e. displaces the Ab_{DCF}) from the electrode surface; this phenomenon is responsible for a decrease of the steric hindrance, which is expected to cause a current increase depending on the DCF concentration (cf. Fig. 1). This original transduction principle based on a displacement equilibrium has been applied successfully to detect atrazine (Tran et al., 2012; Tran et al., 2013) using electropolymerization of quinone-derivatives monomers. Despite the effectiveness of this approach, some drawbacks remain such as the high number of fabrication steps and the time required to equilibrate the thick film with respect to the solution composition.

On the other hand, quinone electroactivity is also highly sensitive to the presence of inter- and intramolecular hydrogen bonds (H bonds) which control to a large extent their charge transfer rate. Biomolecules such as antibodies may interact with the underlying quinone layer through H bonds and then modify its redox behavior. Such approach has been successfully implemented using short DNA probes immobilized on self-assembled monolayers of quinone derivatives. Immobilized quinones are then excellent transducing elements of biomolecular recognition process occurring in their close vicinity. There is hence a strong interest in coupling thin juglone layers and antibodies to achieve highly sensitive electrochemical biosensors.

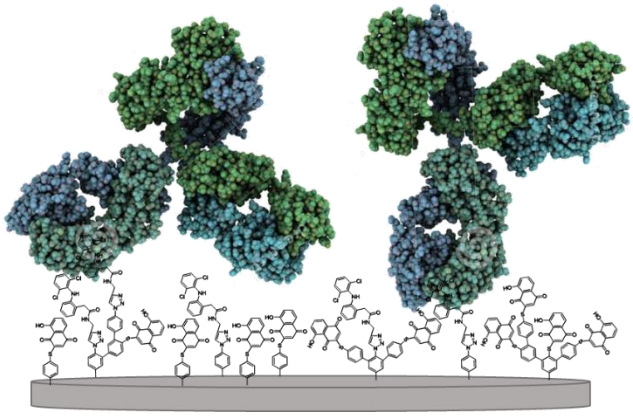

Figure 1. *Illustration of the steric hindrance induced by immunobinding of Ab_{DCF} on the electrode modified by DCF-Probe and E-Probe (elements are roughly at scale).*

In this study, we demonstrated for the first time the selective determination of DCF using an original electrochemical displacement immunosensor which has never been described for DCF detection. It operated within a concentration range between 10^{-14} M and 10^{-10} M. The LoD, estimated at ca. 0.1 pM, i.e. 25 pg L^{-1} is significantly lower than what has been

previously reported for other electrochemical DCF sensors, and even lower than other non-electrochemical sensors (see Table 1).

2. Materials and methods

2.1. Chemicals and reagents

Glassy carbon (GC) working electrodes (area of 0.07 cm^2) were purchased from BASInc, IN, USA. Alumina slurry used for GC polishing was from ESCIL, France. Aqueous solutions were made with ultrapure (18 MΩ cm) water, except for the final application experiments where tap water (Paris, 13th district, pH 7.8) was used. Phosphate buffer saline (PBS), acetonitrile (ACN, HPLC grade), 5-hydroxy-1,4-naphthoquinone, (+)-sodium L-ascorbate, copper(II) sulfate pentahydrate, 4-azidoaniline, *t*-butyl nitrite, HATU [2], N,N-diisopropylethylamine, propargylamine, tetrabutylammonium hexafluorophosphate ($TBAPF_6$) and 2-methyl-4-chlorophenoxyacetic acid (MCPA) were from Sigma-Aldrich. Diclofenac sodium salt was from Cayman Chemical (MI, USA). All other reagents and solvents were practical grade (PA). Anti-diclofenac antibodies (Ab_{DCF}) were provided by Creative Diagnostic (USA), ref#DPAB1703. Anti-bisphenol A antibodies (Ab_{BPA}, rabbit IgG), were purchased from Interchim, France. Anti-ketoprofen antibodies (Ab_{Ket}, sheep IgG), were from OriGene Europe (Germany), ref#AP09737PU-N. Diclofenac contained in a commercially available medicine (namely, Voltarène L.P. 75 mg from Novartis Pharma SAS, France) was used as real sample. It contained 69.8 mg diclofenac and 5.2 mg excipients including saccharose, cetyl alcohol, colloidal silica, polyvidone, magnesium stearate, polysorbate 80, titanium dioxide, red iron oxide and talc.

[2] HATU = 1-[Bis(dimethylamino)methylene]-1H-1,2,3-triazolo[4,5-b]pyridinium 3-oxid hexafluorophosphate, N-[(Dimethylamino)-1H-1,2,3-triazolo-[4,5-b]pyridin-1-ylmethylene]-N-methylmethanaminium hexafluorophosphate N-oxide

2.2. Methods

Thin-layer chromatography (TLC) was performed on TLC plastic sheets of silica gel 60F254 (layer thickness 0.2 mm) from Merck. Column chromatography purification was carried out on silica gel 60 (70-230 mesh ASTM, Merck). NMR spectra were recorded, using $CDCl_3$ or CD_2Cl_2 as solvent, on a Bruker AC 300 or 400 spectrometer at 400 MHz for ^1H and 100 MHz for ^{13}C. Chemical shifts (δ) were expressed in parts per million relative to the signal indirectly (i) to $CHCl_3$ (δ 7.27) for ^1H and (ii) to $CDCl_3$ (δ 77.2) for ^{13}C. Data were processed using TOP-SPIN software (Bruker). Tetramethylsilyl (TMS) was used as an internal standard. Peak multiplicities were designated as follows: s, singlet; d, doublet; t, triplet; td triplet of doublet; m, multiplet. MS data were collected from a LCT Premier XE (Waters). FTIR was performed with a Thermo Nicolet 8700 spectrometer.

For electrochemical experiments, a three-electrode cell was used, consisting of a GC working electrode (3 mm in diameter, 0.07 cm^2), a platinum grid as counter electrode (1 cm^2) and a commercial saturated calomel reference electrode (SCE, Metrohm) used with a short (2 cm) salt bridge containing PBS. Working electrodes were polished before use sequentially with 1 µm then 0.3 µm alumina slurries on a Struers Labopol-2 apparatus and rinsed with MilliQ water under ultrasonication during 5 min, then dried and washed with ACN. Cyclic voltammetry (CV) and square wave voltammetry (SWV) were performed on an Autolab PGSTAT 302N with NOVA 2.0 software. SWVs were recorded using a modulation amplitude of 50 mV, an interval time of 80 ms, a step of 2 mV and a frequency of 12.5 Hz. SWVs shown in this article give absolute currents; only for the calibration curve, relative current changes (before and after incubation) were plotted. All immunodetection experiments were performed in a cell thermostated at 25°C with a Peltier device (Eppendorf Thermomixer Comfort). All solutions were argon-saturated for 20 min before experiments. During

experiments, argon was continuously passed over the solutions to avoid any contamination with oxygen.

SWV experiments were performed before and after immobilization of the antibodies on the electrodes, and before and after displacement assays. Unless stated differently in the text, modified electrodes were re-used for a complete series of experiments, by incubating them serially with increasing concentrations of analyte. The use of a fresh electrode for each concentration was also investigated and gave similar results, although less reproducible. In this case, reproducibility is obtained by calibrating electrodes in standard solutions before use.

2.3. Synthesis

The synthesis developed in this work are described in the Supplementary file.

2.4. Competition ELISA experiments

The affinity of Ab_{DCF} to *DCF-Probe* and DCF was determined by ELISA experiments. The competition ELISA kit (IDEL#-F035, lot IDELF035501) was provided by ID Labs (London, ON, Canada). The kit contained a horseradish peroxidase (HRP)-conjugated secondary antibody, 3,3',5,5'-tetramethylbenzidine (TMB_{Red}) as chromogen HRP substrate, a washing buffer (PBS + 0.1% Tween 20), a stop buffer (0.16 M sulfuric acid, which changes the color of the chromogen to yellow, λ_{max} = 450 nm instead of 605 nm for TMB_{Ox} at pH 7.2), and microtiter plates coated with a DCF competitor. In these experiments, instead of the antibody provided in the kit, we used the anti-DCF (Ab_{DCF}) provided by Creative Diagnostic (USA), ref#DPAB1703, which we also used for the electrochemical experiments.

2.4.a. *Traditional competition ELISA tests*

For the ELISA tests, 100 µL of DCF solution with various concentrations (from 10^{-7} M to 10^{-3} M) were dispensed into the wells of the kit microtiter plate, then 100 µL of Ab_{DCF} were

added into the wells. After incubation for 30 min at room temperature, the wells were washed 3 times with 250 µL of washing buffer. Then, 150 µL of HRP-conjugated secondary antibody were added and the wells were again incubated for 30 min at room temperature. Wells were afterwards washed 3 times with 250 µL of washing buffer, then 100 µL of TMB solution were added in each well and left to incubate for 20 min at room temperature, then the reaction was stopped by adding 100 µL of stop buffer. To read the optical density at 450 nm (Thermo Scientific spectrophotometer Genesys 20), 200 µL were transferred to a 2-mL spectrophotometric quartz cuvette, then 400 µL of ultrapure water were added.

We also performed this procedure using *DCF-Probe*-modified GC electrodes instead of the titer plate provided in the kit. First, *DCF-Probe* was grafted on GC electrodes by diazonium electroreduction (details of experiments are described in Section 3.1). To perform the competitive immunoassay, the *DCF-Probe*-modified electrodes were then incubated in 10 µL DCF (at various concentrations) + 10 µL of Ab_{DCF} in PBS, then we followed the same procedure as described above for the commercial titer plates.

2.4.b. *Electrochemical displacement immunodetection*

E-Probe and DCF-Probe were grafted on GC electrodes as described in Section 3.1 below. 5 µL of Ab_{DCF} solutions (PBS + Ab_{DCF} at various concentrations) were dropped on the modified electrodes, which were capped by an empty Eppendorf tube (1.5 mL) to avoid evaporation and left to react for 2h at 37°C. After rinsing in PBS, Ab_{DCF}/*DCF-Probe/E-Probe/*GC electrodes were dipped into a DCF solution (at various concentrations in tap water or PBS, depending on the experiment) for 1h at 37 °C, then rinsed three times with PBS and kept in PBS before recording CVs and SWVs.

3. Results and discussion

3.1. Electrografting and electroactivity

The diazonium salts were obtained from the corresponding aromatic amine compounds described in Sections 2.3.1 and 2.3.2. Their structures are shown on Fig. SI3a,b. In-situ formation of the diazonium salts from the *E-Probe* and *DCF-Probe* molecules, followed by their electrografting, was performed as follows. A solution of ACN containing 3 mM *t*-butyl nitrite, 0.1 M $TBAPF_6$, 1 mM *E-Probe* and 0.4 mM *DCF-Probe* (this latter concentration was varied for optimization) was prepared and put in an electrochemical cell. After thorough degassing under argon for 20 minutes, the potential of the working electrode was swept between 0.6 V and -0.6 V vs. SCE at 100 mV s^{-1}. Electrodes were then washed under ultrasonication for 2 min in ACN and 2 min in water to remove residual precursors. As shown on Fig. 2A, an irreversible reduction peak occurred at ca. -0.4 V for the first scan, then disappeared for the following scans, which meant that one scan was sufficient to cover the electrode surface and block further electroreduction. Fig. 2B shows a CV of the resulting *DCF-Probe/E-Probe/*GC electrode in PBS, which shows a couple of peaks at -0.35 V/-0.60 V vs SCE, corresponding to the redox process of the quinone group (DCF is not electroactive in this potential range). We calculated the surface coverage of a *E-Probe*/GC electrode (0.07 cm^2) from the coulombic charge (C = 2.97 μC) developed by the anodic peak of the *E-Probe* electroactivity, using the following equation: $\Gamma_{E\text{-}Probe,\ CV} = C / nFA$. With an electrode area A = 0.07 cm^2, the Faraday constant F = 96489 C mol^{-1} and assuming n=2 electrons exchanged per quinone unit, one found a surface coverage $\Gamma_{E\text{-}Probe,\ CV} = (2.2\pm0.2)\times10^{-10}$ mol cm^{-2}, which could be considered as half of a compact monolayer. At open circuit potential, spontaneous grafting of the probe molecules also occurs, giving a surface coverage of $\Gamma_{E\text{-}Probe,\ OC} = (7\pm1)\times10^{-11}$ mol cm^{-2}. Under the same conditions, when a GC electrode was put in 1 mM 5-hydroxy-1,4-naphthoquinone in ACN, the measured quantity adsorbed on the GC electrode

was $\Gamma_{5HNQ, OC} = (2\pm1)\times10^{-11}$ mol cm^{-2}. This shows that co-electrografting of the *E-Probe* and *DFC-Probe* on GC gives a layer three times more electroactive than spontaneous reduction, and ten times more electroactive than passive adsorption. Fig. SI3c illustrates the expected film structure, with *E-Probe* and *DFC-Probe* moieties grafted on the electrode material via a C-C bond between the aryl group and the carbon electrode, but also via coupling of these diazonium salts with already grafted moieties. Considering the relative steric hindrance of the two functional groups (5-hydroxynaphthoquinone for *E-Probe* and diclofenac for *DCF-Probe*), this coupling of diazonium salts on already grafted molecules is not favored but cannot be excluded (Delamar et al., 1992).

Fig. 3, curve a, shows the SWV corresponding to of a *DCF-Probe/E-Probe/*GC electrode in PBS, recorded from -0.55 V to + 0.05 V (modulation amplitude of 50 mV, interval time of 80 ms, step of 2 mV and frequency of 12.5 Hz). Only one SWV peak is present, centered at -0.25 V vs SCE. The redox system was highly stable with respect to multiple cycling; the low potential range avoids interfering oxidations of other electroactive species that may be present in the medium (including DCF, the oxidation of which occurring at potentials over + 0.7 V vs. SCE on glassy carbon).

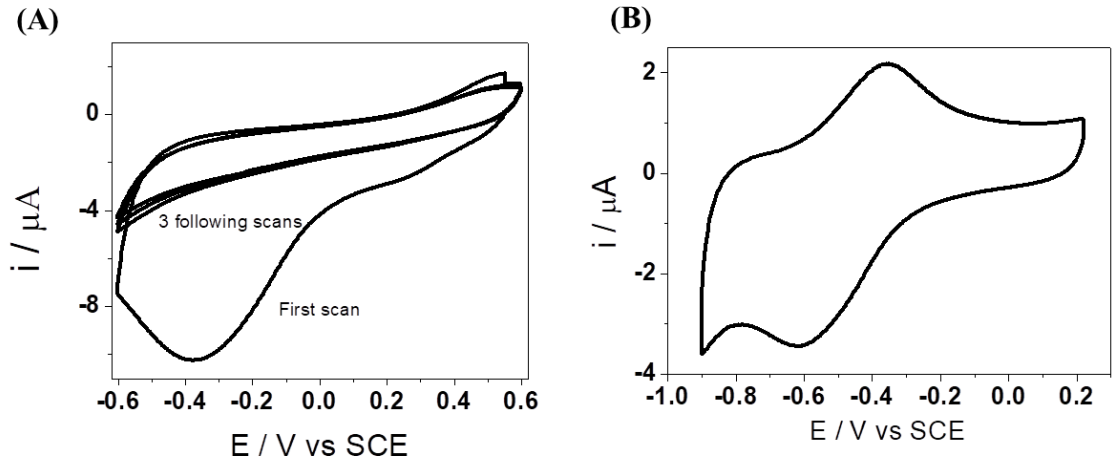

***Figure 2**: **(A)** Cyclic voltammograms corresponding to the electrografting of the DCF-Probe and E-Probe on a GC electrode. Scan rate 100 mV s^{-1}. **(B)** CV of a DCF-Probe/E-Probe/GC electrode in PBS. Scan rate 50 mV s^{-1}. Area = 0.07 cm^2. Solutions deaerated with argon.*

3.2. *Ab_{DCF} immobilization*

For immunobinding between *Ab_{DCF}* in solution and *DCF-Probe* grafted on the electrode surface, 5 µL of *Ab_{DCF}* solutions (PBS + *Ab_{DCF}* at various concentrations) were dropped on *DCF-Probe/E-Probe/*GC electrodes and let to react for 2h at 37°C in humid atmosphere to avoid evaporation. Several antibody concentrations were investigated from 10^{-9} M up to 5×10^{-5} M. To check the binding specificity, two control antibodies (not reactive towards DCF) were used, i.e. *Ab_{Ket}* (anti-ketoprofen; ketoprofen is *RS*-2-(3-benzoylphenyl)propionic acid) and *Ab_{BPA}* (anti-bisphenol A), under the same experimental conditions applied for *Ab_{DCF}*. Then, electrodes were rinsed three times with PBS at room temperature to remove physisorbed *Ab_{DCF}*. Finally, CVs and SWVs were performed to record the *E-Probe* electroactivity after this immunobinding step. It appeared, as it had already appeared on Fig. 2, that *DCF-Probe*/*E-Probe*/GC electrodes presented a strong capacitive current compared to the faradic one, which is consistent with the assumed structure of the thin film, made of a mixture of electroactive (*E-Probe*) and electroinactive (*DCF-Probe*) moieties. For this reason, rather than using cyclic voltammetry for the electrochemical characterization of the

modified electrodes, we used square wave voltammetry to suppress non-faradic background current.

As shown on Fig. 3, the formation of the Ab_{DCF}/*DCF-Probe* immunocomplex causes the current to decrease significantly (curves d and e, compared to curve a, show a current drop up to 60%), whereas it is stable upon addition of Ab_{Ket} and Ab_{BPA} (less than 10 % current decrease, curves b,c). This demonstrates the specificity of the antibody immobilization on the *DCF-Probe/E-Probe*/GC electrode. For the following, we selected an antibody concentration of 5×10^{-7} M, for which the SWV peak current decreased moderately upon binding, of approximately the same value as for an antibody concentration of 5×10^{-7} M but without non-specific adsorption (addition of 5×10^{-7} M Ab_{BPA} or 5×10^{-7} M Ab_{Ket} did not produce any measurable change of the peak current compared to the *DCF-Probe/E- Probe*/GC electrode).

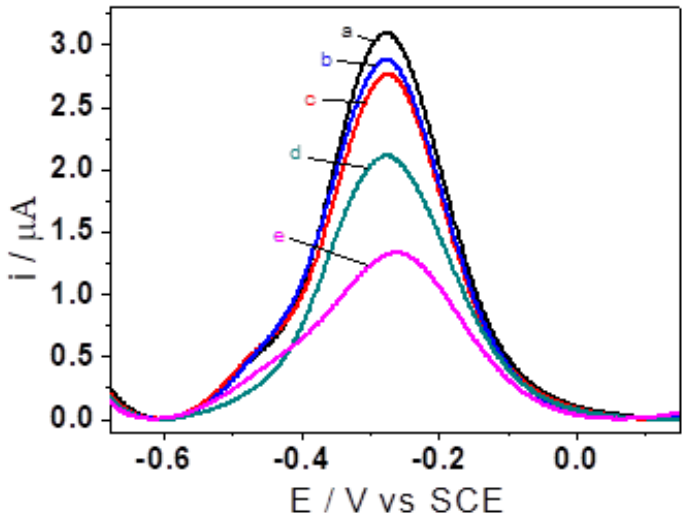

***Figure 3**: SWVs of **(a)** a DCF-Probe/E-Probe/GC electrode, **(b)** addition of 5×10^{-6} M Ab_{BPA}, **(c)** addition of 5×10^{-6} M Ab_{Ket}, **(d)** addition of 5×10^{-6} M Ab_{DCF} and **(e)** addition of 5×10^{-5} M Ab_{DCF}. SWV recorded in the oxidation direction from -0.55 V to + 0.05 V [1] in deaerated PBS. Area 0.07 cm^2.*

The anodic CV peak current of a *DCF-Probe*/*E-Probe*/GC electrode was plotted as a function of the square root of the scan rate ($v^{1/2}$, Fig. 4a) and as a function of the scan rate (v, Fig. 4b). A straight line was obtained as a function of v, which confirms that the electron transfer kinetics of the *DCF-Probe*/*E-Probe* layer behaves as a thin layer, i.e. is not limited by diffusion; this behavior is stable with time. Upon Ab_{DCF} immunobinding to this layer, the CV peak current of the Ab_{DCF} /*DCF-Probe*/*E-Probe*/GC electrode varies linearly as a function of $v^{1/2}$ (Fig. 4c,d**)**, indicating that mass transport becomes limiting. We performed a similar experiment with a non-specific antibody (Ab_{Ket}, a ketoprofen-specific antibody which presents no affinity for the *DCF-Probe*), which evidenced no current change. This tended to indicate that a partial desorption of the *E-Probe* is not responsible for the diffusion-limiting behavior. So, bound Ab_{DCF} seems to slow down ion exchange and consequently lowers the peak current. The principles that underpin transduction are therefore the following: *DCF-Probe* acts as a capture probe able to selectively interact with the binding site of the DCF-specific antibody (Ab_{DCF}). Ab_{DCF} being much bigger than *DCF-Probe* (the IgG antibody makes 150,000 g mol^{-1} and ca. 1000 nm^3, compared to 467 g mol^{-1} and ca. 0.5 nm^3 for *DCF-Probe*), it generates a strong steric hindrance on the electrode surface when coupled to *DCF-Probe*, which impedes mass transport, more particularly ions transport. Not only does the current peak depend on $v^{1/2}$, but it also decreases with the presence of the Ab on the film surface.

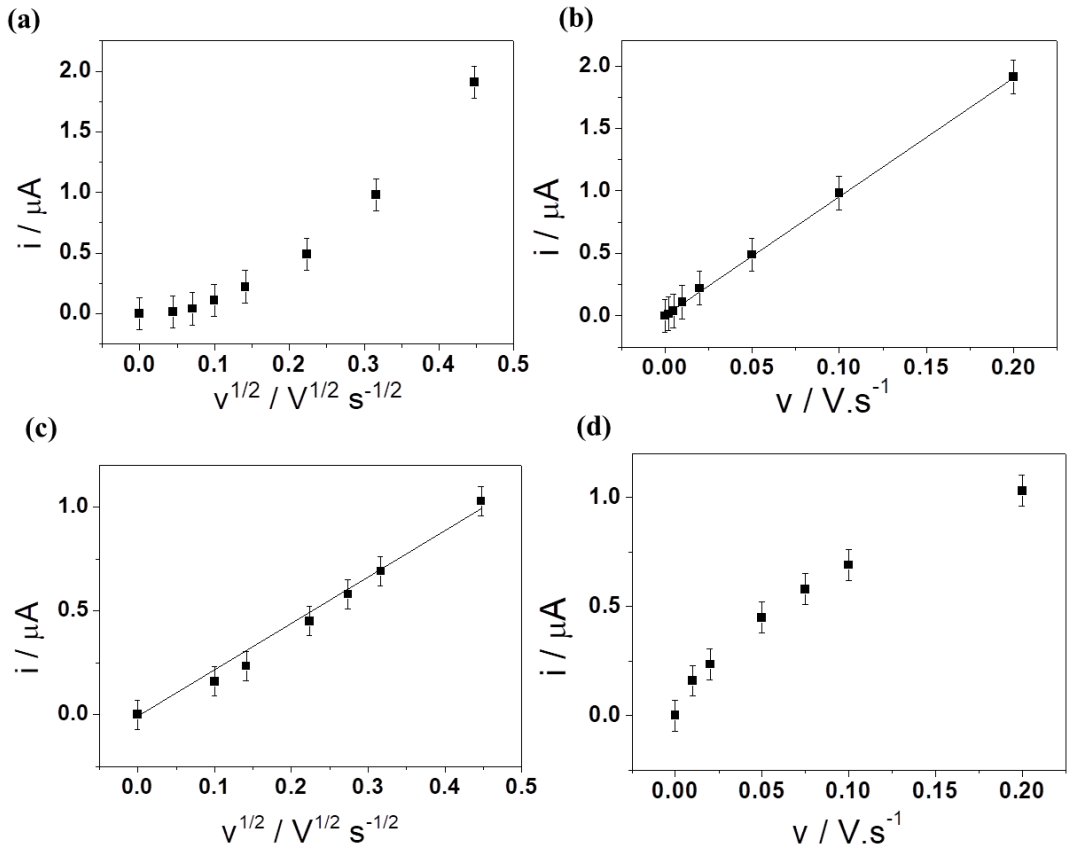

***Figure 4**: Anodic faradic peak currents (normalized) as a function of the square root of scan rate **(a,c)** and as a function of scan rate **(b,d)** extracted from CVs of a **(a,b)** DCF-Probe/E-Probe/GC and **(c,d)** Ab_{DCF}/DCF-Probe/E-Probe/GC electrodes in deaerated PBS. Scan rates from 2 to 200 mV s^{-1}. Area = 0.07 cm^2. Solutions deaerated with argon. Baselines were corrected from the capacitive currents. Currents are normalized relative to the current obtained at the fastest scan rate.*

To evaluate the affinity of Ab_{DCF} for the immobilized *DCF-Probe* compared to that for the unmodified DCF, competitive ELISA experiments were carried out (see the experimental section for details). As shown in Fig. SI4 (blue curve), the IC_{50} (defined as the DCF concentration added in solution for which half of the secondary antibody is removed from the surface) for the native diclofenac used with the commercial ELISA kit equals to ca. 10^{-5} M. Using the *DCF-Probe/E-Probe/*GC electrode, we found an IC_{50} of ca. 5.10^{-5} M (Fig. SI4, red

curve). This shows that Ab_{DCF} bound to the *DCF-Probe/E-Probe/*GC electrode can be removed from the surface by a displacement equilibrium with DCF added in solution.

Several control experiments were performed on the *DCF-Probe/E-Probe/GC* electrodes, detailed on Fig. SI5. A blank experiment (A) for which no DCF was added in solution, therefore no displacement occurred, was taken as reference for normalization of all the other absorbance measurements and two control samples (B) and (C) for which no secondary HRP-labeled antibody or no primary antibody Ab_{DCF} were added. The absorbance of (C) control samples was taken as background signal.

3.3. *Displacement experiments and optimization*

Because the redox activity of the *E-Probe* is strongly dependent on pH (it has been shown that peak potentials follow a -60 mV/ pH unit within 1≤ pH ≤10, as expected, but peak heights also depend on pH), we did not optimize the displacement assay regarding this parameter and we chose to work at fixed pH in phosphate buffer (PBS, pH 7.2). Conditions are given in Section 2.4.b. Fig. 5A shows the SWV peak related to the *E-Probe* electroactivity. As shown, binding of Ab_{DCF} on a *DCF-Probe/E-Probe/GC* electrode led to a current decrease attributed to the steric hindrance induced by the antibody (curve b compared to curve a). Upon incubation of the Ab_{DCF}*/DCF-Probe/E-Probe/GC* electrode in PBS containing 10 pM DCF, a given amount of Ab_{DCF} was removed, so that the steric hindrance decreased correspondingly and the SWV peak current increases (curve c). The higher availability of DCF in solution compared to the *DCF-Probe* immobilized on a surface explains this displacement equilibrium. This process is illustrated by Equation (1) below.

$$(Ab_{DCF} / DCF\text{-}Probe)_{surf} + DCF_{sol} \rightleftharpoons (Ab_{DCF} / DCF)_{sol} + DCF\text{-}Probe_{surf} \qquad \text{(Eq. 1)}$$

with DCF_{sol} the diclofenac in solution, *DCF-Probe*$_{surf}$ the *DCF-Probe* grafted on the electrode, $(Ab_{DCF}$ / *DCF-Probe*$)_{surf}$ the antibody/antigen complex immobilized on the surface, and $(Ab_{DCF}$ / *DCF*$)_{sol}$ the antibody/antigen complex in solution.

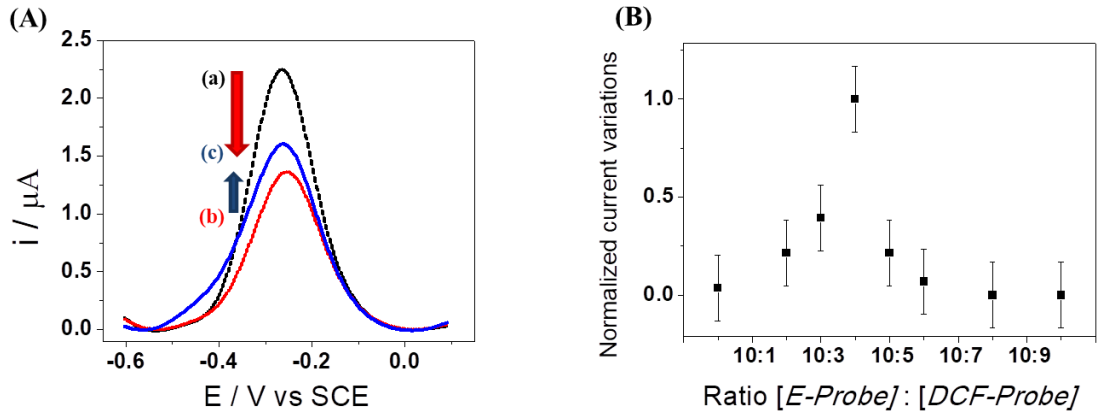

Figure 5. ***(A)*** *Square Wave Voltammograms corresponding to* ***(a)*** *a DCF-Probe/E-Probe/GC electrode,* ***(b)*** *after addition of* 5.10^{-7} *M* Ab_{DCF} *in PBS then* ***(c)*** *after incubation into PBS containing [DCF] = 10 pM.* ***(B)*** *SWV normalized peak current variation (difference of peak current before and after displacement, divided by the maximum current variation) as a function of [E-Probe]:[DCF-Probe] concentration ratio during electrografting. [E-Probe] was kept constant at 1 mM whereas [DCF-Probe] was varied between 0 and 1 mM.*

To optimize the detection sensitivity, the [*E-Probe*]:[*DCF-Probe*] concentration ratio during electrografting was varied between 10:0 (pure *E-Probe* film, no *DCF-Probe* added) and 10:10 (equimolar content of *E-Probe* and *DCF-Probe*). As shown on Fig. 5B, the current variation increases with the proportion of DCF-Probe up to a ratio of 10:4. According to the proposed transduction mechanism, such trend indicates that there is an intimate mixing of both *DCF-* and *E-probes* on the electrode surface, with little segregation of each probe into separate domains. Indeed, in the case of phase segregation of the two molecules inside the film, only the grain boundaries are effectively involved in the transduction process (Lang et al., 2015). The highest sensitivity was obtained for an *E-Probe* concentration of 1 mM and a

DCF-Probe concentration of 0.4 mM (ratio 10:4). For higher proportions of *DCF-Probe*, the current variations were lower. By plotting the absolute peak current as a function of the concentration ratio (see Fig. SI6) one observes that above the 10:4 ratio, the content of electroactive *E-Probe* tends rapidly to zero, which seems to indicate that *DCF-Probe* deposition is more efficient than that of *E-Probe*. We can then conclude that the behavior observed on Fig. 5B is the result of a trade-off between film electroactivity and *DCF-Probe* surface density.

3.4. Diclofenac detection

*Ab_{DCF}/DCF-Probe/E-Probe/*GC electrodes were dipped into DCF solutions (concentrations varying from 1 fM to 10 nM in PBS) for 1h at 37 °C, then rinsed three times with PBS and kept in PBS at 37°C for 30 min. CVs then SWVs were subsequently recorded and experiments were triplicated for each concentration.

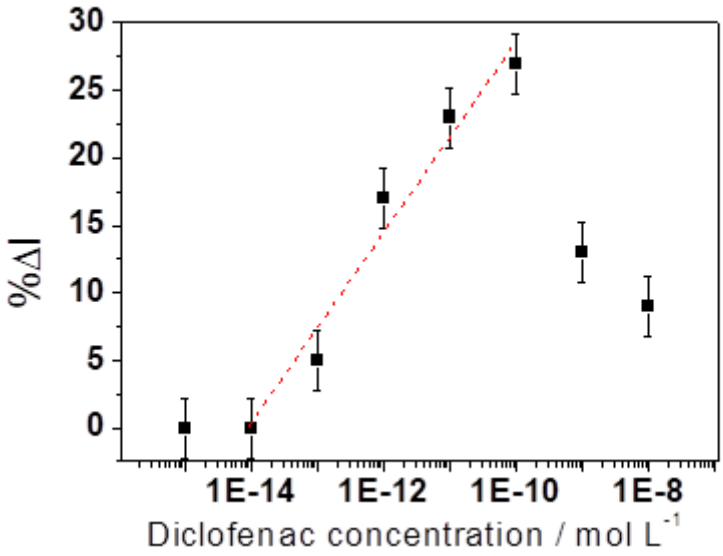

Figure 6. *Calibration curve corresponding to the relative current change percentage ($100 \times \Delta I/I_0$) measured at -0.45 V vs SCE, after addition of DCF, for concentrations from 10^{-15} M up to 10^{-8} M in PBS. $\Delta I = I_{after\ displacement} - I_{before\ displacement}$ and $I_0 = I_{before\ displacement}$.*

Fig. 6 displays an almost linear relationship between $\Delta I/I_0$ and log([DCF]) for DCF concentrations from 10^{-14} M to 10^{-10} M. The current increases to reach a maximum for [DCF] ~ 10^{-10} M. Considering a signal/noise ratio of 2, the detection limit is ca. 0.1 pM diclofenac. For higher DCF concentrations, the relative current variation decreases, which has been also observed in others of our works (Wang et al., 2014; Tran el al., 2012) dealing with bisphenol A and atrazine detection (on conducting polymer-modified electrodes), where this decrease was observed from concentrations above 10^{-8} M; we do not know yet clearly which phenomenon is responsible for this behavior. We did not investigate strategies to extend the linearity domain yet.

Also, to mimic real samples, we investigated the response of the sensor for tap water (pH 7.8) containing or not another organic pollutant (MCPA, 2-methyl-4-chlorophenoxyacetic acid, an herbicide structurally close to diclofenac) which could also be present in surface, ground or tap waters. As shown on Fig. SI7, curve e, 100 pM MCPA in tap water did not lead to a significant change in peak current of a Ab_{DCF}/*DCF-Probe/E-Probe*/GC electrode. On the contrary (curve g), the addition of 100 pM MCPA + 100 pM DCF in tap water led to a current increase equivalent to 100 pM DCF alone, which demonstrated that MCPA did not interfere; the corresponding current change was slightly lower than that occurring for 100 pM DCF in PBS.

In the same experiment, instead of adding DCF, we added quantity of Voltarene tablets (dissolved in tap water), a commercial DCF-containing drug. For a quantity of Voltarene equivalent to 93 pM, we obtained an excellent recovery of 103% (concentration found of 96 pM).

4. Conclusion

We demonstrated an innovative electrochemical displacement assay, based on an electrode modified with an electroactive probe and a specific capture probe, able to detect diclofenac from 0.1 pM to 0.1 nM (25 pg L^{-1} up to 25 ng L^{-1}). As a proof-of-concept, a commercial diclofenac-containing drug was detected in tap water. Its performances were very competitive compared to other electrochemical diclofenac immunosensors already published in the literature (see Table 1), which paves the way for detection in real-samples such as tap water or surface waters where concentrations are from a few tens of pg L^{-1} (a few hundreds of fM) to several tens of ng L^{-1} (a few hundreds of pM) depending on the exposure (Word Health Organization, 2011), or even sewage where the average diclofenac concentration is ca. 400 ng L^{-1} (a few nM). For this, the stability of the sensor will have to be investigated in more aggressive media and over long periods of time.

Acknowledgment

T.T.K. Nguyen thanks the University of Science and Technology of Hanoi (USTH) for providing a PhD grant. H.V. Tran thanks University Paris Diderot for a research stay at ITODYS.

References

Aldekoa, J., Medici, C., Osorio, V., Pérez, S., Marcé, R., Barceló, D., Francés, F., 2013, J. Hazard. Mater. 263, 207-213.

Chmielewska, A., Konieczna, L., Plenis, A., Bieniecki, M., Lamparczyk, H., 2006, Biomed. Chromatogr. 20, 119-124.

Cunha, R.R., Gimenes, D.T., Munoz, R.A., do Lago, C.L., Richter, E.M., 2013, Electrophoresis 34, 1423-1428.

Damiri, S., Oskoei, Y.M., Fouladgar, M., 2016, J. Experiment. Nanosci, 1-18.

Delamar, M., Hitmi, R., Pinson, J., Saveant, J. M., 1992, J. Am. Chem. Soc. 114, 5883-5884.

Derikvand, H., Roushani, M., Abbasi, A. R., Derikvand, Z., Azadbakht, A., 2016, Anal. Biochem. 513, 77-86.

Gimenes, D.T., Cunha, R.R., de Carvalho Ribeiro, M.M.A., Pereira, P.F., Muñoz, R.A.A., Richter, E.M., 2013, Talanta, 116, 1026-1032.

Hai, L.V., Reisberg, S., Chevillot-Biraud, A., Noel, V., Pham, M.C., Piro, B., 2014, Electrochim. Acta 140, 49-58.

Hlaváček A., Farka Z., Hübner M., Horňáková V., Němeček D., Niessner R., Skládal P., Knopp D., Gorris H.H., 2016, Anal. Chem. 11, 6011-6017.

Huebner, M., Weber, E., Niessner, R., Boujday, S., Knopp, D., 2015, Anal. Bioanal. Chem. 407, 8873−8882.

Jin, W., Zhang, J., 2000, J. Chromatogr. A, 868, 101-107.

Kashefi-Kheyrabadi, L., Mehrgardi, M. A., 2012, Biosens. Bioelectron. 33, 184-189.

Karuppiah, C., Cheemalapati, S., Chen, S.M., Palanisamy, S., 2015, Ionics 21, 231-238.

Lang, P., Qin, Z., Noel, V., Seydou, M., Battaglini, N., Zrig, S., Anquetin, G., Maurel, F., Piro, B., Pham, M.C., 2015, *J. Phys. Chem. C*, *119*, 29015-29026.

March, G., Reisberg, S., Piro, B., Pham, M.C., Fave, C., Noel, V., 2010, Anal. Chem., 82, 3523–3530.

Oliveira, M.C., Bindewald, E.H., Marcolino, L.H., Bergamini, M.F., 2014, J. Electroanal. Chem. 732, 11-16.

Petrovic, M., Hernando, M.D., Diaz-Cruz, M.S., Barcelo, D.J., 2005, Chromatogr. A, 1067, 1−14.

Piro, B., Reisberg, S., Noel, V., Pham, M.C., 2007, Biosens. Bioelectron. 22, 3126-3131.

Sacher, F., Lange, F.T., Brauch, H.J., Blankenhorn, I. J., 2001, Chromatogr. A, 938, 199−210.

Sarhangzadeh, S., Khatami, A.A., Jabbari, M., Bahari, S., 2013, J. Appl. Electrochem, 43, 1217–1224

Thiagarajan, S., Rajkumar, M., Chen, S.M., 2012, Int. J. Electrochem. Sci, 7, 2109-2122.

Tran, H.V., Reisberg, S., Piro, B., Nguyen, T.D., Pham, M.C., 2013, Electroanal. 25, 664-670.

Tran, H.V., Yougnia, R., Reisberg, S., Piro, B., Serradji, N., Nguyen, T.D., Tran, L.D., Dong, C.Z., Pham, M.C., 2012, Biosens. Bioelectron. 31, 62-68.

Wang, X., Reisberg, S., Serradji, N., Anquetin, G., Pham, M.C., Wu, W., Dong, C.Z., Piro, B., 2014, Biosens. Bioelectron. 53, 214-219.

Word Health Organization, 2011; Ref. WHO/HSE/WSH/11.05.

Zecca, L., Ferrario, P., Costi, P., 1991, J. Chromatogr. B: Biomed. Sci. Appl., 567, 425-432

Supplementary Materials

1. Synthesis of E-Probe

Synthesis of the *E-Probe* (2-[(4-aminophenyl)sulfanyl]-8-hydroxy-1,4-naphthoquinone) was performed as follows.

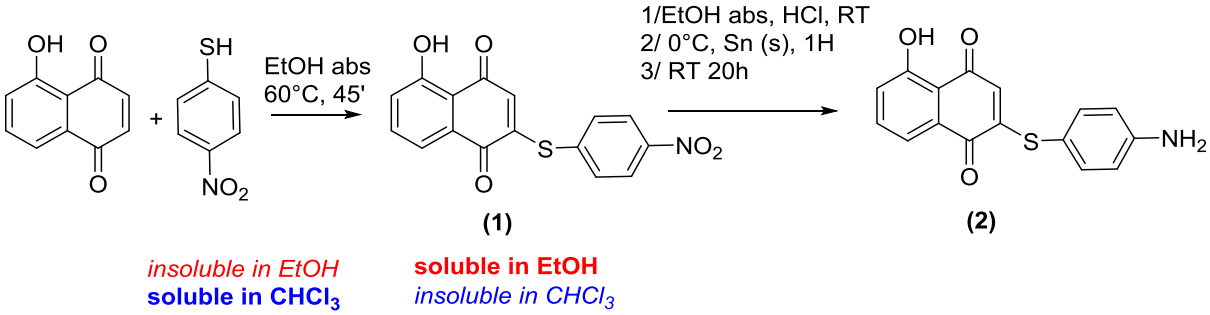

Figure SI1.

Synthesis of 5-hydroxy-2-((4-nitrophenyl)thio)naphthalene-1,4-dione (1)

To 10mL of absolute ethanol in a 50 mL round-bottom flask previously heated to 60°C were added 570mg (2.94 mmol) of *p*-nitrothiophenol (80% purity, techn.) and 400 mg (2.30mmol) of 5-hydroxynaphtoquinone. This solution was stirred 45' at 60°C then put into the freezer for 3h; *p*-nitrothiophenol was not soluble in EtOH and was then filtered out. The solids were washed with cold EtOH. The dark orange filtrate was evaporated under vacuum. Cold chloroform was introduced into the flask to wash the dark orange solid which was filtered. After several washings with cold chloroform, 5-hydroxy-2-((4-nitrophenyl)thio)naphthalene-1,4-dione was obtained as a dark orange solid (690mg, 92%).

Synthesis of 2-((4-aminophenyl)thio)-5-hydroxynaphthalene-1,4-dione (2) (*E-Probe*)

Compound (1) (360 mg, 1.1 mmol) was dissolved in absolute ethanol (10 mL). The reaction mixture was cooled to 0 °C using an ice bath. Tin powder (1.3g, 11 mmol, CAS number: 7440-31-5) was added in one portion. Concentrated HCl (10 mL) was added dropwise, and then the mixture was stirred for 1 h at 55 °C and 20 h at room temperature. The yellow solution was filtered and extracted with ethyl acetate (40mL) and 4 M NaOH (around 150mL, until the pH reached 8-9, the solution became violet). Extraction repeated several times with

water. The organic solution was washed with brine and then dried over $MgSO_4$. All the volatile materials were removed under vacuum. The desired product was obtained as a brown solid in 63% yield.

2. Synthesis of DCF-Probe

This synthesis is given in the main text (Section 2.3.2).

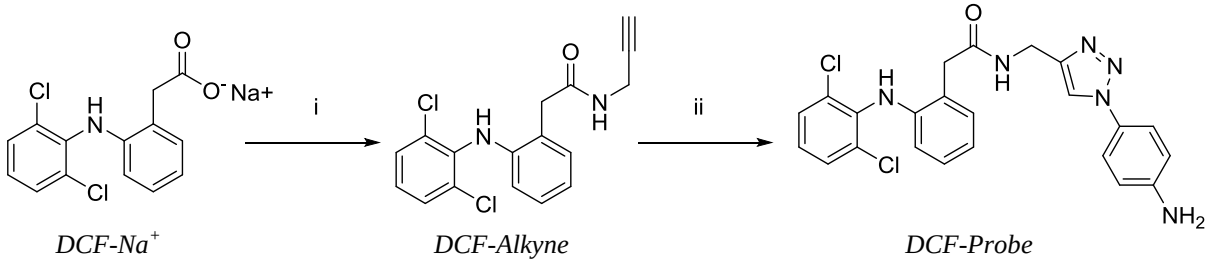

DCF-Na$^+$ *DCF-Alkyne* *DCF-Probe*

Figure SI2. *Synthesis route for DCF-Probe, N-((1-(4-aminophenyl)-1H-1,2,3-triazol-4-yl)methyl)-2-(2-((2,6-dichlorophenyl)amino)phenyl)acetamide. i) DMF, HATU, DIPEA, propargylamine, 50°C, 15h, 75%; ii) DCM/H_2O: 1/1, $CuSO_4$, L-ascorbate, 4-azidoaniline, 24h, 77%.*

3. Electrografting

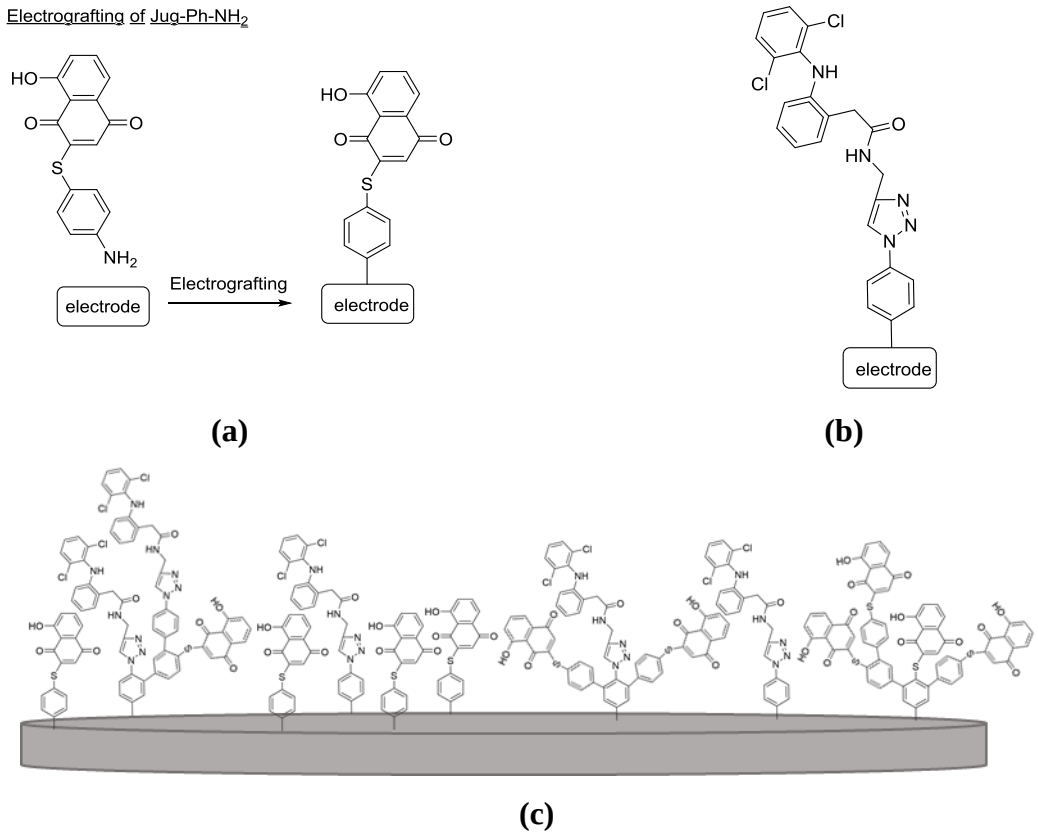

Figure SI3. *Principle of electrografting of* ***(a)*** *the redox probe E-Probe and* ***(b)*** *the molecular probes DCF-Probe on glassy carbon (GC) electrodes. In-situ formation of the corresponding diazonium salts is not shown in this figure.* ***(c)*** *Possible grafting route.*

4. Electroactivity and optimization

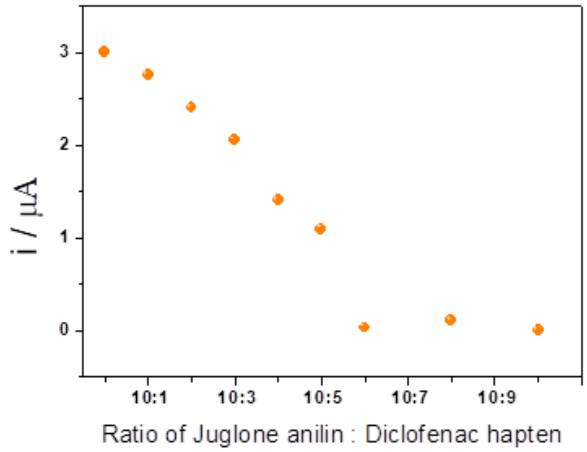

Figure SI4. *SWV peak currents of a Ab/DCF-Probe/E-Probe/GC electrode for various ratio of E-Probe:DCF-Probe during electrografting. [E-Probe] kept constant at 1 mM and [DCF-Probe] varied between 0 and 1 mM.*

5. ELISA experiments

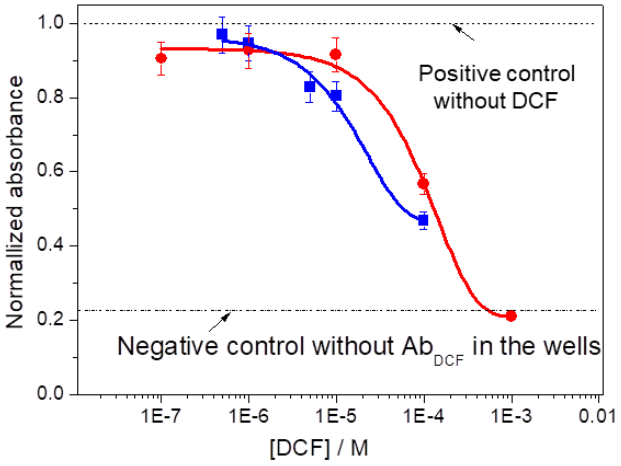

Figure SI5. *Results of competitive ELISA experiments on the kit wells (blue squares ■) and on the electrode (red plain circles ●). Experiments were performed as detailed in the Experimental section. DCF was added in the wells at various concentrations. A sample where no primary Ab_{DCF} was present on the surface of the well was taken as negative control (top dotted line). The positive control (bottom dotted line) corresponds to no DCF added in solution. All absorbance values were normalized relative to this positive control.*

6. Control ELISA experiments

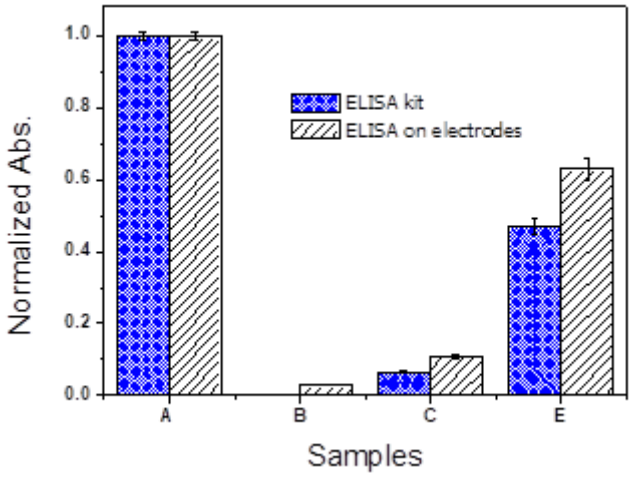

Figure SI6. *Normalized absorbencies from ELISA tests:* ***A****. blank sample (Ab_{DCF} + secondary HRP-coupled Ab, no DCF added in solution);* ***B****. Control sample #1(Ab_{DCF} + 10^{-4} M DCF, no secondary HRP-coupled Ab);* ***C****. Control sample #2 (no Ab_{DCF}, secondary HRP-coupled Ab + 10^{-4} M DCF);* ***D****. Sample (Ab_{DCF} + secondary HRP-coupled Ab + 10^{-4} M DCF). For all experiments: [Ab_{DCF}] = 10^{-8} M in all experiments.*

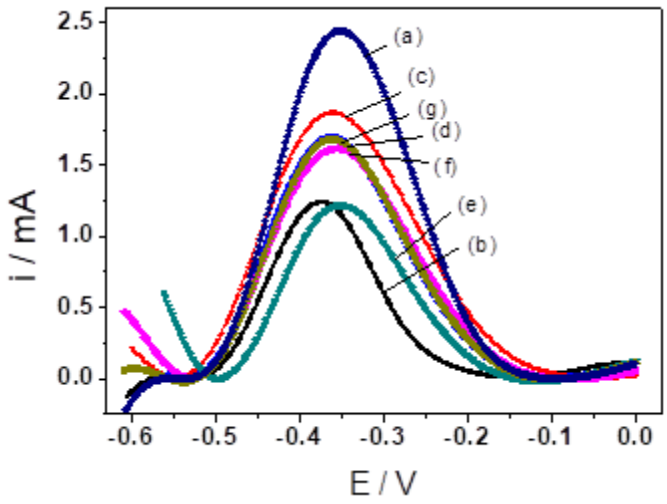

Figure SI7. *Square Wave Voltammograms corresponding to* ***(a)*** *a DCF-Probe/E-Probe/GC electrode,* ***(b)*** *after addition of 5.10^{-7} M Ab_{DCF} ;* ***(c)*** *after incubation into distillated water containing [DCF] = 100 pM ;* ***(d)*** *after incubation into tap water containing [DCF] = 100 pM ;* ***(e)*** *after incubation into distillated water containing [MCPA] = 100 pM ;* ***(f)*** *after incubation into distillated water containing Voltarene for an equivalent concentration of 93.1 pM diclofenac ;* ***(g)*** *after incubation into tap water containing [DCF] = 100 pM and [MCPA] = 100 pM.*

Chapter III GATE FUNCTIONALIZATION OF ELECTROLYTE-GATED ORGANIC FIELD-EFFECT TRANSISTOR USING DIAZONIUM CHEMISTRY: APPLICATION TO BIODETECTION OF 2,4-DICHLOROPHENOXYACETIC ACID (2,4-D)

1 Introduction

World population development requires a more intensive agriculture, in particular the use of herbicides and pesticides. Consequently, large amounts of pollutants are released into the environment all over the World. 2,4-D is a popular herbicide employed to control broad leave in agriculture. This compound presents a serious harm, however. For example, as soon as in 1996, the National Institute for Occupational Safety and Health (NIOSH, USA) reported that in-situ working with high concentrations of 2,4-D for prolonged contact time can lead men to face up with fertility problems.

Table III-1. General information of 2,4-D

Structure, formula, CAS No. and molecular weight	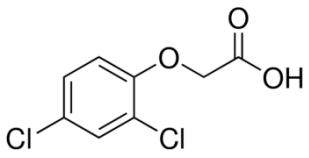 $C_8H_6Cl_2O_3$ CAS 94-75-7 221.04 g mol^{-1}
Solubility in water	890 mg L^{-1}
Usage	Weed killers in agriculture

2 Interest to detect 2,4-D and existing procedures and devices

Several methods have been developed to quantify and eliminate 2,4-D. Except for classical analytical methods (obviously highly sensitive and efficient, such as GC-MS [(1)] and HPLC [(2)], the first method reported to detect 2,4-D was ELISA. In 1994, Fránek *et al*. used ELISA to detect 2,4-D with a sensitivity of 0.7 ng mL^{-1} [(3)]. In 2008, Kaur *et al*. employed microtiter plates to determine 2,4-D by ELISA with a limit of detection (LoD) of 0.7 ng mL^{-1} [(4)]. A way to provide high sensitivity and low LoD to electrochemical immunosensor is to adapt the ELISA scheme to the electrochemical transduction. Kalab *et al*., in 1994, described a screen-printed gold electrode, silanized by APTES, onto which 2,4-D was bound. The assay was based on a competitive format in presence of free 2,4-D and free enzyme-labelled antibody (monoclonal anti-2,4-D antibody-peroxidase conjugate) [(5)]. They obtained a detection limit of 0.1 µg L^{-1} of 2,4-D. Similar results were reported by Skladal *et al*., with the same figures of merit [(6)] and Wilmer *et al.* [(7)], or Bauer *et al.* [(8)], who used alkaline phosphatase (AP) as enzyme label. They also reported a LoD of 0.1 µg L^{-1} [(8)]. The improvement of LoD was achieved by Dequaire *et al*. in 1999, [(9)] who reached a LoD of 0.01 µg L^{-1}. They used magnetic beads (MBs) to have a better collection of the target and amplify the response (Figure III.1).

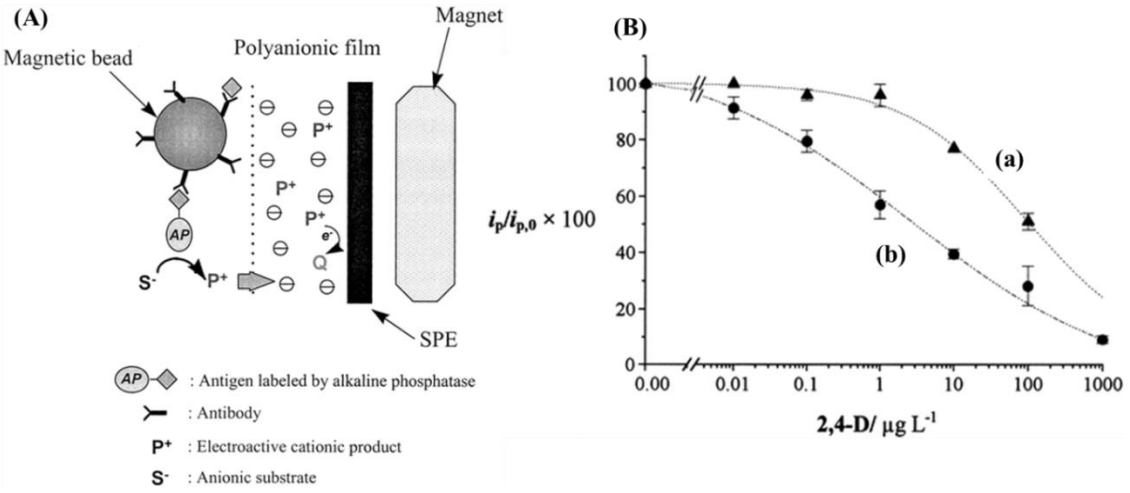

Figure III.1. The magnetic electrochemical immunosensor for 2,4-D detection: (A) Schematic representation of the key step of (B) Calibration curve of 2,4-D obtained for (a) 50 and (b) 15 µL of Ab-MBs stock solution incubated for 40 min at room temperature (total assay volume of 250 µL). $i_{p,o}$ corresponds to the peak current value obtained in the absence of 2,4-D. Methylene blue was used as mediator [(9)].

Acetylcholinesterase was also used, instead of AP, by Kalab *et al*. in 1996 [(5)]. The amperometrical signal was obtained in the presence of acetylthiocholine substrate and 2,4-D conjugated to acetylchoninesterase. This sensor could detect less than 0.01 µg L^{-1} of 2,4-D.

Still within electrochemical transductions, electrochemical impedance spectroscopy was also applied, for example by Navratilova, in 2003 [(10)] for 2,4-D detection. The procedure was quite simple. Anti 2,4-D antibodies were immobilized onto gold electrodes and the impedance monitored as a function of 2,4-D concentration in the medium. The changes of interfacial characters modulated the electrochemical impedance signals. The signal was linear between 45 nmol L^{-1} and 0.45 mmol L^{-1}.

Besides electrochemical sensors, other transductions were also reported, such as piezoelectric or optical (in particular, surface plasmon resonance, SPR). In 1997, Horacek *et al*. reported a competitive immunoassay using gold-coated quartz vibrators. However, the limit of detection was low, 0.24 ng mL^{-1} [(11)]. In 2001, Halamek *et al*. obtained similar results, with a LoD of 5 ng mL^{-1} [(12)]. Instead of a piezoelectric transduction, Gobi *et al*. used plasmon resonance (SPR) imaging to detect 2,4-D with the same procedure than Halamek [(13)]. The linear range was 0.5 - 1000 ng mL^{-1} (Figures III.2 and III.3).

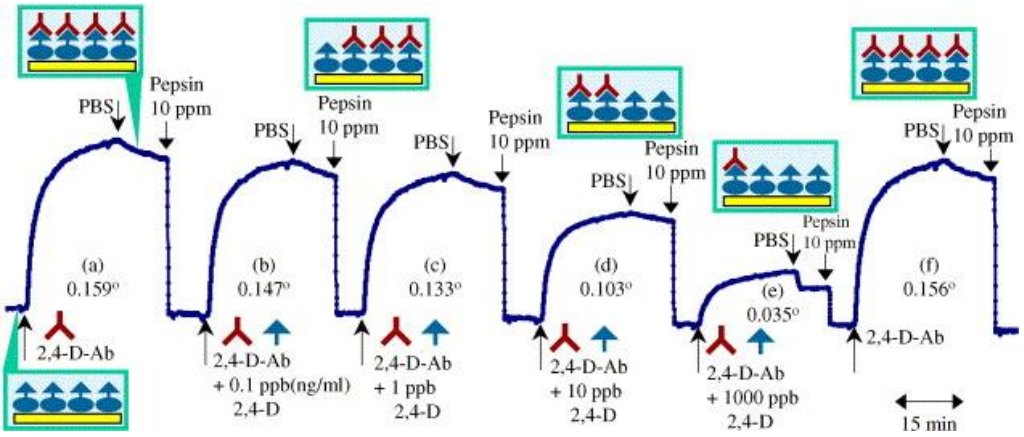

Figure III.2. SPR sensorgram observed under a flow of 2,4-D-Ab solutions of fixed concentration (20 ppm) over the 2,4-D-BSA immobilized sensor chip, in the absence and presence of 2,4-D at various concentrations: 0.1, 1, 10 and 1000 ppb [(14)].

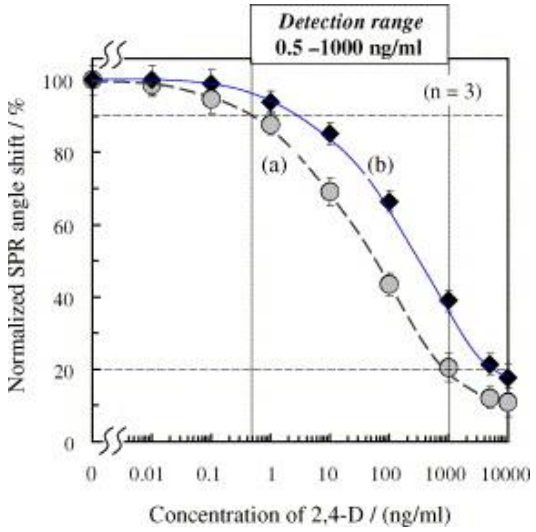

Figure III.3. Variation of normalized SPR angle shift with the concentration of 2,4-D in the competitive immunosensing experiments described in Fig. III.2 and the related text. Two different concentrations, 20 ppm (a) and 40 ppm (b), were used for the amount of antibody, 2,4-D-Ab [14].

More recently, nanoparticles were used to improve sensitivity, such as gold nanoparticles [15], TiO_2 nanotubes [16], or quantum dot [17, 18]. In 2011, Boro *et al*. reached a LoD of 3 ng mL^{-1} using a AuNP-catalyzed chemiluminescence immunoassay [15]. 2,4-D-BSA conjugate was immobilized on microtiter plates, then 2,4-D antibody-conjugated luminol, silver nitrate, gold nanoparticles and free 2,4-D were added to the wells and the competitive assay performed. The luminescence signals were measured at 425 nm (mechanism illustrated on Figure III.4).

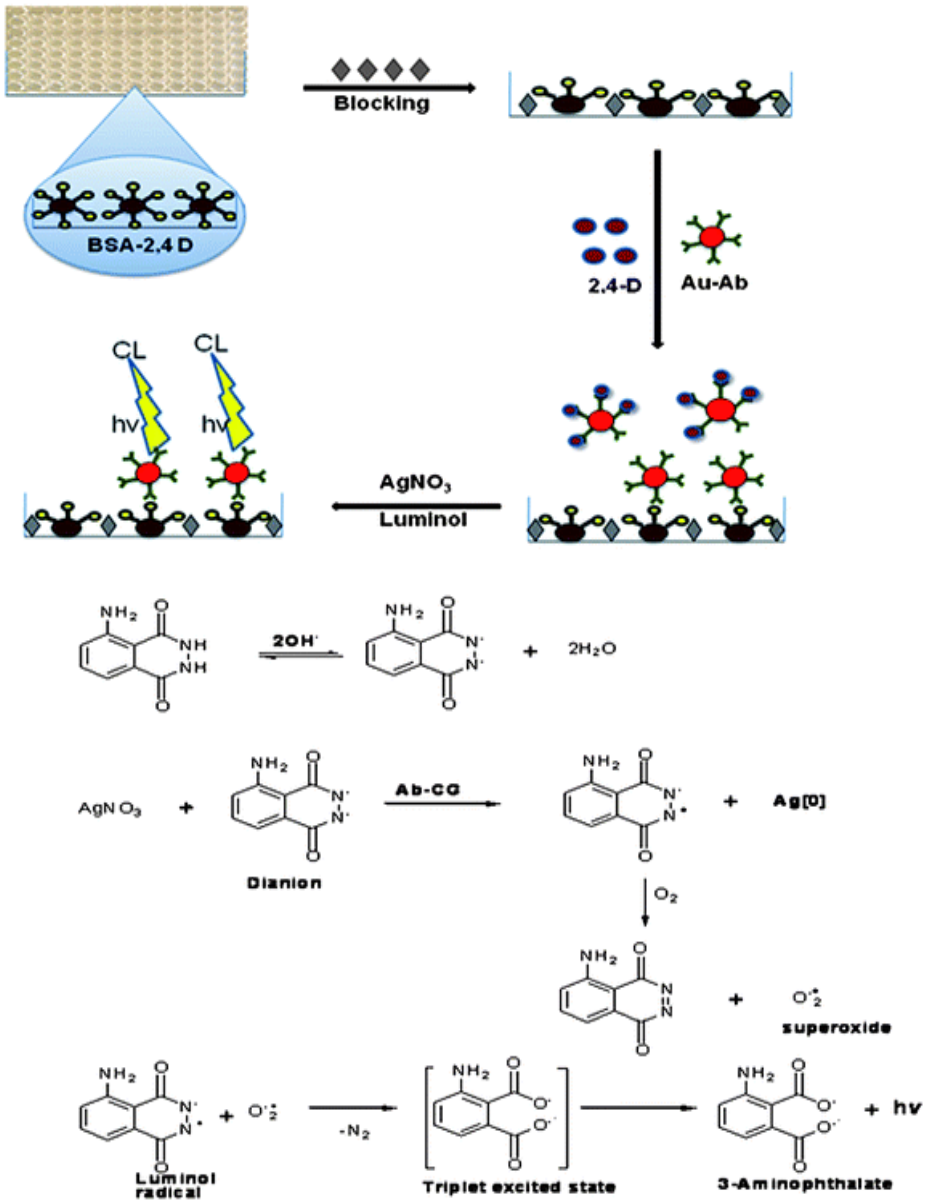

Figure III.4. Gold nanoparticle-catalysed chemiluminescence reaction mechanism showing the catalytic properties of gold nanoparticles in the luminol-silver nitrate system (top); schematic presentation of gold nanoparticle based CL (bottom) [(15)]***.***

Shi *et al*. also reported the used of NPs in 2011 [(16)]. They applied molecularly imprinted polymer-modified TiO_2 nanotubes, which played the role of photochemical catalyst (Figures III.5 and III.6).

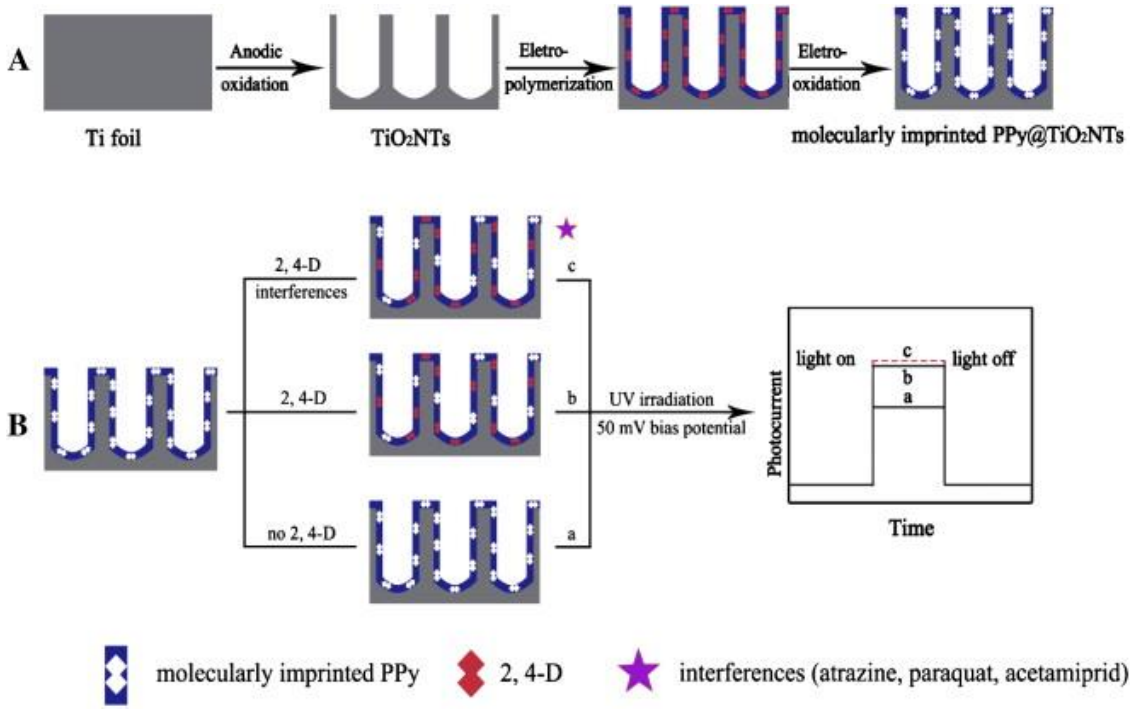

Figure III.5. Schematic illustration for (A) fabrication and (B) detection mechanism of the photoelectrochemical sensor [(16)]***.***

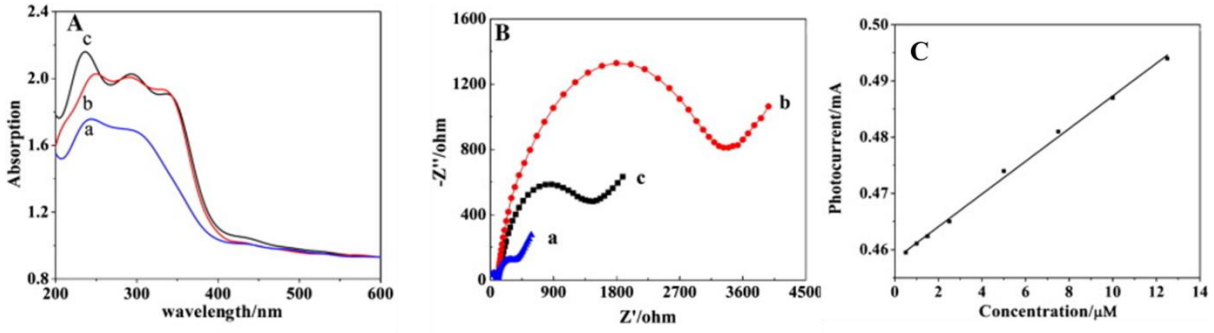

Figure III.6. Photoelectrochemical sensor characteristics: (A) UV-vis spectroscopy of diffuse reflectance (UV-vis DRS) characterization of (a) TiO_2 NTs, (b) molecularly imprinted PPy@TiO_2 NTs, and (c) non-imprinted PPy@TiO_2 NTs (B) AC impedance spectra of (a) TiO_2 NTs, (b) molecularly imprinted PPy@TiO_2 NTs before and (c) after removal of 2,4-D in 0.1 M KCl solution containing 5 mM $Fe(CN)_6^{4-/3-}$. (C) Linear calibration curve. All photocurrents were recorded in 0.1 M PBS (pH = 7) after the electrodes were incubated in the 2,4-D solution for 15 min [(16)]***.***

To conclude, all methods mentioned above are sensitive and efficient to detect 2,4-D. The most frequently reported mechanism is the competitive assay format which requires complex enzyme-labelled compounds, however, and also needs the support of nanomaterials.

Most importantly, these researches have shown that immunosensing is able to change the surface capacitance of the sensing electrode. From this finding, I proposed to take profit of a capacitance-coupled electronic device, namely the electrolyte-gated organic field effect transistor (EGOFET) to detect these capacitance changes, and apply it to immunodetect 2,4-D with a limit of detection and for an operating voltage as low as possible.

Electrolyte-Gated Organic Field Effect Transistors (EGOFETs), also named Liquid-Gated FETs (LG-FETs), are very promising sensing devices; I already presented them in Chapter I. They are thin-film transistors (TFTs) where the non-electronically conducting material in-between the gate and the semiconductor, instead of being a dielectric polymer, is an electrolyte. The electrochemical transistor of Taniguchi and Kawai [(19)], in 2004 was all solid state; it used cyanoethylpullulan as solid electrolyte. Panzer and Frisbie [(20)] used a polymer electrolyte as the gate dielectric in their research in 2006. Kergoat *et al.*, in 2010, have shown that it can even be deionized water or aqueous biological buffers [(21)]. If we apply on EGOFETs the well-known equation of the quadratic model describing the behavior of classical FETs and OFETs (Equation III-1), every parameter is defined in a similar way than for classical FETs but the capacitance corresponds in this case not to the oxide capacitance but to the electrolyte capacitance, i.e. the reciprocal sum of the capacitances of the gate/electrolyte and electrolyte/semiconductor interfaces.

$$I_D = \mu \frac{W}{2L} C_{eff}(V_{GS} - V_{Th})^2 \qquad \text{and } I_D = I_{D,Sat} \text{ for } |V_{DS}| > |V_{GS} - V_{Th}|$$

Equation III-1

with I_D the drain current, W and L the channel width and length, respectively, V_{GS} the voltage difference between the gate electrode (V_G) and the source electrode (V_S-which is generally grounded), V_{Th} the threshold voltage, μ the mobility of the charge carriers and C_{eff} the overall interfacial effective capacitance. $I_{D,Sat}$ is the drain current at saturation when V_{DS} (difference between the drain and source voltages V_D-V_S) is large before V_{GS}-V_{Th}.

Most EGOFETs use p-type semiconductors. Under operation, the gate electrode is negatively polarized as well as the drain electrode, while the source is grounded. This polarization means that mobile charges in the electrolyte (ions) accumulate at the gate/electrolyte and semiconductor/electrolyte interfaces, in the form of two electrical double layer (EDL) of opposite charge, positive at the gate surface and negative at the semiconductor surface. Mirror positive charges (holes) then accumulate within the OSC, forming the conductive channel. As explained above, the density of charge carriers in the channel is directly dependent on the gate potential or, more precisely, on the density of charge at the respective interfaces. For a water/gold interface, for example, the capacitance is of several tens of μF cm^{-2}, i.e. hundred times more than that of a classical dielectric/semiconductor interface. Consequently, instead of the tens of volts that are necessary for operating classical dielectric-based OFETs, EGOFETs can be operated at hundred times lower voltages, i.e. a few hundreds of mV [(22)].

Since the first description of EGOFETs operating in water [(23)], EGOFET-based biosensors have been developing fast. Because EGOFETs are not only sensitive to changes at the semiconductor/electrolyte interface, but also to changes at the electrolyte/gate interface, there are two different approaches to biofunctionalize EGOFETs: at the semiconductor/electrolyte interface, or at the gate/electrolyte interface.

There are some examples mentioning the biofunctionalization of semiconductor/electrolyte interface. Cotrone *et al.*, in 2012, spin-coated phosphatidylchonine (PL) directly onto the P3HT interface which distributed on the OFET surface by spin coating, so that the lipid film was generated [(24)]. Due to an amphiphilic character, these lipid molecules could self-assemble spontaneously between bilayers in order to form vesicles in water. The PL/P3HT/OFET performed well in terms of electrical characteristics. The field-effect mobility was 6.4×10^{-3} $cm^2 V^{-1} s^{-1}$ (compared to P3HT/OFET, of 10^{-4} $cm^2 V^{-1} s^{-1}$) at faster sweeping rate and 10^{-3} $cm^2 V^{-1} s^{-1}$ at lower sweeping rate. The on/off ratio was 10^3, much higher than P3HT/OFET without PL.

Kergoat *et al.*, in 2012, reported a DNA EGOFET sensor which operated at very low voltages (below 1 V) [(22)]. A P3HT bearing carboxylic acid moieties was used to perform covalent ODN (oligonucleotide) grafting, providing that they were modified at one end with a COOH group. Changes in the output characteristics of the device were observed upon DNA immobilization and after DNA hybridization, more precisely a shift of the threshold voltage

of 40 to 60 mV for 100 nM target DNA. This shift towards negative values was attributed to the negative charge of the DNA backbone. The off current was also modified and decreased after DNA immobilization. This behavior was attributed to an electrostatic effect. However, other experiments obtained with various ionic strengths pointed out the importance of the Debye length that can screen negative DNA charges.

The work of Suspène *et al.*, in 2013, is another example of the possibility to functionalize organic semiconductors in water-gated organic field-effect transistors [(25)]. The semiconductor was a copolymer of P3HT and P3HT-biotin (P3HT onto which biotin was grafted). With a charge carrier mobility of up to 7×10^{-3} cm^2 V^{-1} s^{-1}, a threshold voltages of around -0.1 V, and an on/off ratio of around 500, this functionalized semiconductor displayed figures of merit close to that of pure P3HT (Figure III.7), which demonstrated the possibility to functionalize organic semiconductors in EGOFETs. This EGOFET based on P3HT-biotin was able to sense efficiently streptavidin and avidin.

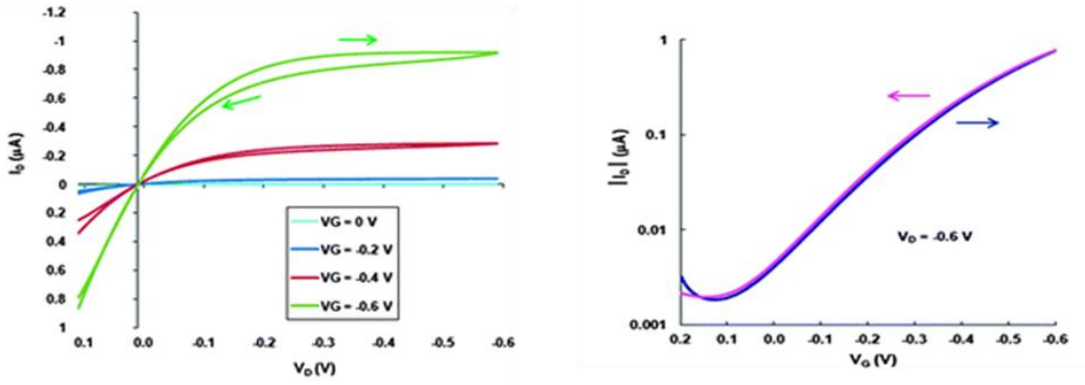

Figure III.7. Output curves (left) and transfer curves (right) for a water-gated OFET based on P3HT-biotin [(25)].

Magliulo *et al.*, in 2016, also reported functionalization of the semiconductor in an EGOFET, to determine the C-reactive protein (CRP) [(27)]. The procedure was quite simple: anti-CRP monoclonal antibodies, were physically adsorbed onto the P3HT surface. The efficiency of this functionalization was proved using surface plasmon resonance (SPR) (Figure III.8).

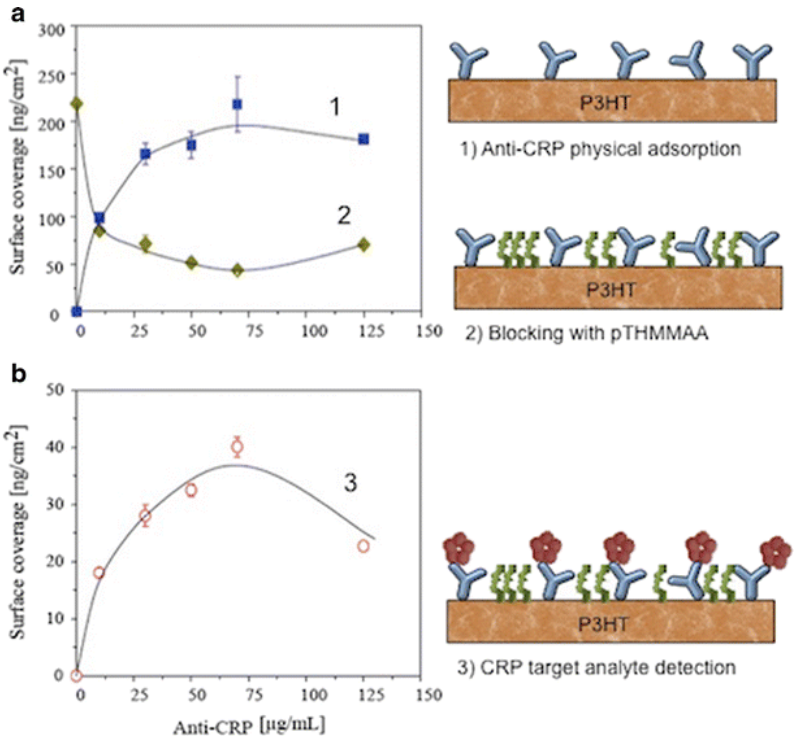

Figure III.8. EGOFET to determine the C-reactive protein: SPR measurements of (a) the amount of the antibodies physisorbed on P3HT layer for different anti-CRP concentrations is reported (blue squares) along with the measured quantity of the pTHMMAA polymer adsorbed on P3HT upon binding of the anti-CRP (green diamonds). (b) Amount of the CRP protein captured by the anti-CRP layer deposited on the P3HT surface at different concentrations [(27)].

Piro *et al.*, in 2017, gave another example of semiconductor funtionalization, to detect bisphenol A (BPA) [(28)]. 4-(2-(4-(hexyloxy)phenyl)propan-2-yl)phenol (a BPA molecule modified with a side alkyl chain, ^{alk}BPA) was mixed to pBTTT (the semiconductor) at a weight ratio of 10%; the resulting semiconductor not only kept its semiconducting properties but the mobility as well as the stability increased. It was shown that, upon interaction of antiBPA with the semiconductor, it led to changes in drain current as well as in threshold voltage shift (Figure III.9).

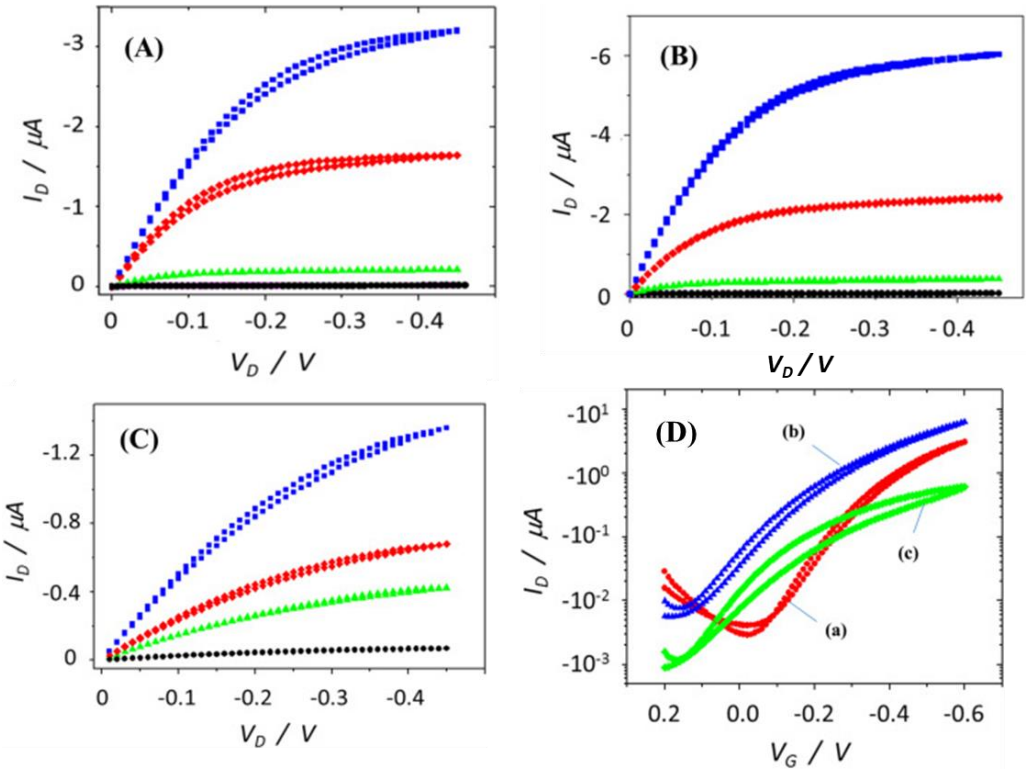

Figure III.9. Detection of bisphenol A via an EGOFET device: Output curves of (A) pBTTT, (B) ^{alk}BPA: pBTTT and (C) ^{alk}BPA: pBTTT after 2 h incubation in a Ab_{BPA} solution. The drain voltage was swept at 170 mV s^{-1}. L=10 µm; W=10 mm in PBS. (D) Transfer curves of (a) pure pBTTT, and ^{alk}BPA: pBTTT EGOFET (b) before and (c) after Ab_{BPA} binding for V_D =−0.45 V [28].

In the other hand, there are few works on the biofunctionalization of the gate/electrolyte interface. Casalini *et al.*, in 2012, was one of the first who utilized gate functionalization of an EGOFET in order to sense dopamine [29]. The gate interface was modified by self-assembly of a mixed monolayer of cysteamine (CA) and 4-formylphenyl boronic acid (BA). The drain current changed as a function of the dopamine concentration (Figure III.10).

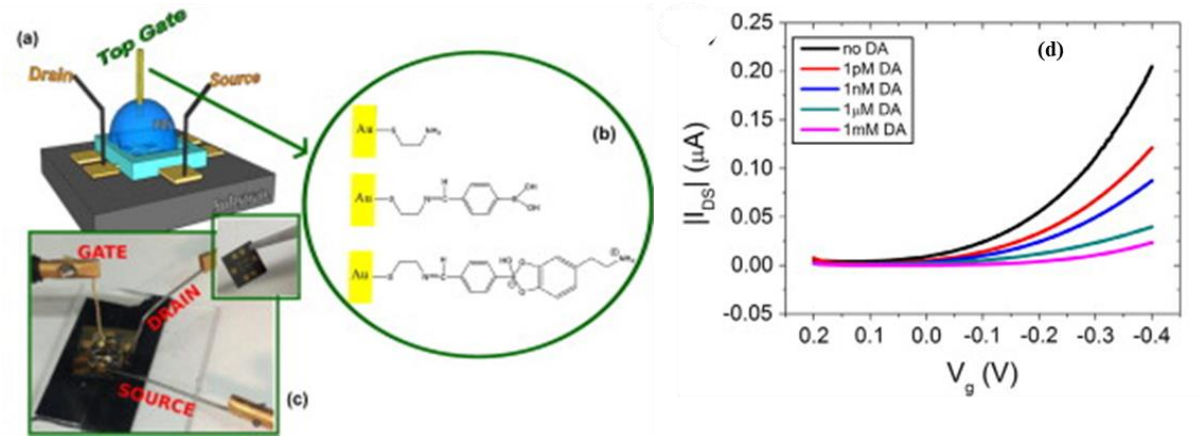

Figure III.10. EGOFET for dopamine sensing: (a) Scheme of the EGOFET device. (b) Gate functionalization with (1) CA, (2) BA and (3) dopamine. (c) Picture of the device. (d) Transfer curves acquired in the linear regime, for various dopamine concentrations [(29)].

Casalini *et al.*, in 2015, also worked on a Au gate as sensing area [(30)]. Thiol-modified protein G were self-assembled, followed by complexation of the antibody (protein G was used here for its property to bind IgG antibodies) on Au gate surfaces. They also modified the gate electrode with 6-aminohexanethiol for covalent coupling of the IgG, and they showed that the best result was obtained with the protein-G approach, because of a best orientation of the antibodies on the gate (Figure I.32). Interleukin-4 (IL4) was sensed down to ca. 5 nM. These results, and particularly the coupling between sensing experiments and surface characterizations were very useful to rationalize the response of an EGOFET using antibodies grafted on the gate.

Mulla *et al.*, in 2015, also described an EGOFET which relied on the modification of the gate [(31)]. They immobilized proteins (a porcine odorant binding protein-pOBP) on the Au gate through a self-assembled monolayer and showed that the transduction capability of the device was governed by the capacitance of the gate/electrolyte interface. The authors applied this architecture to the detection of odorant molecules (carvone; Figure I.33), by following drain current as a function of carvone concentration. The sensor presented a limit of detection around 10 pM and was enantioselective.

M. Berto *et al.*, in 2016, modified the gate contact of an EGOFET for monitoring tumor necrosis factor alpha (TNFα) in human plasma [(32)]. Histidine-tagged protein G was grafted on Au gate surfaces, to anchor anti-TNFα antibodies onto which TNFα targets specifically binds.

The molecular recognitionled to drain current changes, for concentrations as low as 100 pM (Figure III.11).

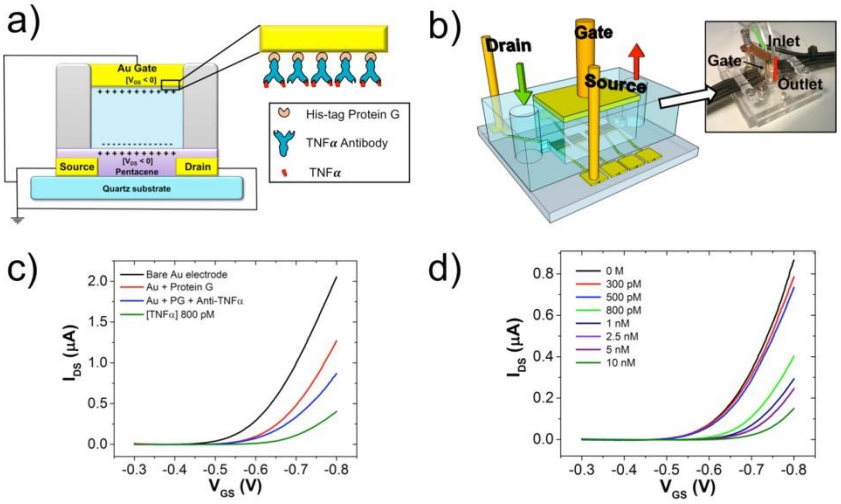

Figure III.11. EGOFET for monitoring tumor necrosis factor alpha (TNFα) in human plasma: (a) Scheme of the EGOFET with a zoom on the functionalized gate. (b) Microfluidics device comprising the electrical connections and fluidic inlets and outlets. (c) Transfer curves recorded for each functionalization step. (d) Transfer curves upon exposure to various TNFα concentrations in PBS buffer [32].

Next Section, I reproduced the article that I published in Biosensors and Bioelectronics in 2018, entitled "*Triggering the Electrolyte-Gated Organic Field-Effect Transistor output characteristics through gate functionalization using diazonium chemistry: Application to biodetection of 2,4-dichlorophenoxyacetic acid*", which illustrates how the capacitive coupling intrinsic to EGOFETs can be applied for immunosensing after proper functionalization of the gate electrode with an antibody.

3 References

1. Anastassiades, M., Schwack, W. (1998) Analysis of carbendazim, benomyl, thiophanate methyl and 2,4- dichlorophenoxyacetic acid in fruits and vegetables after supercritical fluid extraction, *Journal of Chromatography A 825*, 45–54.

2. Deamarantejr, O., Brito, N., Dossantos, T., Nunes, G., and Ribeiro, M. (2003) Determination of 2,4-dichlorophenoxyacetic acid and its major transformation product in soil samples by liquid chromatographic analysis, *Talanta 60*, 115-121.

3. Fránek, M., Kolar, V., Granátová, M. and Nevoránková, Z. (1994) Monoclonal ELISA for 2,4-Dichlorophenoxyacetic Acid: Characterization of Antibodies and Assay Optimization, *J. Agrie. Food Chem 42*, 1369-1374.

4. Kaur, J., Boro, R. C., Wangoo, N., Singh, K. R., and Suri, C. R. (2008) Direct hapten coated immunoassay format for the detection of atrazine and 2,4-dichlorophenoxyacetic acid herbicides, *Analytica chimica acta 607*, 92-99.

5. Kaláb, T., Skládal, P. (1997) Disposable Multichannel Immunosensors for 2,4-Dichlorophenoxyacetic Acid Using Acetylcholinesterase as an Enzyme Label, *Electroanalysis 9*, 293-297

6. Skládal, P., Kaláb, T. (1995) A multichannel immunochemical sensor for etermination of 2,4-dichlorophenoxyacetic acid, *Analytica Chimica Acta 316 316*, 73-78.

7. Wilmer, M., Trau, D., Renneberg, R., and Spener, F. (2006) Amperometric Immunosensor for the Detection of 2,4-Dichlorophenoxyacetic Acid (2,4-D) in Water, *Analytical Letters 30*, 515-525.

8. Bauer, C.G., Eremenko, A.V., Ehrentreich-Forster, E., Bier, F.F., Makower, A., Halsall, H.B., Heineman, W.R. and Scheller, F.W. (1996) Zeptomole-Detecting Biosensor for Alkaline Phosphatase in an Electrochemical Immunoassay for 2,4-Dichlorophenoxyacetic acid, *Analytical Chemistry, 68*, 2453-2458.

9. Dequaire, M, Degrand, C., and Limoges, B. (1999) An Immunomagnetic Electrochemical Sensor Based on a Perfluorosulfonate-Coated Screen-Printed Electrode for the Determination of 2,4-Dichlorophenoxyacetic Acid, *Anal Chem. 71*, 2571-2577.

10. Navratilova, I., and Skladal, P. (2004) The immunosensors for measurement of 2,4-dichlorophenoxyacetic acid based on electrochemical impedance spectroscopy, *Bioelectrochemistry 62*, 11-18.

11. Jiri Horecek, Skladal, P. (1997) Improved direct piezoelectric biosensors operating in liquid solution for the competitive label-free immunoassay of 2,4-dichlorophenoxyacetic acid, *Analytica Chimica Acta 316 347*, 43-50.

12. Halámek J., Hepel, M., Skládal, P. (2001) Investigation of highly sensitive piezoelectric immunosensors for 2,4-dichlorophenoxyacetic acid, *Biosensors & bioelectronics 16*, 253-260.

13. Gobi, K. V., Tanaka, H., Shoyama, Y., and Miura, N. (2005) Highly sensitive regenerable immunosensor for label-free detection of 2,4-dichlorophenoxyacetic acid at ppb levels by using surface plasmon resonance imaging, *Sensors and Actuators B: Chemical 111-112*, 562-571.

14. Alexiadis, O., and Mavrantzas, V. G. (2013) All-Atom Molecular Dynamics Simulation of Temperature Effects on the Structural, Thermodynamic, and Packing Properties of the Pure Amorphous and Pure Crystalline Phases of Regioregular P3HT, *Macromolecules 46*, 2450-2467.

15. Chandra Boro, R., Kaushal, J., Nangia, Y., Wangoo, N., Bhasin, A., and Suri, C. R. (2011) Gold nanoparticles catalyzed chemiluminescence immunoassay for detection of herbicide 2,4-dichlorophenoxyacetic acid, *The Analyst 136*, 2125-2130.

16. Shi, H., Zhao, G., Liu, M., and Zhu, Z. (2011) A novel photoelectrochemical sensor based on molecularly imprinted polymer modified TiO2 nanotubes and its highly selective detection of 2,4-dichlorophenoxyacetic acid, *Electrochemistry Communications 13*, 1404-1407.

17. Vinayaka, A. C., Basheer, S., and Thakur, M. S. (2009) Bioconjugation of CdTe quantum dot for the detection of 2,4-dichlorophenoxyacetic acid by competitive fluoroimmunoassay based biosensor, *Biosensors & bioelectronics 24*, 1615-1620.

18. Jia, M., Zhang, Z., Li, J., Shao, H., Chen, L., and Yang, X. (2017) A molecular imprinting fluorescence sensor based on quantum dots and a mesoporous structure for selective and sensitive detection of 2,4-dichlorophenoxyacetic acid, *Sensors and Actuators B: Chemical 252*, 934-943.

19. Taniguchi, M., and Kawai, T. (2004) Vertical electrochemical transistor based on poly(3-hexylthiophene) and cyanoethylpullulan, *Applied Physics Letters 85*, 3298-3300.

20. Panzer, M. J., and Frisbie, C. D. (2006) High charge carrier densities and conductance maxima in single-crystal organic field-effect transistors with a polymer electrolyte gate dielectric, *Applied Physics Letters 88*, 203504.

21. Kergoat, L., Herlogsson, L., Braga, D., Piro, B., Pham, M. C., Crispin, X., Berggren, M., and Horowitz, G. (2010) A water-gate organic field-effect transistor, *Advanced materials 22*, 2565-2569.

22. Kergoat, L., Piro, B., Berggren, M., Horowitz, G., and Pham, M. C. (2012) Advances in organic transistor-based biosensors: from organic electrochemical transistors to electrolyte-gated organic field-effect transistors, *Analytical and bioanalytical chemistry 402*, 1813-1826.

23. Kergoat, L., Herlogsson, L., Piro, B., Pham, M.C., Horowitz, G., Crispin, X. and Berggren, M. (2011) Tuning the threshold voltage in electrolyte-gated organic field-effect transistors, *Applied physical sciences 1-6*, 6.

24. Cotrone, S., Ambrico, M., Toss, H., Angione, M. D., Magliulo, M., Mallardi, A., Berggren, M., Palazzo, G., Horowitz, G., Ligonzo, T., Torsi, L. (2012) Phospholipid film in electrolyte-gated organic field-effect transistors, *Organic Electronics 13*, 638-644.

25. Suspène, C., Piro, B., Reisberg, S., Pham, M.-C., Toss, H., Berggren, M., Yassar, A., and Horowitz, G. (2013) Copolythiophene-based water-gated organic field-effect transistors for biosensing, *Journal of Materials Chemistry B 1*, 2090.

26. Palazzo, G., De Tullio, D., Magliulo, M., Mallardi, A., Intranuovo, F., Mulla, M. Y., Favia, P., Vikholm-Lundin, I., and Torsi, L. (2015) Detection beyond Debye's length with an electrolyte-gated organic field-effect transistor, *Advanced materials 27*, 911-916.

27. Magliulo, M., De Tullio, D., Vikholm-Lundin, I., Albers, W. M., Munter, T., Manoli, K., Palazzo, G., and Torsi, L. (2016) Label-free C-reactive protein electronic detection with an electrolyte-gated organic field-effect transistor-based immunosensor, *Analytical and bioanalytical chemistry 408*, 3943-3952.

28. Piro, B., Wang, D., Benaoudia, D., Tibaldi, A., Anquetin, G., Noel, V., Reisberg, S., Mattana, G., and Jackson, B. (2017) Versatile transduction scheme based on electrolyte-gated organic field-effect transistor used as immunoassay readout system, *Biosensors & bioelectronics 92*, 215-220.

29. Casalini, S., Leonardi, F., Cramer, T., and Biscarini, F. (2013) Organic field-effect transistor for label-free dopamine sensing, *Organic Electronics 14*, 156-163.

30. Casalini, A. C. D., Francesca Leonardi, Carlo A. Bortolotti, Elena T. Herruzo, Alessandra Campana, Rafael F. de Oliveira, Tobias Cramer, Ricardo Garcia and Fabio Biscarini. (2015) Multiscale Sensing of Antibody - Antigen Interactions by Organic Transistors and Single-Molecule Force Spectroscopy, *ACSNANO 9*, 5051–5062.

31. Mulla, M. Y., Tuccori, E., Magliulo, M., Lattanzi, G., Palazzo, G., Persaud, K., and Torsi, L. (2015) Capacitance-modulated transistor detects odorant binding protein chiral interactions, *Nature communications 6*, 6010.

32. Berto, M., Casalini, S., Di Lauro, M., Marasso, S. L., Cocuzza, M., Perrone, D., Pinti, M., Cossarizza, A., Pirri, C. F., Simon, D. T., Berggren, M., Zerbetto, F., Bortolotti, C. A., and Biscarini, F. (2016) Biorecognition in Organic Field Effect Transistors Biosensors: The Role of the Density of States of the Organic Semiconductor, *Analytical chemistry 88*, 12330-12338.

4 Article (Biosens. Bioelectron. 2018, 113, 32-38)

Triggering the Electrolyte-Gated Organic Field-Effect Transistor output characteristics through gate functionalization using diazonium chemistry: Application to biodetection of 2,4-dichlorophenoxyacetic acid

T.T.K. Nguyen [a,b], T.N. Nguyen, [a,b] G. Anquetin [a], S. Reisberg [a], V. Noël [a], G. Mattana [a], J. Touzeau [a], F. Barbault [a], M.C. Pham [a], B. Piro [a*]

[a] *Univ. Paris Diderot, Sorbonne Paris Cité, ITODYS, UMR 7086 CNRS, 15 rue J-A de Baïf, 75205 Paris Cedex 13, France*

[b] *Department of Advanced Materials Science and Nanotechnology (AMSN), University of Science and Technology of Hanoï (USTH), Vietnam Academy of Science and Technology (VAST), 18 Hoang Quoc Viet, Nghĩa Đô, Cầu Giấy, Hanoi, Viet Nam.*

Corresponding author:
Prof. Benoît Piro; Univ. Paris Diderot, Sorbonne Paris Cité, ITODYS, UMR 7086 CNRS, 15 rue J-A de Baïf, 75205 Paris Cedex 13, France. Telephone number: + 33 157 277 224. Email address: piro@univ-paris-diderot.fr

Abstract

We investigated an Electrolyte-Gated Organic Field-Effect transistor based on poly(N-alkyldiketopyrrolo-pyrrole dithienylthieno[3,2-b]thiophene) as organic semiconductor whose gate electrode was functionalized by electrografting a functional diazonium salt capable to bind an antibody specific to 2,4-dichlorophenoxyacetic acid (2,4-D), an herbicide well-known to be a soil and water pollutant. Molecular docking computations were performed to design the functional diazonium salt to rationalize the antibody capture on the gate surface. Sensing of 2,4-D was performed through a displacement immunoassay. The limit of detection was estimated at around 5 fM.

Keywords: Electrolyte-Gated OFET; Diazonium salt; 2,4-dichlorophenoxyacetic acid; 2,4-D; Immunosensor; Molecular modelling.

Graphical Abstract

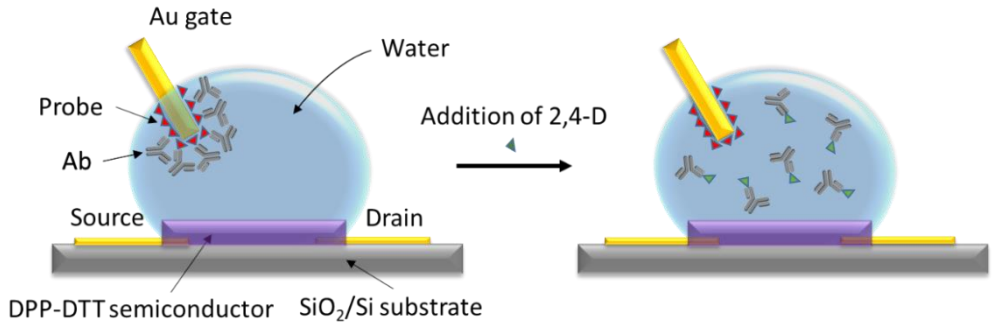

Highlights

► Gate functionalization of an Electrolyte-Gated Organic Field-Effect Transistor by diazonium electrografting ► Immobilization of antibodies on the transistor's gate ► Displacement immunoassay for 2,4-D detection in water samples

1. Introduction

2,4-dichlorophenoxyacetic acid (2,4-D) was one of the ingredients in Agent Orange, an herbicide used during the Vietnam War. 2,4-D is still one of the most widely used herbicides in numerous countries as a weed killer in agriculture. However, since 2015, it has been suspected to be carcinogenic and has been banned in several countries over the world. It is therefore important to find easy, costless and efficient methods to measure 2,4-D levels in soils or water. Apart from classical separative methods such as gas chromatography and high-performance liquid chromatography (Eller and Cassinelli, 1994), sensors would constitute an interesting solution. Without any intention of being exhaustive, some reported 2,4-D sensors are listed below.

Two main approaches are typically deployed to detect low molecular weight organic targets such as 2,4-D, i.e. the use of molecular-imprinted polymers, (MIP) or specific antibodies. Examples of detection devices based on one of these two receptors have been published since the first article of Skládal and Kalab in 1995 (Skládal and Kalab, 1995). In this seminal paper was described an electrochemical immunochemical assay (in a competitive format) made of a nitrocellulose membrane into which antibodies against 2,4-D were adsorbed. A 2,4-D molecule conjugated to Horseradish peroxidase (HRP) was used as a tracer (labeled target) with H_2O_2 and hydroquinone (HQ) as substrates for HRP. The detection limit (LoD) for 2,4-D in water was extremely low, 0.1 pg L^{-1} (0.45 fM). Subsequently, several developments and improvement of this principle have been published (Dtantiev and Zherdev, 1996; Dequaire et al., 1999). Another approach consisted in using molecularly imprinted polymers (MIP) where the polymer acts as a preconcentration matrix into which the target is detected by electrochemical methods (Xie et al., 2010; Shi et al., 2011; S. Kroger et al., 1999). However, the high potentials that have to be applied in order to detect the 2,4-D may lead to lack of selectivity due to the possibility of reducing the interferents always present in real samples such as dissolved oxygen. Impedimetric transduction (Navratilova and Skladal, 2004; Prusty and Bhand, 2017) allows to overcome such problem. To reach higher sensitivity without loss of selectivity, most of the recent works are based on optical transduction (Wang et al., 2016, Jia et al., 2017, Wagner et al, 2018, Fen et al., 2017). However, the use of electrical transduction would clearly represent an important advantage to reduce both the device size and fabrication costs, therefore alternatives to electrochemical as well as impedimetric sensors have to be proposed.

If we look at transistor-based devices for 2,4-D detection, no recent works have been published but one was pioneer nearly 25 years from now. The approach proposed by Khomutov et al, 1994, was significantly distinct from the classical electrochemical techniques; they proposed an immunodetection using a pH-sensitive Field-Effect Transistor (pH-FET). Their strategy was based on the use of a competitive binding, using a 2,4-D-peroxidase conjugate for binding with antibodies being immobilized on porous cellulose membranes. These membranes were attached to the gate region of the pH-sensitive FET. A mixture of ascorbic acid (0.1 mM), *o*-phenylenediamine (1.0 mM) and H_2O_2 (1.0 mM) was used as substrate solution for the enzyme, the activity of which being detected by a pH-shift at the gate; the LoD reached 1 µg L^{-1} (4.5 nM).

If we consider previous works reported on Electrolyte-Gated Organic Field-Effect Transistors (EGOFETs), the seminal works were those from Taniguchi and Kawai, 2004, Bäcklund et al., 2004, and Panzer and Frisbie, 2006. They demonstrated the possibility of fabricating transistors where the classical dielectric is replaced by a polymer electrolyte, and where the semiconductor and the gate, in direct contact with the electrolyte, are impermeable to ions. Polarization of the gate causes migration and accumulation of ions (formation of an electrical double layer, EDL) at the gate/electrolyte and semiconductor/electrolyte interfaces. The latter EDL causes accumulation of carriers at the OSC surface thus forming the channel. Kergoat et al., 2010, demonstrated that polymer electrolytes could be replaced by aqueous solutions as simple as phosphate buffers or even aerated deionized water. Since this date, the interest for EGOFET-based biosensors has kept growing. At first, publications focused on different methods able to biofunctionalize the semiconductor/electrolyte interface (Cotrone et al., 2012; Kergoat et al., 2012; Suspène et al., 2013; Palazzo et al., 2015; Piro et al., 2017). However, such approaches were challenging because they implied covalent or non-covalent functionalization of the semiconductor, which led to significant degradation of its electric properties. That is why the most recent works reported on application of EGOFETs for sensing have been rather based on gate modification (Casalini et al., 2013; Casalini et al., 2015; Mulla et al., 2015). As shown by these works, EGOFETs are not only sensitive to changes at the organic semiconductor/electrolyte interface, but also to those occurring at the electrolyte/gate interface.

Indeed, it was shown that the drain current I_D of an EGOFET depends on the overall capacitance (C) of the device (**Equation 1**), which is itself given by **Equation 2**.

$$\mathrm{I_D} = \mu \frac{\mathrm{W}}{\mathrm{2L}} \mathrm{C}(\mathrm{V_{GS}} - \mathrm{V_{Th}})^2 \qquad \text{(Eq. 1)}$$

$$\mathrm{C^{-1}} = \mathrm{C_{OSC/Elec}^{-1}} + \mathrm{C_{Elec/Gate}^{-1}} \qquad \text{(Eq. 2)}$$

with W the channel width, L its length, C the total interface capacitance per unit area, V_{GS} the operating gate potential, V_{Th} the threshold voltage, μ the mobility of the charge carriers, $\mathrm{C_{OSC/Elec}}$ the OSC/electrolyte capacitance and $\mathrm{C_{Elec/Gate}}$ the electrolyte/gate capacitance. Therefore, physicochemical processes occurring at the electrolyte/gate interface, such as changes in interfacial capacitance induced by molecular recognition of a target molecule onto an immobilized receptor, can be transduced into a drain current variation. This requires the

use of low molecular weight receptors that localize the binding reaction within the EDL over the gate, which excludes the utilization of large receptors such as antibodies (ca. 12 nm in height), for which (smaller) target molecules bind outside the EDL and therefore cannot be sensed (Kergoat et al, 2012; Huang et al, 2015). To overcome this problem, we proposed in a previous work a displacement immunoassay (Nguyen et al., 2017), inspired by previous work of Wijaya et al, 2010. Competition occurs between a target mime (hapten) immobilized onto the organic conducting polymer film and the native target present in the sample. In a first step, the antibody specific to the target binds the target mime immobilized on the polymer; when the target is present in solution, a competitive exchange occurs between the immobilized mime and the diffusing target, which displaces the equilibrium and removes the antibody from the surface (Piro et al., 2017). The large size of the antibody, compared to the small size of the immobilized hapten, allowed a thorough reorganization of the electrolyte/gate interface.

In the present work, for an easy and robust functionalization of the gate, we investigated the electroreduction of a diazonium salt, a methodology which has never been applied for gate modification in EGOFETs, for the covalent immobilization of the molecular probe onto which the specific antibody binds. As a practical example, we used the device for immunodetection of 2,4-D in water samples. A computational investigation was performed, at the atomic scale, to decipher the recognition processes between the immobilized probe and the antibody, through molecular docking computations in order to rationalize the position of the anchoring function with a minimum impact on the probe affinity for 2,4-D. The overall strategy (gate functionalization, antibody immobilization and displacement assay) is illustrated on **Fig. 1**. Concerning the organic semiconductor, it is the first time since its first description by Li et al., 2010 and Li et al., 2012 that poly(N-alkyldiketopyrrolo-pyrrole dithienylthieno[3,2-b]thiophene) (DPP-DTT) has been used in an EGOFET. This semiconductor is particularly pertinent in this type of device for its high hole mobility (*ca*. 1 $cm^2\ V^{-1}\ s^{-1}$), its low HOMO (-5.2 eV) and its high molecular weight (M_w = 280 ± 10 kDa) and well-ordered compact lamellar structure which make it stable in water environment.

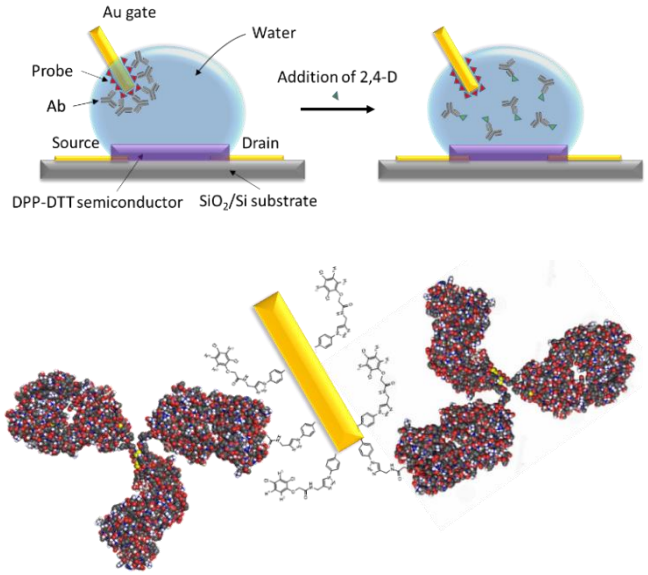

Figure 1. (Top) *schematic view of the gate-modified EGOFET, before (left) and after (right) addition of the target molecule 2,4-D in the electrolyte.* ***(Bottom)*** *Antibodies immobilized by affinity interactions on the 2,4-D-modified gate.*

2. Materials and methods

2.1 Chemicals and reagents

2,4-dichlorophenoxyacetic acid (2,4-D) and 2,4,5-trichlorophenoxyacetic acid (2,4,5-T) were purchased from Sigma-Aldrich. Poly(N-alkyldiketopyrrolopyrrole dithienylthieno[3,2-b]thiophene) (DPP-DTT) was purchased from Ossila (England), with M_w = 280 ± 10 kDa and PDI = 3.8 ± 0.1. Phosphate buffered saline (PBS), tert-butyl nitrite 90%, dichlorobenzene 98%, chlorobenzene - anhydrous, 99.8%, isopropanol, tetrabutylammonium hexafluorophosphate 98%, acetonitrile 99.8% and all other reagents and solvents were purchased from Sigma Aldrich and used without further purifications. Aqueous solutions were made with MilliQ water. Rabbit polyclonal IgG antibodies against 2,4-D ($Ab_{2,4\text{-}D}$), were obtained from ABBIOTEC, CA.

2.2 Synthesis of the two aryl amine-modified 2,4-D derivatives

Because propargylamine is provided by many manufacturers but its derivative with ten carbon atoms between the amino group and the alkyne group is not, we envisaged two

different synthetic routes for the C_1 and the C_{10} compounds. Indeed, although both 2,4-D derivatives were obtained via a Huisgen 1,3-dipolar cycloaddition, the 2,4-D-C_1-aniline was obtained via the coupling between the 2,4-D-C_1-alkyne and the azido aniline, conversely the 2,4-D-C_{10}-aniline was obtained via the coupling between the 2,4-D-C_{10}-azide and the 4-ethynylaniline. The synthesis of 10-azidodecylamine was carried out in two steps (about 30% overall yield) starting from 1,10-dibromodecane according to published procedures (Lee et al., 2001). **Scheme 1** describes the synthesis routes to obtain the two 2,4-D-C_1-aniline and 2,4-D-C_{10}-aniline compounds.

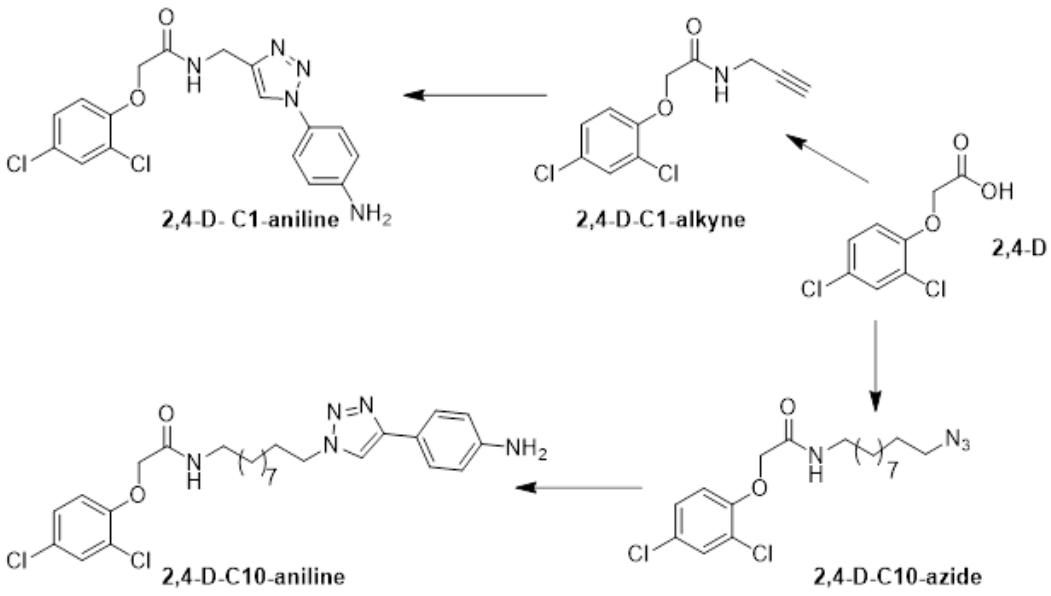

***Scheme 1**: Structure and synthesis of 2,4-D-C_1-aniline and 2,4-D-C_{10}-aniline.*

2,4-D-C_1-alkyne was synthesized as follows. A dichloromethane (DCM) solution (30 mL) of 2,4-D (1000 mg, 4.52 mmol), oxalyl chloride (0.54 mL, 6.30 mmol) and five drops of N,N-dimethylformamide (DMF) was stirred for 24 h at room temperature. The reaction mixture was then subjected to concentrated evaporation under reduced pressure. At 0°C, to this crude was added a solution of propargylamine (430 µL, 6.71 mmol) and **triethylamine** (2.4 mL, 17.2 mmol) in DCM (30 mL). After 48h of stirring at room temperature, the organic layer was washed with a Na_2CO_3 solution (5%, 30 mL) and then with a $KHSO_4$ solution (5%,

30 mL). The organic layer was dried with $MgSO_4$, filtered and then evaporated to afford 2,4-D-C_1-alkyne (960 mg, 3.71 mmol, 82%) as a yellow powder. This crude was used without further purification.

1H NMR (400 MHz, CD_3Cl) δ 7.41 (d, 1H, *J* = 2.5Hz, H_2), 7.23 (dd, 1H, *J* = 8.8Hz, *J* = 2.5Hz, H_4), 6.96 (bs, 1H, NH), 6.83 (d, 1H, *J* = 8.8Hz, H_5), 4.53 (s, 2H, OCH_2), 4.17 (dd, 2H, *J* = 5.5Hz, *J* = 2.6Hz, CH_2(NH)), 2.28 (t, 1H, *J* = 2.6Hz, C≡C-H).

2,4-D-C_{10}-azide was synthesized as follows. To a solution containing 10-azidodecylamine (450 mg, 1.97 mmol), 2,4-D (358 mg, 1.62 mmol), **DMF** (15 mL), and **diisopropylethylamine** (1.15 mL, 6.60 mmol), **HATU** (N,N-diméthylmethaniminium hexafluorophosphate, 1.25 g, 3.29 mmol) was added. After 16h of stirring at 50°C, deionized water (30 mL) was added and the aqueous phase was extracted with ethyl acetate (3×30 mL). The organic layer was washed, dried with $MgSO_4$, filtered and then evaporated. After a flash chromatography (cHex/EtOAc: 9/1 to 1/9), 2,4-D-C_{10}-azide (441 mg, 1.10 mmol, 68%) was obtained as a white powder.

1H NMR (400MHz, CD_3Cl) δ 7.41 (d, 1H, *J* = 2.5Hz, H_2), 7.23 (Dd, 1H, *J* = 8.8Hz, *J* = 2.5Hz, H_4), 6.83 (D, 1H, *J* = 8.8Hz, H5), 4.50 (s, 2H, OCH_2), 3.35 (quad, 2H, *J* = 6.7Hz, CH_2(NH)), 3.25 (t, 2H, *J* = 7.0Hz, CH_2N_3), 1.57 (m, 4H), 1.28 (m, 12H). **13C NMR (100 MHz, CD_3Cl) δ** 167.1 (CO), 151.8 (C_6ar), 130.4 (C_2ar), 128.2 (C_4ar), 127.6 (C_1ar), 123.9 (C_3ar), 114.8 (C_5ar), 68.5 (OCH_2), 51.6 (CH_2N_3), 39.2 (CH_2(CO)), 29.5-26.8 (8 CH_2).

2,4-D-C_1-aniline was synthesized as follows. To a mixture containing 4-azidoaniline (0.293 mmol; 50 mg) and 2,4-D-C_1-alkyne (0.135 mmol; 35 mg) in DCM (15 mL) was added a solution of copper sulfate (0.145 mmol; 36 mg) and L-ascorbic acid (0.35 mmol; 70 mg) in water (15 mL). The reaction was carried out overnight at room temperature. After washing with water and brine, the organic layer was dried over $MgSO_4$, filtered and evaporated. After a flash column chromatography (cHex/EtOAc: 9/1 to 1/1 then DCM/MeOH: 100/0 to 90/10), 16 mg of **2,4-D-C_1-aniline** as a yellow solid was obtained (0.04 mmol, 30%).

1H NMR (400 MHz, CD_2Cl_2) δ 7.84 (s, 1H, H triazole), 7.40-7.45 (m, 3H, 2Har an + H_2), 7.28 (sl, NH, 1H), 7.22 (dd, 1H, *J* = 8.8Hz et 2.4Hz, H_4), 6.88 (d, *J* = 8.9Hz, 1H, H_5), 6.76 (d, 2H, *J* = 8.7Hz, 2Har an), 4.66 (d, 2H, *J* = 5.3Hz, NCH_2), 4.54 (s, 2H, OCH_2), 3.96 (sl, 1H, NH). **IR (cm^{-1})** 3389, 3319, 3275 (NH_2), 3153, 3077 (CHar), 2929 (CHalc), 1657 (C(O)N),

1518 (C=C triazole), 1478 (N=N triazole). **HRMS** calc. mass for ($C_{17}H_{16}N_5O_2Cl_2$) M = 392.0681; exact mass M = 392.0688.

A similar procedure to obtain **2,4-D-C_{10}-aniline** was carried out in DCM/H_2O but after 4 days at room temperature, this reaction resulted in the recovery of the starting materials. Therefore, we followed the classical Huisgen 1,3-dipolar cycloaddition conditions, i.e. in a mixture of *t*-BuOH/H_2O: 1/1. To a *t*-BuOH (6 mL) solution containing 4-ethynylaniline (0.64 mmol; 73 mg) and 2,4-D-C_{10}-azide (0.498 mmol; 200 mg), was added a water solution (6 mL) of copper sulfate (0.264 mmol; 66 mg) and *L*-ascorbic acid (0.87 mmol; 170 mg). The reaction was carried out at 60°C for 3 days, then deionized water (30 mL) was added and the aqueous layer was extracted with DCM (3×40 mL). The organic layer was washed with brine, dried with $MgSO_4$, filtered and then evaporated. After a flash chromatography (cHex/EtOAc: 9/1 to 1/1 then DCM/MeOH: 100/0 to 90/10), 2,4-D-C_{10}-aniline (53 mg, 0.102 mmol, 20%) was obtained as a yellow oil.

1H NMR (400MHz, CD_2Cl_2) δ 7.65 (bs, 1H, H triazole), 7.58 (bd, 2H, 2H aniline), 7.42 (d, 1H, *J* = 2.5Hz, H_2), 7.23 (dd, 1H, *J* = 8.8Hz, *J* = 2.5Hz, H_4), 6.87 (d, 1H, *J* = 8.8Hz, H_5), 6.71 (d, 3H, 2Har aniline + NH), 4.48 (s, 2H, OCH_2), 4.33 (t, 1H, *J* = 7.2Hz, *C*H_2triazole), 3.30 (quad, 2H, *J* = 6.7Hz, CH_2(NH)), 1.90 (m, 2H, CH_2), 1.52 (m, 2H, CH_2), 1.35-1.25 (m, 12H, 6CH_2). **13C NMR (100MHz, CD_2Cl_2) δ** 167.1 (CO), 152.3 (C_6ar), 130.4 (C_2ar), 128.4 (C_4ar), 127.4 (C_1ar), 127.1 (2*C*H aniline), 124.0 (C_3ar), 121.5 (Cqar aniline), 118.7 (CH triazole), 115.4 (2*C*H aniline), 115.2 (C_5ar), 68.8 (OCH_2), 50.7 (*C*H_2.triazole), 39.4 (*C*H_2(NH)), 30.4-26.8 (9*C*H_2).

2.3 Transistor fabrication

Substrates were n-type (100) Si wafers onto which a 200-nm thick oxide layer was thermally grown. Wafers were washed in acetone, then in isopropanol in an ultrasonic bath during 3 min. They were cleaned under ozone during 3 minutes before being dried at 120°C, 10 minutes on a hot plate. They were coated with a photoresist AZ 5214 spin-coated during 30 s at 4000 rpm, then baked at 110°C for 1 minute. Interdigitated source and drain gold electrodes were UV-photolithographied (exposure to UV light during 1.8 s, hard baking for 1 min at 120°C and again exposure to UV light for 1 min), then developed in AZ 326MIF for 17 s. Finally, wafers were washed in water and dried by flushing argon. Before lithography,

wafers were treated under ozone for 2 minutes then an adhesion layer of 10 nm of titanium followed by a gold layer of 100 nm were evaporated through a photomask so that the transistors present a total channel width (*W)* of 10000 µm and a channel length (*L*) of 10 µm (**Scheme SI-1**). Before spin-coating DPP-DTT, wafers were cleaned in acetone and isopropanol for 2 minutes and kept in isopropanol. 2.5 mg mL^{-1} DPP-DTT was dissolved in a mixture of 93:7 v/v chlorobenzene:dichlorobenzene at 110°C under stirring in a round-bottom flask. 300 µL of the DPP-DTT solution at 110°C were dropped onto the silicon wafer and spin-coated at 4000 rpm during 180 s, followed by baking at 110°C for 1 h in air.

2.3 Gate electrodes fabrication

Lab-made gate electrodes were fabricated from gold wires inserted in a capillary glass tube using a laser-based micropipette puller (Sutter Instrument model P-2000 for the 100 µm microelectrode, and a Narishige Needle Puller PC-10 for electrodes of 500, 750 µm and 1 mm). A stainless-steel wire was sealed at the extremity of the electrodes to take the electrical contact with the gold wire and secured with glue. The microelectrodes were carefully and manually polished before use with 0.3 µm alumina slurries on a polishing cloth, thoroughly rinsed with MilliQ water, then with acetonitrile, and finally dried under argon. After every polishing, microelectrodes were characterized by linear sweep voltammetry in a solution of 10^{-3} M ferrocene + tBu_4NBF_4 in acetonitrile) to measure their real active area. If a change of area larger than 10% was measured between two polishing sequences, the electrode was discarded.

2.4 Gate functionalization

For *in-situ* synthesis of the diazonium salt and electrografting, tetrabutylammonium hexafluorophosphate ($TBAPF_6$, 190 mg) was dissolved in 5 mL CH_3CN. 2,4-D-aniline (1 mg) was added in this solution and degassed for 15 minutes. Finally, *tert*-butyl (16 µL) nitrite was added in the solution, to form the diazonium salt, then the potential of the gold microelectrode was swept from +0.2 V down to -0.7 V and back to 0.2 V at 50 mV s^{-1} for one cycle. This procedure forms an insoluble thin layer on top of the metal electrode. Electrode blocking was characterized using dopamine as redox probe. Details are given in **Fig. SI-2a**

and **SI-2b**. The resulting electrodes are named [2,4-D-C_1]-modified gate in the following paragraphs.

2.5 Electrical characterizations

A drop of deionized water was put on the surface of the transistor, and the gate electrode was put in contact with the droplet. Output characteristics were recorded by sweeping the drain-source voltage between 0 V and -0.30 V at 170 mV s^{-1}; the gate voltage V_{GS} was incrementally switched from 0 V to -0.4 V by steps of 0.1 V. The off current (I_{off}) corresponds to V_{GS} = 0 V and the on current (I_{on}) to V_{GS} = -0.4 V. Transfer curves were obtained by sweeping V_{GS} from 0 V to -0.6 V at 170 mV s^{-1} at constant V_{DS} = -0.3 V. The electrical characteristics were recorded using a Keithley 4200 Semiconductor Characterization System.

The electrochemical experiments (cyclic voltammetry, CV, and electrochemical impedance spectroscopy, EIS) were performed on an Autolab PGSTAT 302N controlled by NOVA 2.0 software. A three-electrode setup was used, consisting of the home-made microelectrodes as working electrodes (various diameter from 100 µm to 1 mm), a platinum grid of about 2 cm^2 as counter electrode and a commercial saturated calomel reference electrode (SCE, Metrohm) inserted into a salt bridge containing PBS. EIS data were analyzed using the dedicated software included with NOVA 2.0; fittings were done using a simplified Randles circuit comprising a resistance R_E (corresponding to the electrode+electrolyte resistance) in series with one parallel $R_{DL}C_{DL}$ circuit (corresponding to the resistance and capacitance of the electrical double layer) (**Fig. SI-3**).

2.6 Detection of 2,4-D

[2,4-D-C_1]-modified microelectrodes were first incubated with 10^{-7} mol L^{-1} $Ab_{2,4\text{-}D}$ for 1h in the dark, to bind the antibody on the immobilized antigen, giving [$Ab_{2,4\text{-}D}$/2,4-D-C_1]-modified electrodes. These electrodes were then incubated for 30 min in the dark in 2,4-D solutions prepared at various concentrations from 10^{-16} mol L^{-1} to 10^{-12} mol L^{-1}, and in pure water as blank, then they were rinsed with PBS, argon-dried and used as gate electrodes for electrical characterization in transistor configuration.

2.7 Computational details

Compounds were built with the help of the *Maestro* interface of the *Schrödinger* software package[3]. To date, the structure of the 2,4-D antibody is unknown. Therefore, a cross-docking procedure was employed to identify the consensual structure which corresponds to the PDB code 3CFB (Debler et al, 2008). Autodock software (Morris et al., 2009) was used for the molecular docking calculations where all rotatable dihedral angles were set free to move during the 100 cycles of Lamarckian Genetic Algorithm optimizations (Morris et al., 1998). The resulting docking structures were then clustered into conformation families according to a root mean square deviation lower than 2 Å. The selected conformation was the one which presented the lowest docking free energy of binding in the most populated cluster (Teixeira et al, 2009). The *in-silico* determination of the optimal length for the spacer arm of 2,4-D was interactively made with the Maestro interface. Visualization, analyses and figures of Ab/ligand interactions were made with the help of the visual molecular dynamic software (Humphrey et al., 1996). See **Figure SI-4** for details on the cross-docking procedure.

3. Results and discussion

3.1 Modelling

We firstly investigated how the 2,4-D structurally interacts with its antibody (Ab) through molecular docking computations. We found a negative interaction energy of -5.7 kcal mol^{-1} for the 2,4-D, which indicates a favorable association. The interaction, displayed in **Fig. 2** (top left) reveals that the antigen is deeply inserted in the protein with the 2,4-dichlorophenoxy moiety oriented toward the center of the protein, filling this way the hydrophobic pocket of this cavity. The orientation of the acidic part was found to be pointing outwards, in the solvent direction, indicating that any derivation of 2,4-D should be made by modifying the acidic group. To verify the relevance of this result, molecular modeling was performed by modifying the carboxylic function in the first instance by an amide. We computationally tested the molecular docking of 2,4-D-methyl-amido (E_{dock} = -6.0 kcal mol^{-1};

[3] Schrödinger | Schrödinger is the scientific leader in developing state-of-the-art chemical simulation software for use in pharmaceutical, biotechnology, and materials research., https://www.schrodinger.com/ (accessed November 16, 2017).

Fig. 2, top right). We observed, as for the unmodified 2,4-D, that the 2,4-dichlorophenoxy part is inserted into the antibody cavity. We examined similarly the location of the 2,4-D-C_1 compound within the protein and found a similar orientation (Fig. 2, bottom left; E_{dock} = -9.0 kcal mol^{-1}). Finally, we added ten carbon atoms between the amido group and the 4-azido-benzene part (2,4-D-C_{10}). The 2,4-D-C_{10} is recognized and binds strongly to the Ab epitope (Fig. 2, bottom right). From these results, it is clear that any modification of the 2,4-D must be achieved through the carboxylic function.

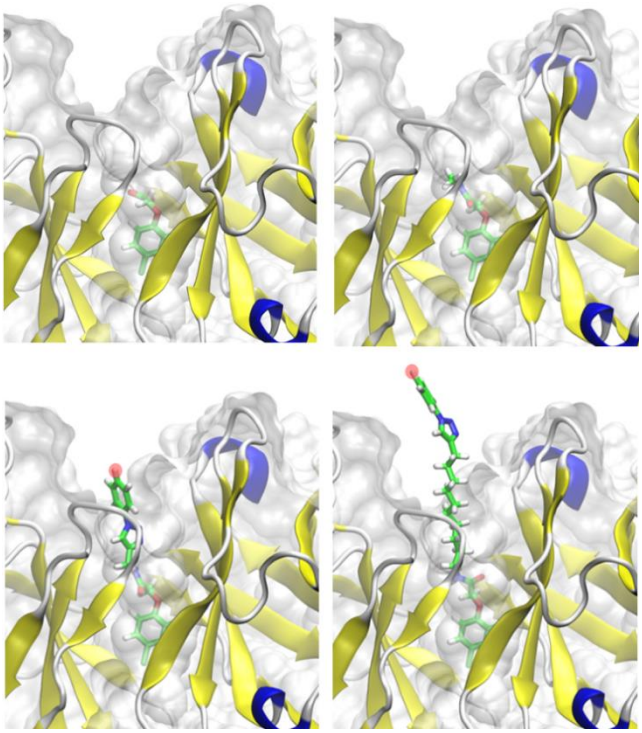

Figure 2*. Structural orientations of the antigens inside the antibody cavity. The cavity is represented with ribbons and its molecular surface in grey shades whereas ligands are displayed with atom-colored sticks.* ***Top, left****: 2,4-D;* ***Top, right****: 2,4-D-methyl-amido;* ***Bottom left****: 2,4-D-C_1;* ***Bottom right****: 2,4-D-C_{10}. The pink circle highlights the position where the grafting on the surface should occur.*

3.2 Electrical characteristics of the DPP-DTT EGOFETs

Output and transfer curves were obtained from EGOFET devices fabricated as described in Section 2. In all cases, aerated MilliQ water was used as electrolyte.

3.2.1 Effect of gate diameter

Output curves were recorded for gate diameters of 1000 µm, 750 µm, 500 µm and 100 µm (**Fig. 3a**). As shown, curves present a typical FET behavior, with a linear region for 0 V < $|V_{DS}|$ < 0.15 V and a saturation regime for $|V_{DS}|$ > 0.15 V. Two other diameters were also used, 50 µm and 25 µm; however, for these diameters, no significant field effect was recorded. The plot of I_D at saturation versus the gate surface area is shown on **Fig. 3b**. A curve fitting assuming that I_D^{-1} is proportional to $C_{OSC/Elec}^{-1} + C_{Elec/Gate}^{-1}$ (see Eq. 1 and Eq. 2) was performed as a function of the gate diameter. The best possible fitting (shown on Fig. 3b) was obtained for a diameter of 100 µm, for which the OSC/electrolyte capacitance ($C_{OSC/Elec}$) is about 15 times higher than that of the gate/electrolyte $C_{Elec/Gate}$. This result justifies the use of gates as small as possible to maximize the sensitivity of the device toward changes in capacitance of the gate/electrolyte interface. EIS experiments performed on bare gate electrodes (**Fig. SI-5**) showed that, in PBS, gate capacitances were in the range of 40 ± 7 µF cm^{-2} (i.e. an absolute capacity of 3.2 ± 0.6 nF for the 100 µm gate). Comparatively, the absolute capacity of the spin-coated DPP-DTT film of the active device area (1 × 0.5 mm, see Fig. SI-1) was measured by EIS and found equal to 35 ± 15 nF, e.g. more than 10 times higher than that of the 100 µm gate, which is consistent with values derived from the fitting of Fig. 3b.

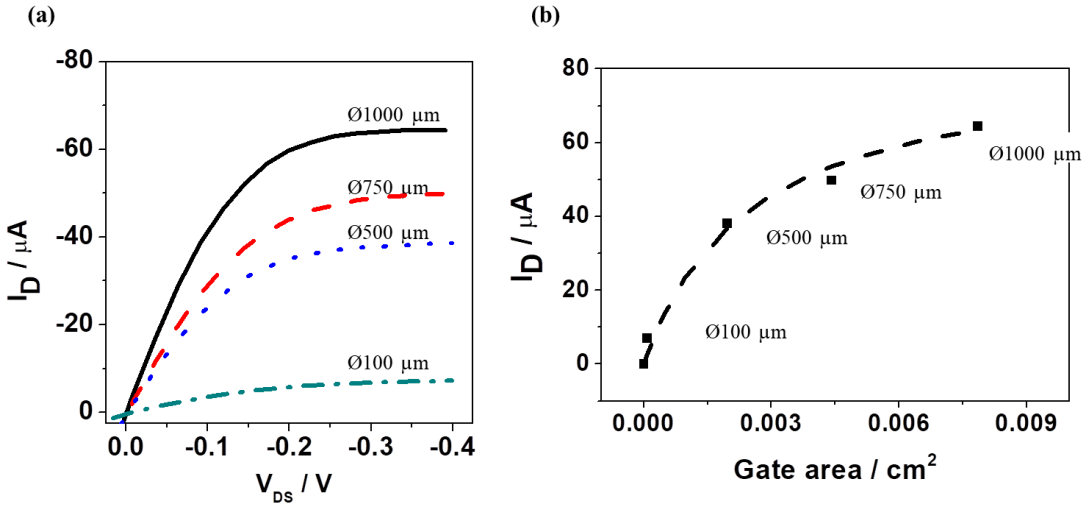

Figure 3. (a) *Output curves of a DPP-DTT EGOFET for different gate diameters (**black solid curve**: 1000 µm; **red dashed curve**: 750 µm; **blue dotted curve**: 500 µm; **green dash-dotted curve**: 100 µm). The drain potential was swept at 170 mV s^{-1}. V_{GS} = -0.4 V. L = 10 µm; W = 10 mm. Electrolyte: air-saturated MilliQ water. **(b) Solid square**: Saturation current (I_{Dsat}) as a function of the gate area, extracted from Fig. 3a; **Dotted line**: fitting of I_D as a function of the gate area, for a fixed value* $C_{OSC/Elec}$ *= 35 ± 15* nF *and a gate capacitance* $C_{Elec/Gate}$ *= 40 ± 7 µF cm^{-2}.*

From the corresponding $\sqrt{I_D}$ = f(V_{GS}) plots at saturation regime for different gate areas, the threshold voltages (V_{Th}) were found within the range -0.4 V < V_{Th} < -0.3 V, with no obvious trend between the gate area and the V_{Th} values. Output and transfer curves obtained for a gate diameter of 100 µm (**Fig. 4**) gave an I_{on}/I_{off} ratio of ca. 2400 and a threshold voltage of ca. V_{Th} = -0.32 ± 0.05 V. The highest transconductance (defined as the peak value of $\frac{\partial I_D}{\partial V_G}$) for a bare gold gate of Ø100 µm was found of 21 µS at V_{GS} = - 0.55 V. The gate current always remained negligible compared to the drain current, in the nA range.

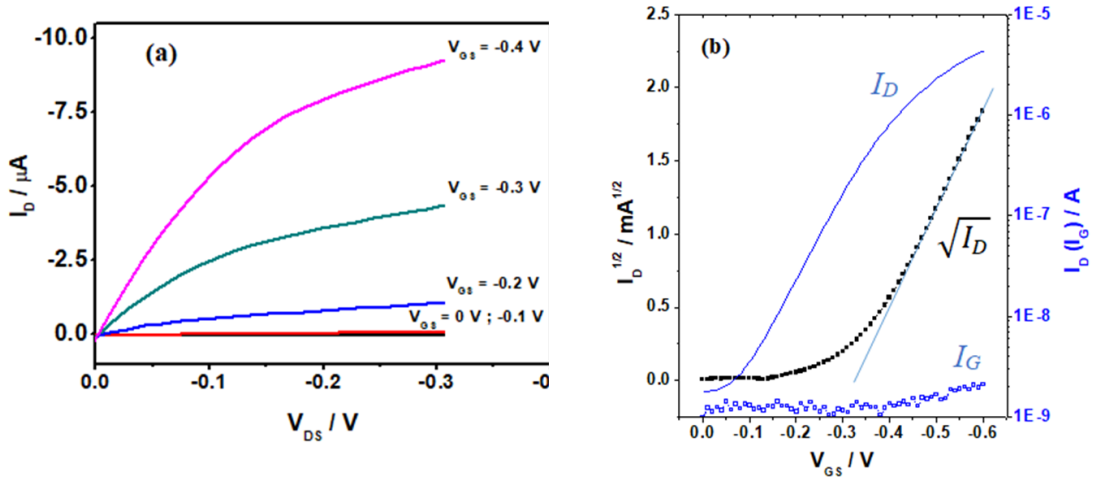

Figure 4. (a) *Output curves of a DPP-DTT EGOFET (gate Ø: 100 µm) for various gate voltages from 0 V down to -0.4 V. The drain potential was swept at 170 mV s^{-1}.* ***(b)*** *Corresponding transfer curve (solid line) obtained by sweeping the gate voltage form 0 V down to -0.6 V at a scan rate of 170 mV s^{-1} at a fixed V_{DS} = -0.4 V; corresponding plot of* $\sqrt{I_D}$ = f(V_{GS}) *(solid squares); corresponding plot of* I_G = *f*(V_{GS}) *(open squares). L = 10 µm; W = 10 mm. Electrolyte: air-saturated MilliQ water.*

3.2.2 Effect of gate functionalization.

Electrical characteristics were measured, under the same experimental conditions as for bare gold gates, after electrografting of 2,4-D-C_1 on the gate electrode, as described in Section 2.4 (**Fig. 5**). With these modified gates, the transfer curves show slightly lower drain current compared to that obtained with bare gold gates; the highest transconductance for this grafted gate was 13 µS at V_{GS} = -0.6 V, I_{on}/I_{off} = 3200 and V_{Th} = -0.30 ± 0.05 V. V_{Th} is not significantly changed compared to that of the bare gold gate, which is consistent with the fact that the grafted 2,4-D-C_1 does not polarize the gate interface. The gate current remained negligible compared to the drain current, even if it starts to increase for V_{GS} values in the range [-0.35; -0.6 V]. The capacitance of grafted gates, measured by EIS under similar experimental conditions than for bare gates, was of 1.4 ± 0.3 nF for the 100 µm gate, i.e. 23 ± 4 µF cm^{-2}, lower than the capacitance obtained for the bare gate (40 ± 7 µF cm^{-2}). This is consistent with the fact that organic layers obtained by diazonium electroreduction are known to be thin and compact, with a very low dielectric constant compared to the electrolyte, so that the capacitance is significantly decreased.

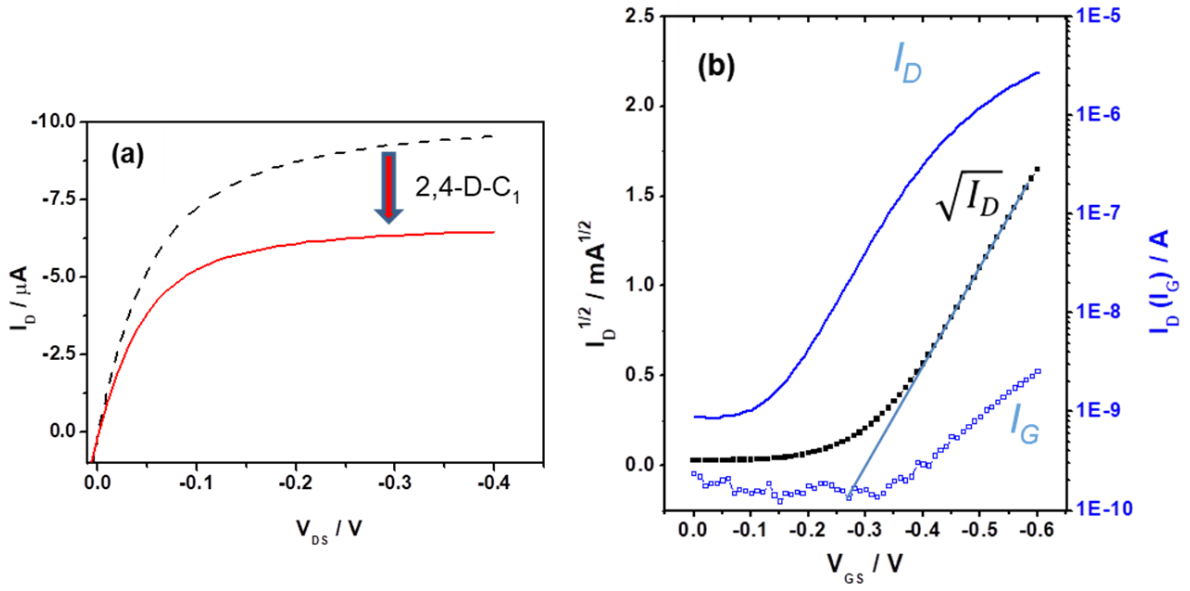

Figure 5. (a) *Output curves of a DPP-DTT EGOFET (gate Ø = 100 µm) at a gate voltage of -0.4 V for a bare gate (dashed curve) and a [2,4-D-C_1]-modified gate (solid red curve). The drain potential was swept at 170 mV s^{-1}.* ***(b)*** *Corresponding transfer curve (solid line) obtained by sweeping the gate voltage form 0 V down to -0.6 V at a scan rate of 170 mV s^{-1} at a fixed V_{DS} = -0.4 V; Corresponding plot of* $\sqrt{I_D}$ = f(V_{GS}) *(solid squares); corresponding plot of* I_G = *f*(V_{GS}) *(open squares). L = 10 µm; W = 10 mm. Electrolyte: air-saturated MilliQ water.*

The same experiment was made for a [2,4-D-C_{10}]-modified gate. However, in this case, the drain current was dramatically decreased down to several hundreds of nanoamps at saturation, consistently with the gate capacitance which dropped down to a few µF cm^{-2}. These unanticipated results, which disqualify the 2,4-D-C_{10} for being used in the following of this work, may be explained by the formation of a denser and more hydrophobic layer compared to that obtained with 2,4-D-C_1; even if expected to be more efficient for antibody immobilization from the computational results, we did not carry on experiments with this molecule.

3.2.3 Immobilization of the antibody

The antibody directed toward 2,4-D was immobilized on the [2,4-D-C_1]-modified gate through affinity interactions (**Eq. 3**). This was performed by dipping the [2,4-D-C_1]-modified gate in a PBS solution containing $Ab_{2,4\text{-}D}$ at 10^{-7} M, at room temperature, for 1 hour, followed by washing with MilliQ water before testing.

$$Ab_{2,4-D} + [2,4-D-C_1]/Gate \rightleftarrows [Ab_{2,4-D}/2,4-D-C_1]/Gate \qquad \textbf{(Eq. 3)}$$

From EIS measurements, we found that after Ab binding, a capacitance of ca. 1.0 ± 0.2 nF for the 100 µm [$Ab_{2,4\text{-}D}$/2,4-D-C_1]-modified gate, i.e. 13 ± 2 µF cm^{-2}, approximately half of the capacitance obtained for the 2,4-D-C_1-modified gate. Moreover, we found a lower drain current with a threshold voltage shifted toward more negative values when compared to the bare and grafted gate, at V_{Th} = -0.42 ± 0.05 V. The highest transconductance for this [$Ab_{2,4\text{-}D}$/2,4-D-C_1]-modified gate was 3.5 µS at V_G = -0.6 V. Consequently, the electrical characterizations of the devices were significantly changed, as shown on **Fig. 6a,b**. Similar experiments were performed with non-specific antibodies such as anti-DCF (anti-diclofenac) and anti-BPA (anti-bisphenol A), which have no affinity for 2,4-D; corresponding output curves are shown on **Fig. 6a**, which shows negligible differences with the curve obtained before incubation with these antibodies, indicating no binding. Corresponding gate capacitances were found close to the grafted gate, at 25 ± 4 µF cm^{-2} for Ab_{BPA} and 19 ± 4 µF cm^{-2} for Ab_{DCF}, to be compared with 23 ± 4 µF cm^{-2} for the 2,4-D-C_1-modified gate. Hence, both capacitance and Vth change specifically upon anti-2,4-D Ab binding to the modified-gate electrode. Such trend has been previously observed for OSC-modified EGOFET (Palazzo et al. 2015; Piro et al., 2017) and is attributed to the formation of Donnan's equilibria within the protein layer, resulting in an extra capacitance in series to the gating system.

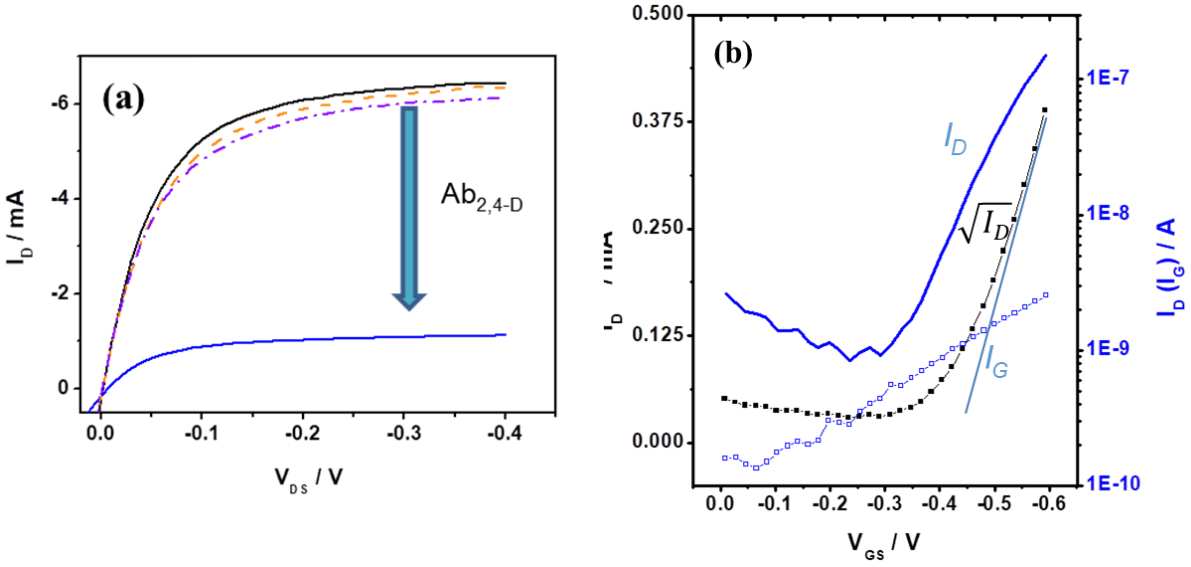

Figure 6. **(a)** *Output curves of a DPP-DTT EGOFET (gate Ø = 100 µm) at a gate voltage of -0.4 V with a 2,4-D-C_1-modified gate before (solid black curve) and after incubation with the specific antibody $Ab_{2,4\text{-}D}$ (solid blue curve) and two non-specific antibodies: Ab_{DCF} (dotted curve) and Ab_{BPA} (dashed curve). The drain potential was swept at 170 mV s^{-1}.* ***(b)*** *Corresponding transfer curve (solid line) obtained by sweeping the gate voltage form 0 V down to -0.6 V at a scan rate of 170 mV s^{-1} at a fixed V_{DS} = -0.4 V; Corresponding plot of* $\sqrt{I_D}$ = f(V_{GS}) *(solid squares); corresponding plot* of I_G = *f*(V_{GS}) *(open squares). L = 10 µm; W = 10 mm. Electrolyte: air-saturated MilliQ water.*

3.2.4 Change of the electrical characteristics upon recognition of 2,4-D

Target recognition was made by means of competition, for binding of the $Ab_{2,4\text{-}D}$ antibody, between the freely diffusing 2,4-D in the electrolyte and the 2,4-D-C_1 hapten grafted on the gate. As shown by **Eq. 4**, if 2,4-D is present in solution, the complexation equilibrium is displaced so that $Ab_{2,4\text{-}D}$ is removed from the gate surface. Consequently, it is expected to lead to an increase of the gate capacitance and therefore to an increase of the drain current.

$$[\mathrm{Ab}_{2,4-\mathrm{D}}/2,4-\mathrm{D}-\mathrm{C}_1]/\mathrm{Gate} \; + \; 2,4-\mathrm{D}_{\mathrm{sol}} \rightleftarrows [2,4-\mathrm{D}-\mathrm{C}_1]/\mathrm{Gate} + [\mathrm{Ab}_{2,4-\mathrm{D}}/2,4-\mathrm{D}]_{\mathrm{sol}}$$

(Eq. 4)

A structural analogue of 2,4-D, namely 2,4,5-trichlorophenoxyacetic acid (2,4,5-T), for which $Ab_{2,4\text{-}D}$ has no affinity, was used as blank. EIS performed on an [$Ab_{2,4\text{-}D}$/2,4-D-C_1]-modified gate (Ø100 µm) incubated with 10^{-14} M 2,4,5-T gave a capacitance of ca. 900 ± 160 pF, i.e. 12 ± 2 µF cm^{-2}, slightly lower than that obtained for the [$Ab_{2,4\text{-}D}$/2,4-D-C_1]-modified gate before incubation (13 ± 2 µF cm^{-2}). On the contrary, the same gate electrode incubated with 10^{-14} M 2,4-D showed an increase of capacitance, up to 16 ± 3 µF cm^{-2}, which confirmed that a significant amount of [2,4-D/$Ab_{2,4\text{-}D}$] complexes were removed from the gate surface.

These changes were also evidenced through changes of the drain current, as shown in **Fig. 7** for 2,4-D (positive) and 2,4,5-T (blank). These results demonstrate the selectivity of the sensor, which delivers a current increase only for the 2,4-D target and no significant current change for the structural analogue 2,4,5-T which is not recognized by the anti-2,4-D antibody. Detection was done in tap water[4] and compared to an experiment performed in aerated MilliQ water. As shown, the drain current was slightly lower for tap water than for MilliQ water, but 2,4-D is still well recognized.

[4] pH 7.7; Total iron: 1.8 µg L^{-1}; Free chlorine: 0.2 mg L^{-1}; Nitrates: 27.7 mg L^{-1}; Calcium: 94.7 mg L^{-1}; Bicarbonates: 250 mg L^{-1}; Chloride: 24.2 mg L^{-1}; Fluoride: 0.1 mg L^{-1}; Potassium: 2.1 mg L^{-1}; Sodium: 8.1 mg L^{-1}; Sulfates: 20.5 mg L^{-1}: Conductivity: 524.7 µS cm^{-1}. Analysis performed in December 2017, 13th district, Paris.

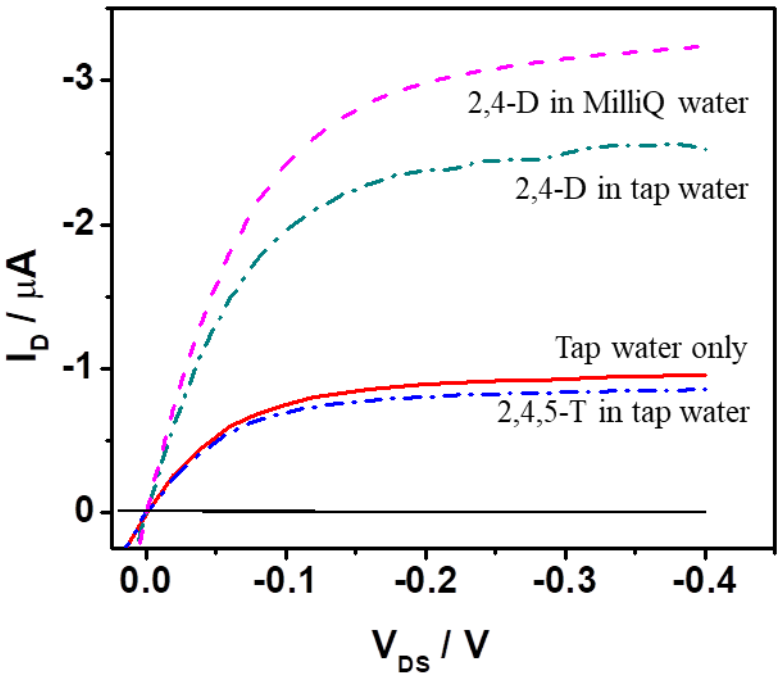

Figure 7. *Output curves of a DPP-DTT EGOFET (gate Ø:100 µm) for a gate voltage of -0.4 V, with a [$Ab_{2,4\text{-}D}$/2,4-D-C_1]-modified gate only (red solid curve), recorded in tap water; after incubation with* 10^{-14} M *2,4,5-T (negative experiment, blue dashed curve), in tap water; with* 10^{-14} M *2,4-D (positive experiment, green dash-dotted curve), in tap water; with* 10^{-14} M *2,4-D (reference experiment, pink dash-dotted curve), in aerated MilliQ water. Solid black curve: gate current (in the nA range). The drain potential was swept at 170 mV* s^{-1}. *L = 10 µm; W = 10 mm.*

3.3 Application to 2,4-D determination in water samples

[$Ab_{2,4\text{-}D}$/2,4-D-C_1]-modified gates were dipped into 2,4-D solutions of concentrations varying from 0.1 fM to 10 pM in water for 1h at 25°C, then rinsed three times with water then used in EGOFET configuration to measure the output characteristics (**Fig. 8**).

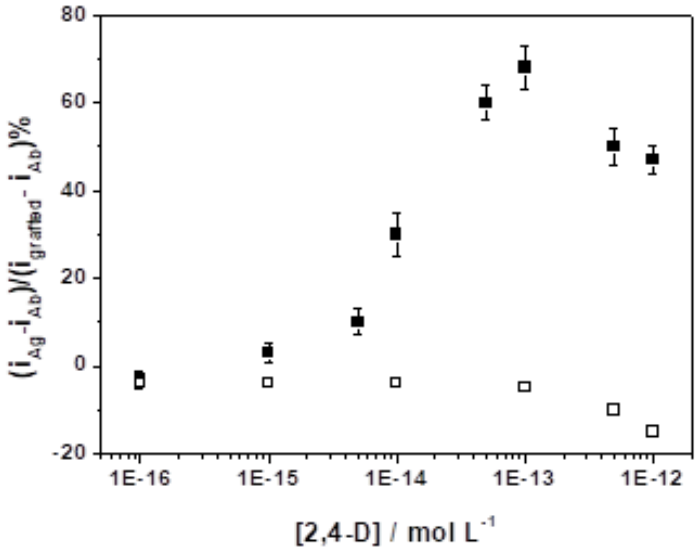

***Figure 8**. as a function of (solid squares) 2,4-D concentration and (open squares) 2,4,5-T. Electrolyte: air-saturated MilliQ water. V_{DS}= -0.4 V, V_{GS} = -0.4 V, for a [$Ab_{2,4\text{-}D}$/2,4-D-C_1]-modified gate (Ø100 µm). Data points show mean values ± SD (n=4).*

It should be noticed that saturation occurs for concentrations above 100 fM, for which the current decreases. This was observed for 2,4-D but also for the non-specific target 2,4,5-T; this behavior has been also observed for other displacement immunosensors (Nguyen et al., 2017) and could be attributed to non-specific adsorption on the gate electrode. Experimental conditions have not been optimized to extend the linearity domain or to shift saturation towards higher 2,4-D concentrations. This could probably be obtained by adding an anti-adsorptive membrane on top of the gate or by decreasing the surface concentration of 2,4-D antibodies. Considering the standard deviation and the peak current obtained for blank experiments, one can estimate a limit of detection of ca. 5 fM, which is competitive if compared to results from the literature. For example, the device described by Wijaya et al, 2010, relying on a competitive immunoassay with a carbon nanotubes-based electrolyte-gated transistor, presented a LoD of 500 fM (0.11 ng L^{-1}).

4. Conclusions

We investigated the functionalization of the gate of an EGOFET by electrografting (through the diazonium route), of two aryl amine-modified 2,4-D derivatives having a short (one carbon) and a long (ten carbons) spacing arm between the 2,4-D moiety and the aryl group.

Even if molecular modelling showed that the longest spacer should be beneficial for binding of the antibody, this C_{10} spacer was not selected because its electrografting induced a too strong decrease in capacitance of the gate electrode, which was detrimental to the functioning of the transistor. Using the C_1 spacer, we showed that the capture of the 2,4-D antibody led to a capacitance decrease, therefore a drain current decrease. Using this antibody-modified gate, addition of 2,4-D led to an increase in gate capacitance, corresponding to a drain current increase, for concentrations as low as 5 fM. This limit of detection is excellent when compared to the existing literature or to known pollution levels. For example, the Word Health Organization (WHO, 2003) reported in its *Guidelines for drinking-water quality* 2,4-D levels in drinking water in US and Canada from 10^{-7} M to 5×10^{-10} M for the most polluted areas, but generally lower than 5×10^{-11} M. In France, where 2,4-D has been forbidden for years, the French Institute for Industrial and Environmental Risks (INERIS, 2012), recommends values lower than 5×10^{-11} M in drinking waters, a threshold value which is obtained for all surveyed waters but which corresponds to the limit of detection of the validated measurement protocols. More sensitive techniques, such as the one described in this manuscript, would be useful to draw a more precise picture of the pollution levels and identify pollution sources.

Acknowledgments

TTKN thanks USTH for providing a PhD grant. TNN thanks University Paris Diderot for an internship grant.

References

Bäcklund, T.G., Sandberg, H.G.O., Österbacka, R., Stubb, H. 2004. Appl. Phys. Lett. 85, 3887.

Casalini, S., Leonardi, F., Cramer, T., Biscarini, F. 2013. Org. Electron. 14, 156 – 163.

Casalini, S., Dumitru, A. C., Leonardi, F., Bortolotti, C. A., Herruzo, E. T., Campana, A., De Oliveira, R.F., Cramer, T., Garcia, R., Biscarini, F. 2015. ACS Nano 9, 5051–5062

Cotrone, S., Ambrico, M., Toss, H., Angione, M.D., Magliulo, M., Mallardi, A., Berggren, M., Palazzo, G.; Horowitz, G., Ligonzo, T., Torsi, L. 2012. Organic Electronics 13, 638-644.

Debler, E.W., Kaufmann, G.F., Meijler, M.M., Heine, A., Mee, J.M., Pljevaljčić, G., Bilio, A.J.D., Schultz, P.G., Millar, D.P., Janda, K.D., Wilson, I.A., Gray, H.B., Lerner, R.A., 2008. Science, 319, 1232–1235.

Dequaire, M., Degrand, C., Limoges, B. 1999. Anal. Chem. 71, 2571-2577.

Dtantiev, B.B., Zherdev, A.V. 1996. Biosens. Bioelectron. 11, 179-185.

Eller, P.M., Cassinelli, M.E. 1994. NIOSH Manual of Analytical Methods, DIANE Publising

Feng, X., Zhang, G., Chin, L.K., Liu, A.Q., Liedberg, B. 2017. ACS Sens. 2, 955-960.

Huang, W., Diallo, A.K., Dailey, Besar, J.L.K., Katz, H.E. 2015. J. Mater. Chem. C, 3, 6445-6470.

Humphrey, W, Dalke, A., Schulten, K., *J. Mol. Graph.*, 1996, **14**, 33–38.

INERIS (French Institute for Industrial and Environnmental Risks), DRC-11-112070-03681B, 2012. https://substances.ineris.fr/fr/substance/getDocument/2929. Accessed January 22nd, 2018.

Jia, M., Zhang, Z., Li, J., Shao, H., Chen, L., Yang, X. 2017. Sens. Actua. B 252, 934–943.

Kergoat, L., Herlogsson, L., Braga, D., Piro, B., Pham, M. C., Crispin, X., Berggren, M., Horowitz, G. 2010. Adv. Mater. 22, 2565-2569.

Kergoat, L., Piro, B., Berggren, M., Pham, M.C., Yassar, A., Horowitz, G. 2012. Organic Electronics 13, 1-6.

Khomutov, S.M, Zherdev, A.V., Dzantiev, B.B., Reshetilov, A.N. 1994. Anal. Lett. 27, 2983-2995.

Kroger, S., Turner, A.P.F., Mosbach, K., Haupt, K. 1999. Anal. Chem. 71, 3698-3702.

Lee, J.W., Jun, S.I., Kim, K. 2001. Tet. Lett. 42, 2709–2711

Li, Y., Samarendra, S., Prashant, S. 2010. Adv. Mater. 22. 4862.

Li, J., Zhao, Y., Tan, H.S., Guo, Y., Di, C.A., Yu, G., Liu, Y., Lin, M., Lim, S.H., Zhou, Y., Su, H., Ong, B.S. 2012. Sci Rep. 2, 754.

Morris, G.M., Goodsell, D.S., Halliday, R.S., Huey, R., Hart, W.E., Belew, R.K., Olson, A.J., *J. Comput. Chem.*, 1998, **19**, 1639–1662

Morris, G.M., Huey, R., Lindstrom, W. Sanner, M.F., Belew, R.K., Goodsell, D.S., Olson, A.J., 2009. J. Comput. Chem., **30**, 2785–2791.

Mulla, M.Y., Tuccori, E., Magliulo, M., Lattanzi, G., Palazzo, G., Persaud, K., Torsi, L. 2015. Nature communications, 6, 6010.

Navratilova, I., Skladal, P. 2004. Bioelectrochem. 62, 11 – 18.

Nguyen, T.T.K., Vu, T.T., Anquetin, G., Tran, H.V. Reisberg, S., Noel, V., Mattana, G., Nguyen, Q.V., Tran Dai Lam, Pham, M.C., Piro, B. 2017. Biosens. Bioelectron. 97, 246-252.

Ozkan, D., Kerman, K., Meric, B., Kara, P., Demirkan, H., Polverejan, M., Pinnavaia, T.J. Ozsoz, M. 2002. Chem. Mater. 14, 1755-1761.

Palazzo, G., Tullio, D.D., Magliulo, M., Mallardi, A., Intranuovo, F., Mulla, M.Y., Favia, P., Vikholm-Lundin, I., Torsi, L. 2015, Adv. Mater. 27, 911–916

Panzer, M. J., Frisbie, C.D. 2006. Adv. Funct. Mater. 16, 1051

Piro, B., Wang, D., Benaoudia, D., Tibaldi, A., Anquetin, G., Noel, V., Reisberg, S., Mattana, G., Jackson, B. 2017, Biosens. Bioelectron 92, 215-220.

Prusty, A.K., Bhand. S. 2017. Mater. Res. Express 4, 035306.

Shi, H., Zhao, G., Liu, M., Zhu, Z. 2011. Electrochem. Commun. 13, 1404–1407.

Kladal, P., Kalab, T. 1995. Anal. Chim. Acta 316, 73-78

Suspène, C., Piro, B., Reisberg, S., Pham, M.C., Toss, H., Berggren, M., Yassar, A., Horowitz, G. 2013. J. Mater. Chem. B, 1, 2090-2097.

Taniguchi, M., Kawai, T., 2004, Appl. Phys. Lett. 85, 3298.

Teixeira, C., Serradji, N., Maurel, F., Barbault, F., Eur. J. Med. Chem., 2009, **44**, 3524–3532.

Wagner, S., Bell, J., Biyikal, M., Gawlitza, K., Rurack. K. 2018. Biosens. Bioelectron. 99, 15, 244-250

Wang, X., Yu, J., Wu, X., Fu, J., Kang, Q., Shen, D., Li, J., Chen, L. 2016. Biosens. Bioelectron. 81, 438.

Word Health Organization (WHO). Guidelines for Drinking-water Quality, 2003. http://www.who.int/water_sanitation_health/dwq/chemicals/24D.pdf. Accessed January 22nd, 2018.

Wijaya, I.P.M., Nie, T.J., Gandhi, S., Boro, R., Palaniappan, A., Hau, G.W., Rodriguez, I., Suric, C.R., Mhaisalkar, S.G. 2010. Lab Chip 10, 634–638.

Xie, C., Gao, S., Guo, Q., Xu, K. 2010. Microchim Acta 169, 145–152.

Supplementary Materials

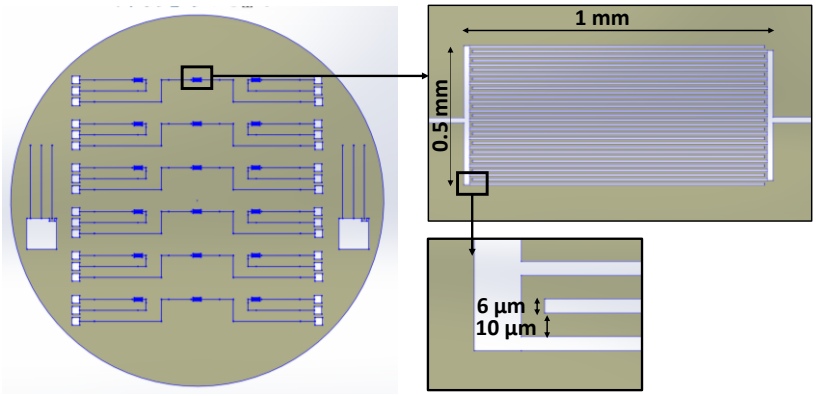

Scheme SI-1. *View of (left) a Si wafer onto which 18 transistors (interdigitated source and drain) are lithographed and (right) details of the device dimensions, including the digit width (6 µm) and channel length (10 µm). The total channel width is 10000 µm.*

1. Gate functionalization

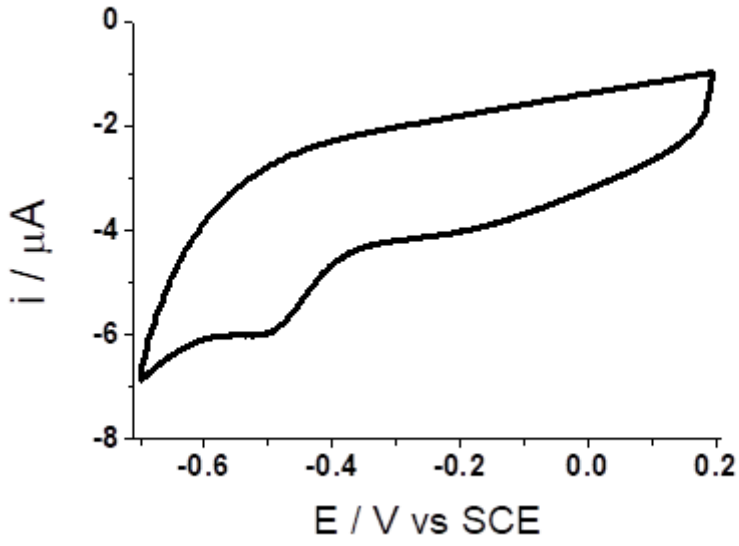

Figure SI-2a. *Cyclic voltammogram corresponding to a 1 mm gold electrode, performed in degassed 5 mL CH_3CN + 190 mg $TBAPF_6$ + 1 mg 2,4-D-aniline + 16 µL tert-butyl nitrite. The potential of the gold electrode was swept from +0.2 V down to -0.7 V and back to 0.2 V at 50 mV s^{-1} for one cycle.*

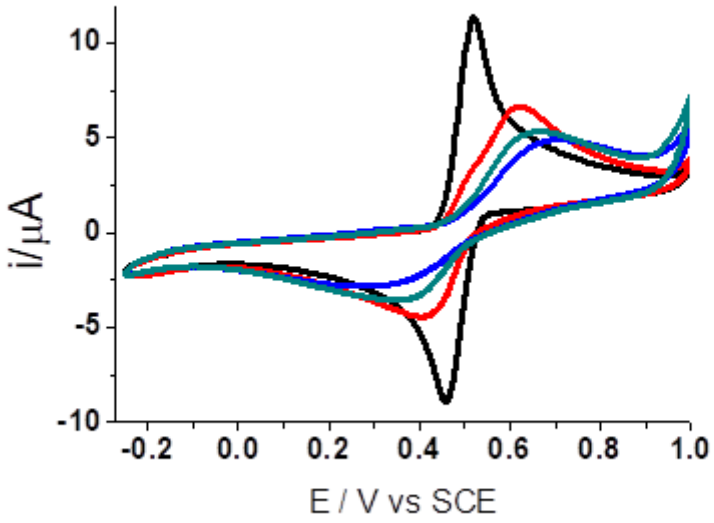

Figure SI-2b. *Cyclic voltammograms recorded in 0.1 M H_2SO_4 + 10^{-3} M dopamine with a 1 mm (black) bare gold electrode; (red) a [2,4-D-C_1]-modified electrode; (blue) a [$Ab_{2,4\text{-}D}$/2,4-D-C_1]-modified electrode and (green) after addition of 2,4-D.*

2. Equivalent electric circuit

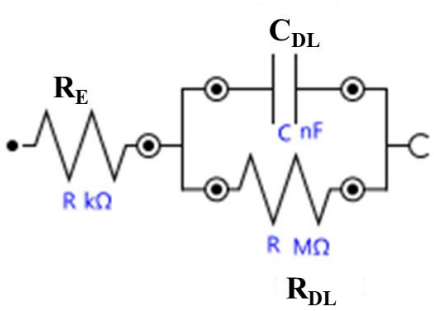

Figures SI-3*. The equivalent circuit used for fitting the EIS spectra of the modified gates*

3. Computational details

To date, there is no structure nor sequence for the 2,4-D antibody (Ab). Nevertheless, we know that this Ab belongs to the G type immunoglobulin (IgG) and that this antibody family recognizes a ligand with the help of its Fast Antigen Binding protein (Fab) domain. Therefore, we realized cross-docking computations to find a consensus Fab structure able to recognize the 2,4-D antigen. This procedure has been already commonly proposed as a tool to

validate molecular docking computations and has demonstrated its reliability and accuracy[1–3] including for Fab.[4]

Currently, 2042 Fab crystal structures are available on the protein data bank.[5] Among these, 325 represent, to date, complexes with Fab and an organic compound with various size. The 2,4-D molecule and our designed molecules are aromatic organic compounds with formula weights ranking from 221 to 503 g mol^{-1}. Therefore, we filtered this database of 325 Fab/ligand structures to keep those which present at least one aromatic carbon and a molecular weight between 200 and 600 g mol^{-1}. According to those criteria, we identified 7 structures of Fab/ligand X-ray structures. We structurally aligned these 7 Fab structures with the multiseq tool[6]. This superimposition is presented on **Figure SI-4** along with the chemical schemes of their ligands.

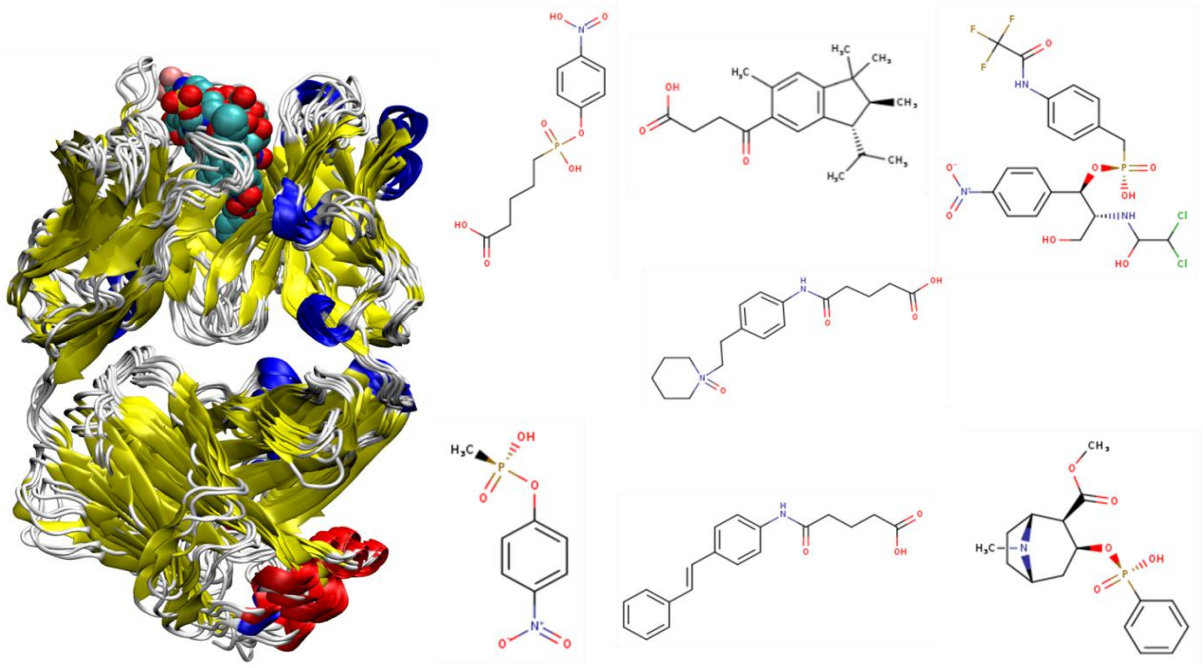

Figure SI-4: Left*: structural alignment of the 7 FAB protein structures (displayed as protein ribbons) with their complexed ligands (with spacefill display).* ***Right****: Molecular schemes of the Fab ligands compounds used for the cross-docking procedure.*

As expected, we observed from the left part of Fig. SI-3 that all ligands are localized on the same protein cavity, illustrating the similar interaction mode for all Ab/Ag complexes. Consequently, a cross-docking process was undertaken in order to identify if one of the

experimental structure was able to reproduce the interaction mode of the 7 experimental ligands. This consensus structure would then be used to identify interaction mode with the 2,4-D ligand. To do that, the 7 ligands were docked in the 7 different Fab targets with the same computational protocol described in the Experimental section of the manuscript. For each of 49 docking calculations, we analyzed the interaction mode and observed if it was similar or not to the one established experimentally. A *yes* (green) or *no* (red) answer of this experimental similarity is summarized in **Table SI-1** below.

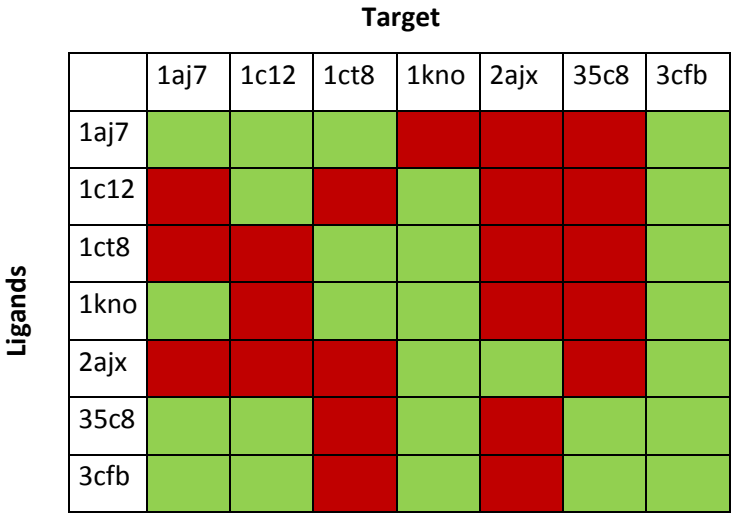

Table SI-1*: Cross-docking results. Columns and rows represent, respectively, the protein targets and ligands for the PDB codes 1aj7, 1c12, 1ct8, 1kno, 2ajx, 35c8 and 3cfb. A green color indicates a reproduction of the experimental binding mode whereas a red color signifies a distinct position when compared to the experimental binding position*

The diagonal of Table SI-1 concerns each ligand with its respective target. The fact that this diagonal is all green implies that our docking protocol efficiently reproduces the experimental position of each ligand with its respective target. This represents a validation of our computational protocol. Besides, the inspection of each column highlights the protein target 3cfb (PDB code) which is able to reproduce each binding modes of all ligands. This consensual target is the one chosen for the molecular docking computations of 2,4-D antigen and their derivatives.

References:

1 J. J. Sutherland, R. K. Nandigam, J. A. Erickson and M. Vieth, *J. Chem. Inf. Model.*, 2007, **47**, 2293–2302.

2 E. J. Bjerrum, *Comput. Biol. Chem.*, 2016, **62**, 133–144.
3 J. Shamsara, *SpringerPlus*, , DOI:10.1186/s40064-016-1972-4.
4 K. P. Kilambi and J. J. Gray, *Sci. Rep.*, 2017, **7**, 8145.
5 RCSB Protein Data Bank - RCSB PDB, https://www.rcsb.org/pdb/home/home.do, (accessed December 13, 2017).
6 E. Roberts, J. Eargle, D. Wright and Z. Luthey-Schulten, *BMC Bioinformatics*, 2006, **7**, 382.

4. Capacitances measurements

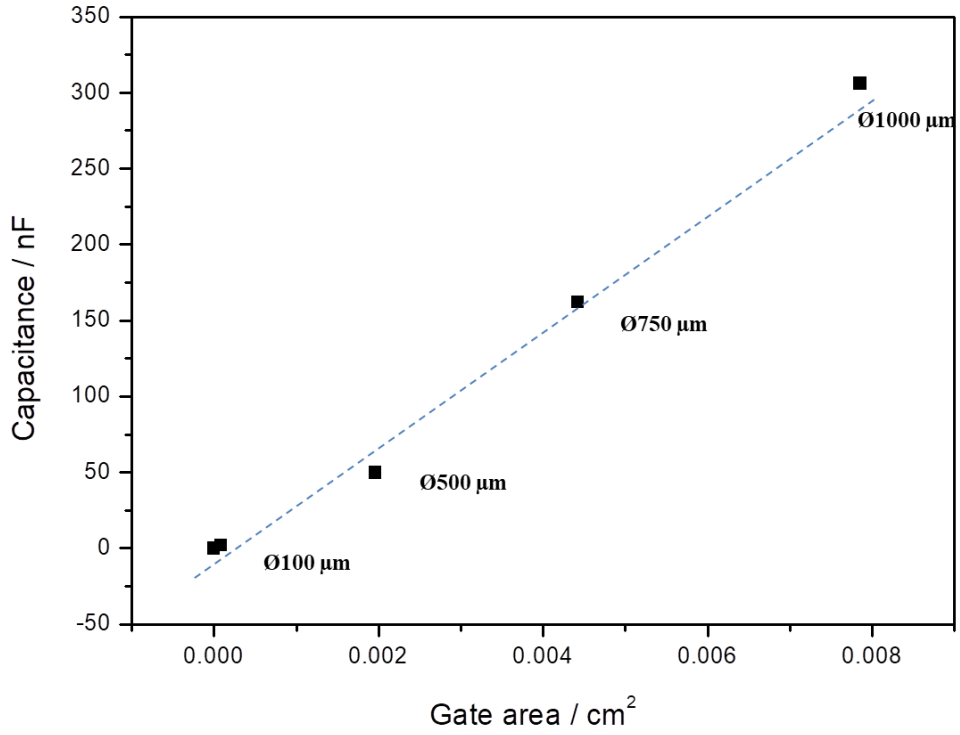

Figure SI-5. *(black squares) Capacitances of the bare gold gate electrodes as a function of their area. (blue dotted line) Expected linear behavior. Capacitances were measured by EIS in a three-electrode electrochemical cell with PBS as electrolyte.*

Table SI-2*: Fitted values of the elements of the simplified Randles circuit of Fig. SI-4.*

Process	Ci	Re (Ω)	Rox
Bare gate	3.20 nF	525	501 kΩ
[2,4-D-C_1]-modified gate	1.40 nF	530	478 kΩ
[$Ab_{2,4\text{-}D}$/2,4-D-C_1]-modified gate	1.01 nF	572	2.22 MΩ
Incubation with 10^{-14} M 2,4,5-T	0.907 nF	567	2.54 MΩ
Incubation with 10^{-14} M 2,4-D	1.26 nF	541	1.60 MΩ
[Ab_{DCF}/2,4-D-C_1]-modified gate	1.18 nF	549	571 kΩ
[Ab_{BPA}/2,4-D-C_1]-modified gate	1.50 nF	550	454 kΩ

Chapter IV PEPTIDE-MODIFIED ELECTROLYTE-GATED ORGANIC FIELD EFFECT TRANSISTORS. APPLICATION TO Cu^{2+} DETECTION

1 Introduction

Copper is a transition metal essential for life. At elevated concentrations, however, it is toxic to living organisms such as algae, fungi, and many bacteria. In humans, it may adversely affect the gastrointestinal, hepatic, and renal systems. It should be stressed that the innocuity of copper in drinking water at concentrations below 2 mg L^{-1}, corresponding to values proposed by the World Health Organization in 1993 has been questioned several times since. For these reasons, it is pertinent to develop a sensitive method for on-site determination of free Cu^{2+} in aqueous media. Of course, copper can be detected and quantify by routine methods, including the most common such as flame atomic absorption spectrometry (FAAS; limit of detection -LoD- in the µg L^{-1} range) or the most sensitive (mass spectrometry coupled to inductively coupled plasma (ICP-MS), or by methods more adapted to a point-of-use format such as colorimetric ones, for example, Liu and Lu (2007) who used ligation DNAzyme complex assembled onto gold nanoparticles [(1)]. In the addition of Cu^{2+}, DNAzyme E47 ligase catalyse the ligation of 2 DNA fragments, which is complementary to 2 kinds of ssDNA self-assembled to AuNPs, respectively. The binding of complementary strands caused the aggregation of AuNPs leading to the change in the size and then of the colour of the AuNP from red to blue (Figure IV.1). This approach was also employed by Xu *et al.* in 2010 [(2)].

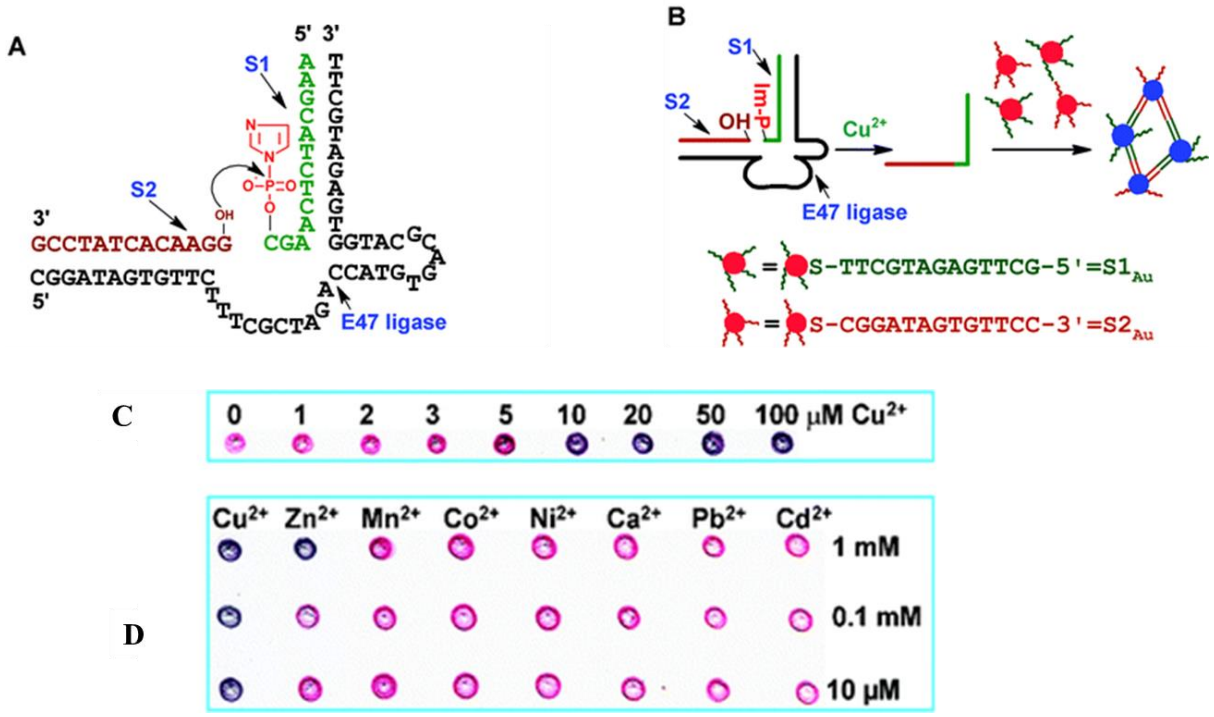

Figure IV.1. Cu^{2+} detection using ligation DNAzyme complex assembled onto gold nanoparticles: (A) Secondary structure of the Cu2+-dependent DNAzyme with DNA ligation activity. (B) Formation of the ligation product and the assembly of AuNPs with it. (C) Colorimetric results for different Cu^{2+} concentrations and (D) for different metal ions [(1)].

Yao *et al.*, in 2013, also monitored Cu^{2+} [(3)]. They used sodium poly(2-(4-methyl-3-thienyloxy)propanesulfonate (PMTPS) as colorimetric probe for Cu^{2+}. The surfactant molecule was formed by reaction of 1-azidododecane (AD) and N,N,N- trimethylprop-2-yn-1-ammonium bromide (TAB) in the presence of catalysts consisting of Cu^{2+} and sodium ascorbate. When the surfactant compound was supplied into the solution of PMTPS containing Cu^{2+}, the solution changed its color from purple to yellow (Figure IV.2). They employed absorption spectrometry to observe the large blue-shift of 150 nm of probe solution in the presence of spiked Cu^{2+}.

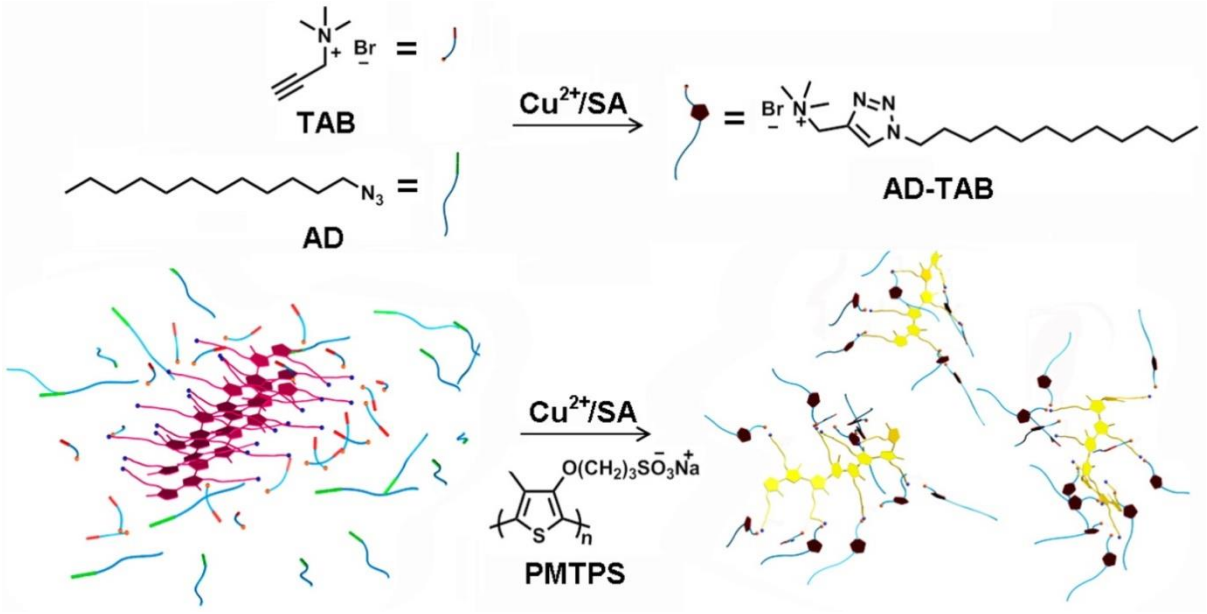

Figure IV.2. Chemical structure of PMTPS, illustration of the formation of AD-TAB and sensing mechanism for the detection of Cu^{2+} (3).

Gan *et al.*, in 2016, reported the specific detection of picomolar Cu^{2+} using an electrochemical sensor (4): p-aminothiophenol (PATP) immobilized on AuNPs decorated with hydrogenated TiS_2 nanosheets were used as solid substrate, and square wave anodic stripping voltammetry (SWASV) was used to measure the electrochemical signal of Cu^{2+} (Figure IV.3). The LoD was 90 pM and the linear range was found from 0.2 nM to 5 µM (Figure IV.4).

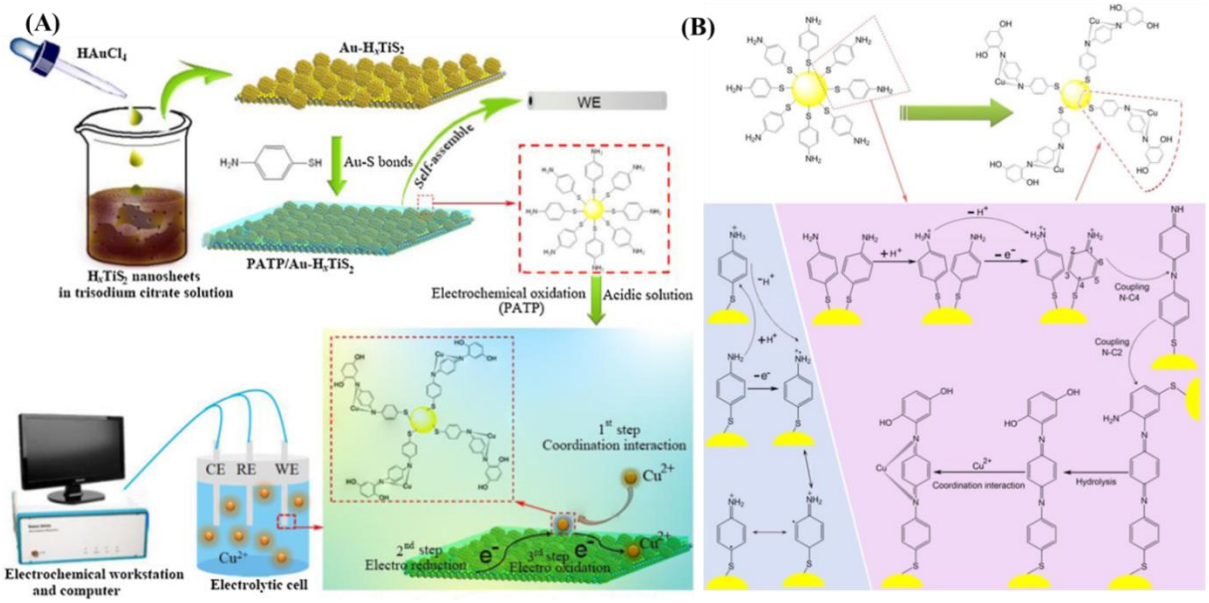

Figure IV.3. The electrochemical sensor for detection of Cu^{2+} applying PATP immobilized on AuNPs decorated with hydrogenated TiS2 nanosheets, by Gan et al. (2016). (A) Sensor design (B) Proposed mechanism for selective detection of Cu^{2+} (4)

.

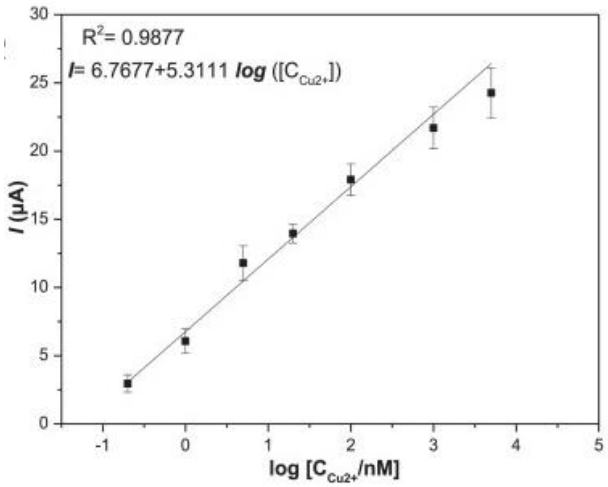

Figure IV.4. Calibration curve corresponding to the detection of Cu^{2+} of the electrochemical sensor investigated by Gan et al. (2016) (4).

Zhu *et al.*, in 2017, followed the same principle (5). The nanomaterial used was gold-labeled multiwalled CNTs and the capture probe was L-histidine (Figure IV.5). The LoD was 10^{-12} M and the linear range between 10^{-11} M and 10^{-7} M (Figure IV.6).

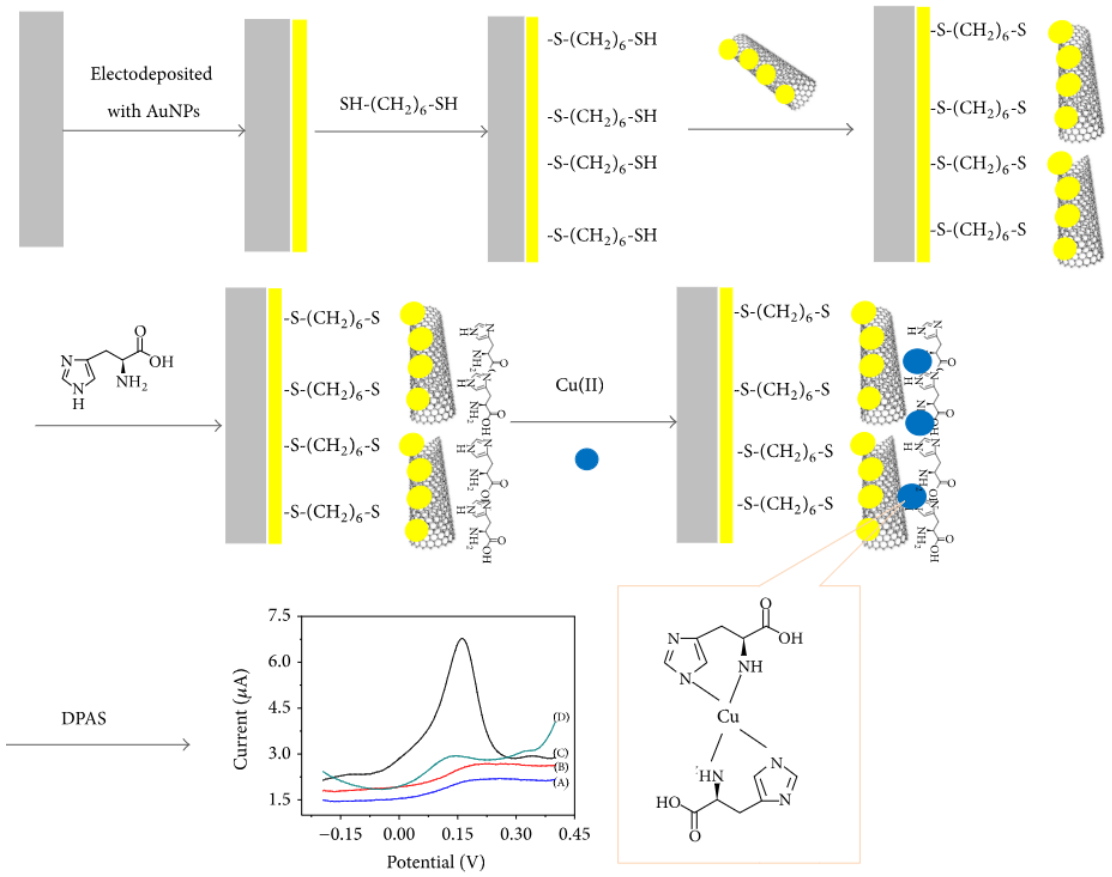

Figure IV.5. Principle of the sensor applying L-histidine immobilized on gold-labeled multiwalled CNTs proposed by Zhu et al. in 2017 [(5)].

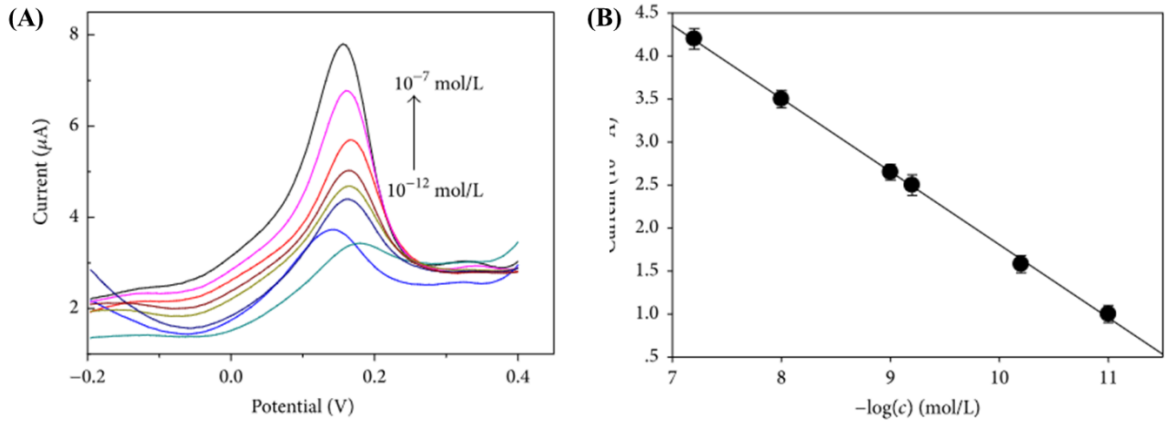

Figure IV.6. The Cu^{+2} detection by L-histidine immobilized on gold-labeled multiwalled CNTs-based sensor (A) Stripping peak currents for various Cu^{2+} concentrations; (B) Corresponding calibration curve [(5)].

As shown, no work has been reported involving EGOFETs for Cu^{2+} detection. However, the transduction principle which has been described in Chapter III for molecular recognition between antibodies and antigens should be also applicable for other kinds of recognition which produce a tiny change in capacitance or some electrostatic effects. For example, Fillaud *et al.*, in 2018, reported a work where the gate electrode was functionalized by an hydrogel responsive to pH changes [(6)]. Hydrogel grafting proceeded by two steps: grafting of 4-bromobenzenediazonium (BrBD) then grafting of an ultrathin poly(acrylic acid) (PAA) layer, which swells or unswells depending on pH. Functionalizing the gate led to a shift of the threshold voltage toward negative values (Figure IV.7). The hydrogel-gated EGOFET was able to sense pH changes between 6 and 9 (Figure IV.8).

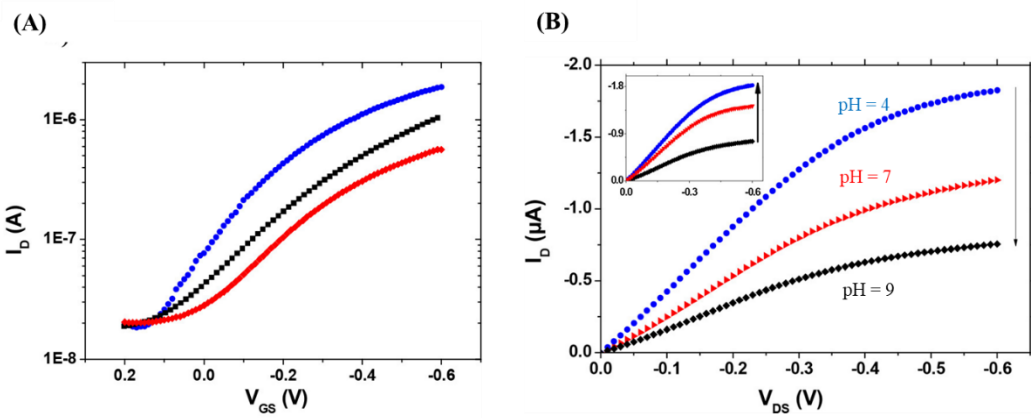

Figure IV.7. Electrical characteristics of an EGOFET with a hydrogel-modified gate electrode: (A) Transfer curves (V_{DS} = −0.6 V) of a (●) bare Au-gated, (■) BrBD-functionalized, and (♦) AA-functionalized EGOFET. In al cases, the electrolyte was PBS. (B) Output curves (V_{GS} = −0.6 V) of a PAA-functionalized EGOFET at different pH [(6)].

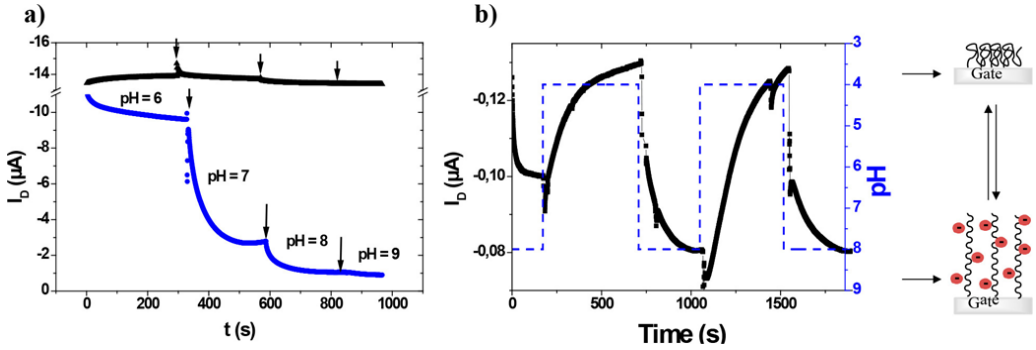

Figure IV.8. Plots of I_D for an EGOFET with a hydrogel-modified gate electrode, versus time: (a) (V_{GS} = V_{DS} = −0.4 V) performed using a (black line) bare gate electrode and (blue line) a PAA-functionalized gate for successive pH jumps (values indicated on the graph); each arrow indicates injection of NaOH. (b) pH was abruptly varied from 8 to 4 and then back to 8 (twice) [(6)].

Significant changes upon binding of the target on the immobilized probe can only be obtained if the probe is sufficiently small not to screen the target from the gate electrode surface or undergoes a thorough structural reorganization upon binding. Keeping this in mind, I developed gate-modified EGOFET immunosensors following a specific strategy [(7)]. Instead of antibodies, DNA or even polymer hydrogels, I used peptide aptamers as probe. Compared to the 4 nucleobases that code DNA, peptides are made of more than 20 amino acids, which makes greater the number of possible combinations (4^n versus 20^n, with n the number of nucleobases or amino acids in the sequence, respectively). Although peptide aptamer have been often reported in electrochemical sensors, it has been described only recently on EGOFETs, by Berto *et al.* in 2018, who described a peptide aptasensor for the detection of TNFα, a protein of 25 kD.

But peptides can also act as very effective and specific capture probes for metal ions [(8)]. To illustrate these properties in view of electrochemical detection, Gooding and colleagues used the copper-binding tripeptide Gly-Gly-His (glycine-glycine-histidine) for detecting Cu^{2+} in aqueous media and published a series of articles on this topic For example, Yang *et al.*, 2001, reported for Cu^{2+} detection using this tripeptide attached to a self-assembled monolayer; comlexation of Cu^{2+} by the tripeptide modulated square wave voltammetry (SWV) signals [(9)]. The detection limit was less than 0.2 ppt. Yang *et al.*, in 2003, reported the same procedure [(10)] (Figure IV.9).

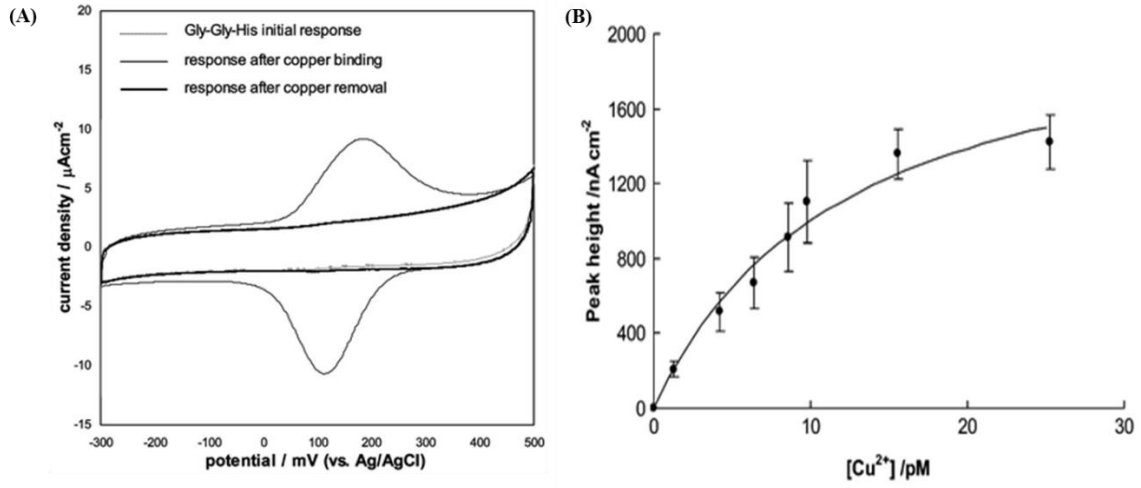

Figure IV.9. Copper-binding tripeptide Gly-Gly-His-based sensor, by Yang et al. (2003) : (A) Cyclic voltammogram of a Gly-Gly-His-modified electrode before and after exposure to copper in 0.05 M ammonium acetate buffer. (B) Plot of I_{SWV} vs. concentration of copper [(10)].

Continueing the study of Gly-Gly-His as probe to detect Cu^{2+}, Gooding's group members, *Liu et al.*, in 2006 [(11)], using cyclic voltammetry on glassy carbon and Au electrodes functionalized by electroreduction of a 4-carboxyphenyl diazonium salt and a SAM, respectively, followed by Gly-Gly-His coupling. They demonstrated that both functionalization procedures lead to similar performances. In 2013, Wawrzyniak *et al.* described a back-side contact miniaturized sensor to electrochemically detect Cu^{2+} [(12)]. Gold electrodes were modified by electroreduction of 4-aminobenzoic acid, onto which the Gly-Gly-His was coupled. Square wave voltammetry was used for the measurements, with a LoD of 100 mM (6.5 ppb) (Figure IV.10).

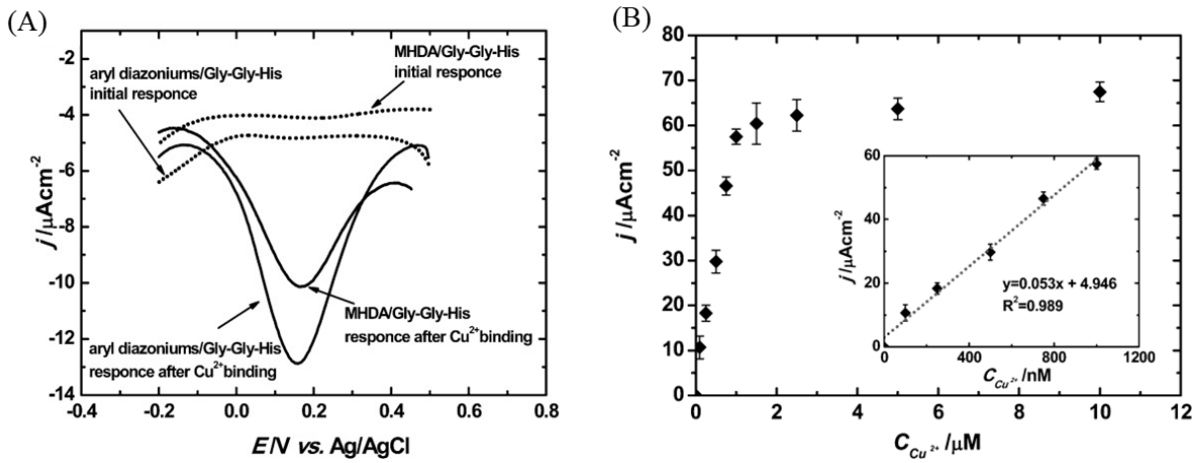

Figure IV.10. Copper-binding tripeptide Gly-Gly-His-based electrochemical sensor, by Wawrzyniak et al: (A) Square wave voltammograms of a carbon electode modified with Gly-Gly-His before and after exposure to copper ions (0.1 µM Cu^{2+}) in 50 mM ammonium acetate solution (pH 7.0), f=25 Hz. (B) Plot of I_{swv} versus concentration of accumulated copper(II) ion [(12)].

In this Chapter IV, I propose an approach which combines the selectivity of the Gly-Gly-His peptide probe (GGH) with the sensitivity of EGOFETs, in particular using the gate-functionalization strategy, where the peptide was immobilized by direct electrooxidation of the primary amine of the first glycine moiety of GGH. Cu^{2+} complexation by grafted GGH was first evidenced electrochemically, using cyclic and square wave voltammetries, then it was demonstrated that GGH-modified EGOFETs can transduce Cu^{2+} complexation through changes of the EGOFETs output and transfer curves, respectively. In particular, the threshold voltage (V_{Th}) shift was identified as a good quantitative parameter.

Next Section, I reproduced the manuscript I am submitting in September 2018 to Biosensors and Bioelectronics, entitled "*Peptide-modified Electrolyte-Gated Organic Field Effect Transistor. Application to* Cu^{2+} *Detection*", which illustrates how charges immobilized on the gate of an EGOFETs can influence the electrical characteristics of the device. I applied this to the sensing of Cu^{2+} in water, using the peptide Gly-Gly-His grated on the gate electrode.

2 References

1. Liu, J., and Lu, Y. (2007) Colorimetric Cu2+ detection with a ligation DNAzyme and nanoparticles, *Chemical communications*, 4872.

2. Xu, X., Daniel, W. L., Wei, W., and Mirkin, C. A. (2010) Colorimetric Cu(2+) detection using DNA-modified gold-nanoparticle aggregates as probes and click chemistry, *Small 6*, 623-626.

3. Yao, Z., Yang, Y., Chen, X., Hu, X., Zhang, L., Liu, L., Zhao, Y., and Wu, H. C. (2013) Visual detection of copper(II) ions based on an anionic polythiophene derivative using click chemistry, *Analytical chemistry 85*, 5650-5653.

4. Gan, X., Zhao, H., Quan, X., and Zhang, Y. (2016) An Electrochemical Sensor based on p-aminothiophenol/Au Nanoparticle-Decorated H x TiS 2 Nanosheets for Specific Detection of Picomolar Cu (II), *Electrochimica Acta 190*, 480-489.

5. Zhu, R., Zhou, G., Tang, F., Tong, C., Wang, Y., and Wang, J. (2017) Detection of Cu(2+) in Water Based on Histidine-Gold Labeled Multiwalled Carbon Nanotube Electrochemical Sensor, *International journal of analytical chemistry 2017*, 1727126.

6. Fillaud, L., Petenzi, T., Pallu, J., Piro, B., Mattana, G., and Noel, V. (2018) Switchable Hydrogel-Gated Organic Field-Effect Transistors, *Langmuir : the ACS journal of surfaces and colloids 34*, 3686-3693.

7. Nguyen, T. T. K., Nguyen, T. N., Anquetin, G., Reisberg, S., Noel, V., Mattana, G., Touzeau, J., Barbault, F., Pham, M. C., and Piro, B. (2018) Triggering the Electrolyte-Gated Organic Field-Effect Transistor output characteristics through gate functionalization using diazonium chemistry: Application to biodetection of 2,4-dichlorophenoxyacetic acid, *Biosensors & bioelectronics 113*, 32-38.

8. Sigel, H. (1982) Coordinating Properties of the Amide Bond. Stability and Structure of Metal Ion Complexes of Peptides and Related Ligands, *Chemical Review 82*, 82.

9. Yang, W., Jaramillo, D., Gooding, J. J., Hibbert, D. B., Zhang, R., Willett, G. D., and Fisher, K. J. (2001) Sub-ppt detection limits for copper ions with Gly-Gly-His modified electrodes, *Chemical communications*, 1982-1983.

10. Yang, W., Chow, E., Willett, G. D., Hibbert, D. B., and Gooding, J. J. (2003) Exploring the use of the tripeptide Gly–Gly–His as a selective recognition element for the fabrication of electrochemical copper sensors, *The Analyst 128*, 712-718.

11. Liu, G., Nguyen, Q. T., Chow, E., Böcking, T., Hibbert, D. B., and Gooding, J. J. (2006) Study of Factors Affecting the Performance of Voltammetric Copper Sensors Based

on Gly-Gly-His Modified Glassy Carbon and Gold Electrodes, *Electroanalysis 18*, 1141-1151.

12. Wawrzyniak, U. E., Ciosek, P., Zaborowski, M., Liu, G., and Gooding, J. J. (2013) Gly-Gly-His Immobilized On Monolayer Modified Back-Side Contact Miniaturized Sensors for Complexation of Copper Ions, *Electroanalysis 25*, 1461-1471.

3 Article (submitted, Biosens. Bioelectron., September 2018)

Peptide-modified Electrolyte-Gated Organic Field Effect Transistor. Application to Cu^{2+} Detection.

T.T.K. Nguyen [a,b], H.V. Tran [c], T.T. Vu [b], V. Noël [a], G. Mattana [a], M.C. Pham [a], B. Piro [a*]

[a] *Univ. Paris Diderot, Sorbonne Paris Cité, ITODYS, UMR 7086 CNRS, 15 rue J-A de Baïf, 75205 Paris Cedex 13, France*

[b] *Department of Advanced Materials Science and Nanotechnology (AMSN), University of Science and Technology of Hanoï (USTH), Vietnam Academy of Science and Technology (VAST), 18 Hoang Quoc Viet, Nghĩa Đô, Cầu Giấy, Hanoi, Viet Nam.*

[c] *Department of Inorganic Chemistry, School of Chemical Engineering, Hanoi University of Science and Technology(HUST), 1st Dai Co Viet Road, Hanoi, Viet Nam*

Corresponding author:
Prof. Benoît Piro; Univ. Paris Diderot, Sorbonne Paris Cité, ITODYS, UMR 7086 CNRS, 15 rue J-A de Baïf, 75205 Paris Cedex 13, France. Telephone number: + 33 157 277 224. Email address: piro@univ-paris-diderot.fr

Abstract

This work proposes an approach for Cu^{2+} sensing in water which combines the selectivity of the Gly-Gly-His peptide probe with the sensitivity of the electrolyte-gated organic field effect transistor. The oligopeptide probe was immobilized onto the gate electrode by electrooxidation of the primary amine of the first glycine moiety of the peptide. Cu^{2+} complexation by the grafted GGH was first evidenced electrochemically, using cyclic and square wave voltammetries, then it was demonstrated that GGH-modified EGOFETs can transduce Cu^{2+} complexation through a significant threshold voltage shift. The limit of detection is ca. 10^{-12} M and the sensitivity in the linear range (10^{-12}-10^{-8} M) is of 20 mV dec^{-1} (threshold voltage changes) and 1 mA dec^{-1} (drain current changes).

Keywords: Electrolyte-Gated OFET; Peptide sensor; Cu^{2+} detection

Graphical Abstract

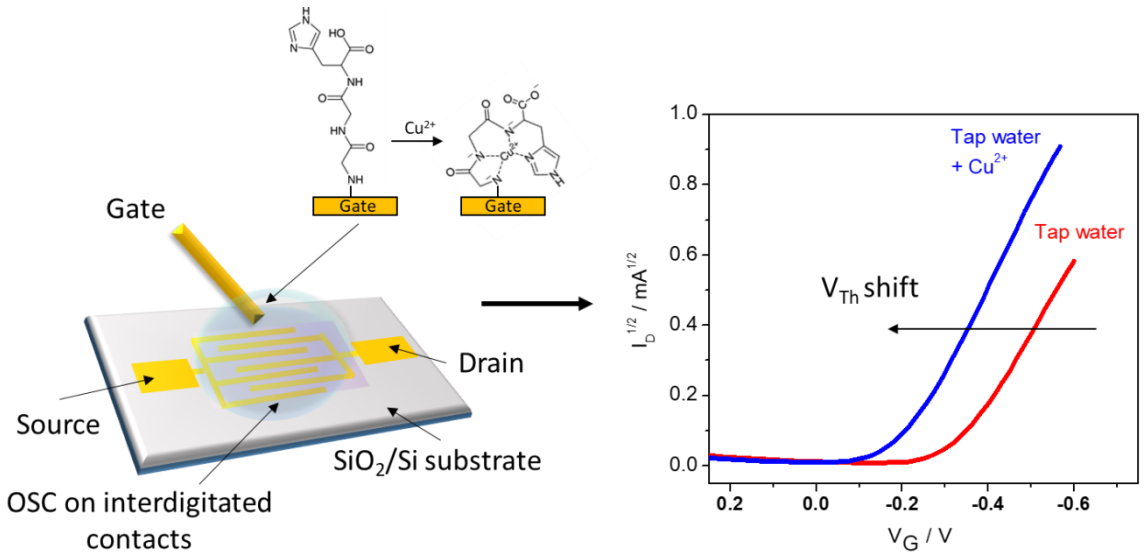

Highlights

► The glycine-glycine-histidine tripeptide was grafted on the gate of an electrolyte-gated organic field-effect transistor ► The tripeptide is specific for complexation of Cu^{2+} ions ► Cu^{2+} complexation is transduced into a positive shift of the threshold voltage of the transistor

1. Introduction

Electrolyte-Gated Organic Field Effect Transistors (EGOFETs), also named Liquid-Gated FETs (LG-FETs), are very promising sensing devices. They are thin-film transistors (TFTs) where the non-electronically conducting material in-between the gate and the semiconductor, instead of being a dielectric polymer, is an electrolyte (Taniguchi and Kawai, 2004, Bäcklund *et al.*, 2004, Panzer and Frisbie, 2006) which can even be deionized water or aqueous biological buffers (Kergoat *et al.*, 2010). If we apply on EGOFETs the well-known equation of the quadratic model describing the behavior of classical FETs and OFETs (Equation 1), every parameter is defined in a similar way than for classical FETs but the capacitance corresponds in this case not to the oxide capacitance but to the electrolyte capacitance, i.e. the reciprocal sum of the capacitances of the gate/electrolyte and electrolyte/semiconductor interfaces.

$$(\mathbf{Eq.\ 1}) \qquad I_D = \mu \frac{W}{2L} C_{eff}(V_{GS} - V_{Th})^2 \text{ and } I_D = I_{D,Sat} \text{ for } |V_{DS}| > |V_{GS} - V_{Th}|$$

with I_D the drain current, W and L the channel width and length, respectively, V_{GS} the voltage difference between the gate electrode (V_G) and the source electrode (V_S), V_{Th} the threshold voltage, μ the mobility of the charge carriers and C_{eff} the overall interfacial effective capacitance. $I_{D,Sat}$ is the drain current at saturation when V_{DS} (difference between the drain and source voltages V_D-V_S) is large before V_{GS}-V_{Th}.

Most EGOFETs use p-type semiconductors. Under operation, the gate electrode is negatively polarized as well as the drain electrode, while the source is grounded. This polarization means that mobile charges in the electrolyte (ions) accumulate at the gate/electrolyte and semiconductor/electrolyte interfaces, in the form of two electrical double layer (EDL) of opposite charge, positive at the gate surface and negative at the semiconductor surface. Mirror positive charges (holes) then accumulate within the OSC, forming the conductive channel. As explained above, the density of charge carriers in the channel is directly dependent on the gate potential or, more precisely, on the density of charge at the respective interfaces. For a water/gold interface, for example, the capacitance is of several tens of µF cm^{-2}, i.e. hundred times more than that of a classical dielectric/semiconductor interface. Consequently, instead of the tens of volt that are necessary for operating classical dielectric-based OFETs, EGOFETs can be operated at hundred times lower voltages, i.e. a few hundreds of mV (Kergoat *et al.*, 2012).

Since the first description of EGOFETs operating in water (Kergoat, Herlogsson *et al.*, 2012), EGOFET-based biosensors are developing fast. Because EGOFETs are not only sensitive to changes at the semiconductor/electrolyte interface, but also to changes at the electrolyte/gate interface, there are two different approaches to biofunctionalize EGOFETs: at the semiconductor/electrolyte interface (Cotrone *et al.*, 2012; Kergoat, Piro *et al.*, 2012; Suspène *et al.*, 2013; Palazzo *et al.*, 2015; Magliulo *et al.*, 2016; Piro *et al.*, 2017), or at the gate/electrolyte interface (Casalini *et al.*, 2013; Casalini *et al.*, 2015; Mulla *et al.*, 2015; M. Berto *et al.*, 2016; Diacci et al., 2017; Thomas *et al.*, 2018; Nguyen *et al.*, 2018; Fillaud *et al.*, 2018; Berto *et al.*, 2018). In the latter case, physicochemical changes occurring on the gate, e.g., for an EGOFET biosensor, a tiny change in capacitance produced by a target/probe recognition, is transduced into a drain current variation, for constant gate and drain voltages.

However, significant changes upon binding of the target on the probe can only be obtained if the probe is sufficiently small not to screen the target from the gate electrode surface or

undergoes a thorough structural reorganization upon binding. Keeping this in mind and following a specific strategy, gate-modified EGOFET immunosensors have been developed (Nguyen *et al.*, 2018). Instead of antibodies, DNA can also be used as capture probes; for example, DNA-based EGOFETs have been described for hybridization of nucleic acids targets (White *et al.*, 2015). Following the same idea, peptide aptamers, which have been thoroughly reported in electrochemical sensing devices or even in classical FETs, may also been used. Compared to the 4 nucleobases that code DNA, peptides are made of more than 20 amino acids, which makes greater the number of possible ligand combinations (4^n versus 20^n, with n the number of nucleobases or amino acids in the sequence, respectively). However, this has been described only recently on EGOFETs, by Berto *et al.*, 2018, who described a peptide aptasensor for the detection of tumor necrosis factor alpha (TNFα), a large protein of 25 kD. Peptides can also act as very effective and specific capture probes for metal ions (Sigel and Martin, 1982, Kozlowski *et al.*, 1999). To illustrate these properties in view of electrochemical detection, Gooding and colleagues used the known copper binding tripeptide Gly-Gly-His (glycine-glycine-histidine) for detecting Cu^{2+} in aqueous media and published a series of articles on this topic (Yang *et al.*, 2001; Gooding *et al.*, 2001; Yang *et al.*, 2003; Chow and Gooding, 2006; Wawrzyniak *et al.*, 2013).

From an analytical point of view, copper is a transition metal essential for life. At elevated concentrations, however, it is toxic to organisms such as algae, fungi, and many bacteria, and in humans may adversely affect the gastrointestinal, hepatic, and renal systems. It should be stressed that the innocuity of copper in drinking water at concentrations below 2 mg L^{-1}, corresponding to values proposed by the World Health Organization in 1993 (WHO, 1993) has been questioned several times since. For these reasons, it is pertinent to develop a sensitive method for on-site determination of free Cu^{2+} in aqueous media. Of course, copper can be detected and quantify by routine methods, including the most common such as flame atomic absorption spectrometry (FAAS; limit of detection -LoD- in the µg L^{-1} range) or the most sensitive mass spectrometry coupled to inductively coupled plasma (ICP-MS), or by methods more adapted to a point-of-use format such as optical (Liu and Lu, 2007; Xu *et al.* 2010; Yao *et al.*, 2013; Udhayakumari *et al.*, 2017) or electrochemical techniques (Wawrzyniak *et al.*, 2013; Gan *et al.*, 2016; Zhu *et al.*, 2017 or other references of Gooding and coworkers already cited above).

In this work, we propose an approach which combines the selectivity of the Gly-Gly-His peptide probe (GGH) with the sensitivity of EGOFETs, in particular using the gate-

functionalization strategy, where the peptide was immobilized by direct electrooxidation of the primary amine of the first glycine moiety of GGH. Cu^{2+} complexation by grafted GGH was first evidenced electrochemically, using cyclic and square wave voltammetries, then it was demonstrated that GGH-modified EGOFETs can transduce Cu^{2+} complexation through changes of the EGOFETs output and transfer curves, respectively. In particular, the threshold voltage (V_{Th}) shift was identified as a good quantitative parameter. **Fig. 1** summarizes the approach followed in this work.

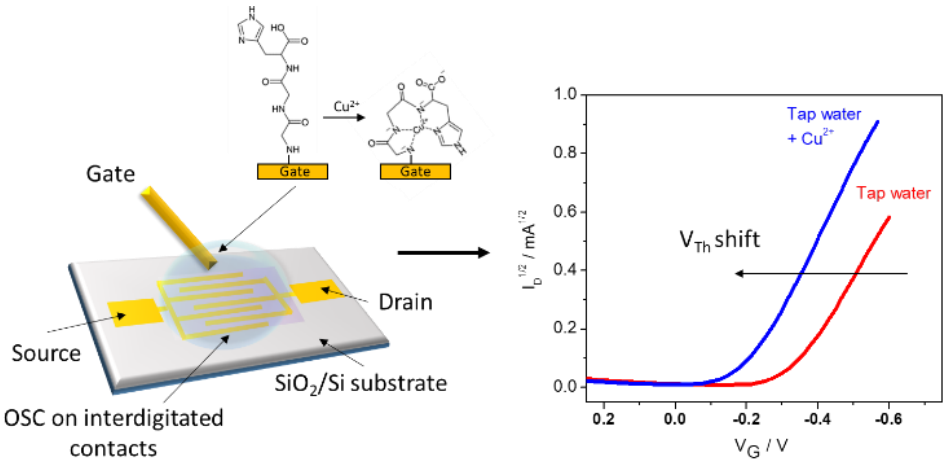

Figure 1. *Schematic representation of the electrolyte-gated organic field-effect transistor with spin-coated DPP-DTT semiconductor on top of interdigitated source and drain contacts, tap water as electrolyte and a gold gate onto which GGH is grafted. Upon the presence of Cu^{2+}, GGH folds, which modifies the gate/electrolyte interface and leads to a positive shift in threshold voltage.*

2. Materials and methods

2.1. Chemicals and materials

The fabrication procedures for the lithographied transistors and the gate microelectrodes are described in Sections SI.1 and SI.2 of the Supplementary Information document, respectively. Gly-Gly-His (diglycyl-histidine, CAS Number 7451-76-5) was purchased from Sigma-Aldrich. Poly(N-alkyldiketopyrrolopyrrole dithienylthieno[3,2-b]thiophene) (DPP-DTT) was purchased from Ossila (England), with M_w = 280 ± 10 kDa and PDI = 3.8 ± 0.1. Lithium perchlorate ($LiClO_4$) 98% was purchased from Alfa Aesar. Copper(II) sulfate pentahydrate ($CuSO_4.5H_2O$) was purchased from Prolabo, France. Phosphate buffer saline (PBS), dichlorobenzene 98%, chlorobenzene-anhydrous, 99.8%, isopropanol, 3-mercapto

propanol (3-MCP) and all other reagents and solvents were purchased from Sigma Aldrich and used without further purification. Aqueous solutions were made with MilliQ water or tap water, depending on conditions.

2.2. Gate functionalization

Gly-Gly-His peptide was grafted on 100 µm diameter homemade gold microelectrodes by sweeping the electrode, in MilliQ water containing 5 mM Gly-Gly-His + 0.1 M $LiClO_4$ as supporting electrolyte, between +0.5 V and +1.5 V at 50 mV s^{-1} for five cycles.

2.3. X-ray photoelectron spectroscopy characterizations

For XPS characterization, 1 cm^2 piece of gold-coated silicon wafers were used instead of gold microelectrodes. The spectrometer was a Thermo ESCALAB using a monochromic Al Kα source at 1486.6 eV.

2.4. Electrochemical and electrical characterizations

Electrografting of the Gly-Gly-His peptide was characterized using dopamine as redox probe. Cyclic voltammetry and square wave voltammetry were performed on an Autolab PGSTAT 302N controlled by NOVA 2.0 software. A conventional three-electrode setup was used, with a platinum grid of about 2 cm^2 as counter electrode, a commercial saturated calomel reference electrode (SCE, Metrohm) used through a salt bridge, and home-made glass-sealed Au microelectrodes as working electrodes (100 µm in diameter). Square wave voltammetry (SWV) was performed using a modulation amplitude of 50 mV, an interval time of 80 ms, a step of 2 mV and a frequency of 12.5 Hz. Electrochemical impedance spectroscopy (EIS) was performed with the same equipment and cell. The frequency ranged from 100 kHz to 100 mHz, with a perturbation amplitude of 10 mV. An equivalent circuit composed of a resistance R_E (electrode+electrolyte resistance) in series with a parallel $R_{DL}C_{DL}$ circuit (resistance and capacitance of the electrical double layer) was used for fitting.

For measurement of the transistors characteristics, a lab-made PDMS cover forming a well (3 mm in diameter, 5 mm in depth) was put over the semiconducting channel and filled with 200 µL of solution (PBS or MilliQ water), into which the gate electrode was dipped. Output characteristics were recorded by sweeping the drain-source voltage between 0 V and -0.40 V at 170 mV s^{-1}; the gate voltage V_{GS} was incrementally switched from +0.3 V to -0.6 V by steps of 0.1 V. The off current (I_{off}) corresponds to V_{GS} = 0 V and the on current (I_{on}) to V_{GS} =

-0.6 V. Transfer curves were obtained by sweeping V_{GS} from 0.2 V to -0.6 V at 170 mV s^{-1} at constant V_{DS} = -0.4 V. The electrical characteristics were recorded using a Keithley 4200 Semiconductor Characterization System.

3. Results and discussion

3.1. Grafting of the Gly-Gly-His peptide probe

There are multiple examples of peptide immobilization on electrodes available in the literature. Among the reported techniques, the two most common approaches which have been already employed for functionalization of EGOFETs gates are self-assembly of alkylthiols on gold (Casalini *et al.*, 2013; Casalini *et al.*, 2015; Mulla *et al.*, 2015; M. Berto *et al.*, 2016; Diacci et al., 2017; Thomas *et al.*, 2018) and, more recently, aryl diazonium electrografting (Nguyen *et al.*, 2018; Fillaud *et al.*, 2018). However, these approaches may imply that the active part of the capture probe is separated from the gate surface by the anchoring moiety (alkylthiol chain or aryl diazonium group). Considering that the sensitivity of EGOFETs is best when the capture probe is immobilized as close as possible from the metallic surface, Berto *et al.*, 2018 were the first to propose the direct immobilization of a histidine-tagged Affimer on the gate electrode of an EGOFET, instead of conventional antibodies (Affimers are commercial 12–14 kDa proteins significantly smaller than IgG antibodies) and reported excellent results.

In this work, we were guided by a similar idea. We propose here the direct electrografting of the Gly-Gly-His peptide (GGH, 0.27 kDa) through the first primary amine-terminated Gly residue. Electrografting of amine-containing compounds has been described first by Barbier *et al.*, 1990, then Deinhammer *et al.*, 1994. Due to steric effects, it has been proved that only primary amines are grafted, with the exclusion of secondary and tertiary amines. The process has been reviewed by Belanger and Pinson, 2011. **Fig. 2A** shows CVs obtained for electrografting of 5 mM GGH in PBS. The first scan evidences glycine oxidation, starting at ca. 0.7 V vs SCE. Further cycling shows passivation of the electrode (the oxidation starts at ca. 1 V during the second scan and can be considered negligible for the following cycles). **Fig. 2B** shows CVs characterizing the electrode state before (red dashed curve) and after (black curve) GGH grafting for 5 cycles, using dopamine as redox probe. As shown,

dopamine still reacts after grafting, through a mixed process which shows that the surface is not completely blocked. A better blocking was achieved after adsorption of 3-mercaptopropanol on a GGH-grafted electrode (GGH-modified electrodes were put in a 10^{-5} M aqueous 3-MCP solution for 2h; blue dotted curve). However, electron transfer still takes place, which shows that it probably occurs accross the thin peptide monolayer.

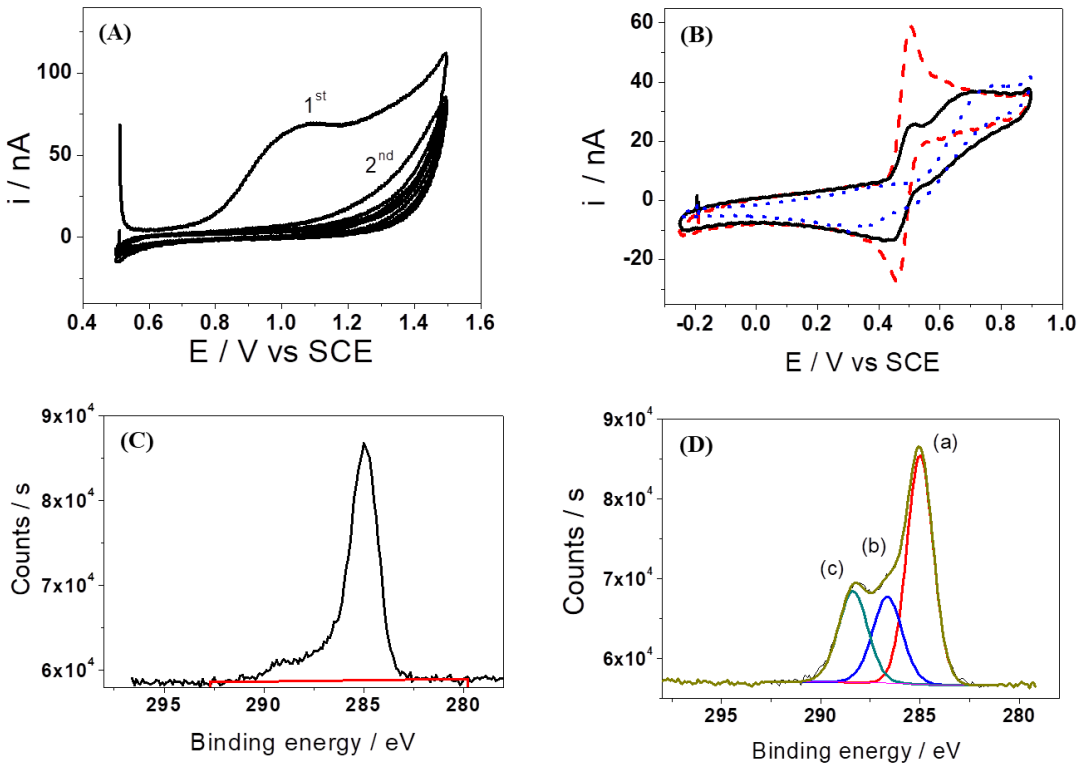

Figure 2. (A) *Cyclic voltammograms (5 cycles, v = 50 mV s^{-1}, between 0.5 V and 1.5 V) corresponding to electrooxidation of Gly-Gly-His (5 mM) on a gold gate (diameter = 100 µm), in argon-saturated PBS. The first cycle shows an oxidation wave corresponding to the oxidation of the primary amine of the first Gly residue. Following cycles show passivation.* ***(B)*** *Cyclic voltammograms recorded in 0.1 M H_2SO_4 + 10^{-3} M dopamine with a 100 µm bare gold gate electrode (red dashed curve), the same electrode modified with GGH as described above (black solid curve) and the same electrode modified with GGH + 3-MCP (blue dotted curve).* ***(C)*** *XPS spectrum of C_{1s} for a bare gold gate electrode and* ***(D)*** *XPS spectrum of C_{1s} for a GGH-modified gold gate electrode.*

XPS was performed on bare (**Fig. 2C**) and GGH-modified electrodes (**Fig. 2D**) to characterize GGH grafting (XPS data are gathered in Table SI.1). The C_{1s} spectrum of the bare gold electrode shows the usual contamination carbons, with a main peak at 285 eV corresponding to C-C and C=C aliphatic carbons and a small proportion (4%) of C-O and O-C=O carbons around 289 eV. Conversely, the C1s peak of the GGH-modified gold electrode is convoluted into 3 contributions at 285 eV (a), 286.6 eV (b) and 288.4 eV (c) which can be attributed to C-C and C=C aliphatic carbons, C-N carbons, and C-O, C=N, C=O and O-C=O carbons, respectively. The GGH peptide (chemical structure shown on Fig. 1) carries 10 carbons, of which only one is purely aliphatic and bound to other carbon atoms (C-C or C=C); it is expected to appear at 285 eV. Considering that the C_{1s} spectrum of the unmodified Au gate shows aliphatic C-C or C=C carbons with a similar intensity that the one observed for the GGH-modified gate, the contribution of this unique carbon from GGH at 285 eV was not considered. 5 other carbons (C-N) from GGH are expected to appear at 286.6 eV and 4 carbons (C-O, C=N, C=O and O-C=O) at 288.4 eV. For a quantitative analysis, we considered only carbons from C-N, C-O, C=N, C=O and O-C=O, and nitrogen N_{1s} (other atoms such as C-C, C=C or O_{1s} were present on bare gold and considered as pollutants of the surface). Ratio given on the last column of Table SI.1 are consistent with the actual atomic ratio, of 33% for C-N (found: 29.7%), 26.7% for C=N, C=O and O-C=O (found: 31.5%) and 33% for N_{1s} (found: 38.8%). The excess of nitrogen partly comes from polluting nitrogen, which represent ca. 10% of the total nitrogen, as measured on the non-modified Au surface.

3.2. Characterization of Cu^{2+} capture

To characterize Cu^{2+} capture by the GGH layer, square wave voltammetry (SWV) was performed on GGH-modified gate electrodes after incubation in PBS, PBS + 10^{-5} M $MnCl_2$, PBS + 10^{-5} M $FeSO_4$ and PBS + 10^{-5} M $CuSO_4$ (**Fig. 3A**). It appears that no change in current was observed for electrodes incubated in Mn^{2+}, and only a small change for electrodes incubated in Fe^{2+}. Conversely, an intense peak current was observed for the electrode incubated in Cu^{2+}, corresponding to the Cu(II)/Cu(0) redox couple (Wawrzyniak et al., 2013). Cyclic voltammetry was performed on GGH-modified gate electrodes after incubation in PBS and PBS + 10^{-5} M $CuSO_4$ (**Fig. 3B**). Peak currents were shown to vary linearly with the scan rate between 10 and 200 mV s^{-1} (not shown), which demonstrates that the process is not diffusion-limited and confirms that the electroactive copper comes from the GGH layer at the extreme vicinity of the electrode. A similar behavior was found by Yang et al., 2003.

Integration of the oxidation and reduction peaks, assuming a 2 electrons process, gave a coulombic charge of $Q_{Cu2+,ox}$ = 24 nC and $Q_{Cu2+,ox}$ = 20 nC, i.e. a surface concentration of accessible Cu^{2+} of Γ_{Cu2+} = 1.3-1.6 × 10^{-9} mol cm^{-2}, which is consistent with the density of a GGH monolayer on a gold electrode and with other reported values for similar systems (Liu et al., 2006; Wawrzyniak et al., 2013).

XPS was performed on a non-modified Au electrode after incubation in a solution containing Cu^{2+} (**Fig. 3C**) and compared to a GGH-modified Au electrode after incubation in the same conditions then used as gate in a transistor (noted Cu^{2+}@GGH-modified gate). On the bare Au gate, no copper is observed; on the contrary, on the GGH-modified gate, four peaks are visible, typical for Cu(II): the strong spin-orbit split (ΔE = 19.8 eV, with an intensity ratio of 0.5) of $Cu_{2p1/2}$ at 934.2 eV **(c)** and $Cu_{2p3/2}$ at 954 eV **(a)**, along with the two strong typical Cu^{2+} satellites at 942.4 eV **(b)** and 962.8 eV **(d)**. The double peak at 943 eV is also typical for Cu(II). No Cu(0) is observed.

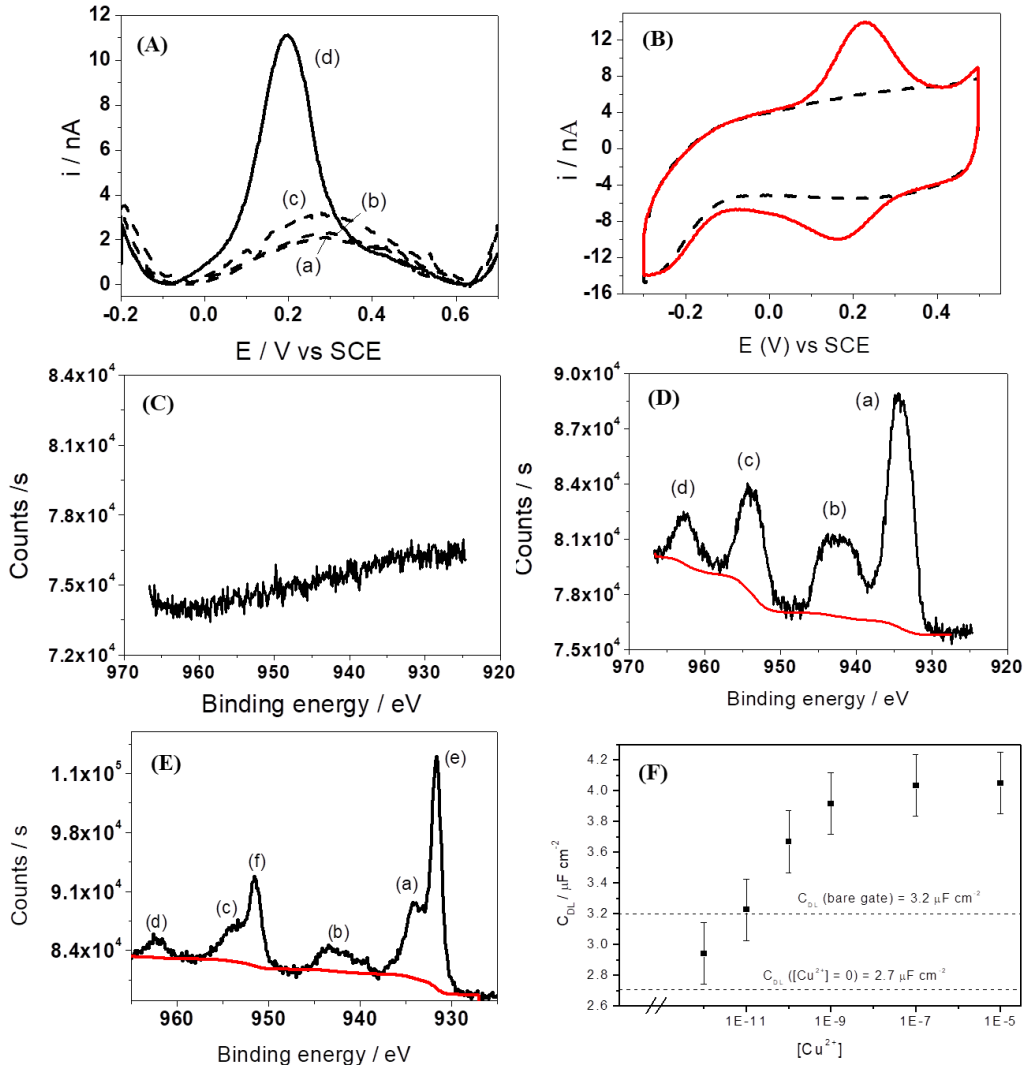

Figure 3. (A) *Square wave voltammograms of (a) a GGH-modified gate electrode (diameter = 100 µm) in PBS; (b) GGH-modified gate electrode incubated in 10^{-5} M $MnCl_2$; (c) GGH-modified gate electrode incubated in 10^{-5} M $FeSO_4$; (d) GGH-modified gate electrode incubated in 10^{-5} M $CuSO_4$.* ***(B)*** *CVs of a GGH-modified gate electrode in PBS (black dashed curve) and after incubation in 10^{-5} M $CuSO_4$* (red curve); scan rate 100 mV s^{-1}. ***(C)*** *XPS spectrum of a bare Au gate incubated in 10^{-5} M $CuSO_4$;* ***(D)*** *XPS spectrum of a GGH-modified Au gate incubated in 10^{-5} M $CuSO_4$ then used as gate electrode in transistor configuration.* ***(E)*** *XPS spectrum of a GGH-modified Au gate incubated in 10^{-5} M $CuSO_4$ then polarized in PBS at -0.1 V vs SCE to reduced Cu^{2+} into Cu(0).* ***(F)*** *Double-layer capacitances (C_{DL}) of GGH-modified gates as a function of $CuSO_4$ concentration. The capacitance for the bare Au electrode and for a GGH-modified gate before complexation of Cu^{2+} are also given. Error bars give the standard deviation for n=3*

XPS was also performed on a GGH-modified Au gate incubated in 10^{-5} M $CuSO_4$ then put back in PBS and polarized at a negative potential (-0.1 V vs SCE) in order to reduce Cu^{2+} ions into Cu(0). As shown on **Fig. 3E**, in addition to the four peaks identified on Fig. 3D, the two peaks corresponding to Cu(0) appear: one at 932 eV ($Cu_{2p3/2}$) **(e)** and the other at 951.8 eV ($Cu_{2p1/2}$) **(f)**. Differences between spectra D and E confirms that no Cu(0) is formed on the gate electrode under transistor operation.

Capacitance measurements were performed at a constant potential of -0.1 V (minimal faradic current) and frequencies between 10^5 and 10^{-1} Hz on bare Au electrode, after GGH-grafting, and after incubation of a GGH-modified electrode with Cu^{2+} (noted Cu^{2+}@GGH-modified gate) The double layer capacitance was extracted by fitting the equivalent $R_E[R_{DL}C_{DL}]$ circuit in the high frequency region. The bare Au electrode showed a capacitance of 3.2 nF, e.g. 40 µF cm^{-2}. For the GGH-modified electrode before Cu^{2+} complexation, the capacitance decreased down to 2.7 nF (33.8 µF cm^{-2}), whereas it increased for Cu^{2+}@GGH-modified gate; saturation occurred for $[Cu^{2+}] > 10^{-9}$ M (**Fig. 3F**).

3.3. Electrical characterizations

As discussed in the introduction, the electrical characteristics of EGOFETs for which the gate capacitance is significantly smaller than that of the channel (channel capacitance was found to be ca. 35 ± 15 nF for an active area of 0.5 mm^2, versus a gate capacitance varying between 2.7 and 4.2 nF) are mostly dependent on the gate/electrolyte interface (we demonstrated this behavior in a previous article, T.T.K. Nguyen *et al.*, 2018). **Fig. 4A** show the transfer curve of a bare Au-gated EGOFET and the corresponding gate current. The device shows a typical field effect behavior, with a weak gate current 50 times lower than the drain current at V_G = -0.5 V) and a maximum transconductance $g_{m,Au} = \frac{\partial I_D}{\partial V_G}$ of ca. 2.5 mA V^{-1} at -0.5 V. **Fig. 4B** shows the corresponding curves of $\sqrt{i_D}$ (and $\sqrt{i_G}$) used to estimate the threshold voltage from the slope in saturation regime, V_{Th} = -0.34 ± 0.01 V. **Fig. 4C** shows the output curves at different V_G from +0.2 V to -0.6 V (only curves from -0.3 V to -0.6 V are visible, curves from 0.2 to -0.2 V overlap). The I_{on}/I_{off} ratio is high, ca. 1200, which demonstrates the excellent quality of the device.

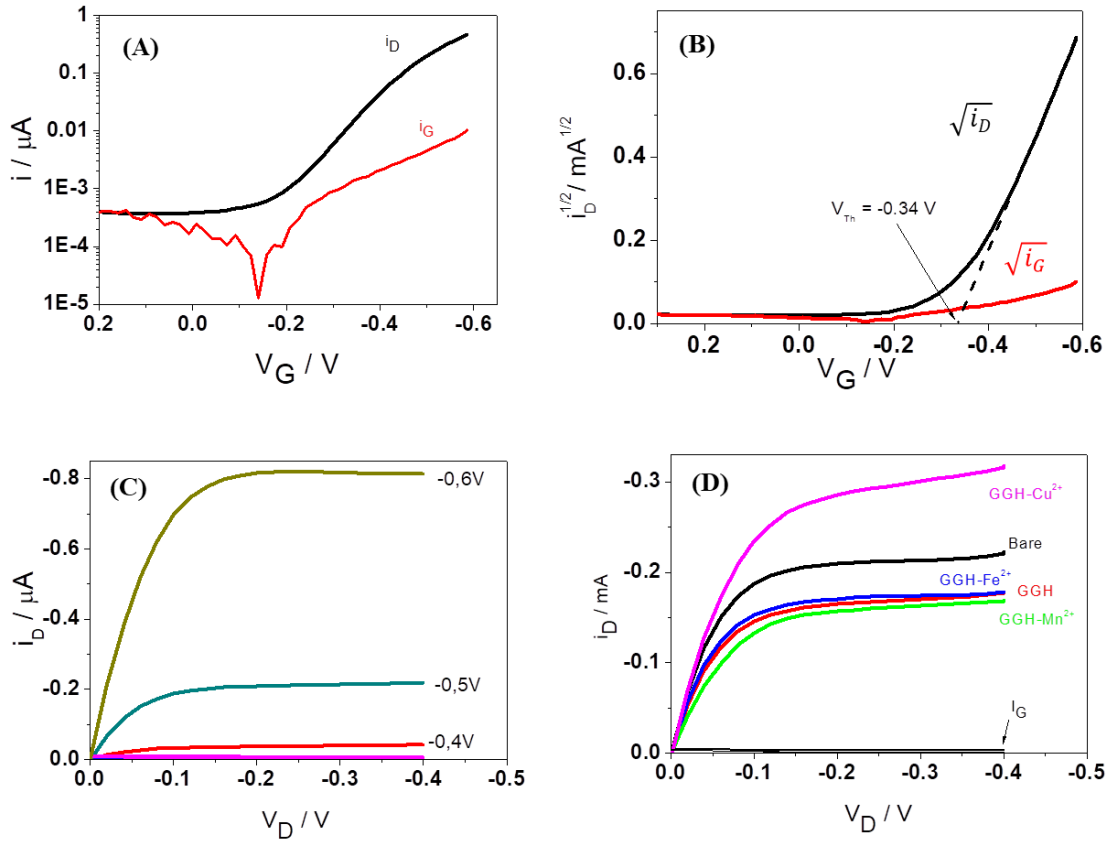

Figure 4. ***(A)*** *Transfer curve (black) of a bare Au gate EGOFET obtained by sweeping the gate voltage form +0.2 V down to -0.6 V. Scan rate of 170 mV* s^{-1}*;* V_D *= -0.4 V. Gate current shown in red.* ***(B)*** *Corresponding plot of* $\sqrt{I_D}$ *=* $f(V_G)$ *(black), and* $\sqrt{I_G}$ *(red curve).* L *= 10* μm*;* W *= 10 mm. Electrolyte: aerated MilliQ water.* ***(C)*** *Output curves at various gate voltages, for a bare Au gate.* ***(D)*** *Output curves (*V_G *= -0.5 V) for bare Au gate, GGH-modified gate and for GGH-modified gates incubated in* 10^{-5} *M* Fe^{2+}, Mn^{2+} *or* Cu^{2+}.

3.4. Characterization of Cu^{2+} capture in transistor configuration

On **Fig. 4D** are shown output curves obtained with bare gate, GGH-modified gate and GGH-modified gates incubated with 10^{-5} *M* Cu^{2+}, Mn^{2+} or Fe^{2+}. Behaviors are consistent with capacitances shown in Section 3.2: I_D decreases after grafting of GGH but increases when Cu^{2+} is complexed. **Fig. 5A** shows the small shift in threshold voltage (V_{Th} = -0.36 ± 0.01 V; ΔV_{Th} = -0.02 ± 0.02 V) induced by the presence of GGH on the gate electrode. The maximum transconductance $g_{m,GGH}$ is ca. 2.2 mA V^{-1} at -0.5 V, i.e. slightly lower than $g_{m,Au}$. **Fig. 5B**

shows that the threshold voltage is significantly shifted upon Cu^{2+} uptake (ΔV_{Th} = + 120 ± 20 mV for [Cu^{2+}] = 10^{-7} M).

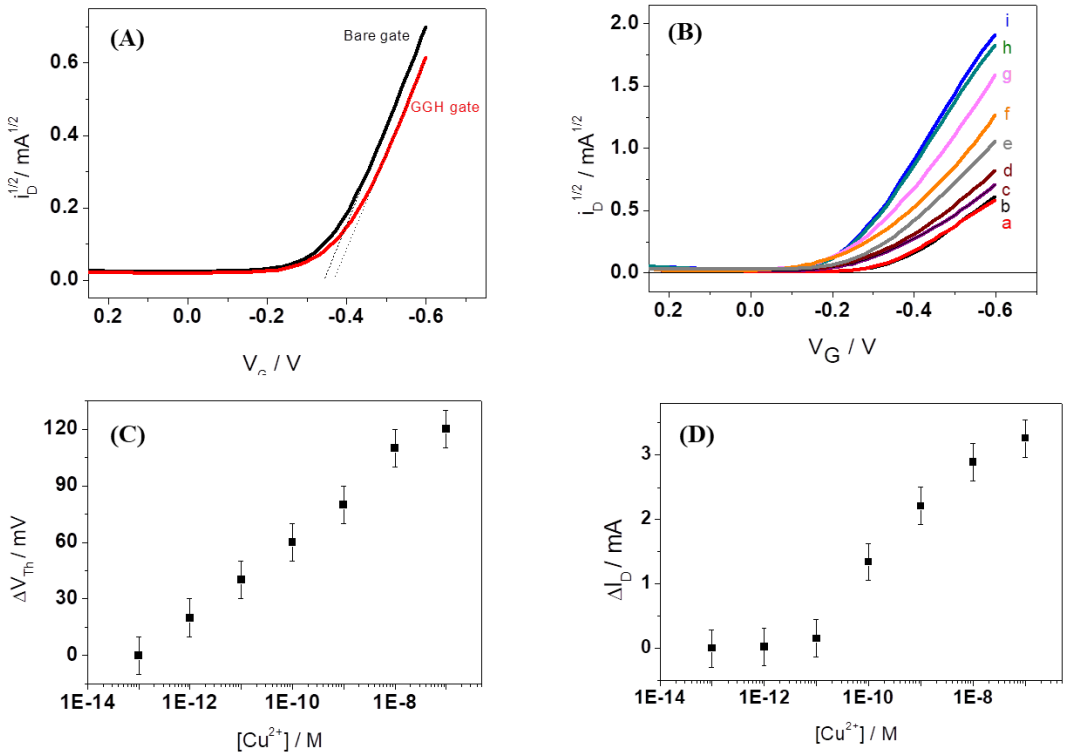

Figure 5. (A) *Plots of $\sqrt{I_D}$ = f(V_G) for a bare Au gate (black) and GGH-modified gate (red); both experiments in aerated MilliQ water. V_{Th} (Bare/MilliQ) = -0.34 ± 0.01 V; V_{Th} (GGH/MilliQ) = -0.36 ± 0.01 V.* ***(B)*** *Plots of $\sqrt{I_D}$ = f(V_G) for Cu^{2+}@GGH-modified gate in tap water for various Cu^{2+} concentrations: a: no Cu^{2+}; b: 10^{-13} M Cu^{2+}; c: 10^{-12} M; d: 10^{-11} M; e: 10^{-10} M; f: 5.10^{-10} M; g: 10^{-9} M; h: 10^{-8} M; i: 10^{-7} M.). V_{Th} (GGH/Tap water) = -0.34 ± 0.01 V. V_{Th} (Cu^{2+}@GGH/Tap water) = -0.22 ± 0.01 V. V_D = -0.4 V.* ***(C)*** *Calibration curve obtained from changes in V_{Th} as a function of [Cu^{2+}]. ΔV_{Th} = V_{Th} (Cu^{2+}@GGH) - V_{Th} (GGH). The R^2 value is 0.99291 for the whole 10^{-13} - 10^{-7} range.* ***(D)*** *Calibration curve obtained from changes in I_D (at V_D = -0.4 V and V_G = -0.6 V) as a function of [Cu^{2+}]. Results obtained from 3 experiments.*

The drain current flowing through EGOFET devices is known to be sensitive to several parameters: the threshold voltage V_{Th}, the effective capacitance C_{eff} and the charge carrier's mobility μ. The transconductance g_m (slope of the transfer curves) is proportional to the

product of the latter two, $g_m = \frac{W}{L} V_D \mu C_{eff}$. Upon copper complexation by GGH, g_m increases: Cu^{2+}@GGH-modified gate devices present a $g_{m,GGH@Cu2+}$ = 16 mA V^{-1} at -0.5 V for 10^{-7} M Cu^{2+}, significantly higher than for GGH-modified gate without copper. This increase is much more pronounced than the capacitance increase shown on Fig. 3F, which indicates that not only the capacitance is responsible for the current increase. Indeed, it is shown that V_{Th} changes more significantly, strongly shifting towards more positive values (shift of ca. +0.12 V for incubation in [Cu^{2+}] = 10^{-7} M). The sensitivity extracted from the slope of ΔV_{Th} (**Fig. 5C**, linear region) is s_{Th} = 20 mV dec^{-1}.

First of all, we have shown by XPS measurements that no Cu(0) is formed at the gate under transistor operation. This is confirmed by the direction of the V_{Th} shift. Indeed, here the V_{Th} shifts towards positive values; conversely, we have shown in a previous work (Kergoat, Herlogsson *et al.*, 2012) that V_{Th} shifts towards more negative values for a copper gate instead of a gold gate. Therefore, the shift may be explained in terms of charge distribution at the interfaces: accumulation of Cu^{2+} at the gate interface, for a given negative gate voltage, increases the amount of positive charges at this interface, so that less negative potential is needed to accumulated a given charge density at the gate and symmetrically a given holes density within the semiconductor. We observed the same behavior in a previous work (Fillaud *et al.*, 2018) in which protonation of a hydrogel on the gate electrode led to a positive V_{Th} shift as well. A similar behavior of the V_{Th} as a function of charges immobilized on the gate electrode has been reported by other authors (Buth *et al.* 2011; Buth *et al.* 2012; Berto *et al.*, 2017; Diacci *et al.*, 2017).

In term of analytical application, we have shown that the influence of tap or MilliQ water is negligible on the transfer characteristics, so that the device was applied to detection of Cu^{2+} cations in tap water. Cu^{2+} ions were added into aerated tap water (pH 7.7) by addition of the corresponding quantity of copper sulfate. The tap water used proved to be completely free of copper ions but contained iron (1.8 µg L^{-1}), free chlorine (0.2 mg L^{-1}), nitrates: (27.7 mg L^{-1}), calcium (94.7 mg L^{-1}), dihydrogenocarbonates (250 mg L^{-1}), chloride (24.2 mg L^{-1}), fluoride (0.1 mg L^{-1}), potassium (2.1 mg L^{-1}), sodium (8.1 mg L^{-1}), sulfates (20.5 mg L^{-1}), for a conductivity of around 500 µS cm^{-1}. **Fig. 5C** shows the calibration curve relative to ΔV_{Th}, with a linear variation of I_D versus log[Cu^{2+}] between 10^{-13} to 10^{-8} M. In terms of threshold voltage, the sensitivity is ca. 20 mV dec^{-1}. **Fig. 5D** shows the calibration curve relative to ΔI_D, for which a linear region is defined between 10^{-11} M and 10^{-8} M, with a sensitivity of 1 mA

dec^{-1}. The limit of detection is ca. 5.10^{-11} M when considering drain current changes, and ca. 10^{-12} M when considering threshold voltage changes.

4. Conclusion

EGOFETs for which the gate electrode was modified with the Cu^{2+}-specific tripeptide Gly-Gly-His can transduce Cu^{2+} complexation through a significant threshold voltage shift or an increase in drain current. The limit of detection is ca. 10^{-12} M and the sensitivity in the linear range (10^{-12} – 10^{-8} M) is of 20 mV dec^{-1} (threshold voltage changes) and 1 mA dec^{-1} (drain current changes). This work demonstrates that functionalization of the gate electrode of an EGOFET is efficient to make a sensor, and that charges carried by the target analyte, providing that experiments are done in low ionic strength solutions, are able to influence the threshold voltage of the device.

References

Barbier, B., Pinson, J., Desarmot, G., Sanchez, M. Electrochemical Bonding of Amines to Carbon Fiber Surfaces Toward Improved Carbon-Epoxy Composites. J. Electrochem. Soc., Vol. 137, No. 6, June 1990. DOI: 10.1149/1.2086794.

Daniel Bélanger, Jean Pinson. Electrografting: a powerful method for surface modification. Chem. Soc. Rev., 2011, 40, 3995-4048. DOI: 10.1039/C0CS00149J.

M. Berto, Stefano Casalini, Michele Di Lauro, Simone L. Marasso, Matteo Cocuzza, Denis Perrone, Marcello Pinti, Andrea Cossarizza, Candido F. Pirri, Daniel T. Simon, Magnus Berggren, Francesco Zerbetto, Carlo A. Bortolotti, and Fabio Biscarini. Biorecognition in Organic Field Effect Transistors Biosensors: The Role of the Density of States of the Organic Semiconductor. Analytical Chemistry 2016 88 (24), 12330-12338. DOI: 10.1021/acs.analchem.6b03522.

M. Berto, C. Diacci, R. D'Agata, M. Pinti, E. Bianchini, M. Di Lauro, S. Casalini, A. Cossarizza, M. Berggren, D. Simon, G. Spoto, F. Biscarini, C. A. Bortolotti, Adv. Biosys. 2018, 2, 1700072. DOI: 10.1002/adbi.201700072

Buth, F., Kumar, D., Stutzmann, M., & Garrido, J. A. (2011). Electrolyte-gated organic field-effect transistors for sensing applications. Applied Physics Letters, 98, 76, 153302. DOI: 10.1063/1.3581882

Buth, F., Donner, A., Sachsenhauser, M., Stutzmann, M., & Garrido, J. A. (2012). Biofunctional Electrolyte- Gated Organic Field- Effect Transistors. Advanced materials, 24(33), 4511-4517.

Casalini, S., Leonardi, F., Cramer, T., & Biscarini, F. (2013). Organic field-effect transistor for label-free dopamine sensing. Organic Electronics, 14(1), 156-163. DOI: 10.1016/j.orgel.2012.10.027.

Casalini, S., Dumitru, A. C., Leonardi, F., Bortolotti, C. A., Herruzo, E. T., Campana, A., De Oliveira, R.F., Cramer, T., Garcia, R., Biscarini, F. 2015. ACS Nano 9, 5051–5062. DOI: 10.1021/acsnano.5b00136.

Chow, E. and Gooding, J. (2006), Peptide Modified Electrodes as Electrochemical Metal Ion Sensors. Electroanalysis, 18: 1437-1448. doi:10.1002/elan.200603558

Cotrone, S., Ambrico, M., Toss, H., Angione, M.D., Magliulo, M., Mallardi, A., Berggren, M., Palazzo, G.; Horowitz, G., Ligonzo, T., Torsi, L. 2012. Organic Electronics 13, 638-644.

Diacci, C., Berto, M., Di Lauro, M., Bianchini, E., Pinti, M., Simon, D. T., F. Biscarini, Bortolotti, C. A. (2017). Label-free detection of interleukin-6 using electrolyte gated organic field effect transistors. Biointerphases, 12(5), 05F401. DOI: 10.1116/1.4997760

Laure Fillaud, Thomas Petenzi, Justine Pallu, Benoit Piro, Giorgio Mattana, and Vincent Noel. S witchable Hydrogel-Gated Organic Field-Effect Transistors. Langmuir 2018 34 (12), 3686-3693. DOI: 10.1021/acs.langmuir.8b00183

X. Gan, H. Zhao, X. Quan, Zhang, Y., 2016. An Electrochemical Sensor based on p-aminothiophenol/Au Nanoparticle-Decorated HxTiS2 Nanosheets for Specific Detection of Picomolar Cu (II). Electrochimica Acta 190, 480-489.

J. Justin Gooding, D. Brynn Hibbert, Wenrong Yan. Electrochemical Metal Ion Sensors. Exploiting Amino Acids and Peptides as Recognition Elements. Sensors 2001, 1(3), 75-90; doi:10.3390/s10300075

Kergoat, L., Herlogsson, L., Piro, B., Pham, M. C., Horowitz, G., Crispin, X., & Berggren, M. (2012). Tuning the threshold voltage in electrolyte-gated organic field-effect transistors. Proceedings of the National Academy of Sciences, 109(22), 8394-8399. DOI: 10.1073/pnas.1120311109.

Kergoat, L., Piro, B., Berggren, M., Horowitz, G., & Pham, M. C. (2012). Advances in organic transistor-based biosensors: from organic electrochemical transistors to electrolyte-gated organic field-effect transistors. Analytical and bioanalytical chemistry, 402(5), 1813-1826.

Kergoat, L., Piro, B., Berggren, M., Pham, M.C., Yassar, A., Horowitz, G. 2012. Organic Electronics 13, 1-6.

Kozlowski, H.; Bal, W.; Dyba, M.; Kowalik-Jankowska, T. Specific structure-stability relations in metallopeptides. Coord. Chem. Rev. 1999, 184, 319–346.

J. Liu, Lu, Y., 2007. Colorimetric Cu2+ detection with a ligation DNAzyme and nanoparticles. Chemical Communications, 4872-4874.

Liu, G., Nguyen, Q. T., Chow, E., Böcking, T., Hibbert, D. B., Gooding, J. J. (2006). Study of Factors Affecting the Performance of Voltammetric Copper Sensors Based on Gly- Gly-His Modified Glassy Carbon and Gold Electrodes. Electroanalysis, 18, 1141-1151. DOI: 10.1002/elan.200603546)

M. Magliulo, D. De Tullio, I. Vikholm-Lundin, W. M. Albers, T. Munter, K. Manoli, G. Palazzo, L. Torsi, *Anal. Bioanal. Chem.* **2016**, *408*, 3943-3952. DOI: 10.1007/s00216-016-9502-3.

Mulla, M.Y., Tuccori, E., Magliulo, M., Lattanzi, G., Palazzo, G., Persaud, K., Torsi, L. 2015. Nature communications, 6, 6010. DOI: 10.1038/ncomms7010.

Palazzo, G., Tullio, D.D., Magliulo, M., Mallardi, A., Intranuovo, F., Mulla, M.Y., Favia, P., Vikholm-Lundin, I., Torsi, L. 2015, Adv. Mater. 27, 911–916

Piro, B., Wang, D., Benaoudia, D., Tibaldi, A., Anquetin, G., Noel, V., Reisberg, S., Mattana, G., Jackson, B. 2017, Biosens. Bioelectron 92, 215-220.

T.T.K. Nguyen, T.N. Nguyen, G. Anquetin, S. Reisberg, V. Noël, G. Mattana, J. Touzeau, F. Barbault, M.C. Pham, B. Piro. Biosensors and Bioelectronics, Volume 113, 2018, Pages 32-38. DOI: 10.1016/j.bios.2018.04.051.

Suspène, C., Piro, B., Reisberg, S., Pham, M.C., Toss, H., Berggren, M., Yassar, A., Horowitz, G. 2013. J. Mater. Chem. B, 1, 2090-2097.

Thomas, M. S., White, S. P., Dorfman, K. D., & Frisbie, C. D. (2018). Interfacial Charge Contributions to Chemical Sensing by Electrolyte-Gated Transistors with Floating Gates. The journal of physical chemistry letters, 9, 1335-1339. DOI: 10.1021/acs.jpclett.8b00285

D. Udhayakumari, S. Naha, Velmathi, S., 2017. Colorimetric and fluorescent chemosensors for Cu2+. A comprehensive review from the years 2013-15. Analytical Methods 9, 552-578.

Scott P. White, Kevin D. Dorfman, and C. Daniel Frisbie. Label-Free DNA Sensing Platform with Low-Voltage Electrolyte-Gated Transistors. Analytical Chemistry 2015 87 (3), 1861-1866. DOI: 10.1021/ac503914x

Sigel, H., Martin, R.B. Coordinating Properties of the Amide Bond. Stability and Structure of Metal Ion Complexes of Peptides and Related Ligands. Chem. Rev. 1982, 82, 385–426.

Wawrzyniak, U.E., Ciosek, P., Zaborowski, M., Liu, G., Gooding, J.J. Gly-Gly-His Immobilized On Monolayer Modified Back-Side Contact Miniaturized Sensors for Complexation of Copper Ions. Electroanalysis 2013, 25, No. 6, 1461 – 1471. DOI: 10.1002/elan.201200667.

WHO (World Health Organization). 1993. Guidelines for Drinking-Water Quality. Vol. 1. Recommendations, 2nd Ed. Geneva, Switzerland: World Health Organization.

X. Xu, W. L. Daniel, W. Wei, Mirkin, C.A., 2010. Colorimetric Cu2+ Detection Using DNA-Modified Gold-Nanoparticle Aggregates as Probes and Click Chemistry. Small 6(5), 623-626.

W. Yang, David Jaramillo, J. J. Gooding, D. B. Hibbert, R. Zhang, G. D. Willett, Fisher, K.J., 2001, 1982-1983. Sub-ppt detection limits for copper ions with Gly-Gly-His modified electrodes. Chemical Communications, 1982-1983

Z. Yao, Y. Yang, X. Chen, X. Hu, L. Zhang, L. Liu, Y. Zhao, Wu, H.-C., 2013. Visual Detection of Copper(II) Ions Based on an Anionic Polythiophene Derivative Using Click Chemistry. Analytical Chemistry 85(12), 5650-5653.

W. Yang, Edith Chow, G.D. Willett, D. Brynn Hibbert, J. J. Gooding. Exploring the use of the tripeptide Gly–Gly–His as a selective recognition element for the fabrication of electrochemical copper sensors.Analyst, 2003,128, 712-718. DOI: 10.1039/B212881K.

R. Zhu, G. Zhou, F. Tang, C Tong, Y. Wang, Wang, J., 2017. Detection of Cu2+ in Water Based on Histidine-Gold Labeled Multiwalled Carbon Nanotube Electrochemical Sensor. International Journal of Analytical Chemistry 2017, Article ID 1727126.

Supplementary Materials

1. Transistor fabrication

Substrates were n-type (100) Si wafers with 200-nm thick thermally grown oxide layer (BT Electronics, France). In cleanroom, wafers were sequentially washed in acetone and isopropanol in an ultrasonic bath during 3 min each, cleaned in an ozone cleaner (UVOCS 10x10 OES, USA) for 3 minutes then dried 10 minutes at 120°C on a hot plate. The AZ 5214 photoresist was spin-coated during 30 s at 4000 rpm, then baked at 110°C for 1 minute.

Interdigitated source and drain gold electrodes were UV-photolithographied (exposure to UV light during 1.8 s in low vacuum contact mode, hard baking for 2 min at 120°C and again exposure the full wafer to UV light for 1 min), then developed in AZ 326MIF for 15 s and in EDI for 60s. Finally, wafers were washed in water and dried by flushing argon.

Before lithography, wafers were treated under ozone for 2 minutes then an adhesion layer of 10 nm of titanium (0.15 nm s^{-1}) followed by a gold layer of 100 nm (0.30 nm s^{-1}) were evaporated through a photomask so that the transistors present a total channel width (*W)* of 30000 µm and a channel length (*L*) of 10 µm (**Scheme SI-1**).

For spin-coating DPP-DTT, a solution of 2.5 mg mL^{-1} DPP-DTT dissolved in a mixture of 93/7 v/v chlorobenzene:dichlorobenzene was prepared in a round-bottom flask and kept at 110°C under stirring. After cleaning in acetone and isopropanol for 2 minutes, wafers were spin-coated with 300 µL of the DPP-DTT solution at 110°C dropped onto the wafer, at 4000 rpm during 180 s, with an acceleration of 500 rpm s^{-1}, then baked at 110°C for 1 h in an oven in air.

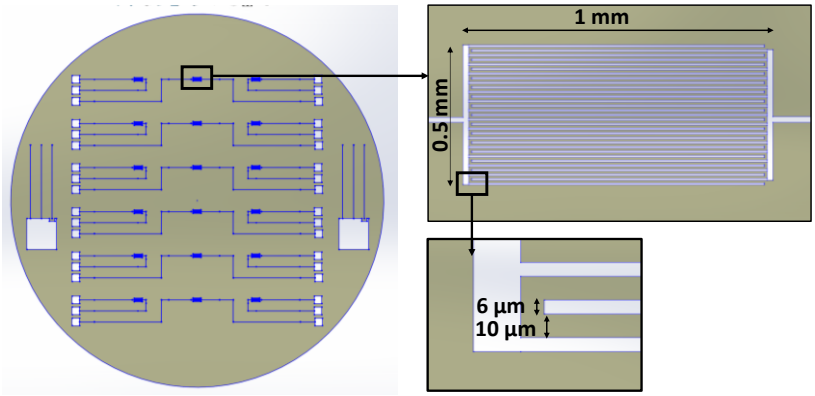

Scheme SI-1. *View of (left) a 2 inches Si wafer onto which 18 transistors (interdigitated source and drain) are lithographed and (right), details of the device dimensions, including the digit width (6 µm) and the channel length (10 µm). The total channel width is 30000 µm.*

2. Gate fabrication

Lab-made gate microelectrodes (100 µm in diameter) were fabricated from gold wires inserted in a capillary glass tube using a laser-based micropipette puller (Sutter Instrument model P-2000).

The borosilicate capillary was cleaned with ethanol then dried before a first pulling (heat = 380; filament: 4; velocity: 15; delay: 120). After this first step, the gold wire was inserted in the capillary, which was pulled a second time under vacuum during 50 s (heat: 300; filament: 4; velocity: 15; delay: 120) in order to seal the gold wire and the glass together, without air bubbles in-between. A thirst pull was done until the capillary break (heat: 300; filament: 4; velocity: 15; delay: 120; pull: 120). The electrical contact was made with a Cu wire using Pb/Sn solder. Electrodes were polished before use during 3 min with 1 µm and 3 min with 0.3 µm alumina slurry. After this step, the electrode area was measured by cyclic voltammetry recorded in 0.1 M H_2SO_4 + 10^{-3} M dopamine; if the expected area (7.85×10^{-5} cm^2 ± 10%) was not found, the electrode was recycled.

3. XPS

Table SI.1. *XPS data for GGH-modified gate electrode: binding energy, area and relative atomic percentage.*

Element	Binding energy / eV	Area / CPS.eV	Atomic %	Atomic %
Au_{4f}	84.2	969943	20.7	Excluded
C_{1s} A	285	48126	23.9	Excluded
C_{1s} B	286.6	20366	10.1	29.7
C_{1s} C	288.4	21413	10.7	31.5
N_{1s}	401.1	41075	13.2	38.8
O_{1s}	532.0	104076	21.4	Excluded

GENERAL CONCLUSIONS

In this work, two types of biosensors have been developed, having excellent selectivity and detection limits, i.e. within the picomolar range. The versatility of the techniques provided powerful tools for detection of pollutants (diclofenac, 2,4-D and heavy metals). In Chapter II, I demonstrated an innovative electrochemical displacement assay, based on an electrode modified with an electroactive probe and a specific capture probe, with the ability to detect diclofenac from 0.1 pM to 0.1 nM (25 pg L^{-1} up to 25 ng L^{-1}). Applying this method, a commercial diclofenac-containing drug was detected in tap water. Its performances were very competitive compared to other electrochemical diclofenac immunosensors already published in the literature. This work definitely paved the way for detection of diclofenac in real-samples such as tap water or surface waters in which concentrations are from a few tens of pg L^{-1} (a few hundreds of fM) to several tens of ng L^{-1} (a few hundreds of pM) depending on the geographical context (Word Health Organization, 2011), or even sewage in which the average diclofenac concentration is approximately 400 ng L^{-1} (a few nM). For further studies, the stability of the sensor needs to be investigated in more aggressive media and over long periods of time.

In Chapter III, I moved from classical electrochemistry to an innovative device: I investigated the electrolyte-gated organic field effect transistor and I showed that the gate electrode can be used as the sensing area in such device. I applied the gate-modified EGOFET for detection of 2,4-D, a well-known broad leave killer. The gate was first functionalized by a molecule similar to 2,4-D, then a 2,4-D antibody was complexed. The capture of the 2,4-D antibody led to a capacitance decrease, therefore a drain current decrease. Using this antibody-modified gate, addition of 2,4-D led to an increase in gate capacitance, corresponding to a drain current increase, for concentrations as low as 5 fM. This limit of detection is excellent compared to the existing literature or to pollution levels. For example, the WHO reported in its Guidelines for drinking-water quality, 2,4-D levels in drinking water in US and Canada from 10^{-7} M to 5×10^{-10} M for the most polluted areas, but generally lower than 5×10^{-11} M (2003). In France, where 2,4-D has been forbidden for years, the French Institute for Industrial and Environmental Risks (INERIS) recommended in 2012 values lower than 5×10^{-11} M in

drinking water. Sensitive techniques, such as the one described in this Chapter III, would be useful to draw a more precise picture of the pollution levels and identify pollution sources.

In Chapter IV, I demonstrated that EGOFETs can be sensitive not only to changes in capacitance at the gate electrode (demonstrated in Chapter III) but also to charges accumulated on the gate. As an example, I have shown that the capture of Cu^{2+} by the Gly-Gly-His peptide electrografted on the gate led to a positive shift of the threshold voltage (shift toward less negative values), for concentrations as low as 5×10^{-13} M (3×10^{-8} mg L^{-1}). This limit of detection is low compared to the published literature and significantly lower than values reported in the Guidelines of the WHO for copper concentrations in drinking water (2 mg L^{-1}).

From a more general point of view, I believe that these studies brought a significant contribution in the understanding of the transduction mechanisms involved whether in the field of amperometric immunosensors as well as in that of electrolyte-gated field effect transistors. From these works, I was able to write three articles, from which to have been already published in high impact ISI journals.